



**AFRL-RB-WP-TR-2011-3040**

# **REDUCED-ORDER MODELS FOR ACOUSTIC RESPONSE PREDICTION**

**Robert W. Gordon and Joseph J. Hollkamp**

**Analytical Structural Mechanics Branch  
Structures Division**

**JULY 2011  
Final Report**

**Approved for public release; distribution unlimited.**

*See additional restrictions described on inside pages*

**STINFO COPY**

**AIR FORCE RESEARCH LABORATORY  
AIR VEHICLES DIRECTORATE  
WRIGHT-PATTERSON AIR FORCE BASE, OH 45433-7542  
AIR FORCE MATERIEL COMMAND  
UNITED STATES AIR FORCE**

## NOTICE AND SIGNATURE PAGE

Using Government drawings, specifications, or other data included in this document for any purpose other than Government procurement does not in any way obligate the U.S. Government. The fact that the Government formulated or supplied the drawings, specifications, or other data does not license the holder or any other person or corporation; or convey any rights or permission to manufacture, use, or sell any patented invention that may relate to them.

This report was cleared for public release by the USAF 88<sup>th</sup> Air Base Wing (88 ABW) Public Affairs Office (PAO) and is available to the general public, including foreign nationals. Copies may be obtained from the Defense Technical Information Center (DTIC) (<http://www.dtic.mil>).

AFRL-RB-WP-TR-2011-3040 HAS BEEN REVIEWED AND IS APPROVED FOR PUBLICATION IN ACCORDANCE WITH THE ASSIGNED DISTRIBUTION STATEMENT.

\*//Signature//

---

ROBERT W. GORDON  
Project Engineer  
Analytical Structural Mechanics Branch  
Structures Division

//Signature//

---

MICHAEL J. SHEPARD, Chief  
Analytical Structural Mechanics Branch  
Structures Division

//Signature//

---

DAVID M. PRATT, PhD  
Technical Advisor  
Structures Division  
Air Vehicles Directorate

This report is published in the interest of scientific and technical information exchange, and its publication does not constitute the Government's approval or disapproval of its ideas or findings.

\*Disseminated copies will show “//Signature//” stamped or typed above the signature blocks.

REPORT DOCUMENTATION PAGE				Form Approved OMB No. 0704-0188	
<p>The public reporting burden for this collection of information is estimated to average 1 hour per response, including the time for reviewing instructions, searching existing data sources, gathering and maintaining the data needed, and completing and reviewing the collection of information. Send comments regarding this burden estimate or any other aspect of this collection of information, including suggestions for reducing this burden, to Department of Defense, Washington Headquarters Services, Directorate for Information Operations and Reports (0704-0188), 1215 Jefferson Davis Highway, Suite 1204, Arlington, VA 22202-4302. Respondents should be aware that notwithstanding any other provision of law, no person shall be subject to any penalty for failing to comply with a collection of information if it does not display a currently valid OMB control number. <b>PLEASE DO NOT RETURN YOUR FORM TO THE ABOVE ADDRESS.</b></p>					
1. REPORT DATE (DD-MM-YY) July 2011		2. REPORT TYPE Final		3. DATES COVERED (From - To) 01 October 2003 – 30 April 2011	
4. TITLE AND SUBTITLE REDUCED-ORDER MODELS FOR ACOUSTIC RESPONSE PREDICTION				5a. CONTRACT NUMBER In-house	
				5b. GRANT NUMBER	
				5c. PROGRAM ELEMENT NUMBER 62201F	
6. AUTHOR(S) Robert W. Gordon and Joseph J. Hollkamp				5d. PROJECT NUMBER 2401	
				5e. TASK NUMBER	
				5f. WORK UNIT NUMBER A0830G	
7. PERFORMING ORGANIZATION NAME(S) AND ADDRESS(ES) Analytical Structural Mechanics Branch (AFRL/RBSM) Structures Division Air Force Research Laboratory, Air Vehicles Directorate Wright-Patterson Air Force Base, OH 45433-7542 Air Force Materiel Command, United States Air Force				8. PERFORMING ORGANIZATION REPORT NUMBER AFRL-RB-WP-TR-2011-3040	
9. SPONSORING/MONITORING AGENCY NAME(S) AND ADDRESS(ES) Air Force Research Laboratory Air Vehicles Directorate Wright-Patterson Air Force Base, OH 45433-7542 Air Force Materiel Command United States Air Force				10. SPONSORING/MONITORING AGENCY ACRONYM(S)  AFRL/RBSM	
				11. SPONSORING/MONITORING AGENCY REPORT NUMBER(S) AFRL-RB-WP-TR-2011-3040	
12. DISTRIBUTION/AVAILABILITY STATEMENT Approved for public release; distribution unlimited.					
13. SUPPLEMENTARY NOTES PAO Case Number: 88ABW-2011-2884; Clearance Date: 24 May 2011. Report contains color.					
14. ABSTRACT This report documents an in-house research effort to evaluate, refine, and validate reduced-order methods for computing the response of air vehicle skin panels to extreme acoustic and thermal loading. These methods reduce a finite element model to a reduced-order system of nonlinear modal equations. A short historical review of acoustic response prediction methods is presented followed by a detailed discussion of the methods. Several refinements to the methods are developed. The methods are applied to several example problems ranging from a clamped-clamped beam to a curved panel. Model predictions are compared to results from full-order simulations and well-characterized experiments. Effects of nonlinear large deformation, thermal loading and acoustic coupling are included in the methods. The reduced-order methods are shown to provide accurate prediction of acoustic response with orders-of-magnitude reductions in computational cost over full-order finite element analysis.					
15. SUBJECT TERMS sonic fatigue, reduced-order models, acoustic response, modal models, thermal loads, nonlinear, random vibration					
16. SECURITY CLASSIFICATION OF:			17. LIMITATION OF ABSTRACT: SAR	18. NUMBER OF PAGES 228	19a. NAME OF RESPONSIBLE PERSON (Monitor) Robert W. Gordon
a. REPORT Unclassified	b. ABSTRACT Unclassified	c. THIS PAGE Unclassified			19b. TELEPHONE NUMBER (Include Area Code) N/A

## TABLE OF CONTENTS

<u>Section</u>	<u>Page</u>
List of Figures .....	iii
List of Tables .....	ix
Acknowledgements.....	x
1. Summary .....	1
2. Background .....	3
2.1 Sonic Fatigue and Nonlinear Response .....	3
2.2 Prediction Capability .....	6
2.3 Nonlinear Reduced-Order Models.....	7
2.3.1 The Modal Basis .....	9
2.3.2 Condensation of Membrane Effects.....	11
2.3.3 Nonlinear Stiffness Evaluation .....	12
2.3.4 Acoustic Coupling .....	13
3. Methods Development.....	15
3.1 Estimating the Bending Coefficients with Implicit Condensation .....	15
3.2 The Load Cases.....	20
3.3 The Expansion Process and the ICE Method.....	22
3.4 Explicit Condensation of Membrane Effects.....	25
3.5 Thermal Effects.....	27
3.6 Acoustic Coupling using Uncoupled Mode Shapes.....	29
3.7 Acoustic Coupling using Mode Shapes of the Coupled System.....	31
3.8 Implementation .....	34
3.9 Implementation Example .....	38
4. Applications.....	41
4.1 The 9-inch Clamped-Clamped Beam.....	41
4.1.1 Reduced-Order Models.....	41
4.1.2 Experiment Design.....	47
4.1.3 Characterization Testing .....	49
4.1.4 Random Response Testing.....	51
4.1.5 Comparison of ROM and Experimental Results .....	58
4.2 The 18-inch Clamped-Clamped Beam.....	66
4.2.1 The Example Problem.....	66
4.2.2 The Reduced-Order Models.....	66
4.2.3 Discussion of Results.....	68
4.3 The Curved Beam .....	72
4.3.1 The Example Problem.....	72
4.3.2 Reduced-Order Models.....	72
4.3.3 Discussion of Results.....	73
4.4 The Clamped Plate.....	78
4.4.1 Test Article Description.....	78
4.4.2 Initial Shaker Test.....	80
4.4.3 Vacuum Shaker Test.....	93
4.4.4 Finite element Prediction of Acoustic Radiation Damping .....	103
4.4.5 Initial Acoustic Test of the Clamped Plate .....	111

<u>Section</u>	<u>Page</u>
4.4.6 Acoustic Test of the Clamped Plate with an Improved Fixture.....	126
4.4.7 Coupled Models of the Plate Test Article in the SEF .....	138
4.4.8 Structural-Acoustic Coupling Sensitivity Analysis .....	146
4.5 The Curved Panel.....	155
4.5.1 Test Article Description.....	156
4.5.2 Numerical Study of the Clamped Panel.....	157
4.5.3 Initial Acoustic Test of the Curved Panel Test Article .....	170
4.5.4 Elevated Temperature Tests of the Curved Panel Test Article.....	173
4.6 Coupled Structural-Acoustic Examples.....	184
4.6.1 2-D Beam in an Exterior Acoustic Domain using Complex Reduced- Order Models .....	184
4.6.2 2-D Beam Coupled Structural-Acoustic Examples using the Uncoupled Modes Method.....	194
5. Conclusions .....	203
6. References .....	207

## LIST OF FIGURES

<u>Figure</u>	<u>Page</u>
1. Straight beam with clamped ends .....	3
2. RMS strain vs sound pressure level for an aluminum alloy panel.....	4
3. Strain PSD for an aluminum alloy panel at several sound pressure levels .....	5
4. Probability density functions of displacement and strain for a clamped beam.....	6
5. Procedure for an indirect method.....	35
6. The PSD of the response of the center of the beam due to an 8g, 0-500 Hz base excitation using one-mode models .....	44
7. The PSD of the response of the center of the beam due to an 8g, 0-500 Hz base excitation using two-mode models .....	46
8. The PSD of the response of the center of the beam due to a 2g, 0-500 Hz base excitation using two-mode models .....	47
9. The PSD of the response of the center of the beam due to an 8g, 0-500 Hz base excitation using two-mode models .....	48
10. Beam specimen and fixture mounted on the electrodynamic shaker.....	49
11. Idealized model of the beam with estimated boundary springs.....	50
12. Frequency and amplitude estimates for a set of free response data from Case A and a linear curve fit through the estimates .....	52
13. Displacement at the beam mid-span for Case A.....	55
14. Displacement at the beam mid-span for Case B .....	55
15. Surface strain at the mid-span of the beam for Case B.....	56
16. Displacement at the mid-span of the beam for Case B and for Case A with a frequency shift of -13.8 Hz .....	56
17. Displacement at the mid-span of the beam for Case C .....	57
18. Surface strain at the mid-span of the beam for Case C.....	57
19. Experimental displacement data and predictions for the 1-g excitation case .....	60
20. Experimental displacement data and predictions for the 4-g excitation case .....	61
21. Experimental surface strain and predictions for the 1-g excitation case .....	62
22. Experimental surface strain and predictions for the 4-g excitation case .....	62
23. Displacement spectra for 4-g excitation case using variations of the IC method .....	63
24. Displacement spectra for the 4-g excitation case showing the effects of damping upon predictions.....	64
25. Experimental displacement data (solid) and predictions (dotted) for a thermally preloaded beam.....	64
26. Experimental surface strain and predictions for a thermally preloaded beam.....	65
27. Membrane displacement 4" from the clamped end for a FEM and the ROM's.....	68
28. Transverse displacement 4" from the clamped end for a FEM and the ROM's .....	69
29. Membrane stress 3.625" from the clamped end of the beam.....	69
30. Total stress at the top of the beam, 3.625" from the clamped end.....	70
31. Membrane stress from various implementations of the IC method.....	71
32. Total stress from various implementations of the IC method.....	71
33. Geometry of the curved beam.....	72
34. Mode shapes of the curved beam from the FEM.....	73
35. Y-displacement PSD at the beam center, 0.2304 lb/in .....	74

<u>Figure</u>	<u>Page</u>
36. Y-displacement PSD at the beam quarter point, 0.2304 lb/in.....	75
37. X-displacement PSD at the beam center, 0.2304 lb/in .....	75
38. X-displacement PSD at the beam quarter point, 0.2304 lb/in.....	76
39. Y-displacement PSD at the beam center, 0.6517 lb/in .....	76
40. Y-displacement PSD at the beam quarter point, 0.6517 lb/in.....	77
41. X-displacement PSD at the beam center, 0.6517 lb/in .....	77
42. X-displacement PSD at the beam quarter point, 0.6517 lb/in.....	78
43. The test article shown mounted on flexures with a solid mounting plate.....	80
44. The plate test article mounted on a shaker.....	82
45. The first 3 symmetric bending modes of the plate test article FEM.....	83
46. PSD of plate center displacement for the undamped article at 0.45 g .....	84
47. RMS values of center displacement for the undamped article .....	85
48. Center displacement PSD for the undamped test article at 1.8g and 7.2g.....	86
49. Center displacement PSD for the undamped test article at 1.8g and 7.2g.....	87
50. RMS values of center displacement as a function of input level for the damped test article.....	88
51. Center displacement PSD for the damped test article at 1.8g and 7.2 g.....	89
52. Center displacement PSD for the damped test article at 1.8g and 7.2 g .....	89
53. RMS values of strain in the short direction for the damped article .....	90
54. RMS values of strain in the long direction for the damped test article.....	91
55. Strain in the short-direction for the damped test article at 1.8g and 7.2 g.....	91
56. Strain in the long-direction for the damped test article at 1.8g and 7.2 g.....	92
57. Atmospheric test setup.....	94
58. Vacuum chamber test setup .....	94
59. Measured plate center velocity PSD at atmosphere and near-vacuum.....	96
60. Measured plate center velocity PSD at atmosphere and predicted PSD using measured damping values.....	98
61. Measured plate center velocity PSD at near-vacuum and predicted PSD using measured damping values.....	99
62. Measured plate center velocity PSD at atmosphere and predicted PSD using increasing linear damping for first mode.....	100
63. Measured plate center velocity PSD of the damped test article at atmosphere and predicted PSD using measured damping values .....	101
64. Measured plate center velocity PSD of the damped test article at near-vacuum and predicted PSD using measured damping values .....	101
65. Measured plate center velocity PSD of damped and undamped test article at atmosphere and 7.2g RMS excitation .....	102
66. Abaqus acoustic pressure results of the clamped, baffled plate.....	106
67. Real part of complex first mode of baffled rectangular plate in infinite acoustic domain with in-house code.....	107
68. Baffled plate center displacement response to initial pressure in Abaqus.....	108
69. Abaqus acoustic pressure of the unbaffled case cross section view .....	109
70. Unbaffled plate center displacement response to initial distributed pressure in Abaqus .....	110

<u>Figure</u>	<u>Page</u>
71. The Sub-Element Acoustic Test Facility .....	112
72. The plate test article mounted on a rigid cart undergoing a modal test .....	113
73. The experimentally measured modes of the test article before mounting in the test facility .....	114
74. The sub-element facility with the plate test article in place .....	115
75. Measured center displacement PSD compared to the model prediction using a flat input spectrum, both at 133.5 dB SPL .....	117
76. The measured pressure PSD's in front of the test article and behind the test article for the 133.5 dB SPL test .....	118
77. The PSD of the differential pressure for the 133.5 dB SPL test .....	118
78. Measured center displacement PSD compared to the model prediction using the measured differential pressure and nominal viscous damping for the 121.7 and 133.5 dB SPL test levels .....	119
79. Measured center displacement PSD for the 139.5 dB SPL test level compared to the model prediction using the measured differential pressure and damping values of $\zeta_1=0.04$ , and $\zeta_1=0.05$ .....	120
80. Measured center displacement PSD compared to the model prediction using the measured differential pressure and $\zeta_1=0.05$ , for the 121.7 and 133.5 dB SPL test levels .....	120
81. Measured strain PSD in the X-direction at the center compared to the model prediction using the measured differential pressure and $\zeta_1=0.05$ , for the 121.7 and 133.5 dB SPL test levels .....	121
82. Measured strain PSD in the Y-direction at the center compared to the model prediction using the measured differential pressure and $\zeta_1=0.05$ , for the 121.7 and 133.5 dB SPL test levels .....	121
83. Measured center displacement PSD compared to the prediction using the differential pressure and velocity squared damping values of 100 and 200 for the 1st mode, for the 139.5 dB SPL test level .....	122
84. Measured center displacement PSD at 121.7 dB compared to the prediction using: a flat input spectrum and nominal damping, differential pressure and nominal damping, differential pressure and $\zeta_1=0.05$ , and differential pressure and velocity squared damping in the 1st mode .....	123
85. Measured center displacement PSD at 127.4 dB compared to the prediction using: a flat input spectrum and nominal damping, differential pressure and nominal damping, differential pressure and $\zeta_1=0.05$ , and differential pressure and velocity squared damping in the 1st mode .....	123
86. Measured center displacement PSD at 133.5 dB compared to the prediction using: a flat input spectrum and nominal damping, differential pressure and nominal damping, differential pressure and $\zeta_1=0.05$ , and differential pressure and velocity squared damping in the 1st mode .....	124
87. Measured center displacement PSD at 139.5 dB compared to the prediction using: a flat input spectrum and nominal damping, differential pressure and nominal damping, differential pressure and $\zeta_1=0.05$ , and differential pressure and velocity squared damping in the 1st mode .....	124



<u>Figure</u>	<u>Page</u>
88. The test article on a facility cart using a mounting plate with a rectangular cutout.....	127
89. Experimental measured mode shapes of the plate area of the test article.....	128
90. The progressive-wave facility with the test article installed.....	128
91. Comparisons for the center location from a three-mode model with the un-installed parameters driven by a random, spatially uniform pressure .....	132
92. Comparisons for the off-center location from a three-mode model with the un-installed parameters driven by a random, spatially uniform pressure .....	132
93. Comparisons for the center location from a 6-mode model with the installed parameters driven by a random, traveling pressure wave.....	133
94. Comparisons for the off-center location from a 6-mode model with the installed parameters driven by a random, traveling pressure wave .....	133
95. Measured pressure spectra for the 122dB test level.....	135
96. The reference and the differential pressure spectra for the 122dB test level.....	135
97. Measured pressure spectra for the 140dB test level.....	136
98. The reference and the differential pressure spectra for the 140dB test level.....	136
99. Comparisons for the center location from a 6-mode model with the installed parameters driven by a traveling differential pressure.....	137
100. Comparisons for the off-center location from a 6-mode model with the installed parameters driven by a traveling differential pressure .....	137
101. Finite element mode shapes for the clamped plate test article.....	139
102. The Power spectral density (PSD) of the center displacement when the test article is driven by a shaker at 7.2 g RMS .....	139
103. The PSD of the displacement near the center when the test article is driven acoustically at 140dB .....	140
104. The acoustic finite element mesh.....	141
105. An acoustic mode near the first structural resonance .....	141
106. The interior and exterior acoustic meshes .....	142
107. Modes of the infinite acoustic domain behind the test article .....	142
108. Displacement PSD near the plate center for the 140dB loading case.....	145
109. The displacement near the plate center as the damping of the interior acoustic is varied from 1% to 4% .....	145
110. The prediction for a duct with a constant cross section in comparison to the facility model .....	146
111. The configuration of the example problem111. The configuration of the example problem.....	147
112. The lowest frequency acoustic modes of the duct model .....	148
113. The first mode of the plate .....	148
114. Response for the 0.02"thick plate with $\zeta_s=0.005$ for 140dB OASPL .....	150
115. Response for the 0.10" thick plate with $\zeta_s=0.005$ for 140dB OASPL.....	150
116. Response for the plate ( $\zeta_s=0.005$ , 140dB) as the thickness varies. The PSD of the structure only model is shown in blue, the coupled response in red.....	151
117. RMS center displacement as the thicknesses varies ( $\zeta_s=0.005$ , 140dB).....	151

<u>Figure</u>	<u>Page</u>
118. Response for the 0.06" thick plate ( $\zeta_s=0.005$ ) as the excitation varies. The structure only model is shown in blue, the coupled response in red.....	152
119. RMS center displacement for 0.06" thick plate ( $\zeta_s=0.005$ ) as the excitation varies .....	152
120. RMS of the center displacement as the thicknesses varies ( $\zeta_s=0.05$ , 140dB).....	153
121. Response for the 0.02" thick plate ( $\zeta_s=0.05$ ) for 128-152dB. The structure only model is shown in blue, the coupled response in red.....	154
122. RMS of the center displacement as the thicknesses varies ( $\zeta_s=0.001$ , 140dB).....	154
123. A 0.06" thick plate ( $\zeta_s=0.005$ ) with a softened stiffness.....	155
124. The curved panel test article .....	156
125. Finite element mesh of the curved panel test article.....	157
126. The clamped panel finite element mesh.....	158
127. Frequencies and mode shapes at ambient temperature .....	159
128. Frequencies and mode shapes at 20°F above ambient temperature.....	160
129. Frequencies and mode shapes at 50°F above ambient temperature.....	160
130. PSD of displacement at the center, 160dB, ambient temperature.....	161
131. PSD of strain at the center of the long edge, 160dB, ambient temperature.....	162
132. PSD of strain at the center of the long edge, 140-170dB, ambient temperature, for the 7-mode model.....	162
133. Static deformation due to applied temperature .....	163
134. Center displacement vs time for ramped static pressure, +20°F, using the cold-mode models .....	164
135. Post-buckled shapes for -4psi static pressure, +20°F .....	164
136. PSD of strain at the center of the long edge, 160dB, +20°F, for 7-mode model.....	165
137. PSD of strain at the center of the long edge, 140-170dB, +20°F, for the 7-mode cold model.....	165
138. PSD of strain at the center of the long edge, 160dB, +50°F, for cold-mode models.....	167
139. PSD of strain at the center of the long edge, 140-170dB, +50°F, for the 7-mode cold model.....	167
140. Center displacement vs time for -4 psi pressure, +20°F, 160dB, for 9-mode model.....	168
141. PSD of center displacement, -4psi, +20°F, 160dB, for 9-mode models.....	169
142. Mode shapes and frequencies of the curved panel test article .....	171
143. Velocity near the panel center for several sound pressure levels .....	172
144. Velocity at a point in the upper left quadrant of the panel for several sound pressure levels.....	172
145. Resonant frequencies and mode shapes of the test article FEM.....	173
146. Resonant frequencies and mode shapes of the second curved panel test article .....	175
147. Temperature distribution on the test article for the +50 °F case.....	175
148. Temperature distribution (°F) for the FEM and ROM for the +50 °F case.....	176
149. Predicted displacements (in) of the FEM for the +50 °F case.....	177
150. Temperature distribution on the test article for the +110 °F case.....	178
151. Temperature distribution (°F) for the FEM and ROM for the +110 °F case.....	178
152. Predicted displacements (in) of the FEM for the +110 °F case.....	179

<u>Figure</u>	<u>Page</u>
153. Measured PSD of panel velocity near the center .....	180
154. Measured PSD of panel velocity at the corner point .....	180
155. Panel center velocity from test and IC ROM at ambient temperature .....	181
156. Panel corner velocity from test and IC ROM at ambient temperature .....	181
157. Measured PSD of panel velocity near the center for the +50 °F case .....	182
158. Measured PSD of panel velocity near the center for the +50 °F case .....	182
159. Natural frequencies and mode shapes of the FEM for the +50 °F case .....	183
160. Natural frequencies and mode shapes of the FEM for the +110 °F case .....	183
161. The example problem .....	185
162. Acoustic pressure PSD at source and beam center at 122 dB .....	186
163. Example problem finite element mesh .....	187
164. The magnitude of the first three complex structural modes of the coupled model .....	189
165. Beam center displacement PSD from linear and nonlinear simulation with <u>acoustic loading</u> of the full-order model at 152dB .....	190
166. Beam center displacement PSD from nonlinear simulation of the full-order model with <u>acoustic loading</u> and <u>direct loading</u> .....	190
167. Beam center displacement PSD from nonlinear simulation of the structure- only ROM with <u>direct loading</u> and the full-order model with <u>acoustic loading</u> at 122 and 152dB .....	191
168. Beam center displacement PSD from linear simulation with <u>acoustic loading</u> of three-mode and 120-mode CROM's and full-order model at 122dB .....	192
169. Beam center displacement PSD from linear simulation with <u>direct loading</u> of a three-mode CROM and the full coupled model at 122 dB .....	192
170. Beam center displacement PSD from nonlinear simulation with <u>acoustic</u> <u>loading</u> of three-mode and 11-mode CROM's and the full-order model at 152dB .....	193
171. Beam center displacement PSD from nonlinear simulation with <u>direct loading</u> of a three-mode CROM, the full-order model, and a three-mode ROM at 152dB .....	194
172. The uncoupled acoustic modes of a rectangular cavity .....	195
173. The displacement PSD of the beam center using linear models .....	196
174. The displacement PSD of the beam center using nonlinear models .....	197
175. The displacement PSD of the beam center using nonlinear models .....	198
176. The first twelve acoustic mode shapes for the exterior example .....	199
177. The displacement PSD at the center of the beam for the exterior example problem .....	200

## LIST OF TABLES

<u>Table</u>	<u>Page</u>
1. Estimated Coefficients for the Clamped Beam Example .....	39
2. Single Mode Nonlinear ROM's from Various Methods .....	43
3. Nonlinear Coefficients from the Two-Mode Models .....	44
4. The RMS Displacement of the Center of the Beam from Simulations.....	46
5. Estimated Parameters from Free Response and Hammer Tests .....	53
6. RMS Displacements and Strains from the Random Tests .....	54
7. Comparison of RMS Values of Displacement at the Mid-Span of the Beam .....	59
8. Comparison of RMS Values of Surface Strain at the Mid-Span of the Beam.....	60
9. Natural Frequencies and Modal Damping Ratios for the Target Modes .....	83
10. RMS Values of Plate Center Displacement for the Undamped Test Article.....	85
11. RMS Values of Plate Center Displacement for the Test Article with Damper .....	87
12. RMS Values of Strain at the Plate Center in the Short Direction for the Test Article with Damper .....	90
13. RMS Values of Strain at the Plate Center in the Long Direction for the Test Article with Damper .....	90
14. Natural Frequencies and Modal Damping Ratios for the Target Modes .....	97
15. First Mode Linear Damping Value Needed at Pressure/Excitation to Match Experimental Results .....	99
16. Natural Frequencies and Modal Damping Ratios for the Target Modes of the Damped Test Article at Atmosphere.....	100
17. Abaqus Complex Eigensolution Results for the Clamped, Baffled Case .....	107
18. Modal Damping Ratios for the Clamped, Baffled Case .....	108
19. Abaqus Complex Eigensolution Results for the Clamped, Unbaffled Case.....	110
20. Modal Damping Ratios of the Clamped, Unbaffled Case .....	110
21. Modal Damping Ratios of the Simply-Supported, Baffled Case.....	111
22. Natural Frequencies and Modal Damping Ratios for the Target Modes .....	114
23. Natural Frequencies and Modal Damping Ratios .....	130
24. Natural Frequencies and Modal Damping Ratios for the Test Article .....	140
25. Resonant Frequencies of the Curved Panel Test Articles .....	175
26. Predicted versus Measured Panel Displacements for the +50 °F Case.....	177
27. Predicted versus Measured Panel Strains for the +50 °F Case .....	177
28. Predicted versus Measured Panel Displacements for the +110 °F Case.....	179
29. Predicted versus Measured Panel Strains for the +110 °F Case .....	179
30. Modal Frequencies and Damping Ratios for the Example Problem.....	189

## ACKNOWLEDGEMENTS

The authors would like to acknowledge the contributions of several individuals to the work reported herein. First, we recognize the extensive contributions of Mike Spottswood and Tim Beberniss of the Analytical Structural Mechanics Branch of the Air Vehicles Directorate for support in ROM development and experimentation, respectively. We also acknowledge the support of Travis Wyen of the Experimental Validation Branch of the Air Vehicles Directorate for acoustic facility operation and data measurement. The authors recognize the contributions of Steve Rizzi, NASA Langley Research Center, and Adam Przekop, Analytical Services and Materials, Inc., for their generous advice in the development and implementation of nonlinear ROM's. Finally, we recognize the support of Marc Mignolet, Arizona State University, for his advice in understanding some of the many complexities of the nonlinear ROM.

## 1. INTRODUCTION

This report describes in-house research performed by the Analytical Structural Mechanics Branch to develop and refine computational methods for simulating the nonlinear response of thin aircraft skins exposed to high-level aero-acoustic pressure fluctuations.

In the late 1990's the Structures Division began a project called Durability Patch to experimentally evaluate the performance of damped, adhesively bonded patches to repair sonic fatigue damage in aircraft skin panels. Although the project was primarily experimental, some effort was made to predict the nonlinear response of the test articles using finite element analysis. It quickly became evident that linear analysis was not accurate for the high acoustic levels being investigated and that full-order nonlinear analysis was much too computationally expensive. It was clear at that point that an analysis and simulation tool was needed that could accurately capture the nonlinear response with reasonable computational cost. The concept of the nonlinear reduced-order model (ROM) was adopted from earlier work and refined and demonstrated in this project.

This report is divided into four major sections. Section 2 presents a brief background on sonic fatigue, the development of prediction tools for acoustic response leading up to the nonlinear ROM concept, and a discussion of the basic technical challenges to be addressed. Section 3 gives a detailed description of the methods developed for building nonlinear ROM's including the effects of thermal loading and acoustic coupling. Section 4 describes several applications of nonlinear ROM's to a series of example problems beginning with a simple clamped-clamped beam and culminating with a curved panel with thermal loading. The applications include numerical examples and experiments. For each application, a ROM is used to generate response predictions which are compared to numerical and experimental data. Finally, Section 5 presents conclusions derived from the development and application of the ROM concept.

This project resulted in several major contributions to the state of the art of nonlinear acoustic response prediction. These contributions include a method for synthesizing modal membrane displacements from computed bending displacements, an efficient approach for including acoustic coupling effects in a ROM, and an extensive quantity of experimental acoustic response data from well-characterized experiments. To the authors' knowledge, this project was the first to compare a high fidelity prediction of the response of a test article in an acoustic progressive wave facility to measured data. This comparison resulted in the important realization that the acoustic characteristics of a test facility can significantly alter the response of a test article!

The primary conclusion of this project is that nonlinear ROM's can provide a very accurate prediction of the response of thin skin panels to combined acoustic and thermal loads. What this really means is that a nonlinear ROM with less than 10 degrees of freedom can be a very accurate approximation of a nonlinear finite element model with thousands of degrees of freedom. However, a nonlinear ROM can never provide a better prediction than the finite element model from which it is computed. Moreover, a ROM cannot account for the effect of physics that are not included in the full-order model.

This project has significantly advanced the capability to predict the response of future air vehicles to extreme aeroacoustic environments. However, improvements to the methods for computing nonlinear ROM's are still needed. One of the most important areas for improvement is in the selection of a modal basis for the ROM. Current methods require either a trial and error approach or a short simulation of a full-order model. In addition, more work is needed in the application of nonlinear ROM's to structures with thermal loads. Only moderate success was achieved in this project applying ROM's to a heated, curved panel. Finally, the ultimate improvement to acoustic response prediction is the development of methods that can directly predict nonlinear, random response statistics without the need to perform time simulations as an intermediate step.

## 2. BACKGROUND

### 2.1 Sonic Fatigue and Nonlinear Response

Sonic fatigue has been a concern for many Air Force aircraft since the introduction of the jet engine. High-level acoustic loads can produce cracks in thin, stiffened, aircraft skins or panels. The acoustic input is typically a band-limited random excitation due to jet engine exhaust, turbulent boundary layer or separated flow. Fatigue occurs when there are lightly damped resonant vibration modes of the skins/panels within the excitation bandwidth. The dynamic response becomes highly nonlinear for large response amplitudes.

Sonic fatigue problems range from nuisance cracking of secondary structures to flight safety critical failures of primary structures. Maintenance and repair due to sonic fatigue cracks in secondary structures like leading edges, fairings or flap skins have been estimated to cost the Air Force more than \$20M per year [1]. The upper-outer wing skin (UOWS) of the F-15 is a good example of sonic fatigue in primary structures. The F-15 UOWS was originally designed for a 8,000 hour life. However, sonic fatigue cracks limited the initial service life to only 250 hours [2].

Future hypersonic vehicles will face an even more critical challenge from sonic fatigue. Large thermal stresses from aerodynamic heating will couple with aerodynamic loads and extreme acoustic pressures to produce a combined environment very conducive to sonic fatigue. Even cracks in secondary structures can produce catastrophic structural failure. Therefore, accurate, computationally efficient analysis and simulation methods are needed to ensure that future air vehicle structures can meet their design lives in extreme operating environments.

The response of thin air vehicle skins exposed to aeroacoustic pressures can be highly nonlinear. The structural response is characterized by geometric nonlinearity as defined by von Karman large deflection theory. The two-dimensional straight beam with clamped ends shown in Figure 1 is used here as an example. Axial (membrane) and transverse (bending) displacements  $u$ , and  $v$ , occur in coordinate directions  $x$ , and  $y$ , respectively. The nonlinear strain-displacement equation for the beam is

$$\epsilon_x = \frac{du}{dx} + \frac{1}{2} \left\{ \frac{dv}{dx} \right\}^2, \quad (1)$$

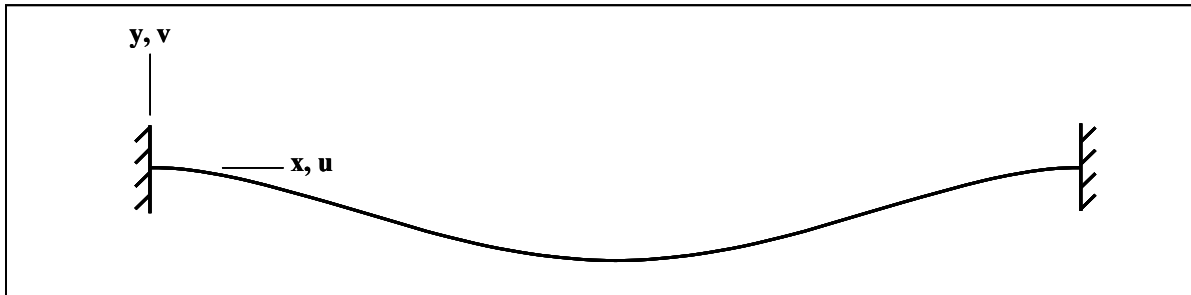


Figure 1. Straight Beam with Clamped Ends



where  $\varepsilon_x$  is the membrane strain, the first term on the right hand side is linearly dependent on membrane displacement, and the second term is nonlinearly dependent on bending displacement.

Equation 1 creates nonlinear coupling between bending and membrane displacements. This nonlinearity is manifested in the behavior of the beam in Figure 1 as stiffness that varies as the cube of bending displacement. A one-mode dynamic model of the beam is given by Duffing's equation,

$$\ddot{q} + \omega_n^2 q + \alpha q^3 = f(t), \quad (2)$$

where  $q$  is a modal coordinate,  $\omega_n$  is the natural frequency,  $\alpha$  is the cubic stiffness coefficient and the double over-dots denote two differentiations with time. The cubic nonlinear stiffness term in Equation 2 results in classic hard spring behavior which causes the resonant frequency of the one-mode model to increase with amplitude. The physical mechanism at play is the transfer of strain energy from relatively soft bending deformation to relatively stiff membrane deformation with increasing bending displacement.

The geometric nonlinearity produces interesting characteristics in the response of thin skin panels to broadband aeroacoustic loading. First, the nonlinearity tends to limit the maximum response amplitude. This is illustrated in Figure 2, which shows the root mean square (RMS) strain at the edge of an aluminum panel exposed to increasing levels of acoustic pressure. Measured strain is plotted as a function of overall sound pressure level (OASPL). An extrapolation of the linear strain is plotted in the figure for comparison. The measured (nonlinear) response is essentially capped at high sound pressure levels.

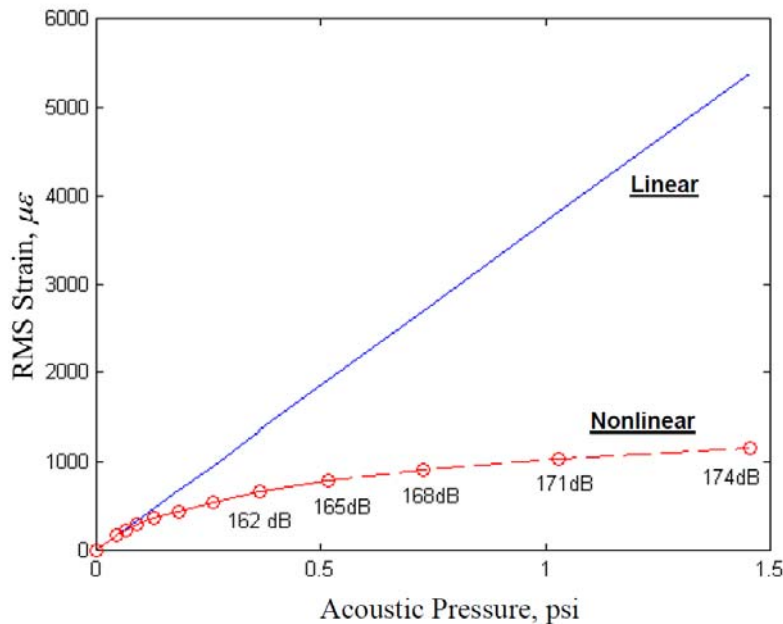


Figure 2. RMS strain vs sound pressure level for an aluminum alloy panel

The second characteristic of nonlinear acoustic response is the broadening of resonant peaks. This is shown in Figure 3. The power spectral density (PSD) of strain at the edge of an

aluminum test panel is plotted for four levels of acoustic excitation. The response at 147 dB OASPL is nearly linear and is characterized by narrow resonant peaks typical of a lightly damped structure. As the sound pressure level is increased to 165 dB, the resonant peaks broaden considerably. In linear response, broadening of a resonant peak is indicative of increased damping. Indeed, early studies of sonic fatigue behavior attributed this peak broadening to nonlinear damping [3]. Later, it was shown by Reinhall and Miles [4] that peak broadening could be observed in the response of a stiffened panel with random acoustic excitation and no damping! Peak broadening is simply the averaged response of a system with amplitude dependent resonances excited by a loading with randomly varying amplitude.

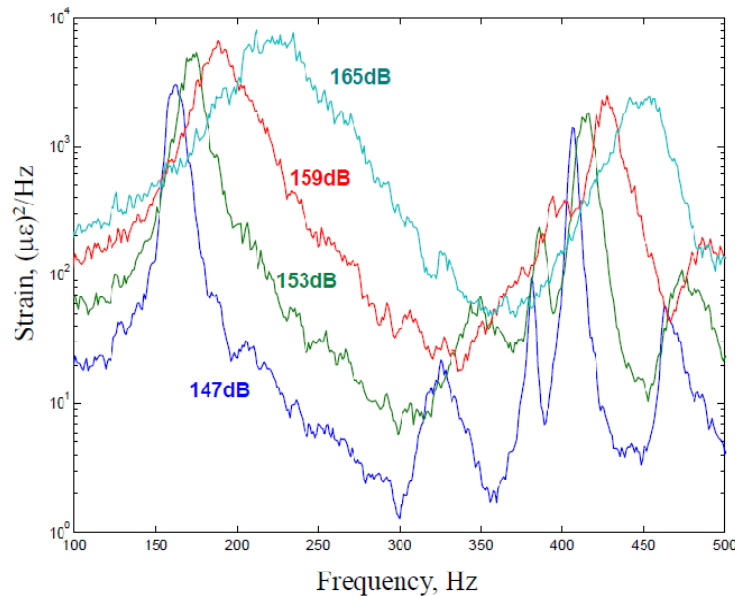


Figure 3. Strain PSD for an aluminum alloy panel at several sound pressure levels

The third characteristic of nonlinear response is the shifting of response peaks to higher frequencies with increasing load level. This is also illustrated in Figure 3. This characteristic is again the result of a system with hard spring nonlinearity. As the excitation amplitude is increased, the structure stiffens, increasing the average frequency of the response. Finally, nonlinear response of a structure can affect other response statistics. Figure 4 shows probability density functions (PDF) of displacement and strain for a beam with clamped ends excited by random base motion. The excitation level is high enough to cause significant nonlinearity. The response of a linear system to a band limited random load with Gaussian amplitude distribution should also be Gaussian. This is obviously not the case in Figure 4. Both the displacement and strain PDF's show a marked departure from normal distributions. It is important that an analysis method for predicting nonlinear acoustic response be able to capture these salient characteristics.

The nonlinear acoustic response of curved panels can be more complex than that of flat panels. Curvature adds linear coupling to the equations of motion in addition to the nonlinear coupling from large amplitude response. This linear coupling produces normal mode shapes which possess both bending and membrane displacements. In contrast, the normal modes of flat plates contain either bending or membrane displacements exclusively. Furthermore, curved structures can exhibit nonlinear softening resulting from quadratic nonlinear effects. Nonlinear softening is

physically expressed as resonant frequencies that decrease with increasing response amplitude and RMS response amplitude that grows at a higher rate than linear response. The latter effect is non-conservative.

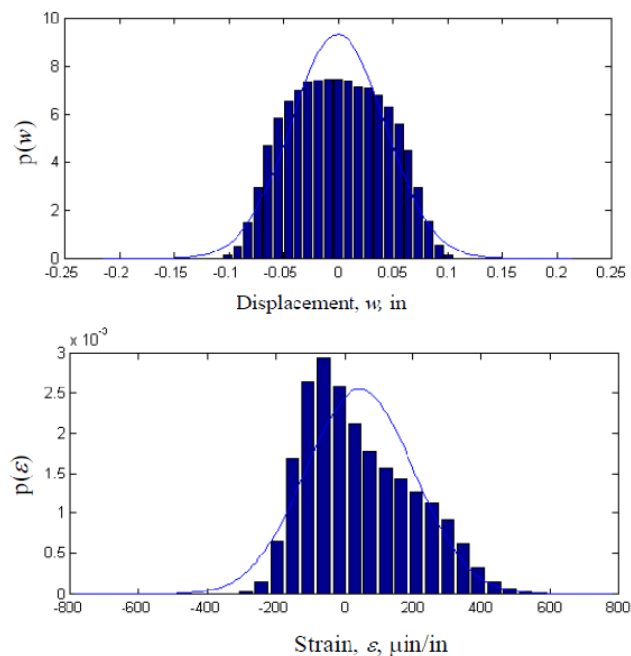


Figure 4. Probability density functions of displacement and strain for a clamped beam

Temperature changes can have a significant effect on the acoustic response of skin panels. Thermal stresses resulting from the constrained thermal expansion of flat panels under heating induce linear stress softening which will reduce resonant frequencies and ultimately cause buckling. The post-buckled panel can then oscillate about the buckled position under acoustic loading or snap-through dynamically if the acoustic loading is high enough. The response of curved panels to applied temperatures is more complex. Thermal stresses produce stress stiffening and a change in the geometry which can cause resonant frequencies to increase or decrease depending on the specific problem. Thermal stress directly affects linear stiffness, but the acoustic response of curved or post-buckled panels is still greatly affected by nonlinearity.

## 2.2 Prediction Capability

Since the late 1950's, the Air Force has conducted research to understand the phenomenon of sonic fatigue and develop analysis methods to aid in the design of fatigue resistant structures. The earliest work was primarily experimental with some effort on analysis methods based on analytical models of beams and plates. The early work culminated in the publication of a sonic fatigue design guide [5] in 1975. The response prediction methods in the report employed linear plate and shell theories and were based on the assumption that a single vibration mode dominated the response. They did not include nonlinear or multi-mode effects.

Methods for predicting the response of structures to acoustic loading improved significantly with the advent of practical finite-element modeling (FEM) tools in the 1980's. Linear frequency

domain techniques allowed computation of linear response with stochastic loading. Linear modal models, retaining only a few low frequency modes, enabled very efficient computation of structural response. Although these methods produced accurate and efficient linear predictions, they could not account for nonlinear effects.

Nonlinear finite-element codes came of age in the 1990's, offering hope for accurate nonlinear prediction of acoustic response. The finite-element equations of motion including geometric nonlinearity are (neglecting damping)

$$\mathbf{M} \ddot{\mathbf{w}} + [\mathbf{K} + \mathbf{K1}(\mathbf{w}) + \mathbf{K2}(\mathbf{w}, \mathbf{w})] \mathbf{w} = \mathbf{f}(t), \quad (3)$$

where  $\mathbf{w}$  is the time-varying vector of nodal displacements,  $\mathbf{M}$  and  $\mathbf{K}$  are the linear mass and stiffness matrices, respectively,  $\mathbf{K1}$  is the quadratic nonlinear stiffness matrix (a linear function of the nodal displacements), and  $\mathbf{K2}$  is the cubic nonlinear stiffness matrix (a quadratic function of the nodal displacements.) The vector,  $\mathbf{f}(t)$ , represents the nodal forces as a function of time. Although nonlinear models of the form of Equation 3 provided accurate results, computational cost became a primary obstacle. The nonlinearity necessitated direct time integration of the model. The nonlinear stiffness matrices,  $\mathbf{K1}$  and  $\mathbf{K2}$ , can be very large—many thousands of degrees of freedom (DOF). The nonlinear matrices are functions of the instantaneous displacement and thus must be updated at every time step. In addition, the time step must be very small to capture high frequency dynamic response. These facts coupled with the need to compute relatively long time records (10's of seconds) resulted in computational costs prohibitively high for the methods to be used in design trade studies.

Equivalent linearization [6] was adapted for the sonic fatigue problem to circumvent the computational burden. A linear model that produces the same mean squared response replaces the nonlinear FEM. Equivalent linearization was a popular sonic fatigue research topic at the turn of the millennium and was adapted for use with commercial codes [7]. However, the major drawback with equivalent linearization is that only a single statistic is matched—the mean squared response value. The predicted time and frequency response from the equivalent model differs significantly from the full nonlinear response.

The methods described above have served the air vehicle designer reasonably well over the years since the 1950's, but methods with high accuracy, spatial resolution and computational efficiency are needed for the design of future air vehicles to be flown in extreme hypersonic environments. The nonlinear reduced-order model (ROM) promises to meet these goals.

### 2.3 Nonlinear Reduced-Order Models

Nonlinear ROM's provide an analysis method for acoustic response that captures the geometric nonlinearity and offers very efficient computation for direct time integration. This section will present an overview of nonlinear ROM's including historical development, technical challenges, and implementation approaches.

Finite-element models with a large number of degrees of freedom (DOF) can be reduced to a low order system of modal equations using the classic modal transformation. The linear finite-

element equations are given by neglecting the nonlinear stiffness terms in Equation 3 as

$$\mathbf{M} \ddot{\mathbf{w}} + \mathbf{K} \mathbf{w} = \mathbf{f}(t). \quad (4)$$

The linear equations of motion can be uncoupled by transforming the physical coordinates,  $\mathbf{w}$ , to modal coordinates,  $\mathbf{q}$ ,

$$\mathbf{w}(t) = \sum_{i=1}^m \boldsymbol{\psi}_i q_i(t), \quad (5)$$

where  $m$  is the number of DOF in the FEM. The normal mode shapes (eigenvectors),  $\boldsymbol{\psi}_i$ , are the basis vectors in the modal expansion. The normal modes are computed from the eigensolution of the homogeneous form of Equation 4. The solution also produces the natural frequencies,  $\omega_i$ . The mode shapes are scaled so that

$$\boldsymbol{\Psi}^T \mathbf{M} \boldsymbol{\Psi} = \mathbf{I} \quad \text{and} \quad \boldsymbol{\Psi}^T \mathbf{K} \boldsymbol{\Psi} = \bar{\mathbf{K}} = \text{diag}(\omega_1^2, \omega_2^2, \dots, \omega_m^2), \quad (6)$$

where  $\mathbf{I}$  is the identity matrix. Typically only a few low frequency modes are retained in the expansion and the displacement vector is approximated.

For a linear problem, the  $r$ th uncoupled modal equation can be obtained by substituting Equation 5 into Equation 4 and pre-multiplying by  $\boldsymbol{\psi}_r^T$  resulting in

$$\ddot{q}_r + 2\zeta_r \omega_r \dot{q}_r + \omega_r^2 q_r = \boldsymbol{\psi}_r^T \mathbf{f}(t). \quad (7)$$

A term with the modal damping ratio,  $\zeta_r$ , has been inserted into the equation at this point to model the energy dissipation. For a nonlinear problem, the equation for the  $r$ th mode can be written generally as

$$\ddot{q}_r + 2\zeta_r \omega_r \dot{q}_r + \omega_r^2 q_r + \theta_r(q_1, q_2, \dots, q_n) = \boldsymbol{\psi}_r^T \mathbf{f}(t), \quad (8)$$

where  $\theta_r$  represents a nonlinear function of the modal coordinates. Note that only  $n$  modes have been retained in the modal expansion. The nonlinear modal equations differ from the linear modal equations in that they are coupled through the nonlinear function. Typically for structural applications, the nonlinear function has quadratic and cubic terms. The most general form of the nonlinear function is

$$\theta_r = \sum_{i=1}^n \sum_{j=i}^n B_r(i,j) q_i q_j + \sum_{i=1}^n \sum_{j=i}^n \sum_{k=j}^n A_r(i,j,k) q_i q_j q_k, \quad (9)$$

where the quadratic coefficients,  $B_r$ , and the cubic coefficients,  $A_r$ , belong to the  $r$ th modal equation and have indices to denote which group of terms they multiply.

The nonlinear ROM given in Equation 8 has several computational advantages over the full-order FEM. First, typically less than ten DOF are retained in the modal model compared to many thousands in the FEM. Second, the nonlinear coefficients in Equation 9 are constants that

are evaluated only once when the model is formed. Finally, the step size used in direct time integration can be larger than that used with a full model since the ROM does not contain high frequency modes.

The nonlinear ROM is integrated in time with appropriate time dependent loading to compute time histories of the modal displacements. Time histories of selected physical displacements are then computed from the modal displacements. Element strains are computed from the physical displacements using finite-element strain-displacement equations. Strains can also be computed directly from the modal displacements using a derived nonlinear strain function [8,9].

The most comprehensive early work in the development of nonlinear ROM's is that of Nash [10] in 1977. The form of the nonlinear modal equations he presented is used in most of the current methods. Although considerable research was performed in the 1980's and 1990's on acoustic response prediction, effort on nonlinear ROM's didn't become significant until the mid 1990's. At that time groups at Old Dominion University (ODU) and NASA Langley Research Center led the development. The studies by Mei and Moorthy [11] and Shi and Mei [12] represent significant work in nonlinear ROM's. The NASA group developed an ingenious method for evaluating the nonlinear stiffness terms in a ROM based on static nonlinear enforced displacement solutions from a commercial finite-element code [13]. In the UK, McEwan, et al., presented an effective method that also used results from a commercial finite-element code [8,9]. However, their method used nonlinear applied loads solutions instead of enforced displacements. The authors began studying nonlinear ROM's in the early 2000's. They developed improvements [14] to the method of McEwan, and validated the method with several experimental studies [15-18]. Other significant contributions to the development of nonlinear ROM's include studies by Mignolet and collaborators, see [19, 20] for example.

There are four key challenges to the implementation of nonlinear ROM's for the acoustic response prediction problem—modal basis selection, condensation of membrane displacements, evaluation of nonlinear stiffness coefficients, and acoustic coupling effects. These challenges will be discussed in detail in the next sections.

### **2.3.1 The Modal Basis**

The modal basis used with a nonlinear ROM will have a significant effect on the accuracy of acoustic response prediction for stiffened aircraft panels. Typically, low-frequency modes involving bending displacements are of primary importance in the response. However as a thin skin undergoes large displacement, it also stretches. The geometric nonlinearity couples bending displacements with membrane displacements through quadratic stiffness terms. Therefore, the modal basis must include independent membrane vectors to accommodate the induced membrane displacements. Membrane modes are not directly excited by acoustic loading in most cases. They respond quasi-statically through nonlinear coupling. Straight beams and flat plates possess independent bending and membrane modes; panels with curvature or asymmetric composite laminates do not. In these cases, the low frequency modes that are directly excited may contain both bending and membrane displacements. However, additional basis vectors will still be required to fully capture the membrane effects.

Pure bending and membrane modes do not generally exist for any built-up or curved structure. The low frequency modes that have predominantly bending motion will be referred to generically as bending modes. The higher frequency modes that have predominantly membrane motion will be referred to generically as membrane modes.

Assuming linear response, the modal basis should include all bending modes which would be excited by the acoustic loading. For example, given a spatially symmetric acoustic pressure field with energy in the 0-500 Hz bandwidth, only symmetric modes up to 500 Hz should be included in the basis. However, if the response is assumed to be nonlinear, this basis would be inadequate. First, nonlinear modal coupling can cause modes above the loading bandwidth to be excited. In addition, nonlinear effects can cause anti-symmetric modes to be excited by symmetric loading. So, a good approach is to include in the basis all bending modes with frequencies up to 1.5-2 times the maximum frequency in the loading. Trial and error may be required to add or delete modes to achieve an accurate ROM with a minimum number of modes. Recent work by Rizzi and Przekop [21] and Przekop, et al. [22] explored a structured approach to identification of a modal basis including membrane vectors. The approach is based on proper orthogonal decomposition (POD) of a short time record of full-order model response. Proper orthogonal modes are then identified from the time record and a set of normal modes is selected based on modal assurance criterion (MAC) values compared to the POD modes.

Several approaches have been investigated for selecting membrane basis vectors for a nonlinear ROM. The first approach is to simply neglect the membrane basis and include only bending modes in the model. The nonlinear ROM will have cubic nonlinear terms that are too large resulting in a model which is too stiff. The second approach is to form a membrane basis from normal membrane modes. For straight beams or planar structures, these are normal modes that involve only in-plane motion and are much higher in frequency than the bending modes included in the model. Although normal membrane modes are relatively easily to find for a planar structure, a decision on which and how many modes to include is difficult. As the structure becomes more complex or non-planar, normal modes may contain both membrane and bending displacements, making it very difficult to identify a membrane basis set. Including normal membrane modes in the ROM can cause integration instability if the time step of integration is too large due to the potentially high frequencies of the membrane modes. The stability concerns and additional computational burden due to the larger modal model can be alleviated through modal condensation, which will be explained in a following section.

A third approach to forming a membrane basis is to synthesize the necessary vectors. Hollkamp et al.[24] introduced the concept of a *companion* membrane mode. A companion membrane mode is generated for each bending mode in the model using a nonlinear finite-element static solution. The linear force due to the enforced displacement of a selected bending mode is found. This force is scaled and applied to the FEM in a nonlinear static solution. A nonlinear deflected shape containing both bending and membrane displacement is then computed. The bending mode's projection on the nonlinear deflected shape is then removed through a Gram-Schmidt procedure leaving only the induced membrane displacement. A companion mode provides a membrane basis to span the nonlinear membrane response of a single bending mode. If the nonlinear ROM contains multiple bending modes, the companion modes will not be orthogonal to each other and will not form a complete membrane basis due to nonlinear coupling among the

bending modes. Mignolet and Radu [19-20] describe a procedure to compute *dual* modes, similar to companion modes, which produces a more complete membrane basis. Hollkamp and Gordon [14] presented an approach for synthesizing a complete membrane basis for a nonlinear ROM. The approach, termed *estimated membrane basis*, is based on the assumption that a complete set of membrane modal displacements can be formed from quadratic combinations of the bending modal displacements. The approach was originally intended for recovering membrane modal displacements from computed bending displacements. Finally, Shi and Mei [12] proposed an approach for computing a nonlinear ROM which doesn't use a membrane basis explicitly, but does compute a basis as part of the model formulation. Their approach is analogous to the estimated membrane basis of [14] but is performed in physical coordinates rather than modal coordinates.

### 2.3.2 Condensation of Membrane Effects

The previous section discussed means of forming a membrane basis for a nonlinear ROM. Membrane *condensation* is the elimination of membrane modes by incorporation of membrane effects directly in the bending equations. In an early work, Nash [10] describes an approach for linking a high frequency membrane mode to a low frequency bending mode. The equations of motion for the two modes are

$$\ddot{q}_1 + \omega_1^2 q_1 + A_1(I, I, I) q_1^3 + B_1(I, 2) q_1 q_2 = f_1(t), \quad (10)$$

$$\ddot{q}_2 + \omega_2^2 q_2 + B_2(I, I) q_1^2 = 0, \quad (11)$$

where  $q_1$  and  $q_2$  are the modal coordinates of a bending mode and a membrane mode, respectively,  $\omega_1^2$  and  $\omega_2^2$  are the modal stiffnesses, the  $A$  and  $B$  terms are cubic and quadratic nonlinear stiffness coefficients, respectively, and  $f_1(t)$  is time-varying modal force. Mass normalized modal vectors are assumed and damping is neglected. The membrane mode in Equation 11 is assumed to respond quasi-statically so the inertial term can be neglected. Also, there is no direct force applied to the membrane mode, so it can be thought of as being forced by the nonlinear coupling term,  $B_2(I, I)$ . So, the membrane modal displacement can be expressed in terms of the bending displacement as

$$q_2 = -\frac{B_2(I, I)}{\omega_2^2} q_1^2. \quad (12)$$

Substituting Equation 12 into Equation 10 yields

$$\ddot{q}_1 + \omega_1^2 q_1 + \left( A_1(I, I, I) - \frac{B_2(I, I)}{\omega_2^2} B_1(I, 2) \right) q_1^3 = f_1(t). \quad (13)$$

The effect of the membrane mode is *condensed* into the bending mode equation by softening the cubic stiffness. This condensation process eliminates the need to explicitly include the membrane mode in the basis. Although Equation 13 applies to one bending mode and one membrane mode, a general form of the condensation process can be used to condense the effects of several membrane modes into several bending equations [24].



Another approach to membrane condensation, employed by Shi and Mei [12], uses static condensation (Guyan reduction) in physical coordinates. The finite-element equations of motion given by Equation 3 can be expressed in partitioned form as

$$\begin{bmatrix} \mathbf{M}_b & \mathbf{0} \\ \mathbf{0} & \mathbf{M}_m \end{bmatrix} \begin{Bmatrix} \ddot{\mathbf{w}}_b \\ \ddot{\mathbf{w}}_m \end{Bmatrix} + \left( \begin{bmatrix} \mathbf{K}_b & \mathbf{0} \\ \mathbf{0} & \mathbf{K}_m \end{bmatrix} + \begin{bmatrix} \mathbf{K}\mathbf{I}_{Nm} & \mathbf{K}\mathbf{I}_{bm} \\ \mathbf{K}\mathbf{I}_{mb} & \mathbf{0} \end{bmatrix} + \begin{bmatrix} \mathbf{K}2_b & \mathbf{0} \\ \mathbf{0} & \mathbf{0} \end{bmatrix} \right) \begin{Bmatrix} \mathbf{w}_b \\ \mathbf{w}_m \end{Bmatrix} = \begin{Bmatrix} \mathbf{f}_b \\ \mathbf{f}_m \end{Bmatrix}, \quad (14)$$

where the mass matrix and the linear, quadratic and cubic stiffness matrices have been partitioned by bending and membrane DOF. If we again assume that the membrane response is quasi-static, the lower partition of Equation 14 becomes

$$\mathbf{w}_m = -\mathbf{K}_m^{-1} \mathbf{K}\mathbf{I}_{mb} \mathbf{w}_b. \quad (15)$$

The membrane DOF have been expressed in terms of the bending DOF in an analogous fashion to Equation 12. The bending equations in modal coordinates with condensed membrane DOF can be derived with some additional manipulation. This approach suffers from the fact that the structure being modeled must have DOF that can be partitioned into bending and membrane components. This limits its applicability to planar structures or non-planar structures that can be modeled in curvilinear coordinates.

McEwan [8-9] presented a method to generate a nonlinear ROM using only bending modes. In this method, termed *implicit condensation* [24], the coefficients of the cubic nonlinear terms are identified from the results of static nonlinear solutions using applied forces proportional to combinations of bending basis vectors. The results of the nonlinear static solutions (displacement vectors) contain the membrane stretching effects of large displacements. Therefore, the identified nonlinear cubic coefficients are implicitly softened by the membrane displacements.

Nonlinear ROM's which use membrane condensation contain only bending modal equations. So, time integration of these models produces only bending modal displacements. Thus, an additional operation is necessary to recover membrane displacements. This can be performed in the modal or physical domains. The implicit condensation method recovers membrane modal displacements from bending modal displacements and then transforms the total displacements to the physical domain using a modal basis consisting of the bending modes and a set of estimated membrane vectors [14]. This topic is discussed in more detail in the Section 3. The method of Shi and Mei [12] performs the membrane expansion in the physical domain using Equation 15 after the bending modal displacements have been transformed to the physical domain.

### 2.3.3 Nonlinear Stiffness Evaluation

The evaluation of the nonlinear stiffness coefficients is another key area in the development of nonlinear ROM's. These coefficients—the  $A$ 's and  $B$ 's in Equation 9—can be computed directly with the nonlinear finite-element equations or indirectly through a series of static nonlinear solutions. Both approaches will be discussed in the next paragraphs.

The direct methods for evaluating the nonlinear coefficients are of two general types. The first type is that of Shi and Mei [12], in which the finite-element nonlinear stiffness is directly evaluated with combinations of bending modal vectors. The resulting matrices are then transformed to the modal domain using the bending modal basis. With some additional manipulation, the nonlinear coefficients are computed. The second type of direct method is that investigated by Tiso and Jansen [25]. Their approach computes the nonlinear coefficients from derivatives of finite-element strain energy with respect to the modal coordinates.

The indirect approaches are based on nonlinear static solutions of the finite-element equations using either applied modal loads or enforced displacements. The method originally developed by McEwan [8-9], and refined by the authors [14, 24], uses the applied loads approach. This method, termed the implicit condensation (IC) method, starts by generating a series of load vectors as combinations of the bending modes. The load vectors are scaled so that they result in physically meaningful displacements applied in nonlinear static solutions. The load vectors are designed to exercise the FEM in the large displacement regime so that the resulting displacement vectors contain a rich participation of nonlinear response. The displacement vectors resulting from the nonlinear solutions are then transformed to the modal domain where an identification scheme is used to estimate the nonlinear coefficients. A significant advantage of using applied modal loads is that membrane basis vectors are not required. The nonlinear static deformation of the FEM to bending modal loads naturally contains induced membrane displacements. One drawback to this method is that the results can be sensitive to the number and scaling of the applied modal load cases. The development of this approach is discussed in detail in Section 3.

The other indirect method was developed by Muravyov and Rizzi [13, 26]. Their approach uses linear combinations of modal basis vectors as enforced displacement vectors in a series of nonlinear static solutions of the FEM. These solutions form a set of induced nodal force vectors which are then transformed to the modal domain. Finally, an ingenious method is used to determine the nonlinear coefficients through a series of arithmetic manipulations. The primary advantage of this approach is that the nonlinear coefficients are determined (as opposed to estimated) so that they are insensitive to the scaling of the enforced displacements. The disadvantage of this method is that the enforced displacement vectors must span the range of membrane displacements due to large deformations. So, the modal basis must contain membrane vectors.

### **2.3.4 Acoustic Coupling**

Nearly all the early work in ROM's for acoustic response prediction treated the loading as an uncoupled pressure, neglecting the re-radiation of sound from the structure. One notable exception is Dowell [27] in which linear modal models of a structure and an acoustic domain are formed independently and then coupled. The approach was shown to accurately approximate the response of a flexible wall coupled to an interior sound field and excited by an exterior field. However, the approach is limited to response levels at which the structure and acoustic fields behave linearly.

The need for structural-acoustic coupling in nonlinear response prediction methods was not well

understood until recently. This was true because no one had compared predictions from a high fidelity model, either full- or reduced-order, to experimental results at sound pressure levels high enough to cause nonlinear response. An experimental study by the authors [17] compared the measured acoustic response of a thin aluminum alloy plate in an acoustic progressive wave test facility to predictions from a nonlinear ROM. The plate was mounted in the sidewall of the progressive wave duct and was excited by acoustic energy traveling down the duct. The ROM predictions did not compare well with the experiment. The ROM of the plate had been validated previously with experimental data from a base excitation test [16], so the poor results were a surprise. The predictions were improved with the addition of nonlinear damping to the ROM, but there was no physical justification for the nonlinear damping. In a second experiment [18], the differential pressure between the front and back surface of the plate was measured and applied to the ROM instead of the front side pressure only, as had been done in the first experiment. The results from the ROM with modified loading agreed much more closely with the test. It was then determined that un-modeled acoustic coupling was the likely source of the model error. The physical phenomenon not captured in the ROM was determined to be coupling of resonant modes of the plate to axial acoustic standing waves (modes) of the duct. The duct was found to possess heavily damped axial acoustic modes at 15 Hz intervals across the frequency spectrum of the acoustic loading. The broadband nonlinear response of the plate modes coupled with these duct modes effectively adding significant damping to the lightly damped modes of the plate.

Two approaches to building coupled, nonlinear structural acoustic ROM's were investigated by the authors. In the first study [28], modes of a coupled structural-acoustic FEM were used to generate a coupled ROM. Non-symmetry and non-proportional damping in the finite-element equations resulted in complex modal equations with left and right eigenvectors. This approach proved to be impractical due to the complex mathematics. A second approach [29], based on Dowell's work [27], was developed. In this approach, modes of the uncoupled plate and duct models were combined to form a coupled modal model. Geometric nonlinearity was added to the structural model. Results from this coupled ROM agreed well with the experimental data. More detail on the coupled ROM formulations is presented in Section 3.

### 3. METHODS DEVELOPMENT

This section describes developments and refinements of the methods for computing nonlinear ROM's performed under this project. The bulk of the work is focused on the IC method. The basis IC method is described first including details of load case selection and the concept of constrained IC. The addition of an estimated membrane basis to the IC method, resulting in the *implicit condensation and expansion* (ICE) method is covered next. Explicit condensation of membrane effects is then presented. The remaining sections discuss thermal effects, acoustic coupling, and implementation of the ICE method including an example problem.

A fundamental characteristic of large amplitude nonlinear structural response is the membrane displacement induced by finite bending displacement. One way to capture the membrane displacements in a ROM is to explicitly include a membrane basis. In the previous section, it was shown that it is possible to condense the membrane modes into the bending modes, softening the nonlinear coefficients of the bending modes. The IC method similarly seeks to incorporate the membrane effects directly into the nonlinear bending terms through an estimation process. The IC method uses static load cases to estimate the nonlinear coefficients. The static cases use applied loads with membrane stretching allowed to occur in the solution process. The resulting displacements have membrane effects naturally in them. Parameters estimated from the displacements will have the softening effects *implicitly* incorporated. The major advantage of the method is that a membrane basis is not used in the construction of the ROM. The resulting ROM contains only bending modes. Time integration of the ROM results in simulated bending modal amplitudes. The effects of membrane stretching upon the simulated bending displacements are implicitly included because the nonlinear bending coefficients have been softened in the estimation process. The physical displacements spanned by the membrane modes cannot be directly obtained since there is no membrane basis. As a result, accurate strains cannot be recovered from displacement using the finite-element strain-displacement equations.

The ICE method is a variant of the IC method. The purpose of the ICE method is to complement the IC method with membrane displacement estimates to enable finite-element based stress/strain recovery. ICE uses the bending modal displacements resulting from time integration of an IC model with an additional post-processing step to recover membrane displacements. The static load cases are used to estimate a membrane basis based upon an assumed functional relationship between membrane and bending modal amplitudes.

#### 3.1 Estimating the Bending Coefficients with Implicit Condensation

One of the major tasks in the use of any of reduced-order methods is the determination of the nonlinear coefficients. The IC method does not directly involve manipulation of the finite-element nonlinear stiffness matrix to determine the coefficients. The method is an indirect method, since it determines the coefficients from finite-element solution results. Access to the internal workings of the finite-element code is not required. The method estimates the coefficients from a set of static nonlinear solutions from any suitable finite-element code. Code that implements the method is external to the finite-element program.

The initial steps in the IC method are straightforward. First, a FEM of the structure is constructed. Second, a normal modes analysis is performed on the FEM. The appropriate modes are selected from the linear modal set to determine the linear portions of the ROM. These are usually the bending modes. A set membrane modes is not explicitly included. Thus the basis is a truncated set of the bending mode shapes,

$$\Psi_b = [\psi_1 \ \psi_2 \ \dots \ \psi_n]. \quad (16)$$

The IC method is an applied loads method. An appropriate set of static loads must be selected and applied to the FEM. More information on the selection process will be discussed later. At this point, assume that static load cases have been selected and nonlinear solutions from a FEM have been obtained. The next step is the estimation of the nonlinear coefficients.

Recall that the ROM can be written as

$$\ddot{\mathbf{q}} + \bar{\mathbf{C}} \dot{\mathbf{q}} + \bar{\mathbf{K}} \mathbf{q} + \boldsymbol{\theta}(q_1, q_2, \dots, q_n) = \Psi_b^T \mathbf{f}(t) = \bar{\mathbf{f}}(t), \quad (17)$$

where

$$\mathbf{w} \approx \Psi_b \mathbf{q}, \quad (18)$$

and  $\mathbf{q}$  is a vector ( $n \times 1$ ) of generalized displacements or modal amplitudes and the dimensions of  $\Psi_b$  are  $m \times n$ . The dimensions of the reduced matrices  $\bar{\mathbf{C}}$  and  $\bar{\mathbf{K}}$  are  $n \times n$ . The reduced force vector,  $\bar{\mathbf{f}}(t)$ , is time varying with dimensions of  $n \times 1$ . The static form of Equation 17 can be written as

$$\boldsymbol{\theta}(q_1, q_2, \dots, q_n) = \bar{\mathbf{f}} - \bar{\mathbf{K}} \mathbf{q}. \quad (19)$$

The nonlinearity appears as an internal force vector function,  $\boldsymbol{\theta}$ , with dimensions of  $n \times 1$ . The nonlinearity is expressed as a function of the  $n$  generalized displacements (scalar functions of time). The function for the  $r$ th equation is given by Equation 9. Since  $\bar{\mathbf{K}}$  is diagonal, Equation 19 can be written for each mode. The equation for the  $r$ th mode is

$$\theta_r(q_1, q_2, \dots, q_n) = \bar{f}_r - \omega_r^2 q_r, \quad (20)$$

which is valid for each of the static load cases. For instance for the  $k$ th static load case, we can write Equation 20 as

$$\begin{aligned} & B_r(1,1) q_1^2[k] + B_r(1,2) q_1 q_2[k] + B_r(1,3) q_1 q_3[k] + \dots + B_r(n,n) q_n^2[k] + A_r(1,1,1) q_1^3[k] \\ & + A_r(1,1,2) q_1^2 q_2[k] + A_r(1,1,3) q_1^2 q_3[k] + \dots + A_r(n,n,n) q_n^3[k] = \bar{f}_r[k] - \omega_r^2 q_r[k], \end{aligned} \quad (21)$$

where the notation  $q_r[k]$  represents the modal amplitude of the  $r$ th mode for the  $k$ th load case. The individual modal amplitudes from each load case can be determined from the inverse of Equation 18 as

$$\mathbf{q}[k] = \Psi_b^{\#} \mathbf{w}[k], \quad (22)$$

where  $\mathbf{w}[k]$  is the vector of displacements from the  $k$ th load case and the superscript  $\#$  denotes the pseudo-inverse.

We can write Equation 21 for the  $N$  static load cases as

$$\begin{bmatrix} q_1^2[1] & q_1 q_2[1] & \dots & q_n^2[1] & q_1^3[1] & q_1^2 q_2[1] & \dots & q_n^3[1] \\ q_1^2[2] & q_1 q_2[2] & \dots & q_n^2[2] & q_1^3[2] & q_1^2 q_2[2] & \dots & q_n^3[2] \\ \vdots & \vdots & \ddots & \vdots & \vdots & \vdots & \ddots & \vdots \\ q_1^2[N] & q_1 q_2[N] & \dots & q_n^2[N] & q_1^3[N] & q_1^2 q_2[N] & \dots & q_n^3[N] \end{bmatrix} \begin{Bmatrix} B_r(1,1) \\ B_r(1,2) \\ \vdots \\ B_r(n,n) \\ A_r(1,1,1) \\ A_r(1,1,2) \\ \vdots \\ A_r(n,n,n) \end{Bmatrix} = \begin{Bmatrix} \bar{f}_r[1] - \omega_r^2 q_r[1] \\ \bar{f}_r[2] - \omega_r^2 q_r[2] \\ \vdots \\ \bar{f}_r[N] - \omega_r^2 q_r[N] \end{Bmatrix}, \quad (23)$$

or in matrix form

$$\mathbf{G} \mathbf{x}_r = \mathbf{b}_r. \quad (24)$$

The parameters for the  $r$ th mode can be found through the use of the pseudo-inverse of the modal data matrix,  $\mathbf{G}$ , as

$$\mathbf{x}_r = \mathbf{G}^\# \mathbf{b}_r. \quad (25)$$

Note that  $\mathbf{G}$  does not depend on  $r$ , so only a single pseudo-inverse has to be constructed to determine the nonlinear parameters for all the modes.

The IC method as presented includes all the possible nonlinear terms. In some cases, some of the terms can be neglected and Equation 23 can be easily modified to eliminate any negligible terms. For the case of a flat plate or beam, the quadratic terms can be neglected since the bending modes are not coupled through the quadratic terms. The method as proposed by McEwan [8, 9] restricted the nonlinear function to cubic stiffness terms. Terms involving coupling between three modes were also neglected. Cubic terms involving three modes will be referred to as *triple cubic terms*. The nonlinear function with these restrictions can be written as

$$\theta_r = \sum_{i=1}^n A_r(i,i,i) q_i^3 + \sum_{i=1}^{n-1} \sum_{j=i+1}^n \{A_r(i,i,j) q_i^2 q_j + A_r(i,j,j) q_i q_j^2\}. \quad (26)$$

In the case of a curved structure, the bending modes are coupled to each other through the quadratic terms and cubic terms. Triple cubic terms can be neglected since the entire matrix of coefficients can indirectly account for coupling between three modes. However in practice, it has been found that the inclusion of the triple cubic terms in the estimation process sometimes produces a more stable integration at high dynamic input levels. In general, it is best to include the triple cubic terms.

The number of quadratic terms per mode in the IC method is

$$\text{number of quadratic terms} = n + {}_nC_2, \quad (27)$$

where

$${}_nC_k = \frac{n!}{(n-k)! k!}. \quad (28)$$

The number of cubic terms per mode is

$$\text{number of cubic terms} = n^2 + {}_nC_3, \quad (29)$$

if the triple cubic terms are included. The number of cubic terms per mode is

$$\text{number of cubic terms} = n^2, \quad (30)$$

if the triple cubic terms are neglected. The total number of terms increases geometrically as the number of modes increases. For a ten mode model, there can be 275 terms per mode for a total of 2750 terms for all the modes.

McEwan [8, 9] suggested an estimation scheme to eliminate some of the coefficients. The scheme starts with the terms in Equation 26 and removes unnecessary terms in a regression scheme. The coefficients are estimated for an assumed form using a least squares algorithm and the static solution set. Terms in the nonlinear model are eliminated based on their individual contributions to the overall static solution set. The process is repeated until a correlation factor becomes minimally acceptable. The goal of the regression procedure is to build the ROM with the least number of nonlinear terms. However, the final model is sensitive to the particular static solution set used in the regression and it is possible that important terms can be omitted from the final model. The benefit of a single data matrix and pseudo-inverse is lost as columns of the data matrix are eliminated as coefficients are removed. The IC method used here foregoes the coefficient elimination scheme. The total integration time will be slightly increased, but no important dynamics are neglected.

The estimated coefficients from Equation 25 for each mode are independent from the other modal coefficients. However, several linear dependencies exist between nonlinear terms of different modes. The dependencies are

$$\begin{aligned} A_i(i, i, j) &= 3A_j(i, i, i), \quad A_i(i, j, j) = A_j(i, i, j), \quad A_i(i, j, k) = A_k(i, j, l), \\ A_j(i, j, k) &= 2A_i(j, j, k) = 2A_k(i, j, j), \end{aligned} \quad (31)$$

for the cubic terms and

$$B_k(i, j) = B_j(j, k) = B_j(i, k), \text{ and } B_i(i, j) = 2B_j(i, i), \quad (32)$$

for the quadratic terms. In the implementation of the IC method as defined by Equation 25, the dependencies are ignored. Therefore, the resulting set of coefficients for a multi-mode model can be mathematically inconsistent. An improved approach can be implemented that identifies the independent coefficients for all modes in a single operation. The dependent coefficients are then

computed in a second step using Equations 31-32. This approach, referred to as constrained IC, results in a consistent set of nonlinear coefficients. Anecdotal evidence suggests that constrained IC models are somewhat more stable when integrated at very high sound pressure levels compared to models using the original formulation, but this is not proven. A minor drawback to the constrained IC approach is the increased order of the estimation problem in Equation 24 which can increase the possibility of numerical ill-conditioning and result in errors in the identified coefficients.

The constrained IC method is demonstrated by example. Assume a two mode, all cubic, model. There are four cubic coefficients for each mode for a total of eight coefficients. The modal data matrix for the IC method would look like

$$\mathbf{G} = \begin{bmatrix} q_1^3[1] & q_1^2 q_2[1] & q_1 q_2^2[1] & q_2^3[1] \\ q_1^3[2] & q_1^2 q_2[2] & q_1 q_2^2[2] & q_2^3[2] \\ \vdots & \vdots & \vdots & \vdots \\ q_1^3[N] & q_1^2 q_2[N] & q_1 q_2^2[N] & q_2^3[N] \end{bmatrix} = [\mathbf{g}_1 \mathbf{g}_2 \mathbf{g}_3 \mathbf{g}_4] . \quad (33)$$

where the  $\mathbf{g}$ 's on the right hand side of Equation 33 denote columns of the data matrix,  $\mathbf{G}$ . In the IC method, the four coefficients for each mode would be solved independently from the other modes. We can write the two solutions together as

$$\begin{bmatrix} \mathbf{g}_1 & \mathbf{g}_2 & \mathbf{g}_3 & \mathbf{g}_4 & \mathbf{0} & \mathbf{0} & \mathbf{0} & \mathbf{0} \\ \mathbf{0} & \mathbf{0} & \mathbf{0} & \mathbf{0} & \mathbf{g}_1 & \mathbf{g}_2 & \mathbf{g}_3 & \mathbf{g}_4 \end{bmatrix} \begin{Bmatrix} A_1(1,1,1) \\ A_1(1,1,2) \\ A_1(1,2,2) \\ A_1(2,2,2) \\ A_2(1,1,1) \\ A_2(1,1,2) \\ A_2(1,2,2) \\ A_2(2,2,2) \end{Bmatrix} = \begin{Bmatrix} \mathbf{b}_1 \\ \mathbf{b}_2 \end{Bmatrix} . \quad (34)$$

The two nonlinear coefficients that are not related to other coefficients are

$$\begin{aligned} A_1(1,1,1) &= \alpha_1, \\ A_2(2,2,2) &= \alpha_5 . \end{aligned} \quad (35)$$

The coefficient dependencies for this example are

$$\begin{aligned} A_1(1,1,2) &= 3A_2(1,1,1) = 3\alpha_2, \\ A_1(1,2,2) &= A_2(1,1,2) = \alpha_3, \\ A_2(1,2,2) &= 3A_1(2,2,2) = 3\alpha_4, \end{aligned} \quad (36)$$

There are three dependencies, thus there are only five independent coefficients. The independent coefficients are assigned in Equations 35-36. Equation 34 can be rewritten in terms of the independent coefficients as



$$\begin{bmatrix} g_1 & g_2 & g_3 & g_4 & 0 & 0 & 0 & 0 \\ 0 & 0 & 0 & 0 & g_1 & g_2 & g_3 & g_4 \end{bmatrix} \begin{Bmatrix} \alpha_1 \\ 3\alpha_2 \\ \alpha_3 \\ \alpha_4 \\ \alpha_2 \\ \alpha_3 \\ 3\alpha_4 \\ \alpha_5 \end{Bmatrix} = \begin{Bmatrix} b_1 \\ b_2 \end{Bmatrix}, \quad (37)$$

or compactly as,

$$\begin{bmatrix} g_1 & 3g_2 & g_3 & g_4 & 0 \\ 0 & g_1 & g_2 & 3g_3 & g_4 \end{bmatrix} \begin{Bmatrix} \alpha_1 \\ \alpha_2 \\ \alpha_3 \\ \alpha_4 \\ \alpha_5 \end{Bmatrix} = \begin{Bmatrix} b_1 \\ b_2 \end{Bmatrix}. \quad (38)$$

The five independent coefficients can be found by forming a pseudo-inverse. In this example, the unconstrained IC method requires the calculation for a pseudo-inverse of a  $N \times 4$  matrix, where  $N$  is the number of load cases in the static solution. The constrained method requires calculation of a pseudo-inverse of a  $2N \times 5$  matrix.

The number of independent quadratic coefficients in the constrained IC method is

$$\text{number of independent quadratic coefficients} = n^2 + {}_n C_3. \quad (39)$$

The number of independent cubic coefficients is

$$\text{number of independent cubic terms} = n^2 + {}_n C_2 + 3({}_n C_3) + {}_n C_4, \quad (40)$$

if the triple cubic terms are included. The number changes to

$$\text{number of independent cubic terms} = n^2 + {}_n C_2 + 3({}_n C_3), \quad (41)$$

if the triple cubic terms are neglected.

For an example of 10 modes, if the quadratic and all the cubic terms are included, there are 275 coefficients per mode. The unconstrained IC method would require a pseudo-inverse of an  $N \times 275$  matrix. This same pseudo-inverse can be used for all ten modes to estimate all 2750 coefficients. The constrained IC method would estimate coefficients for all ten modes at once, but only 935 are independent, requiring a pseudo-inverse of a  $10N \times 935$  matrix.

### 3.2 The Load Cases

The most critical part of the IC method is the selection of load cases. The quality of the nonlinear estimates depends on the scaling and quantity of the load set. The set must exercise all the appropriate nonlinear effects and the modes that are in the ROM. The estimation process

constructs models in the modal domain by transforming the physical displacements into modal displacements using modal filtering. A load set based upon mode shapes will enhance the modal filtering process and insure that the solution set will contain the modal amplitudes required to build the data matrix. Each load case in the set is a scaled linear combination of one, two, or three of the modes in the basis. The scaling factors are chosen based upon linear estimates of desired displacements at one or more locations of maxima or minima as

$$a_i = \frac{\omega_i^2}{\phi_i^T \phi_i} \frac{w_c}{\{\phi_i\}_c} \quad (42)$$

where  $a_i$  is the force scaling factor for the  $i$ th mode,  $w_c$  is the desired linear displacement at point  $c$  and  $\{\phi_i\}_c$  denotes the entry for node  $c$  in the  $i$ th mode shape. The desired displacement should be large enough to cause nonlinear effects. Typically, a displacement of one panel thickness is sufficient for the primary modes to become nonlinear. Higher frequency modes generally require lower displacements. If the desired displacements are too high, the finite-element program may fail to converge. If the displacements are too low, the displacements will be in the linear range. After the static solutions are obtained, the resulting nonlinear modal displacements can be extracted and compared to the desired modal amplitudes to insure that the nonlinear effects are reasonably exercised. A trial and error process may be necessary to arrive at good load scaling.

A good choice for the load set is a set of permutations of the sums and differences of the mode shapes scaled by the load scaling factor. For instance, for a three mode model without triple cubic terms, the permutations of force scaling factors would be

$$\begin{aligned} \text{load set } A = [ & \{a_1, 0, 0\}, \{0, a_2, 0\}, \{0, 0, a_3\}, \{-a_1, 0, 0\}, \{0, -a_2, 0\}, \{0, 0, -a_3\}, \\ & \{a_1, a_2, 0\}, \{-a_1, a_2, 0\}, \{a_1, -a_2, 0\}, \{-a_1, -a_2, 0\}, \\ & \{a_1, 0, a_3\}, \{-a_1, 0, a_3\}, \{a_1, 0, -a_3\}, \{-a_1, 0, -a_3\}, \\ & \{0, a_2, a_3\}, \{0, -a_2, a_3\}, \{0, a_2, -a_3\}, \{0, -a_2, -a_3\} ], \end{aligned} \quad (43)$$

for a total of 18 permutations. In general, the number of load permutations for a model without triple cubic terms is

$$\text{number of load permutations} = 2n + 4(nC_2). \quad (44)$$

For a three-mode model with triple cubic terms, the load set should also have permutations involving three modes

$$\begin{aligned} \text{load set } B = \text{load set } A + [ & \{a_1, a_2, a_3\}, \{a_1, -a_2, a_3\}, \{a_1, a_2, -a_3\}, \{a_1, -a_2, -a_3\}, \\ & \{-a_1, a_2, a_3\}, \{-a_1, -a_2, a_3\}, \{-a_1, a_2, -a_3\}, \{-a_1, -a_2, -a_3\} ], \end{aligned} \quad (45)$$

for a total of 26 permutations. In general, the number of permutations for a model with triple cubic terms is

$$\text{number of permutations} = 2n + 4(nC_2) + 8(nC_3). \quad (46)$$

The number of permutations needed to identify the triple cubic terms becomes a large portion of the total number as the number of modes increases. For a ten mode model, 200 load cases would be required without triple cubic terms and 1160 load cases would be required with triple cubic terms.

In some cases, the estimation process may provide more robust models if multiple sets of permutations are used with different sets of scaling factors. This was found to be true for curved structures in particular. The scaling factors may also have to be adjusted to account for solution convergence issues. Sometimes the finite-element solution for load cases involving a single scaling factor will converge, but those involving two or three diverge. For these load cases, it is recommended to divide each scaling by a factor of two or three depending on whether two or three scaling factors are used in the permutation.

It may be possible to decrease the number of permutations by omitting some based upon the sign of the scaling factors. For instance, a flat plate will deform with the same magnitude in an opposite direction for load cases that are the same magnitude but have opposite signs. However, this is not true for curved structures and any built-up structure. In general, when the unconstrained IC method is used, it is recommended to use all permutations.

The constrained method may offer a means to decrease the number of load cases required. There are some triple cubic terms that are related by dependencies to non-triple terms. There may be enough information from two mode loading permutations to identify those terms. The constrained approach was used successfully with load set solutions that omitted three mode permutations [30]. In this approach, there are triple cubic terms of the type,  $A_l(i,j,k)$ , which are not related to non-triple terms. These terms were most likely negligible in Reference 30.

The most uncertain aspect of the IC method is the selection of load cases. As a general rule, a model that integrates well at high excitation levels has been properly estimated. Models that fail to integrate need more information from other load cases to get better estimates. There is no restriction on the number of load cases that can be used in the data matrix of Equation 24.

### **3.3 The Expansion Process and the ICE Method**

One of the attractive features of the IC method is that a membrane basis is not needed in the construction of the ROM. Unfortunately, the physical displacements spanned by the membrane modes cannot be directly obtained since there is no membrane basis. But the effects of membrane stretching have been implicitly condensed into the model. Therefore, it seems logical that membrane displacements can be somehow extracted from the results. The ICE method uses the static load cases to estimate a membrane basis based upon an assumed relationship between membrane and bending modal amplitudes. The membrane displacements are recovered from the bending amplitudes, the estimated membrane basis, and the assumed relationship in a post-processing expansion step.

The IC model can only predict those displacements spanned by the bending modes. The predicted displacement is an approximation

$$\mathbf{w} \approx \mathbf{w}_b = \boldsymbol{\Psi}_b \mathbf{q} . \quad (47)$$

Let's assume that the approximation could be improved by adding the membrane displacements to the bending displacements

$$\mathbf{w} \approx \mathbf{w}_b + \mathbf{w}_m , \quad (48)$$

where  $\mathbf{w}_m$  is a full length vector ( $m \times 1$ ) in physical coordinates. Notice that the displacement vectors in Equation 48 are not partitioned. Rather, the displacement vector is separated into two additive vectors. Each physical DOF has an entry in both vectors. Any structure can be modeled. In the case of a planar structure, many of the entries will be zero in either  $\mathbf{w}_b$  or  $\mathbf{w}_m$ . In the case of a curved structure modeled in a Cartesian coordinate system, the vectors will be fully populated.

The added displacement vector can be decomposed into a basis set and generalized amplitudes

$$\mathbf{w}_m = \mathbf{T} \mathbf{r} , \quad (49)$$

where  $\mathbf{r}$  is the vector of generalized membrane amplitudes, and  $\mathbf{T}$  is a matrix whose columns are membrane basis vectors. The membrane basis vectors are not normal membrane mode shapes except for the simplest structures. But let's assume that the membrane basis vectors are orthogonal to the columns of  $\boldsymbol{\Psi}_b$ . The number of generalized membrane amplitudes has not been determined yet. For convenience, let that number be  $k$ . Therefore, the vector dimension of  $\mathbf{r}$  is  $k \times 1$  and the dimensions of  $\mathbf{T}$  are  $m \times k$ .

The expansion process by which  $\mathbf{T}$  and  $\mathbf{r}$  are derived is presented here. Recall that a set of static solutions are used in the IC method to estimate the nonlinear coefficients. Those static solutions can also be used to estimate the membrane basis set. A single static solution is represented by

$$\mathbf{w} \approx \mathbf{w}_b + \mathbf{w}_m = \boldsymbol{\Psi}_b \mathbf{q} + \mathbf{T} \mathbf{r} . \quad (50)$$

Considering  $N$  static solutions, the equation becomes

$$\mathbf{W} \approx \boldsymbol{\Psi}_b \mathbf{Q} + \mathbf{T} \mathbf{R} , \quad (51)$$

where the columns of the matrices,  $\mathbf{W}$ ,  $\mathbf{Q}$ , and  $\mathbf{R}$ , correspond to the individual static solution cases. The dimensions of  $\mathbf{W}$ ,  $\mathbf{Q}$ , and  $\mathbf{R}$ , are  $m \times N$ ,  $n \times N$ , and  $k \times N$ , respectively.

Noting that columns of  $\mathbf{T}$  are orthogonal to the columns of  $\boldsymbol{\Psi}_b$ , the modal bending amplitudes in the static solution set are found by

$$\mathbf{Q} = (\boldsymbol{\Psi}_b^\#) \mathbf{W} , \quad (52)$$

Equation 51 can then be rearranged as,

$$\mathbf{T} \mathbf{R} \approx \mathbf{W} - \boldsymbol{\Psi}_b \mathbf{Q} . \quad (53)$$

If the matrix of generalized membrane amplitudes,  $\mathbf{R}$ , were known, a membrane basis set could be estimated from

$$\mathbf{T} \approx [\mathbf{W} - \Psi_b \mathbf{Q}] \mathbf{R}^{\#}. \quad (54)$$

However, the generalized membrane amplitudes are not defined at this point.

Since membrane effects are condensed into the bending equations in the implicit condensation method, it is assumed that the generalized membrane amplitudes are directly related to the modal bending amplitudes. The form of the relationship must be defined to compute the estimated membrane basis. Recall that Equation 12 showed that for a single bending-membrane pair of modes, the membrane modal amplitude was proportional to the square of the bending modal amplitude. Equation 15 shows (for a structure with DOF that can be partitioned) that the membrane DOF are forced by quadratic combinations of the bending DOF. It will also be shown in the next section, that it is possible to condense membrane modal amplitudes into the bending equations. The resulting modal membrane amplitudes are approximated by linear combinations of quadratic terms involving the modal bending amplitudes.

A quadratic relationship between modal bending amplitudes and the generalized membrane amplitudes is assumed in order to estimate a membrane basis. The generalized membrane amplitudes are defined as

$$\mathbf{r} = [q_1^2 \quad q_1 q_2 \quad q_1 q_3 \quad \dots \quad q_1 q_n \quad q_2^2 \quad q_2 q_3 \quad \dots \quad q_2 q_n \quad \dots \quad q_{n-1}^2 \quad q_{n-1} q_n \quad q_n^2]^T. \quad (55)$$

This set of generalized membrane amplitudes spans all the possible quadratic combinations of the modal bending amplitudes. The number of quadratic combinations is

$$k = n + {}_n C_2 \quad (56)$$

which defines the number of generalized membrane amplitudes and the number of columns in  $\mathbf{T}$ . Given the modal bending amplitudes,  $q_i$ , from the static load cases, a set of generalized membrane amplitudes can be generated from Equation 55 and the membrane basis set can then be estimated from Equation 54.

The estimated membrane basis is not used to construct the ROM, but rather to expand modal bending displacement results to obtain estimated membrane displacements. The time integration uses the low-order bending modes model from the IC method. The time integration provides bending modal amplitudes. After the time integration is complete, Equation 55 can be used to estimate generalized membrane amplitudes from the modal bending amplitudes for any given time. The estimated membrane basis and bending modes are used in Equation 50 to convert the bending modal amplitudes and generalized membrane amplitudes to physical displacement. The estimation of membrane displacements is a post-processing step and does not effect the computations required to perform the time integration.

The membrane stretching is included in the ICE results. The final post-processing step is stress/strain recovery. Stress/strain recovery can be accomplished using the commercial finite-element software directly for the entire model by applying the computed nodal displacements as enforced displacements and requesting stress or strain output. If the stress/strain time history is required for a single element, a single dummy element can be constructed or it may be more convenient to compute strain outside the finite-element software.

### 3.4 Explicit Condensation of Membrane Effects

The IC method is just one of many methods to construct the nonlinear ROM. Other methods explicitly include a set of membrane equations in the ROM. Notable methods include those by Rizzi et al. [13, 21, 22, 26] and Mignolet et al. [19, 20]. In a modified approach, the membrane modes could be condensed explicitly into the bending equations. The frequencies of the bending modes are much lower than the membrane modes and hence, a condensed ROM could be integrated with a larger time step.

Several approaches for selecting membrane basis vectors are discussed in the following paragraphs. The first option is to use the normal membrane modes. For straight beams or planar structures, these are normal modes that involve only in-plane motion and are much higher in frequency than the bending modes included in the model. Although normal membrane modes are relatively easy to find for a planar structure, a decision on which and how many membrane modes to include can be difficult. The membrane modes are not directly excited by the external forcing, but are only excited indirectly through quasi-static, nonlinear coupling with bending modes. As the structure becomes more complex or non-planar, normal modes may contain both membrane and bending displacements, making it very difficult to identify a membrane basis set.

An alternate strategy for the modeling of membrane effects is to synthesize the necessary membrane displacement vectors. The synthesized modes have been termed *companion* membrane [15] or *dual* [19] modes. A companion membrane mode is generated for each bending mode to provide a basis vector for the membrane stretching induced by the large displacement nonlinearity. The companion membrane mode is generated using a nonlinear finite-element static solution. The linear reaction force due to the enforced displacement of a selected bending mode is found. This force,  $\mathbf{K}\psi_b$ , is scaled and applied to the finite-element model in a nonlinear static solution. A nonlinear deflected shape,  $\psi_{nl}$ , containing both bending and induced membrane displacement is then computed from

$$[\mathbf{K} + \mathbf{K1}(\psi_{nl}) + \mathbf{K2}(\psi_{nb}, \psi_{nl})] \psi_{nl} = \alpha \mathbf{K}\psi_b, \quad (57)$$

where  $\alpha$  is a scalar. The bending mode's projection on the nonlinear deflected shape is removed through a Gram-Schmidt procedure.

The companion membrane modes are representations of the nonlinear membrane displacements resulting from large amplitude response in a particular bending mode. For all but the simplest structures, a companion membrane mode will not be a normal mode of the structure. Instead, it will be a linear combination of several normal modes. If more than one companion membrane mode is used in the nonlinear modal model, the companion membrane modes may not be

orthogonal to each other. The lack of orthogonality is not a concern if the companion membrane modal displacements are condensed into the bending modal displacements.

There is a family of methods that can be constructed based upon how the membrane modes are obtained. These include the bending and (normal) membrane modes method, the bending and companion modes method, the bending and dual modes method, and a bending and estimated membrane modes (BEM) method where the membrane modes are determined from the procedure outlined in the previous section. Regardless of the source of the membrane modes, the membrane equations can be condensed into the bending equations.

Modal condensation requires expressing the membrane modal displacements in terms of the bending modal displacements. Condensation in the modal domain is analogous to static condensation in the physical domain. The first step in modal condensation is to partition the ROM into bending and membrane equations. The membrane modes are not directly forced and respond quasi-statically. Neglecting the acceleration and velocity terms, the membrane equations become

$$\bar{\mathbf{K}}_m \mathbf{q}_m + \boldsymbol{\theta}_m(q_1, q_2, \dots, q_n) = \mathbf{0}, \quad (58)$$

where  $\mathbf{q}_m$  is the vector of membrane modal amplitudes and  $\bar{\mathbf{K}}_m$  is the linear modal membrane stiffness. For the membrane modes, the only significant terms in the nonlinear function are the quadratic terms coupled to the bending modes. Equation 58 can therefore be solved for the membrane modal amplitudes and the expressions substituted into the bending equations. For example, for a case with two bending modes and three normal membrane modes, the solution is

$$\begin{Bmatrix} q_3 \\ q_4 \\ q_5 \end{Bmatrix} = -\bar{\mathbf{K}}_m^{-1} \begin{bmatrix} B_3(1,1) & B_3(2,2) & B_3(1,2) \\ B_4(1,1) & B_4(2,2) & B_4(1,2) \\ B_5(1,1) & B_5(2,2) & B_5(1,2) \end{bmatrix} \begin{Bmatrix} q_1^2 \\ q_2^2 \\ q_1 q_2 \end{Bmatrix} \quad (59)$$

where the subscripts 1 and 2 denote the bending modes, and the subscripts 3, 4, and 5 denote the membrane modes. When substituted into the bending equations, the expressions for the membrane modal amplitudes convert the quadratic terms involving both bending and membrane modes to cubic terms involving one or more of the bending modes. The result is a nonlinear model with only bending modes where the resulting cubic terms have been softened. This condensation approach will be referred to as *general condensation*. It should be noted that  $\bar{\mathbf{K}}_m$  in Equation 58 will be a diagonal matrix for normal membrane modes but not for estimated membrane modes.

The condensation of companion membrane modes is much simpler than the general condensation of normal membrane modes. The condensation process is restricted so that a companion membrane mode can only affect the bending mode from which it was synthesized. The condensation for a bending and membrane pair is described in Equation 12.

### 3.5 Thermal Effects

Many of the structures that are exposed to high acoustic loading are also exposed to thermal loading. Thermal expansion is a major concern in many cases. Although thermal expansion causes primarily compressive stresses, panels can buckle, curved panels can bow out into the air stream, and tensile stresses can develop from dissimilar materials or non-uniform temperature distributions. Our concern is the thermal effect upon vibration response and in particular the ROM.

The thermal effect is typically modeled in the structural FEM with the addition of two terms,

$$\mathbf{M} \ddot{\mathbf{w}} + [\mathbf{K} - \mathbf{K}_{AT}(\Delta T) + \mathbf{K}1(\mathbf{w}) + \mathbf{K}2(\mathbf{w}, \mathbf{w})] \mathbf{w} = \mathbf{f} + \mathbf{f}_{AT}, \quad (60)$$

where  $\mathbf{K}_{AT}(\Delta T)$  is the change in linear stiffness due to induced thermal stresses and  $\mathbf{f}_{AT}$  is the thermal force vector. The thermal force vector is a vector of equivalent nodal forces due to the thermal expansion. The corresponding ROM becomes

$$\ddot{\mathbf{q}} + \bar{\mathbf{C}} \dot{\mathbf{q}} + \bar{\mathbf{K}}_T \mathbf{q} + \boldsymbol{\theta}(q_1, q_2, \dots, q_n) = \boldsymbol{\Psi}_b^T (\mathbf{f} + \mathbf{f}_{AT}), \quad (61)$$

where a modal damping matrix has been added and the linear modal stiffness *at temperature* is defined as

$$\bar{\mathbf{K}}_T = \boldsymbol{\Psi}_b^T (\mathbf{K} - \mathbf{K}_{AT}(\Delta T)) \boldsymbol{\Psi}_b = \bar{\mathbf{K}} - \bar{\mathbf{K}}_{AT}. \quad (62)$$

For a flat structure, the thermal force vector acts in the plane of the structure and is orthogonal to the bending modes. Hence there is no static, out-of-plane displacement due to the thermal load. The thermal stress does affect the stiffness, and buckling can occur when the stiffness matrix becomes singular. The nonlinear coefficients are not a function of the thermal stress and the mode shapes do not change appreciably with thermal load. The total effect of thermal loading on the ROM for a flat structure is simply a change in natural frequencies.

For a structure with curvature, the thermal force causes the structure to deform. The ROM—Equation 61—is still valid as the structure statically deforms. The nonlinear coefficients do not change, since they are not a function of the thermal stress. However, the modal stiffness matrix,  $\bar{\mathbf{K}}_T$ , is not diagonal. The mode shapes are defined based on a non-thermally loaded structure. These mode shapes are termed the *cold modes*; the model defined by Equation 61 is termed the cold-modes model; and the model with no thermal effects is termed the stress-free model. The cold modes are not an optimal basis for either the static or dynamic deformation of a structure with thermal stress. More modes are necessary in the cold-modes model to represent these deformations.

Alternatively, a *hot-modes* model can be formed at a particular thermal loading condition. The displacement vector is recast as the displacement minus the static displacement due to the thermal load

$$\mathbf{x} = \mathbf{w} - \mathbf{w}_\theta. \quad (63)$$



The FEM is rewritten as

$$\mathbf{M} \ddot{\mathbf{x}} + [\tilde{\mathbf{K}} + \tilde{\mathbf{K}}1(\mathbf{x}) + \tilde{\mathbf{K}}2(\mathbf{x}, \mathbf{x})]\mathbf{x} = \mathbf{f}, \quad (64)$$

where the linear stiffness,  $\tilde{\mathbf{K}}$ , is the updated stiffness matrix for the deformed state which is different from  $\mathbf{K}$ . The nonlinear stiffness functions,  $\tilde{\mathbf{K}}1$  and  $\tilde{\mathbf{K}}2$ , are also different from the previous nonlinear functions. A ROM can be built to approximate Equation 64. This is the hot-modes model. Mathematically, the hot-modes model has the same form as the stress-free model, but has different mode shapes, natural frequencies, and nonlinear coefficients.

A ROM can be built with Equation 64 and a set of hot modes using virtually the same the procedure described above for a stress-free model. The thermal load is applied in the normal modes solution and in conjunction with the static load cases. The resulting static deflections used to estimate the model have to be referenced to the static displacement,  $\mathbf{w}_0$ . The applied loads used in the estimation routine do not contain the thermal forces.

The cold-modes model is an extension of the stress-free model. The nonlinear coefficients, mode shapes, and natural frequencies are the same. Only the thermal force vector and linear modal stiffness at temperature need be determined. Both can be determined indirectly from static results from the FEM. The thermal force vector is found by constraining the model at all DOF ( $\mathbf{w} = \mathbf{0}$ ) and applying the thermal field. Equation 60 becomes

$$\mathbf{0} = \mathbf{f} + \mathbf{f}_{AT}, \quad (65)$$

which can be solved as

$$\mathbf{f}_{AT} = -\mathbf{f}. \quad (66)$$

The thermal force vector is the opposite of the applied force necessary to constrain the structure from expansion. This applied load is found as the reaction force in commercial finite-element codes. The linear modal stiffness at temperature can be computed directly in a custom finite element code. However, if the ROM is computed from a commercial code, the linear modal stiffness is estimated from additional applied load cases at temperature. A more direct approach is to determine the linear stiffness from enforced displacement solutions. This procedure was first used by Mignolet and Radu [19] and is utilized by the RANSTEP approach [26].

Consider the static version of Equation 60, pre-multiplied by  $\Psi_b^T$

$$\Psi_b^T [\mathbf{K} - \mathbf{K}_{AT}(\Delta T) + \mathbf{K}1(\mathbf{w}) + \mathbf{K}2(\mathbf{w}, \mathbf{w})]\mathbf{w} = \Psi_b^T (\mathbf{f} + \mathbf{f}_{AT}). \quad (67)$$

Let the enforced displacement vector equal an arbitrary scalar multiple of a single bending mode shape

$$\mathbf{w} = q_i \Psi_i. \quad (68)$$

Equation 67 evaluated at this displacement is

$$q_i \Psi_b^T [\mathbf{K} - \mathbf{K}_{AT}(\Delta T)] \Psi_i + q_i^2 \Psi_b^T \mathbf{K}1(\Psi_i) \Psi_i + q_i^3 \Psi_b^T \mathbf{K}2(\Psi_i, \Psi_i) \Psi_i = \Psi_b^T (\mathbf{f} + \mathbf{f}_{AT}), \quad (69)$$

which can be rewritten as

$$q_i \{\bar{\mathbf{K}}_T\}_i + q_i^2 \mathbf{a}_i + q_i^3 \mathbf{b}_i = \mathbf{f}_1, \quad (70)$$

by redefining some of the vector terms. A second equation is written for an enforced displacement of in the opposite direction ( $\mathbf{w} = -q_i \boldsymbol{\psi}_i$ )

$$-q_i \{\bar{\mathbf{K}}_T\}_i + q_i^2 \mathbf{a}_i - q_i^3 \mathbf{b}_i = \mathbf{f}_2. \quad (71)$$

A third equation is written for a second arbitrary enforced displacement ( $\mathbf{w} = \hat{q}_i \boldsymbol{\psi}_i$ )

$$\hat{q}_i \{\bar{\mathbf{K}}_T\}_i + \hat{q}_i^2 \mathbf{a}_i + \hat{q}_i^3 \mathbf{b}_i = \mathbf{f}_3. \quad (72)$$

Equations 70-72 are the same expressions (with different notation) as in [19, 26]. These equations can then be solved to determine the  $i$ th column of the linear modal stiffness at temperature as

$$\{\bar{\mathbf{K}}_T\}_i = \frac{1}{\hat{q}_i q_i^3 - q_i \hat{q}_i^3} \left[ -\frac{1}{2} (\hat{q}_i^3 + \hat{q}_i^2 q_i) \mathbf{f}_1 + \frac{1}{2} (\hat{q}_i^3 - \hat{q}_i^2 q_i) \mathbf{f}_2 + q_i^3 \mathbf{f}_3 \right]. \quad (73)$$

Each column of the linear stiffness matrix at temperature is determined by a set of reaction forces from enforced displacements solutions. The total number of enforced displacement solutions required for determination of the entire matrix is three times the number of bending modes.

Once the linear modal stiffness at temperature is determined, the change in the linear modal stress stiffness,  $\bar{\mathbf{K}}_{AT}$ , can be determined by Equation 62. The change in the stiffness is useful, because it and the thermal force are proportional to the thermal load. If the thermal load varies in magnitude, but not spatially,  $\bar{\mathbf{K}}_{AT}$  and  $\mathbf{f}_{AT}$  can be scaled proportionally. The linear modal stiffness at temperature can then be determined for another thermal load without another set of enforced displacements.

### 3.6 Acoustic Coupling using Uncoupled Mode Shapes

The previous derivations have not considered interaction between structural dynamics and the dynamics of the surrounding acoustic environment. The models are structural ROM's; acoustic effects enter the models only as an excitation pressure that is modeled as an external structural force. However, any structure produces sound as it vibrates. The sound radiated by the structure will change the effective loading and alter the structural response.

Two approaches for including acoustic coupling in a nonlinear ROM were investigated in this project. One approach uses uncoupled mode shapes of the structure and the acoustic environment. This approach was originally studied by Dowell, et al., [27]. The derivation begins with the coupled structural-acoustic FEM in a displacement-pressure formulation [31]

$$\begin{bmatrix} \mathbf{M}_s & \mathbf{0} \\ \rho \mathbf{S} & \mathbf{M}_a \end{bmatrix} \begin{Bmatrix} \ddot{\mathbf{w}} \\ \ddot{\mathbf{p}} \end{Bmatrix} + \begin{bmatrix} \mathbf{C}_s & \mathbf{0} \\ \mathbf{0} & \mathbf{C}_a \end{bmatrix} \begin{Bmatrix} \dot{\mathbf{w}} \\ \dot{\mathbf{p}} \end{Bmatrix} + \begin{bmatrix} \mathbf{K}_s & -\mathbf{S}^T \\ \mathbf{0} & \mathbf{K}_a \end{bmatrix} \begin{Bmatrix} \mathbf{w} \\ \mathbf{p} \end{Bmatrix} = \begin{Bmatrix} \mathbf{f}_s \\ \mathbf{f}_a \end{Bmatrix}, \quad (74)$$

where  $\mathbf{M}_s$  is the structural mass matrix,  $\mathbf{M}_a$  is the acoustic mass matrix,  $\mathbf{K}_s$  is the structural stiffness matrix,  $\mathbf{K}_a$  is the acoustic stiffness matrix,  $\mathbf{S}$  is the structural-acoustic coupling matrix,  $\mathbf{f}_s$  is the vector of external structural forces,  $\mathbf{f}_a$  is the vector of external acoustic forces,  $\rho$  is the acoustic fluid density,  $\mathbf{w}$  is the vector of structural displacements, and  $\mathbf{p}$  is the vector of acoustic pressures. The formulation by Craggs [31] does not include a damping matrix. One has been added here for completeness. The nonlinear structural stiffness matrices have been omitted from the equations at this point.

The equations of motions can be transformed using the uncoupled structural and acoustic mode shapes. The uncoupled structural modes are obtained from a structure-only FEM. The uncoupled acoustic modes are obtained from an acoustic-only FEM or the undamped, coupled model with a constrained structure. The physical-to-modal transformation is

$$\begin{Bmatrix} \mathbf{w} \\ \mathbf{p} \end{Bmatrix} = \begin{bmatrix} \mathbf{\Psi}_b & \mathbf{0} \\ \mathbf{0} & \mathbf{\Phi} \end{bmatrix} \begin{Bmatrix} \mathbf{q} \\ \mathbf{a} \end{Bmatrix}, \quad (75)$$

where  $\mathbf{\Phi}$  is a truncated set of uncoupled, mass normalized, acoustic mode shapes and  $\mathbf{a}$  is the vector of acoustic modal coordinates. The coupled structural-acoustic equations can be transformed to modal space as

$$\ddot{\mathbf{q}} + \bar{\mathbf{C}}_s \dot{\mathbf{q}} + \bar{\mathbf{K}}_s \mathbf{q} = \mathbf{D}^T \mathbf{a} + \mathbf{\Psi}_b^T \mathbf{f}_s(t), \quad (76)$$

and

$$\ddot{\mathbf{a}} + \bar{\mathbf{C}}_a \dot{\mathbf{a}} + \bar{\mathbf{K}}_a \mathbf{a} = -\rho \mathbf{D} \ddot{\mathbf{q}} + \mathbf{\Phi}^T \mathbf{f}_a(t), \quad (77)$$

where the modal coupling matrix is defined as

$$\mathbf{D} = \mathbf{\Phi}^T \mathbf{S} \mathbf{\Psi}_b. \quad (78)$$

The acoustic modal stiffness matrix,  $\bar{\mathbf{K}}_a$ , is a diagonal matrix constructed from the acoustic natural frequencies in a manner analogous to the construction of the structural modal stiffness matrix. The acoustic modal damping matrix,  $\bar{\mathbf{C}}_a$ , is defined as

$$\bar{\mathbf{C}}_a = \mathbf{\Phi}^T \mathbf{C}_a \mathbf{\Phi}. \quad (79)$$

The acoustic modal damping matrix may not be diagonal, since the acoustic matrix damping,  $\mathbf{C}_a$ , is not necessarily proportional to the acoustic mass and stiffness matrices. The structural modal stiffness and damping matrices,  $\bar{\mathbf{K}}_s$  and  $\bar{\mathbf{C}}_s$ , respectively, are the same as those used in Equation 17.

The use of linear, coupled, modal equations to describe the structural-acoustic interaction problem can be found in literature [27, 32]. The concept is extended here to describe nonlinear response dynamics. Equation 76 becomes nonlinear by adding the nonlinear terms from the structural ROM to obtain a set of coupled equations

$$\ddot{\mathbf{q}} + \bar{\mathbf{C}}_s \dot{\mathbf{q}} + \bar{\mathbf{K}}_s \mathbf{q} + \boldsymbol{\theta}(q_1, q_2, \dots, q_n) = \mathbf{D}^T \mathbf{a} + \boldsymbol{\Psi}^T \mathbf{f}_s(t), \quad (80)$$

$$\ddot{\mathbf{a}} + \bar{\mathbf{C}}_a \dot{\mathbf{a}} + \bar{\mathbf{K}}_a \mathbf{a} = -\rho \mathbf{D} \ddot{\mathbf{q}} + \boldsymbol{\Phi}^T \mathbf{f}_a(t), \quad (81)$$

Conversely, Equation 80 can be viewed as augmenting the structural ROM with terms to couple it to an acoustic modal equation. The important fact is that the nonlinear function in Equation 80 is the same as the nonlinear function in Equation 17. That is, the coefficients can be directly imported from the structural ROM.

The modal coupling matrix,  $\mathbf{D}$ , needs to be determined to build the coupled modal equations. This matrix can be determined directly with access to the finite element code using Equation 78 or indirectly from results from commercial codes using a linear coupled FEM. The first step in implementing the indirect approach is to constrain the structure ( $\dot{\mathbf{w}} = \dot{\mathbf{w}} = \mathbf{w} = \mathbf{0}$ ). The top equation in Equation 74 becomes

$$-\mathbf{S}^T \mathbf{p} = \mathbf{f}_s(t). \quad (82)$$

If a harmonic acoustic pressure is enforced on the structure proportional to the  $i$ th uncoupled acoustic mode,  $\phi_i$ , at an arbitrary frequency,  $\omega$ , Equation 82 becomes

$$-\mathbf{S}^T \phi_i e^{j\omega} = \{\mathbf{f}_s\}_i e^{j\omega}, \quad (83)$$

where  $\{\mathbf{f}_s\}_i$  denotes the magnitude of the external force (the reaction force) at the structural DOF. The reaction force can be readily extracted from most commercial codes. The coupling matrix is found by enforcing each of the uncoupled acoustic modes, one at a time, and extracting the reaction forces. The coupling matrix is thus determined from

$$\mathbf{D}^T = \boldsymbol{\Psi}_b^T \mathbf{S}^T \boldsymbol{\Phi} = -\boldsymbol{\Psi}_b^T [ \{\mathbf{f}_s\}_1 \{\mathbf{f}_s\}_2 \{\mathbf{f}_s\}_3 \dots \{\mathbf{f}_s\}_{na} ], \quad (84)$$

where  $na$  is the number of acoustic modes in the ROM

### 3.7 Acoustic Coupling using Mode Shapes of the Coupled System

A logical approach to building a coupled structural-acoustic ROM is to use the modes of the coupled system. The coupled-modes approach is investigated in this section. The approach is applied to the problem of a structure coupled to an exterior acoustic domain, as is the case for a skin panel on the outer surface of an aircraft. The approach is academically interesting, but ultimately proved to be impractical due to the complex mathematics required. An application of this method is presented in Section 4.6.1.

The fundamental benefit of the classic modal model is that the resulting equations of motion are uncoupled. Unfortunately, the equations of motion for the coupled structural-acoustic system in Equation 74 can not be uncoupled using the modes of the coupled system. However, an uncoupled modal system can be obtained using a state space formulation. This approach is described below. The potential benefit of the coupled modes approach is that only a few

structure-dominated modes of the coupled system should be required to achieve an accurate ROM. This is true because the acoustic pressure portion of a structurally dominated mode is the acoustic radiation pattern for the structural mode. An additional acoustic basis is not needed to capture the radiation. The uncoupled modes approach, in contrast, requires many modes of the acoustic domain to capture the sound radiation from the structure since these modes are computed independently of the structure. The complexity in the coupled formulation derives from the fact that the combined mass and stiffness matrices in Equation 74 are unsymmetric due to coupling terms,  $\rho\mathbf{S}$  and  $\mathbf{S}^T$ . As a result, each coupled mode will have a left and right eigenvector. An additional complication of the coupled modes approach is that the eigenvectors will be complex due to non-proportional damping.

The modes of a structure coupled to an exterior domain of air will be of two general classes: structure-dominated and acoustic-dominated. An unbounded acoustic domain does not possess normal modes like an enclosed cavity does. However, when the outer surface of the domain is modeled with infinite elements, computational acoustic modes exist. The structure-dominated modes, as the classification implies, primarily involve motion of the structure with induced acoustic radiation in the air. These modes are lightly damped and the damping, in the absence of any structural damping, is due to acoustic radiation. The acoustic-dominated modes are generally heavily damped, even critically damped, and can involve motion of the structure. These are not standing waves as would occur in an enclosed cavity but provide a mathematical basis to represent the acoustic pressure field.

The coupled equations of motion can be expressed in state space form as originally shown by Foss [33] as

$$\mathbf{A}\dot{\mathbf{x}} + \mathbf{B}\mathbf{x} = \tilde{\mathbf{f}} \quad (85)$$

The state space matrices are

$$\mathbf{A} = \begin{bmatrix} \mathbf{C}_c & \mathbf{M}_c \\ \mathbf{M}_c & \mathbf{0} \end{bmatrix} \text{ and } \mathbf{B} = \begin{bmatrix} \mathbf{K}_c & \mathbf{0} \\ \mathbf{0} & -\mathbf{M}_c \end{bmatrix}, \quad (86)$$

where sub-matrices  $\mathbf{M}_c$ ,  $\mathbf{C}_c$ , and  $\mathbf{K}_c$  are the coupled system matrices from Equation 74. The state space displacement vector,  $\mathbf{x}$ , and load vector,  $\tilde{\mathbf{f}}$  are

$$\mathbf{x} = [\mathbf{w}^T \mathbf{p}^T \dot{\mathbf{w}}^T \dot{\mathbf{p}}^T]^T \text{ and } \tilde{\mathbf{f}} = [\mathbf{f}_s^T \mathbf{f}_a^T \mathbf{0} \mathbf{0}]^T. \quad (87)$$

The state space equations of motions are transformed to the modal domain using the complex eigenvectors of the coupled system. The eigenvalue problem is

$$-\mathbf{B}\mathbf{X} = \boldsymbol{\lambda}\mathbf{A}\mathbf{X} \quad \text{and} \quad -\mathbf{Z}\mathbf{B} = \boldsymbol{\lambda}\mathbf{Z}\mathbf{A} \quad (88)$$

where  $\mathbf{X}$  is the matrix of right eigenvectors,  $\mathbf{Z}$  is the matrix of left eigenvectors and  $\boldsymbol{\lambda}$  is the diagonal matrix of eigenvalues. The eigenvalues of the coupled system must either be real or complex conjugate pairs. When an eigenvalue is real, the mode is critically damped and the associated eigenvector will also be real. When eigenvalues occur as a complex conjugate pair, the mode is under-damped and the associated eigenvectors will occur as a complex conjugate pair. Here, a complex conjugate pair of eigenvectors will be referred to as a single mode.

The state space equations in the modal domain have the form

$$\bar{A} \dot{q} + \bar{B} q = \bar{f} \quad (89)$$

where

$$\bar{A} = Z^T A X, \quad \bar{B} = Z^T B X, \quad \text{and} \quad \bar{f} = Z^T \tilde{f}. \quad (90)$$

The vector of state space modal coordinates,  $q$ , is computed from the physical coordinates by

$$x = X q. \quad (91)$$

Note that the right eigenvectors are used to transform the physical coordinates, while the left eigenvectors are used to transform the external forces. Finally, the eigenvectors can be normalized so that

$$Z^T A X = I \quad \text{and} \quad Z^T B X = -\lambda \quad (92)$$

where  $I$  is the identity matrix and Equation 89 simplifies to

$$\dot{q} - \lambda q = \bar{f}, \quad (93)$$

which is a set of uncoupled first-order equations.

The normalized state space form of the equations of motion in Equation 93 constitute a ROM of the coupled linear system if the eigenvector matrices are truncated to include just a few dominant, low-frequency modes of the structure. The equations of motion must now be modified to include the nonlinear geometric stiffness terms used in the structure-only model. The resulting reduced-order equations of motion with nonlinear stiffness becomes

$$\dot{q} - \lambda q + \theta(q) = \bar{f} \quad (94)$$

The nonlinear modal force term,  $\theta(q)$ , has the form

$$\theta(q) = \hat{Z}^T (K1 + K2) \hat{X}, \quad (95)$$

where  $\hat{Z}$  and  $\hat{X}$  are the upper halves of the left and right eigenvector matrices, respectively. Not surprisingly, Equation 95 has the same form as the nonlinear stiffness function in the structure-only model. Note that nonlinear acoustic behavior is not considered in this approach, but could potentially be added in the future. Writing Equation 94 for a single complex mode neglecting quadratic nonlinear terms yields the conjugate pair of equations

$$\dot{q}_r - \lambda_r q_r + A_r(r, r, r) q_r^3 + A_r(r, r, s) q_r^2 q_r^* + A_r(r, s, s) q_r (q_r^*)^2 + A_r(s, s, s) (q_r^*)^3 = \bar{f}_r \quad (96)$$

$$\dot{q}_r^* - \lambda_r^* q_r^* + A_s(r, r, r) q_r^3 + A_s(r, r, s) q_r^2 q_r^* + A_s(r, s, s) q_r (q_r^*)^2 + A_s(s, s, s) (q_r^*)^3 = \bar{f}_r^* \quad (97)$$

where an  $*$  denotes the complex conjugate and the  $r$ th and  $s$ th equations correspond to the equations for conjugate pairs. There are 8 nonlinear coefficients in Equations 96-97 for the complex conjugate pair of first order equations while a real, second order model would have one equation with only one nonlinear term! This fact suggests that it should be possible to condense Equations 96-97 into one equation with a single nonlinear coefficient. However, this condensation was not derived.

The nonlinear stiffness coefficients in Equations 96-97 can be evaluated using the IC procedure. Only the nodal DOF of the structure are used to evaluate the nonlinear coefficients. The nonlinear stiffness coefficients are complex-valued since the modal vectors used to compute them are complex.

The coupled modes approach to the acoustic coupling problem is mathematically complicated. The uncoupled modes approach is much simpler to implement. And although many acoustic modes are required in the ROM, the acoustic modal equations are linear and can be integrated with little additional computation cost. The drawback of the uncoupled approach is that the modal damping matrix is not diagonal when infinite acoustic elements or absorbing boundaries are used in the model. Hence a damping value is difficult to assign to a particular mode. If damping values are needed, the uncoupled equations can be recast as a first order set of equations in state space form and a complex eigensolution performed.

### **3.8 Implementation**

Details of the implementation of the nonlinear ROM's investigated in this project are presented in this section. A simple example of the ICE approach applied to a clamped-clamped beam is also presented.

The IC method is an indirect method in that a ROM is computed from nonlinear static solutions of the FEM. The general implementation of an indirect method is shown schematically in Figure 5. The indirect methods build ROM's and perform time integration in a computing environment separate from the finite element code. The finite element code does not need to be altered to implement the methods.

The IC and ICE methods were initially implemented using the MSC.Nastran [34] finite-element code and later converted to Abaqus [35]. They were also implemented using an in-house finite-element code written in MATLAB [36]. The computing environment used to build and integrate the models was MATLAB. When the computing environment is separate from the finite-element code a major part of the effort is writing input files for the FE code and reading the FE results into the computing environment. Input and output with MSC.Nastran is straightforward since the results can be written in ASCII format as a "punch" file. Implementation with Abaqus required a series of Python [35] programs to translate the data from the binary output database format to an ASCII format.

The first step in the process of building an ICE ROM is to perform a normal modes analysis. Frequencies and mode shapes are read into the computing environment and used to build the static load cases. The loads are used as input to nonlinear static solutions in the finite-element

code to provide displacement results. The displacement results are read into the computing environment and the nonlinear coefficients are estimated. The model at this point is in the form of Equation 17.

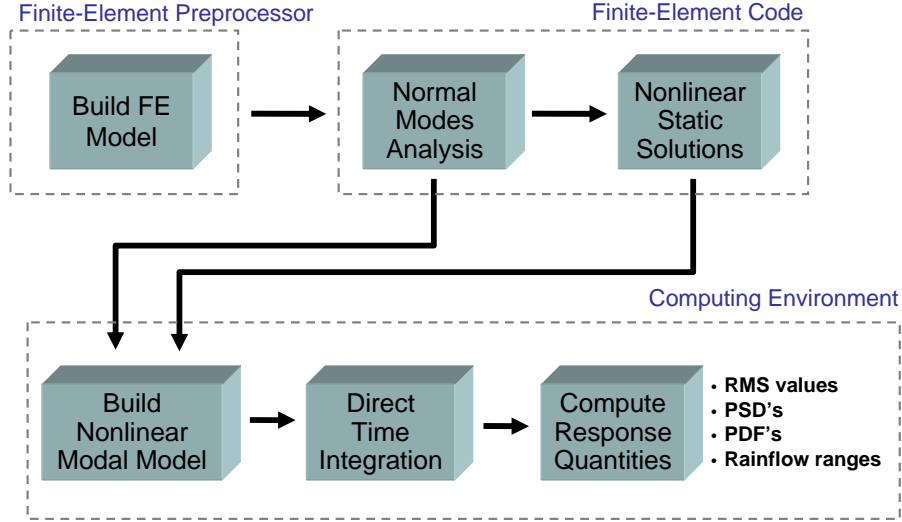


Figure 5. Procedure for an indirect method

If applied temperatures are present and a cold modes approach is used, a set of enforced displacement solution is also run in the finite-element code to provide reaction forces and the thermal forces necessary to determine the linear modal stiffness at temperature. The model would be in the form of Equation 61.

If a coupled structural-acoustic model is needed, the uncoupled acoustic modes are extracted from a normal modes analysis of the acoustic domain, and the coupling coefficients determined from a set of enforced, harmonic, acoustic solutions and Equation 84. The model would be in the form of Equations 80-81. The model may contain a thermal stiffness matrix if a cold modes approach is necessary for the structural part of the model.

The ROM, whether it contains a thermal component, a coupled acoustic component, or neither, is a modal model with nonlinear terms. The equations are second-order differential equations with a nonlinear component. The equations can be written at any time step  $k$  as

$$\mathbf{M} \mathbf{a}[k] + \mathbf{C} \mathbf{v}[k] + \mathbf{K} \mathbf{u}[k] + \mathbf{K}_{nl} \hat{\mathbf{u}}[k] = \mathbf{f}[k] \quad (98)$$

where the  $\mathbf{M}$ ,  $\mathbf{C}$ , and  $\mathbf{K}$  matrices generically represent whichever linear, or coupled linear, modal mass, damping, or stiffness matrices are in the ROM. The forcing function is also represented by a generic vector,  $\mathbf{f}$ . The modal acceleration, velocity, and displacement are represented by the vectors  $\mathbf{a}$ ,  $\mathbf{v}$ , and  $\mathbf{u}$ . In the case of a coupled problem, the modal displacement vector would also contain the acoustic modal displacement (i.e. the modal pressures). The nonlinear function is represented by the last term on the left hand side. A matrix of the nonlinear coefficients is



represented by  $\mathbf{K}_{nl}$  and the appropriate quadratic and cubic combinations of the modal displacements are in a vector represented by  $\hat{\mathbf{u}}$ .

Given a dynamic forcing function, the model can be directly integrated to provide the modal time response. There are many methods available to perform the time integration. The method used in this report is a version of the Newmark family of methods. Specifically, the method was a modification of the Hilber, Hughes and Taylor (HHT) algorithm or the so-called alpha method [37]. The modification entailed an incorporation of the nonlinear terms into the method. In HHT, two integration coefficients depend on the constant,  $\alpha$ ,

$$\gamma = 1/2 (1-2\alpha) \text{ and } \beta = 1/4 (1-\alpha)^2. \quad (99)$$

In this implementation of the method, the alpha coefficient was set to zero to provide integration with average acceleration and no artificial or numerical damping. If the differential equations are linear, selection of zero for alpha also guarantees unconditional stability. Initial velocity and displacements are needed to start the integration, these can be input to the algorithm, but usually they are assumed to be zero. An initial estimate of the acceleration is also required, this is found from an approximation of Equation 98 as

$$\mathbf{a}[0] = \mathbf{M}^{-1} (\mathbf{f}[I] - \mathbf{C} \mathbf{v}[0] - \mathbf{K} \mathbf{u}[0] + \mathbf{K}_{nl} \hat{\mathbf{u}}[0]). \quad (100)$$

During each time step,  $k$ , in the integration, there are vectors of constants that are based upon the previous values of acceleration, velocity, and displacement and the current force. These are

$$\mathbf{a}^{constant}[k] = (1 + \alpha) \mathbf{M}^{-1} \mathbf{f}[k] - \alpha \mathbf{a}[k-1], \quad (101)$$

$$\mathbf{v}^{constant}[k] = \mathbf{v}[k-1] + \Delta t (1 - \gamma) \mathbf{a}[k-1], \quad (102)$$

$$\mathbf{u}^{constant}[k] = \mathbf{u}[k-1] + \Delta t \mathbf{v}[k-1] + (1/2)(\Delta t)^2 (1-2\beta) \mathbf{a}[k-1], \quad (103)$$

where  $\Delta t$  is the time step. The initial estimate of the acceleration, velocity, and displacement at each time, is the value at the previous time. The algorithm updates the estimates at each time,  $k$ , using

$$\mathbf{a}^{i+1}[k] = \mathbf{a}^{constant}[k] - (1 + \alpha) \mathbf{M}^{-1} (\mathbf{C} \mathbf{v}^i[k] - \mathbf{K} \mathbf{u}^i[k] + \mathbf{K}_{nl} \hat{\mathbf{u}}^i[k]), \quad (104)$$

$$\mathbf{v}^{i+1}[k] = \mathbf{v}^{constant}[k] + \Delta t \gamma \mathbf{a}^{i+1}[k], \quad (105)$$

$$\mathbf{u}^{i+1}[k] = \mathbf{u}^{constant}[k] + (\Delta t)^2 \beta \mathbf{a}^{i+1}[k], \quad (106)$$

where the superscript  $i$  denotes the previous estimate and  $i+1$  denotes the updated estimate. The algorithm iterates at the time step until some convergence criteria is met. The convergence criteria used is

$$| (u_j^{i+1}[k] - u_j^i[k]) / u_j^{i+1}[k] | < \varepsilon, \quad (107)$$

for all modes  $j$ , where  $\varepsilon$  is the tolerance. Typically, the tolerance is set to 0.001. When the tolerance is met, the updated estimates become the value of acceleration, velocity, and displacement at time  $k$ , as well as, the initial estimates at the next time step and the algorithm marches forward in time.

The forcing function is evaluated at the beginning of each time step and is held constant until convergence is achieved for that step. The forcing function is usually an acoustic load. However for a structure-only model, the force appears as a mechanical force not an acoustic pressure. Therefore, the acoustic pressure has to be converted to equivalent nodal forces. This was also done for the coupled structural-acoustic model. The pressure in the coupled model therefore represents the response of the acoustic domain to the vibratory motion of the structure.

The acoustic loads used in this report were Gaussian random time histories with a specified overall sound pressure level (OASPL) in decibels (dB)

$$OASPL = 20 \log_{10} \frac{P_{rms}}{P_{ref}} \quad (108)$$

where  $P_{rms}$  is the root-mean-squared acoustic pressure in a specified frequency band, and  $P_{ref}$  is a reference pressure ( $P_{ref} = 2 \cdot 10^{-5}$  Pa or  $2.9 \cdot 10^{-9}$  psi). The spectrum level was considered to be constant in the frequency band, although there is no requirement for a constant spectrum level. In order to produce a time domain pressure signal, first, a complex Discrete Fourier Transform (DFT) was generated with the proper spectrum level but with a uniform random phase at each frequency bin. The inverse of the DFT was then calculated. The resulting time series is Gaussian [38].

The acoustic pressure on the surface of a flight vehicle skin can have complex amplitude and phase content. However, the pressure is often assumed to be a plane wave with either normal or grazing incidence to simplify response prediction. Sonic fatigue testing is often performed in a progressive wave duct, which provides a plane wave acoustic environment with grazing incidence, often referred to as a traveling wave. The pressure amplitude in a traveling wave varies with time in the propagation direction but is spatially uniform in the direction normal to the propagation direction. The scheme for simulating traveling wave acoustic loading used in this project was adopted from [11]. In this scheme, the panel is divided into zones based upon the relative propagation speed of the wave and the sample rate of the integration. The pressure is considered spatially uniform in each zone. The pressure amplitude varies randomly in a zone, but the pressure is time correlated across the various zones since it is marching in time. The pressure can be uniform across the entire panel in some cases. A uniform pressure field is often considered simply because it is easier to model. In the uniform case, the loading is simulated as a spatially uniform pressure with the amplitude of the pressure varying in time. A uniform pressure field can directly excite only the symmetric modes of a structure. Anti-symmetric modes can be excited parametrically if coupling exists between the symmetric and anti-symmetric modes. A traveling wave can directly excite symmetric and anti-symmetric modes.

Recall that the integration scheme is unconditionally stable for linear systems. However, the set of equations that is being integrated is nonlinear. A very fine step size was required to keep the integration stable, typically the sample rate used in this report was between 10kHz and 100kHz.

Since the forcing function is random, a long time history is necessary to generate good statistical averages. The time history length typically ranged between 60 and 100 seconds. For a model with ten modes, sampled at 100kHz, with a 100 second time history, there are a total of  $10^8$  samples of modal amplitudes in a record. That seems like a lot of data, but it is very compact considering that the data stored for a FEM with 100 thousand DOF would be  $10^{12}$  data samples.

### 3.9 Implementation Example

A clamped-clamped beam example problem is used in this section to demonstrate the implementation of the method. The example is from Section 4.1 and Reference 24. The beam is rigidly clamped at both ends and is 9.0 inches long, 0.5 inch wide, and 0.031 inch thick. The beam material is steel with a Young's modulus of 29.7 Mpsi, a shear modulus of 11.6 Mpsi, and a mass density of  $7.36 \cdot 10^{-4}$  lb-s<sup>2</sup>/in<sup>4</sup>. The beam is free from preload and is to be subjected to a uniform random acceleration with a flat, band-limited (0-500 Hz) spectrum. The input is capable of exciting only the symmetric bending modes of the beam.

A 2-D FEM with 20, 2-node beam elements is used to model the example problem. Only half of the beam is modeled, using symmetry, since the inertial loading could only excite symmetric bending modes. MSC.Nastran is the finite-element code used to model the beam. A normal modes analysis is capable of producing only the symmetric modes of the beam. The first two modes occur at 79.0 Hz and 427 Hz and are the only modes in the bandwidth of interest. The ROM for the IC method contains only these two modes. Since the beam is flat, there is no quadratic coupling expected between these two modes so only cubic nonlinear terms are included in the model. The form of the model becomes

$$\ddot{q}_1 + 2\zeta_1\omega_1\dot{p}_1 + \omega_1^2q_1 + A_1(1,1,1)q_1^3 + A_1(1,1,2)q_1^2q_2 + A_1(1,2,2)q_1q_2^2 + A_1(2,2,2)q_2^3 = f_1(t) \quad (109)$$

$$\ddot{q}_2 + 2\zeta_2\omega_2\dot{p}_2 + \omega_2^2q_2 + A_2(1,1,1)q_1^3 + A_2(1,1,2)q_1^2q_2 + A_2(1,2,2)q_1q_2^2 + A_2(2,2,2)q_2^3 = f_2(t) \quad (110)$$

The amplitudes for the load cases are determined using Equation 42. The desired linear displacements,  $w_c$ , are referenced to the center of the beam, and are twice the beam thickness for the first mode and a tenth of the thickness for the second mode. There are no triple cubic terms for a two mode model. The number of load cases determined by Equation 44 is eight, which are

$$\text{load set } A = [\{a_1, 0\}, \{0, a_2\}, \{-a_1, 0\}, \{0, -a_2\}, \\ \{a_1, a_2\}, \{-a_1, a_2\}, \{a_1, -a_2\}, \{-a_1, -a_2\}]. \quad (111)$$

The coefficients can be estimated from the original unconstrained approach. The size of the modal data matrix for this example is eight by eight. This matrix is inverted once, and used for each of the two modes. The estimated coefficients are given in Table 1.

Note that the coefficients in the table are based on mass-normalized mode shapes. The coefficients can also be estimated from the constrained approach. The constrained coefficient dependencies for this example are given in Equation 36. There are five independent coefficients in this example, and the data matrix is 16 by five. For comparison, the estimated coefficients for

the constrained approach are also given in Table 1. The coefficients for this simple example are nearly equal.

Table 1. Estimated coefficients for the clamped beam example

Parameter	Unconstrained	Constrained
$A_1(1,1,1)$	$8.97 \times 10^{12}$	$8.97 \times 10^{12}$
$A_1(1,1,2)$	$2.08 \times 10^{13}$	$2.03 \times 10^{13}$
$A_1(1,2,2)$	$8.33 \times 10^{13}$	$8.20 \times 10^{13}$
$A_1(2,2,2)$	$4.62 \times 10^{13}$	$5.33 \times 10^{13}$
$A_2(1,1,1)$	$6.98 \times 10^{12}$	$6.98 \times 10^{12}$
$A_2(1,1,2)$	$8.20 \times 10^{13}$	$8.20 \times 10^{13}$
$A_2(1,2,2)$	$1.59 \times 10^{14}$	$1.60 \times 10^{14}$
$A_2(2,2,2)$	$3.48 \times 10^{14}$	$3.46 \times 10^{14}$

**THIS PAGE INTENTIONALLY LEFT BLANK**

## 4.0 APPLICATIONS

The nonlinear reduced-order modeling methods developed in this effort were applied to several example structures to determine their accuracy and computational efficiency. In addition, a few simple numerical examples of coupled structural-acoustic response were also investigated. The example structures included two straight beams, a curved beam, a rectangular plate, and a curved panel. Full-order finite element simulations were performed on each example and experiments were performed on all of the example structures except the curved beam to generate response data to compare with ROM predictions. This section presents detailed descriptions of the example structures, nonlinear ROM development, test procedures and a comparison of ROM predictions with full order simulations and experimental data.

### 4.1 The 9-Inch Clamped-Clamped Beam

The first example problem studied in this effort was a straight beam with clamped ends. This was the simplest structure that exhibited the nonlinear characteristics present in sonic fatigue. Nonlinear ROM's were generated for a perfectly clamped beam using several of the methods described in the previous sections. Nonlinear stiffness coefficients and random response were computed. A steel test article was fabricated and tested with random base excitation on an electrodynamic shaker. Reduced-order models were computed for the experimental model with measured boundary stiffnesses. Details of the experiment, ROM development, and comparison of results are presented in the following paragraphs. This work was originally presented in References [15, 24, 39].

The beam used in the example problem is the same beam as in the example in Section 3.7. The beam was free from preload and was subjected to a random base motion. The input was Gaussian with a flat, band-limited (0-500 Hz) spectrum. Root mean square input acceleration levels of 0.5, 1, 2, 4 and 8 g's were used in the simulations. The input spectrum excited the first two symmetric bending modes of the beam. These two modes occurred at 79.0 Hz and 427 Hz in the linear FEM. Modal damping ratios of 0.003 and 0.005 were assumed for these two modes, respectively.

#### 4.1.1 Reduced-Order Models

Nonlinear ROM's of the beam with perfectly clamped ends were generated using five methods. The first method, referred to as the *bending modes* method, includes only bending modes in the nonlinear modal model. This method is based on the approach described in [13] and uses the enforced displacement procedure to evaluate nonlinear stiffness coefficients. The second method is the *bending and membrane modes* (BM) method. This method uses bending and normal membrane modes to compute the nonlinear coefficients. The enforced displacement procedure is again used to compute the nonlinear coefficients. Generalized condensation is then used to incorporate the membrane modes into the bending equations for time integration. The third method is the *companion modes* method. It uses pairs of bending and companion membrane modes in the basis set. The enforced displacement procedure is used to compute the nonlinear coefficients. Modal condensation is then used to express each companion membrane mode in terms of its bending mode twin. This is the method reported in [24]. The fourth method is

referred to as the *physical condensation* method. It is the method of Shi and Mei [12]. The fifth and final method evaluated was the IC method. This method uses the applied loads procedure to evaluate the nonlinear coefficients and thus uses only bending modes in the modal basis. This is the method described in References [8, 9, 24] and discussed in detail in Section 3.

A 2-D FEM with 20, two-node beam elements was used to model the perfectly clamped beam. Only half of the beam was modeled, using symmetry, since the inertial loading could only excite symmetric bending modes. MSC.Nastran was used to compute the necessary solutions for all the methods except the physical condensation method. This method used an in-house code implemented in MATLAB. The first six normal membrane modes were used in the BM method. These modes had frequencies of 22.3 kHz, 44.8 kHz, 67.6 kHz, 90.8 kHz, 114 kHz, and 139 kHz. A companion membrane mode was generated for each of the two bending modes in the companion modes method.

The candidate methods were first used to form one-mode ROM's. The first bending mode was used in the models since it dominates the response of the beam to base excitation. A one-mode model was used so that nonlinear stiffness coefficients could be compared to published analytical results [40]. However, the one-mode models were not as accurate in predicting response as the two-mode models discussed later. The companion membrane mode or normal membrane modes were condensed into the one-mode model according to the particular method.

A one-mode version of the nonlinear modal model expressed in Equation 8 is given by

$$\ddot{q}_1 + 2\zeta_1 \omega_1 \dot{q}_1 + \omega_1^2 q_1 + A_1(1,1,1)q_1^3 = \psi_1^T f(t) \quad (112)$$

This model can be converted to an equivalent model in physical coordinates using the mode shape. This is done to compare the models obtained from the candidate methods to the one derived from the literature. By selecting the out-of-plane displacement at the center of the beam,  $w_c$ , as the physical coordinate of interest, the model becomes

$$\ddot{w}_c + 2\zeta_1 \omega_1 \dot{w}_c + \omega_1^2 w_c + \tilde{A}_1(1,1,1) w_c^3 = \psi_{1c} \psi_1^T f(t) \quad (113)$$

where  $\psi_{1c}$  denotes the row entry of the first mode shape vector that corresponds to the center DOF. The cubic coefficient is expressed in physical units and is denoted as  $\tilde{A}_1(1,1,1)$ .

An analytical value for the cubic nonlinear coefficient was determined by curve fitting data found in [40] for frequency ratios at several amplitude ratios. The curve fit procedure found in [41] was used to estimate the coefficient from an approximation to the nonlinear backbone curve. The resulting expression for the cubic coefficient is

$$\tilde{A}_1(1,1,1) = (0.0585) \frac{\omega_1^2}{r^2} \quad (114)$$

where  $r$  is the radius of gyration and  $\omega_1$  is the first linear natural frequency. The cubic coefficient was determined and is presented in Table 2.

The cubic coefficients for a one-mode model computed with the five nonlinear modal methods are presented in Table 2 in physical units. The analytical value from Reference [40] is included

for comparison. All the methods except the bending modes method produce cubic coefficients that agree well with the analytical value. The cubic coefficient from the bending modes method is 50% higher than the analytical value. That is, all the methods, except the bending modes methods, have softened the cubic coefficient. The impact of the difference in cubic coefficients on the RMS displacement at the center of the beam is also shown in Table 2. The loading was a zero-mean, normal, 8g RMS, 0-500 Hz band-limited, base motion input. All the methods except for the bending modes method yielded values of 0.047 or 0.048 in. The value from the bending modes method was somewhat lower at 0.044 in.

Table 2. Nonlinear coefficients for single mode nonlinear ROM's

Method	$\tilde{A}_I(1,1,1)$ (in <sup>-2</sup> s <sup>-2</sup> )	displacement* (in)
analytical	$1.80 \cdot 10^8$	--
bending modes	$2.70 \cdot 10^8$	0.044
bending and membrane modes	$1.84 \cdot 10^8$	0.048
companion modes	$1.84 \cdot 10^8$	0.048
physical condensation	$1.83 \cdot 10^8$	0.047
implicit condensation	$1.79 \cdot 10^8$	0.047

\* - RMS displacement of the center of the beam for a simulated 8g, 0-500 Hz random load.

The power spectral densities of beam center displacement were estimated for each of the methods. The PSD's for the IC and the bending modes method are shown in Figure 6. The PSD of the predicted response for the other three methods are essentially the same as that for the IC method and are omitted from the figure for clarity. The results shown in Table 2 and Figure 6 show that the higher value for the cubic coefficient obtained when the membrane stretching is neglected (the bending modes method) results in: 1) a lower RMS value, 2) a lower peak in the PSD of the response, 3) a peak that is shifted higher in frequency, and 4) a broader peak.

Traditionally, a single-mode model is thought to be adequate to model the response of most stiffened-skin aircraft structures since they are assumed to respond predominantly in their first mode. However, a multi-mode nonlinear model has terms that couple the first mode to higher modes in the model. In the clamped-clamped beam example problem, nonlinear coupling terms can cause response in the second mode to affect the first mode and vice versa. It is shown here that the nonlinear coupling terms in a two-mode model will affect the response in the first mode. It will also be shown that the way in which the membrane stretching is modeled affects the magnitude of the coupling terms and thus affects the predicted response.

A two-mode nonlinear ROM has the form

$$\ddot{q}_1 + 2\zeta_1\omega_1\dot{q}_1 + \omega_1^2q_1 + A_1(1,1,1)q_1^3 + A_1(1,1,2)q_1^2q_2 + A_1(1,2,2)q_1q_2^2 + A_1(2,2,2)q_2^3 = f_1(t) \quad (115)$$

$$\ddot{q}_2 + 2\zeta_2\omega_2\dot{q}_2 + \omega_2^2q_2 + A_2(1,1,1)q_1^3 + A_2(1,1,2)q_1^2q_2 + A_2(1,2,2)q_1q_2^2 + A_2(2,2,2)q_2^3 = f_2(t) \quad (116)$$

where  $f_1$  and  $f_2$  are modal force components. Note that there are no quadratic nonlinear terms since they have been condensed into the cubic terms. The modal equations are transformed to



physical coordinates by selecting the out-of-plane displacement at the center of the beam as the coordinate of interest. The two-mode nonlinear coefficients for the five modeling methods were computed and converted to physical units. The coefficients are listed in Table 3.

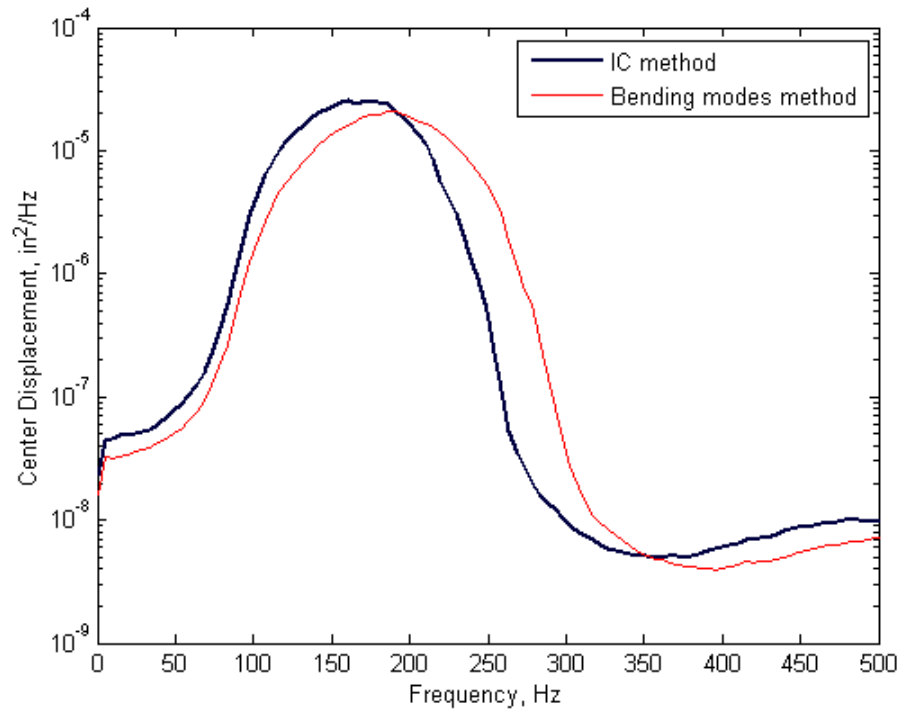


Figure 6. The PSD of the response of the center of the beam due to an 8g, 0-500 Hz base excitation using one-mode models.

Table 3. Nonlinear coefficients from the two-mode models.

Coefficient* (in <sup>-2</sup> s <sup>-2</sup> )	Method:				
	bending modes	bending & membrane modes	companion modes	physical condensation	implicit condensation
$\tilde{A}1(1,1,1)$	$2.70 \cdot 10^8$	$1.84 \cdot 10^8$	$1.84 \cdot 10^8$	$1.83 \cdot 10^8$	$1.82 \cdot 10^8$
$\tilde{A}1(1,1,2)$	$6.41 \cdot 10^8$	$4.92 \cdot 10^8$	$6.41 \cdot 10^8$	$4.90 \cdot 10^8$	$4.79 \cdot 10^8$
$\tilde{A}1(1,2,2)$	$5.56 \cdot 10^9$	$2.17 \cdot 10^9$	$5.56 \cdot 10^9$	$2.17 \cdot 10^9$	$2.16 \cdot 10^9$
$\tilde{A}1(2,2,2)$	$4.31 \cdot 10^9$	$1.68 \cdot 10^9$	$4.31 \cdot 10^9$	$1.68 \cdot 10^9$	$1.36 \cdot 10^9$
$\tilde{A}2(1,1,1)$	$1.68 \cdot 10^8$	$1.29 \cdot 10^8$	$1.68 \cdot 10^8$	$1.23 \cdot 10^8$	$1.26 \cdot 10^8$
$\tilde{A}2(1,1,2)$	$4.36 \cdot 10^9$	$1.70 \cdot 10^9$	$4.36 \cdot 10^9$	$1.63 \cdot 10^9$	$1.67 \cdot 10^9$
$\tilde{A}2(1,2,2)$	$1.01 \cdot 10^{10}$	$3.94 \cdot 10^9$	$1.01 \cdot 10^{10}$	$3.79 \cdot 10^9$	$3.66 \cdot 10^9$
$\tilde{A}2(2,2,2)$	$2.44 \cdot 10^{10}$	$1.50 \cdot 10^{10}$	$1.50 \cdot 10^{10}$	$1.45 \cdot 10^{10}$	$9.03 \cdot 10^9$

\*- the coefficients are from nonlinear modal models written in physical coordinates

The  $\tilde{A}_1(1,1,1)$  coefficient for the bending modes method, shown in Table 3, is still 50% larger than the  $\tilde{A}_1(1,1,1)$  coefficients from the other methods. The  $\tilde{A}_1(1,1,1)$  coefficients for the two-mode models all agree with the corresponding one-mode cubic terms in Table 2. The coefficients for the companion modes method are identical to those from the bending modes method except for two values. Simple condensation restricted the condensation of the companion membrane modes from affecting the cross coupling terms. Thus only the primary cubic terms,  $\tilde{A}_1(1,1,1)$  and  $\tilde{A}_2(2,2,2)$ , were softened by the companion membrane modes. All the coefficients of the BM modes method were affected by general condensation. Before condensation of the membrane modes, the nonlinear coefficients of the bending modes in the BM method are exactly the same as those from the bending modes method. After condensation, all of the coefficients are different from the bending modes method. Only the primary cubic terms,  $\tilde{A}_1(1,1,1)$  and  $\tilde{A}_2(2,2,2)$ , from the BM method agree with the companion modes method. Thus, the softening of the primary nonlinear terms is the same for the two methods. The coefficients from the physical condensation, IC, and the BM methods are all very similar. These three methods use very different means of modeling the membrane stretching and very different means of extracting the nonlinear coefficients. Yet, the coefficients from the physical condensation method vary only slightly from the coefficients from the BM method. The coefficients from the IC method vary a bit more; only the  $\tilde{A}_2(2,2,2)$  term is significantly different from the other two methods.

Simulations were run using the two-mode models. Response was calculated for the same input as the single-mode model (a zero-mean, normal, 8g RMS, 0-500 Hz band-limited, base motion input). The PSD of the beam center displacement is shown in Figure 7 for the IC, companion modes, and bending modes methods. The PSD's from the physical condensation method and the BM method are omitted from the figure since they are essentially the same as the PSD plot from the IC method, as one would expect from the similarity of their model coefficients. The PSD's for the bending modes method and companion modes method are very similar to their respective single-mode PSD plots shown in Figure 6 with variations occurring only at the higher frequencies. Thus, the two-mode models for the bending modes method and companion modes methods simply added response for the second mode when compared to the one-mode models. Little coupling between the two modes occurs with these models. However, with the IC, physical condensation, and the BM methods, coupling between the two modes did occur. The PSD from the IC method is significantly different from the PSD's of the bending modes method and the companion modes method. The first-mode peak is significantly narrower and the amplitude of the second mode is raised in the PSD for the IC method. This indicates that vibration energy from the first mode has been transferred to the second mode.

The RMS displacements for the 8g load case simulations are given in Table 4. The only value that is significantly different from the others is the value for the companion modes method. The close agreement between the RMS values for the bending modes method and the other methods masks the fact that their PSD's are significantly different. RMS displacements for simulations with 2g loading are also listed in Table 4. At this reduced input level the RMS displacements for each of the methods are now nearly equal. Figure 8 shows the PSD's for the 2g simulation cases.

Note that, again, the PSD's for the physical condensation method and the BM method agree closely with the IC method and are not shown for the sake of clarity. Differences in the PSD plots can be seen, but they are much smaller than for the 8g load case.

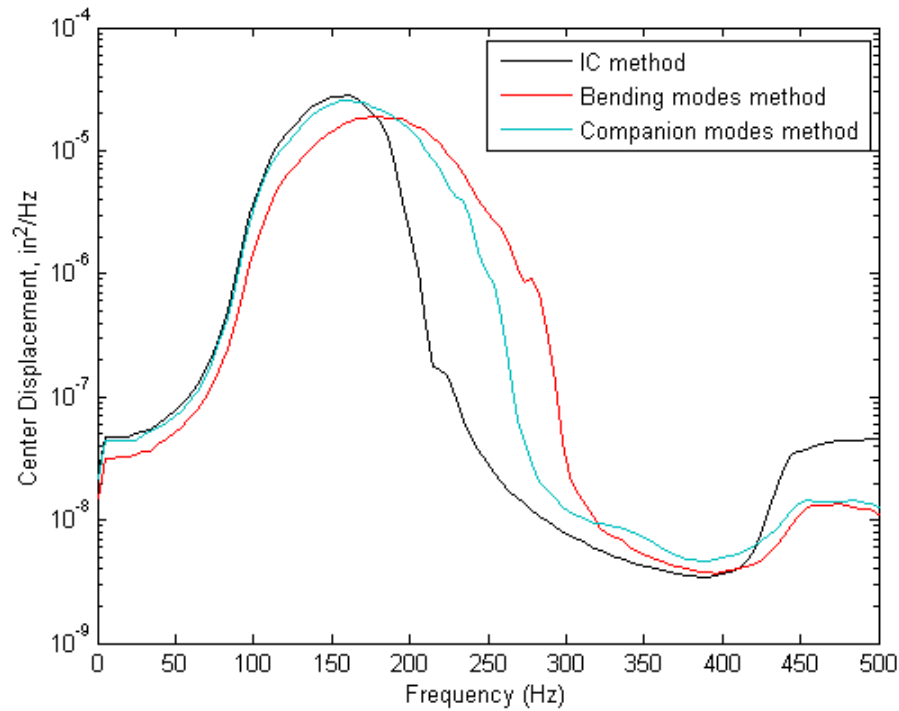


Figure 7. The PSD of the response of the center of the beam due to an 8g, 0-500 Hz base excitation using two-mode models.

Table 4. The RMS displacement of the center of the beam from simulations.

Case	Method:				
	bending modes	bending & membrane modes	companion modes	physical condensation	implicit condensation
	(in)	(in)	(in)	(in)	(in)
8g loading ( $\zeta_1=0.3\%$ , $\zeta_2=0.5\%$ )	0.043	0.043	0.046	0.042	0.042
2g loading ( $\zeta_1=0.3\%$ , $\zeta_2=0.5\%$ )	0.019	0.020	0.020	0.020	0.020
8g loading ( $\zeta_1=1\%$ , $\zeta_2=1\%$ )	0.031	0.033	0.032	0.033	0.032

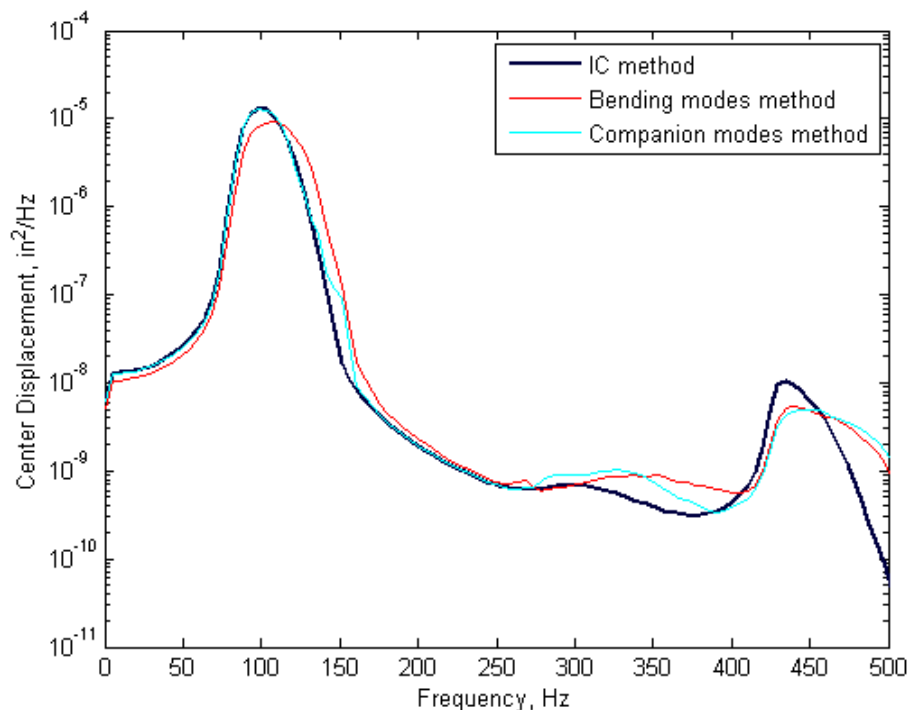


Figure 8. The PSD of the response of the center of the beam due to a 2g, 0-500 Hz base excitation using two-mode models.

RMS displacements for simulations with 8g loading and modal damping ratios for both modes increased to 0.01 are also listed in Table 4. The increased damping has reduced the RMS displacements compared to the nominal damping case. In addition, the value for the companion modes method is nearly equal to the values for the other methods. The PSD's for the models with increased damping are shown in Figure 9. The added damping has reduced the differences among the curves.

#### 4.1.2 Experiment Design

The clamped beam experiment described here was designed with several requirements in mind. First, the beam must have two symmetric bending mode natural frequencies in the range of 50-500 Hz. The test fixture should be rigid compared to the beam, have a coefficient of thermal expansion as close to that of the beam as possible, and allow a simple procedure to introduce axial preload into the beam. The excitation method must be capable of applying distributed loads without otherwise affecting beam mass, stiffness, or damping. The response measurement system must be capable of measuring displacement and strain at the beam mid-span, again without significantly affecting beam response.

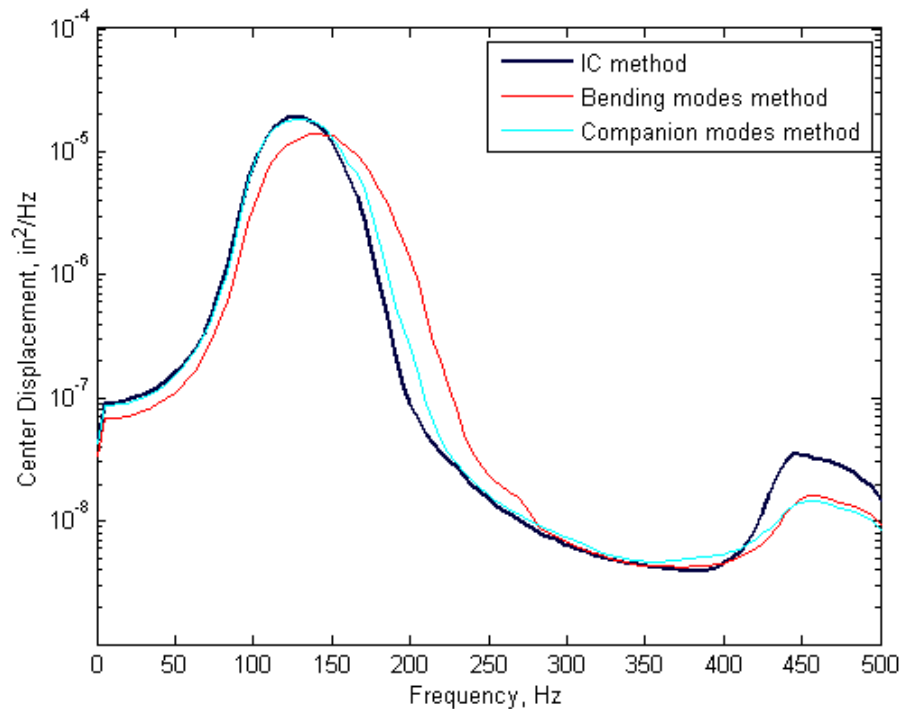


Figure 9. The PSD of the response of the center of the beam due to an 8g, 0-500 Hz base excitation using two-mode models. The damping for the two modes is increased to 1% of critical for this plot.

The testing was conducted utilizing high-carbon, spring-steel beams in a clamped-clamped configuration. The beams were 12-in-long precision-machined feeler gages, with an effective length of 9.0 in, a nominal width of 0.5 in, and a nominal thickness of 0.031 in. The high-carbon steel material had a Young's modulus of 29.7 Mpsi and a mass density of  $7.36 \cdot 10^{-4} \text{ lb-s}^2/\text{in}^4$ . The fixture was machined from A36 hot-rolled steel, with a configuration similar to that used in Yamaki and Mora [42]. The beam and fixture are displayed in Figure 10. The specimens were clamped into the fixture using 0.5 in-thick end caps covering a 1.5 in length of each beam end. Clamping force was applied to the beam via two bolts at each end tightened to 70 in-lb. A 0.025 in-deep groove was machined into the mating surface of the fixture in order to ensure proper beam alignment in the axial direction. A thin layer of cyanoacrylate glue was applied between the beam and the mating surface of the fixture to increase the rigidity of the clamp. Axial preload could be added to the beam by heating or cooling the beam relative to the fixture before clamping.

The beam and fixture were designed for base excitation on a large electrodynamic shaker. Base excitation provided distributed inertial loads to the beam without the need to attach an exciter directly to the beam. A 1200 lb shaker was used in this effort. A closed-loop shaker controller was used with an accelerometer on the shaker head to maintain the desired RMS input level and spectrum shape during testing. The shaker was oriented horizontally so that the beam was positioned in a vertical plane to minimize lateral loading due to gravity.

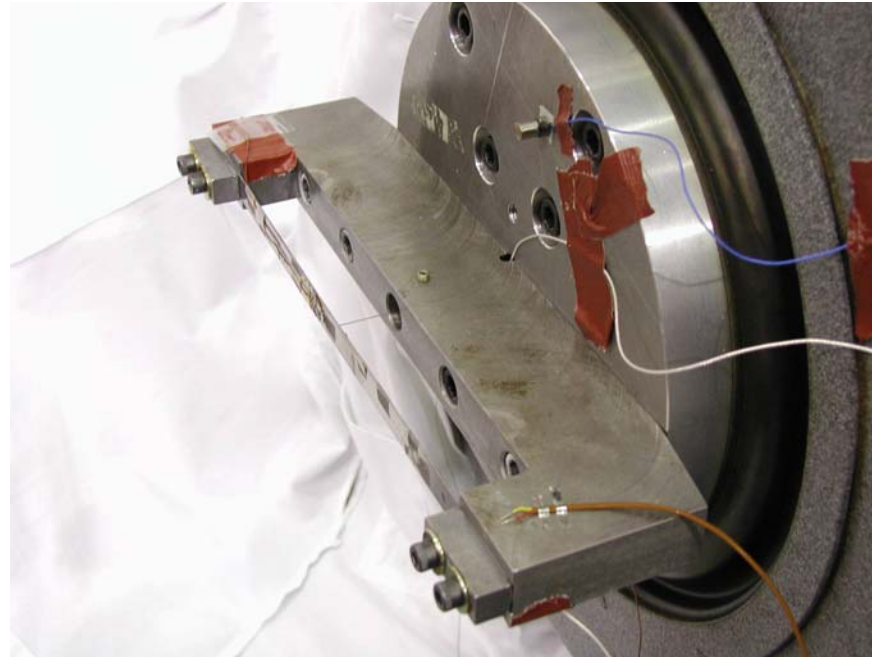


Figure 10. Beam specimen and fixture mounted on the electrodynamic shaker.

Mechanical strains at the mid-span of one beam specimen were measured with a pair of resistive strain gages thermally matched to the beam. The gages were bonded on the top and bottom surfaces of the beam in a ‘back-to-back’ symmetric configuration, oriented in the axial direction. This configuration was used in order to distinguish between total, bending and membrane strain. A miniature differential variable reluctance transducer (DVRT) with signal conditioner and power supply was selected to measure the dynamic displacement of the beam. The DVRT incorporates a plunger rod, which slides inside a core housing generating a voltage proportional to relative displacement between the plunger and core. The DVRT had an overall stroke of 0.35 in, a sensitivity of 13.5 mV/0.001 in, and a resolution of  $1.8 \cdot 10^{-4}$  in. In addition, the DVRT plunger had a mass of only 25 mg, which was negligible compared to the mass of the beam. The DVRT housing was mounted in the fixture, aligned perpendicular to the surface of the beam, while the 0.020-in diameter DVRT plunger was attached to the beam at its mid-span with a small drop of epoxy. The DVRT plunger, attached to the specimen mid-span, can be seen in Figure 10. Due to temperature variations expected during testing, small thermocouples were welded to both the fixture and each beam approximately 0.5 in from one end. Of particular concern were the transient thermal effects resulting from differences in the thermal mass of the beam and fixture. Signals from the shaker table accelerometer, the DVRT, and the strain gages were monitored and recorded with a multi-channel digital data acquisition system. The thermocouple readings were monitored throughout the test sequence to insure no significant temperature variations occurred.

#### 4.1.3 Characterization Testing

An initial series of tests was performed with several clamped-clamped and cantilevered beams in the test fixture to verify material properties, determine actual boundary conditions, investigate the effect of axial preload on linear natural frequencies, and characterize the cubic nonlinear stiffness coefficient. The accuracy of the nominal material property values was verified by test

and FE analysis of 4-inch and 5-inch cantilever beams bolted into one end of the test fixture. It was determined that the small differences ( $< 2\%$ ) between measured and predicted first mode bending frequencies were due to rotational stiffness of the fixture rather than differences between nominal and actual Young's modulus and density values for the steel beam material.

Tests and linear analyses were performed to determine the actual boundary conditions provided by the fixture. Approaching the classical boundary conditions for a clamped-clamped beam requires a very stiff fixture. This is especially true in the axial direction where forces from mid-plane stretching due to large displacements can be very high. The fixture stiffness in the axial direction was determined from measured axial mode frequencies of a clamped-clamped beam and predicted frequencies from a FEM. The first two axial natural frequencies were measured using a pair of small piezoelectric strain actuators, one on each side of the beam near one end, for excitation. A MSC.Nastran model of the beam was generated with linear springs connecting the axial degree of freedom (DOF) at each end node to ground. The measured frequencies were then used to tune the stiffness coefficient,  $K_x$ , of the linear spring so that the model produced the measured frequencies. A value of  $2 \cdot 10^6$  lb/in resulted. The accuracy of this value was verified by static analysis of a detailed MSC.Nastran model of the fixture. The rotational stiffness at the beam root,  $K_t$ , was determined from measured cantilever beam frequencies and a MSC.Nastran model with rotational springs at the ends by the same approach used for axial stiffness. A value of 1000 in-lb/radian resulted. A value of  $3 \cdot 10^6$  lb/in was determined for the out-of-plane boundary stiffness,  $K_y$ , from static analysis of the detailed fixture model. The boundary stiffness values determined for the test fixture are listed in Figure 11 along with beam dimensions and material properties.

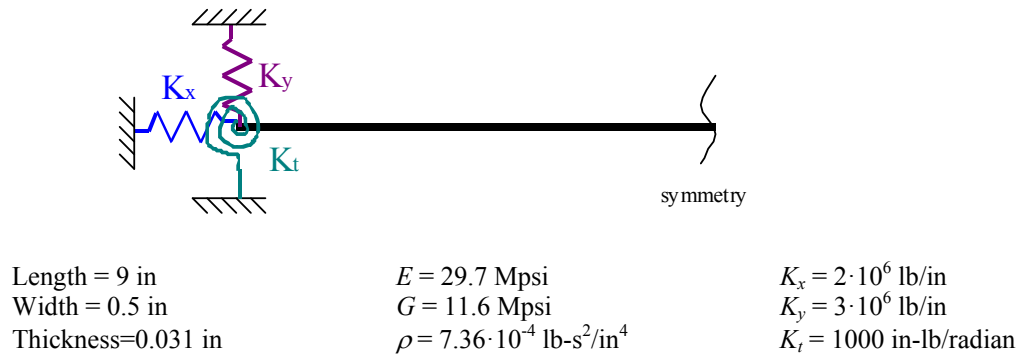


Figure 11. Idealized model of the beam with estimated boundary springs.

The linear frequency of a clamped-clamped beam will change due to thermal or mechanical preloading. Some amount of preloading is unavoidable given the fixture design. Since the preload could not be directly measured, the effects of the preload were measured as changes in the linear first mode frequency of the beam. The linear frequency can be estimated using a variation of a procedure proposed by Schudt [41]. The beam is assumed to vibrate as a single degree of freedom (SDOF) system with a cubic nonlinearity. The SDOF assumption is valid at displacement amplitudes up to the beam thickness. The equation of motion is the well known Duffing equation with a cubic hardening spring and viscous damping. An approximation to the frequency backbone curve for the Duffing equation is given in [41] as

$$\Omega^2 = \omega_0^2 + \frac{3}{4}\beta A^2 \quad (117)$$

where  $\omega_0$  is the linear natural frequency of oscillation,  $\Omega$  is the nonlinear natural frequency of oscillation,  $A$  is the displacement amplitude, and  $\beta$  is the cubic stiffness coefficient. Points on the backbone curve can be obtained experimentally as jump-down frequency and amplitude pairs obtained from sinusoidal excitation tests [41]. The backbone curve is a straight line when plotted as  $\Omega^2$  versus  $A^2$ . The linear natural frequency,  $\omega_0$ , is estimated from the y-intercept of the straight line.

The backbone curve can also be obtained from free response data [43]. A free-response test is considerably shorter in duration than harmonic tests, which minimizes the temperature variations during testing. In a typical test, the beam is initially deflected near its mid-span and allowed to vibrate, decaying freely. Temporal frequencies and amplitudes are estimated using a variant of a method proposed by Agneni and Balis Crema [44]. Here, the time record of displacement is converted to an analytic function via the Hilbert transform. Small segments of the analytic function are analyzed locally as linear oscillation. The amplitude and frequency of each small segment are estimated and plotted as a point on the backbone curve. Once the backbone curve is estimated, the procedure proposed by [41] is used to extract the linear frequency.

The primary goal of the free-response test was to estimate the linear frequency, but two other useful estimates can be extracted. An average linear viscous damping value can also be obtained from free decay via the Hilbert transform [44] and the cubic stiffness coefficient,  $\beta$ , can be extracted from the slope of the  $\Omega^2$  versus  $A^2$  plot. The estimated cubic stiffness coefficient is useful in comparisons to theoretical and analytical models.

There are many assumptions and approximations used in the linear frequency estimation procedure. The free response is assumed to be a single mode with viscous damping and only cubic displacement nonlinearity. The backbone curve relationship for the assumed Duffing equation is a small displacement approximation. The conversion of the free response signal to an analytic signal via the Hilbert transform is a numerical approximation. The segmentation analysis of the data approximates the data as linear response over a short time period. The estimation procedure was tested using simulated data with added noise and performed well, but real data may have processes and occurrences that can not be simulated or anticipated.

#### 4.1.4 Random Response Testing

Three beam configurations were tested in the study. Case A was a beam without strain gages and had no intentional axial preload. For Case B, a second beam with strain gages was tested, and again, there was no intentional preload. Case C was the same beam with strain gages used in Case B, but with a thermally induced tensile preload. The preload was applied by heating the beam with a heat gun until the temperature of the beam was approximately 10 °F higher than the temperature of the fixture. The beam was then bolted into the fixture as quickly as possible. Tensile preload developed in the beam as it cooled to an equilibrium temperature. The precise temperature difference between the beam and fixture was not measured. Beams with and



without strain gages attached were tested in order to see the effects of the gages and wiring on the dynamic response. For all configurations, the DVRT was attached to the beam mid-span in order to record the dynamic displacement.

The intent of the random vibration portion of the testing was to record random displacement for all beam configurations and to also record strain signals for Cases B and C. Five inertial load cases with nominal RMS shaker table accelerations of 0.5, 1, 2, 4, and 8 g's RMS were performed for each beam configuration. Actual RMS input levels varied slightly from the nominal values due to limitations of the shaker controller. A flat input spectrum with band limits of 20-500 Hz was utilized for Cases A and B. For Case C, the spectrum was extended to 20-800 Hz, but with the same RMS levels. The upper frequency limit for Case C was raised to 800 Hz in order to capture the increased third bending mode frequency resulting from the tensile preload.

The beams were extremely sensitive to changes in temperature relative to the fixture. Changes in relative temperature manifested themselves as changes in axial preload which directly affected linear natural frequencies. So, the previously described free-response test was accomplished before and after each random load case to measure any change in the first mode frequency and thus any change in preload. Parameters of a Duffing equation were estimated from frequency backbone curves computed from the free-response tests. The backbone curve should be a straight line when plotting the square of the nonlinear frequency versus the square of the amplitude. Figure 12 shows results for a typical free-response test. The data do indeed form a straight line.

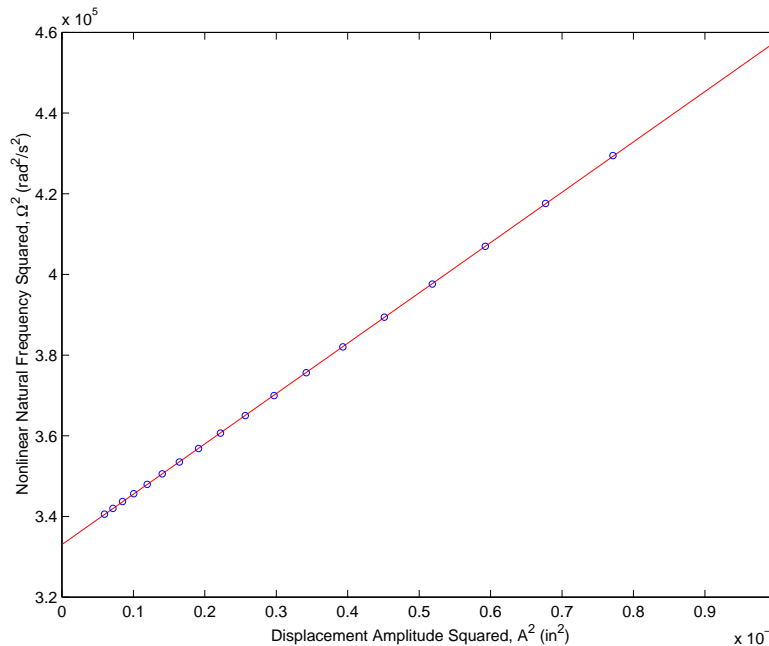


Figure 12. Frequency and amplitude estimates for a set of free response data from Case A (circles) and a linear curve fit through the estimates (solid).

Estimated parameters from the free-response tests are given in Table 5. The theoretical frequencies for an ideal clamped-clamped beam, with material properties given in Figure 11, are

79.0 and 427.2 Hz for the first and third bending modes, respectively. The analytical frequencies from a MSC.Nastran finite-element model for a beam with the boundary conditions defined in Figure 11 are 77.7 and 420.1 Hz. Therefore, results in Table 5 show that Case A is slightly pre-tensioned, Case B is nominally unloaded, and Case C is significantly pre-tensioned. There are small variations in fundamental frequencies in each case, indicating small excursions in temperature during the random tests. The added mass of strain gages and wiring on the beams in Cases B and C probably had some small effect on natural frequencies. However, the effect could not be separated from the effect of tensile preload which could not be directly measured. The frequency of the third bending mode could not be determined from the free response tests. A single frequency response function was experimentally measured for each case using a calibrated hammer test. The first and third mode frequencies and damping ratios were estimated from these tests and are listed in Table 5.

Table 5. Estimated parameters from free response and hammer tests.

	Case A	Case B	Case C
<u>Natural frequency for 1<sup>st</sup> bending mode (Hz)</u>			
lowest from free response tests	90.9	77.0	147.0
highest from free response tests	92.2	78.6	150.8
mean from free response test	91.5	77.7	149.1
estimate from hammer tests	92.1	77.7	151.2
<u>Damping ratio (<math>\zeta</math>) for 1<sup>st</sup> bending mode</u>			
lowest from free response tests	0.0011	0.0021	0.0006
highest from free response tests	0.0014	0.0025	0.0008
mean from free response test	0.0012	0.0023	0.0007
estimate from hammer tests	0.003	0.004	0.002
<u>Cubic coefficients for 1<sup>st</sup> bending mode (<math>\text{in}^{-2}\text{s}^{-2}</math>)</u>			
lowest from free response tests	$1.59 \cdot 10^8$	$1.37 \cdot 10^8$	$1.41 \cdot 10^8$
highest from free response tests	$1.65 \cdot 10^8$	$1.47 \cdot 10^8$	$1.51 \cdot 10^8$
mean from free response test	$1.62 \cdot 10^8$	$1.43 \cdot 10^8$	$1.48 \cdot 10^8$
<u>Natural frequency for 3<sup>rd</sup> bending mode (Hz)</u>			
estimate from hammer tests	440.8	414.1	561.9
<u>Damping ratio (<math>\zeta</math>) for 3<sup>rd</sup> bending mode</u>			
estimate from hammer tests	0.001	0.005	0.004

Modal damping ratio estimates from free-response and hammer tests are shown in Table 5 for the three test cases. The value estimated from the hammer test was roughly twice the mean value from the free-response tests for each case. Variations also occurred among the test cases. Case B had the highest values while Case C had the lowest. It is not clear why Case B had the highest damping ratios or why Case C had the lowest. Strain gages wires used in Cases B and C could increase modal damping compared to Case A, but Case C had lower damping values than Case

A. All the measured damping ratios are very low for typical aerospace structures subject to sonic fatigue. Therefore, variations in damping ratios on the order of those in Table 5 can have a significant effect on response predictions.

Cubic stiffness coefficients were extracted from the free-response test results and are given in Table 5. These can be compared to analytical and theoretical estimates to determine how well the experiments agree with models. The theoretical cubic stiffness coefficient for a clamped-clamped beam was determined using the theoretical first natural frequency for an unloaded beam, the nonlinear frequency ratios and amplitudes given by Singh [40], and Equation 117. The resulting value was  $1.80 \cdot 10^8 \text{ in}^{-2}\text{s}^{-2}$ . A value for the cubic coefficient of the beam model with realistic boundary conditions shown in Figure 7 was estimated using the IC method [8, 9, 24]. The estimate was  $1.67 \cdot 10^8 \text{ in}^{-2}\text{s}^{-2}$ . The cubic coefficient is not a function of preload so the values from the three test cases can be directly compared to the analytical estimate. The value for Case A, the beam without strain gages, is almost identical to the predicted value. Values for Cases B and C are slightly different from the prediction. Un-modeled mass of strain gages and lead wires may be the cause of this discrepancy.

Table 6 lists measured values of RMS displacement for all three cases and strain for Cases B and C. The results of the random tests are given in PSD form in Figures 13-18. The nominal excitation levels are labeled in the figures. Results for the nominally 8g case appear in the table but are omitted in the figures. Also note that a 140 Hz peak appears in most of the PSD figures for the 0.5g excitation level. This resonance resulted from the shaker's power amplifier. It is less noticeable at the higher excitation levels. This resonance had little effect on the RMS values and was ignored.

Table 6. RMS displacements and strains from the random tests

<b><u>CASE A (excitation bandlimits: 20 - 500 Hz)</u></b>					
Excitation (g)	0.49	0.99	1.98	3.93	7.85
Mid-span displacement (in)	0.006	0.012	0.020	0.033	0.045
<b><u>CASE B (excitation bandlimits: 20 - 500 Hz)</u></b>					
Excitation (g)	0.49	0.99	1.97	3.91	7.85
Mid-span displacement (in)	0.007	0.011	0.019	0.031	0.043
Surface strain at mid-span ( $\mu\epsilon$ )	25	40	68	109	161
<b><u>CASE C (excitation bandlimits: 20 - 800 Hz)</u></b>					
Excitation (g)	0.50	1.00	2.00	3.95	7.98
Mid-span displacement (in)	0.003	0.007	0.013	0.022	0.034
Surface strain at mid-span ( $\mu\epsilon$ )	10	22	39	69	115

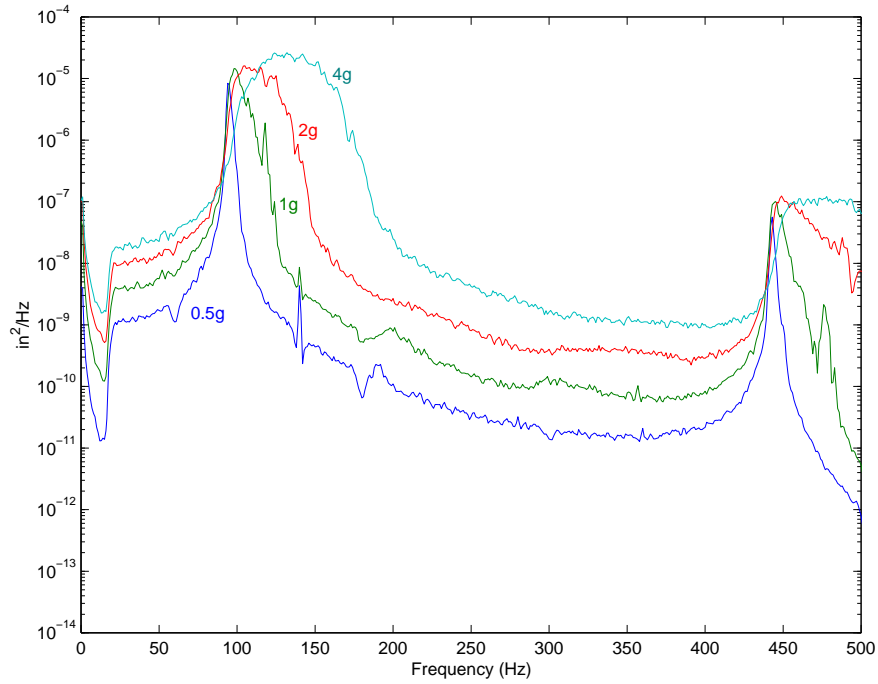


Figure 13. Displacement at the beam mid-span for Case A.

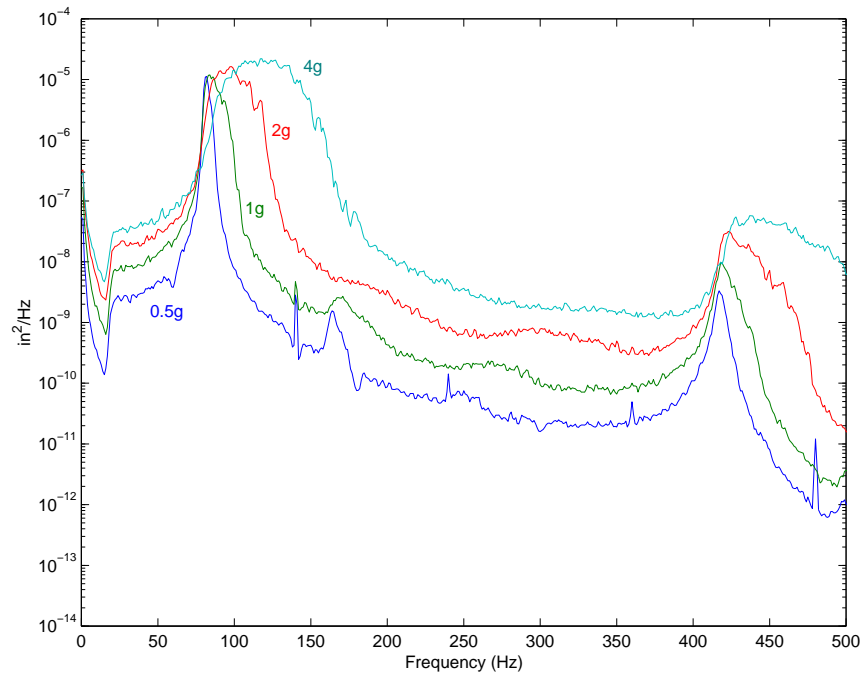


Figure 14. Displacement at the beam mid-span for Case B.

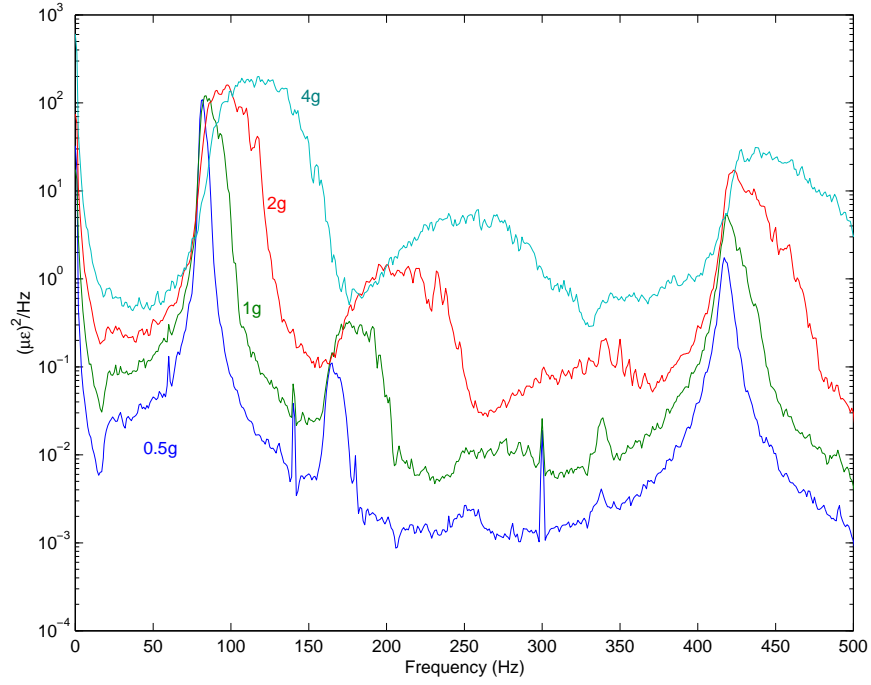


Figure 15. Surface strain at the mid-span of the beam for Case B.

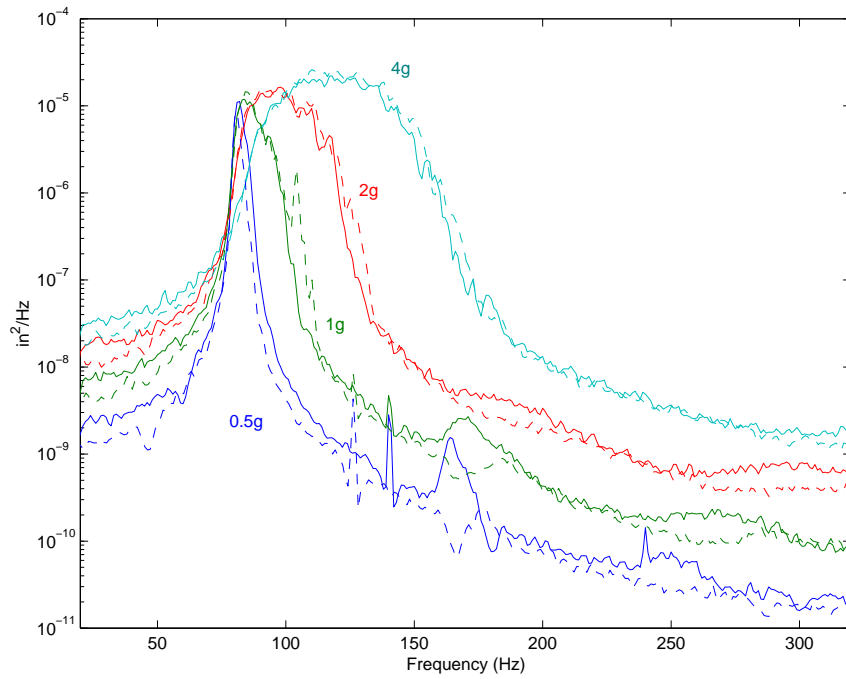


Figure 16. Displacement at the mid-span of the beam for Case B (solid) and for Case A (dashed) with a frequency shift of  $-13.8$  Hz.

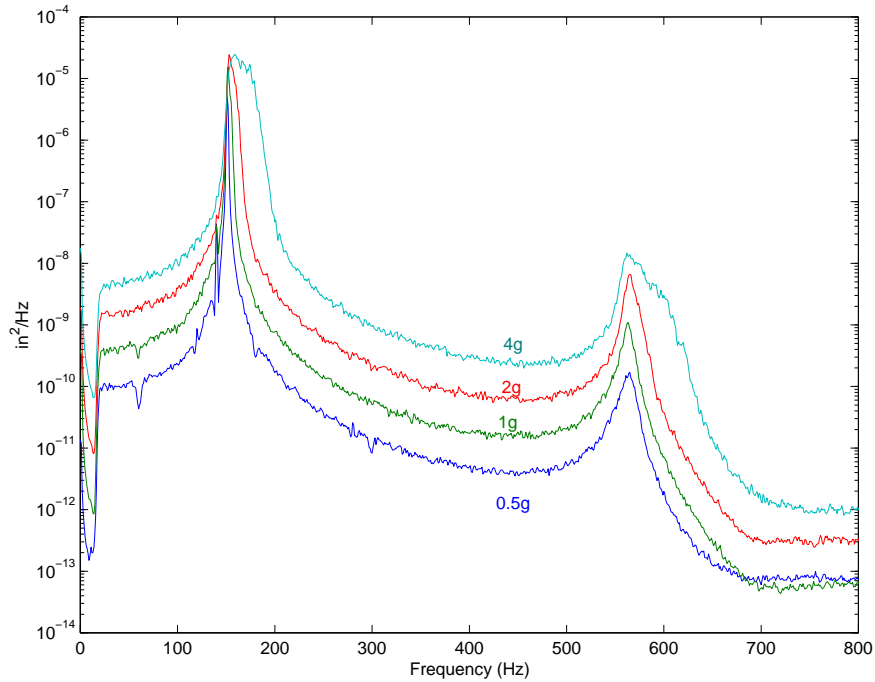


Figure 17. Displacement at the mid-span of the beam for Case C.

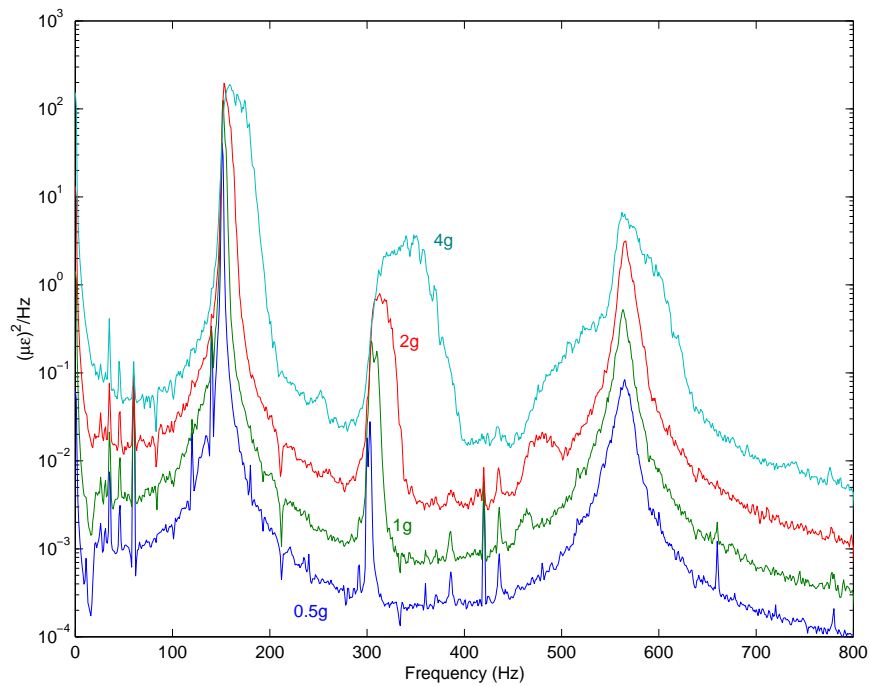


Figure 18. Surface strain at the mid-span of the beam for Case C

The displacement PSD plots show frequency shifting and peak broadening with increasing excitation levels. This is a characteristic of randomly excited systems with cubic nonlinearity. The characteristic trait is much less pronounced in the displacement PSD for Case C, Figure 17.

The beam in Case C is much stiffer due to preloading. The cubic coefficient in the Duffing equation should be the same as in the other two cases, but because of the larger linear stiffness term for Case C, the nonlinear effect in the total response is smaller. The displacement PSD plots for Cases A and B are overlaid in Figure 16 with the response for Case A frequency-shifted by the difference of linear first mode estimates. The two cases agree well, indicating that the primary difference between the two cases is the linear frequency shift due to preloading. The effects of the nonlinearity are very similar in these two cases. Even if the nonlinear terms for the two cases are the same, which they should be except for mass of instrumentation, the expression of the nonlinear terms will vary slightly because of the difference in the linear stiffness terms. The strain PSD's shown in Figures 15-18 are from one gage. The PSD's from the other gage are very similar and are omitted from the figures. The RMS values of strain shown in Table 6 are averages of the values from the two gages. The strain PSD plots show a broad peak between the peaks for the first and third bending modes. This peak is approximately twice the frequency of the first peak, indicating a quadratic nonlinearity. The quadratic nonlinearity is present in the strain-displacement relationship and is due to membrane stretching. Also note that the strain PSD's show significant static values. This is the static component of the membrane strain resulting from nonlinear membrane displacement.

#### 4.1.5 Comparison of ROM and Experimental Results

The experimental results are compared to predictions from ROM's of the beam with realistic boundary conditions built using the IC method, the physical condensation method and the companion modes method. All ROM's were computed using a 2-D FEM with 20, two-node beam elements. Only half of the beam was modeled since the inertial loading could only excite symmetric bending modes. A MSC.Nastran model was used to compute normal modes and the nonlinear static solutions for the IC method. An in-house code implemented in MATLAB was used to compute the results for the physical condensation and companion modes methods.

There is no ambiguity in determining the nonlinear coefficients using the BM and physical condensation methods. However, the nonlinear coefficients for the IC method vary somewhat depending on the static solution set used. Before proceeding with the comparison, we must first discuss how the model for the IC method was estimated.

The nonlinear function for the IC method has four nonlinear terms in each mode

$$\theta_1 = A_1(1,1,1) p_1^3 + A_1(1,1,2) p_1^2 p_2 + A_1(1,2,2) p_1 p_2^2 + A_1(2,2,2) p_2^3 \quad (118)$$

$$\theta_2 = A_2(1,1,1) p_1^3 + A_2(1,1,2) p_1^2 p_2 + A_2(1,2,2) p_1 p_2^2 + A_2(2,2,2) p_2^3 \quad (119)$$

for the two-mode system. The load cases in the static solution set are permutations of the two mode shapes. The scaling of the loads has to be chosen. Typically, nonlinear effects become significant when deflections approach the thickness of the beam. It was decided to scale the static load for the first mode so that it would produce a linear deflection of 0.06 in (about twice the beam thickness) to ensure the nonlinear effects are produced. The loading for the third bending mode was based on a preliminary dynamic analysis of the beam. The maximum dynamic load was a 10 g, 20-500 Hz, random excitation and the damping of the third mode was

anticipated to be approximately 0.1% of critical. The predicted linear response for the third bending mode for this loading and damping was 0.007 in RMS at the beam mid-span. This estimate was rounded to 0.01 in. Thus, the loading for the third bending mode was picked to produce a static linear deflection of 0.01 in.

The two basic load cases can be combined in various proportions to produce any number of load cases in the load set. The load set with the minimum number of permutations has eight static load cases. The load set for this case is

$$P = [a_1 \phi_1 \ a_2 \phi_2] \begin{bmatrix} 1 & 0 & 1 & 1 & -1 & 0 & -1 & -1 \\ 0 & 1 & 1 & -1 & 0 & -1 & -1 & 1 \end{bmatrix} \quad (120)$$

where  $a_1$  and  $a_2$  are the scaling factors for the two basic load cases. These scaling factors were determined based upon the desired static linear deflections. Nonlinear static deflections were then calculated for this load set using MSC.Nastran. The nonlinear deflections at the beam mid-span for the two basic loads were 0.034 in and 0.009 in, respectively for the two modes. Comparison of the nonlinear and linear static deflections confirms that the nonlinear effects of both modes are exercised. The static solution set was then used in the estimation of the modal model for the IC method.

Once the modal models were evaluated for the IC, BM and physical condensation methods, the equations were integrated for the five input levels. The integration used a Newmark beta scheme. The sample rate was chosen to be 10 KHz, which produced adequate convergence of the time responses. The integrations were run to produce 100-second time records of modal response. A different realization of a 1-g input force time history was used for each of the three modal models. The 1-g force time history was then scaled to produce the five input levels for each method. Time records for the nodal displacement and strain were then calculated from the modal records. RMS values and PSD's of displacement and strain were computed from the time records using typical data processing techniques.

The RMS displacement values for five excitation cases are presented in Table 7 in comparison to the experimental results. The RMS values compare extremely well with the experimental values for excitation levels up to 4 g's. For the 8-g case, the only significant discrepancy occurs for the BM method. This discrepancy is not major. The 8-g case is very nonlinear and is the most difficult case to predict.

Table 7. Comparison of RMS values of the displacement at the mid-span of the beam

Excitation Level (g)	Exp. Results (in)	IC Method (in)	Physical Condensation (in)	BM Method (in)
0.49	0.007	0.006	0.006	0.006
0.98	0.011	0.012	0.012	0.012
1.97	0.019	0.020	0.021	0.021
3.91	0.031	0.031	0.031	0.032
7.85	0.043	0.044	0.044	0.049



The RMS values of surface strain at the beam mid-span are compared to experimental values in Table 8. Again, the agreement is very good. All the methods slightly under-predict the strain for all the input cases except the 8-g case. At 8 g's, the BM method over-predicts the strain, but the difference is less than 10%.

Table 8. Comparison of RMS values of the surface strain at the mid-span of the beam

Excitation Level (g)	Exp. Results ( $\mu\epsilon$ )	IC Method ( $\mu\epsilon$ )	Physical Condensation ( $\mu\epsilon$ )	BM Method ( $\mu\epsilon$ )
0.49	25	20	20	21
0.98	40	37	37	38
1.97	68	63	65	56
3.91	109	98	99	103
7.85	161	158	156	171

The predicted PSD's of mid-span displacement for the 1-g and 4-g cases are shown in Figures 19-20, respectively. The experimental results are also shown in the figures for comparison. The displacement spectra for each of the predictions match the experimental 1-g case almost exactly for the first mode. There are some differences for the third bending mode (the second mode in the models), but the response of this mode is not significant in the overall response.

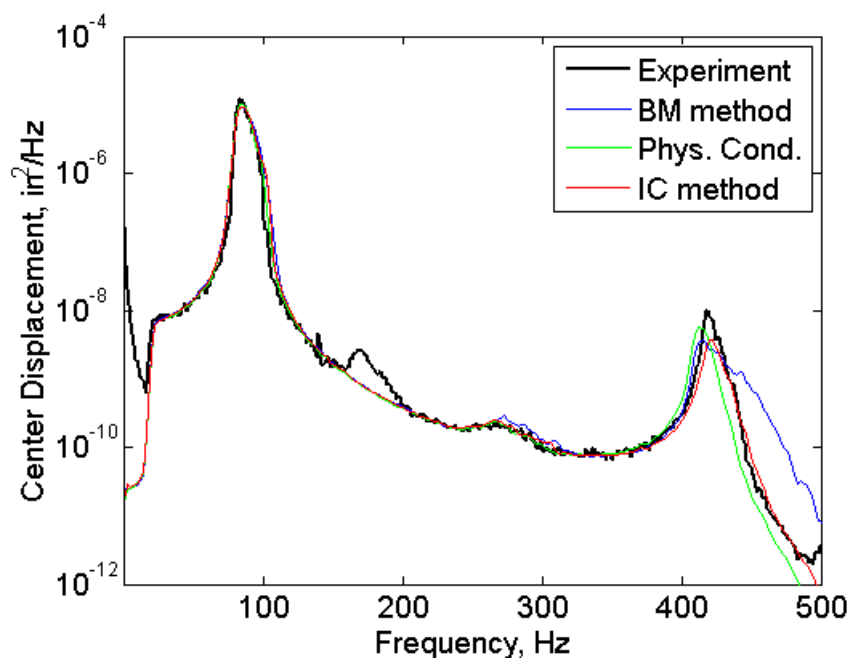


Figure 19. Experimental displacement data and predictions for the 1-g excitation case.

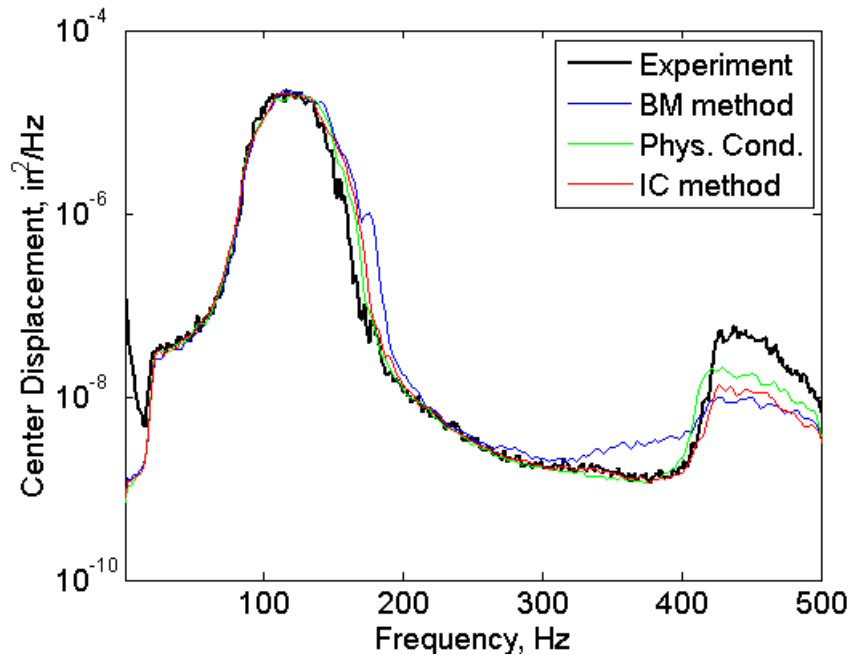


Figure 20. Experimental displacement data and predictions for the 4-g excitation case.

The predicted displacement spectra for the 4-g case also match the experiment well. The first-mode peak for the BM method is slightly broader than predicted by the other two methods. The difference is minor and results in only a 0.001" variation in the RMS value. Small differences like this can arise from stochastic variations in realizations of the input time history and are acceptable in an engineering analysis.

Predicted mid-span surface strain PSD's are plotted in Figures 21 and 22 for the 1-g and 4-g cases along with experimental results. The strain predictions are also very good for the 1-g case. The quadratic strain component, the broad peak around 175 Hz due to nonlinear mid-plane stretching, is predicted very well. The predicted strain spectra for the 4-g case are generally good, with small differences between the predictions.

The estimated modal model from the IC method is sensitive to the static solution set. Difficulty occurs when a regression scheme is used with a poorly scaled static solution set. An example is presented here to emphasize the difficulties that may arise. The loading for the first mode is kept the same as in the previous example and the loading for second mode is increased to produce a linear deflection of about 0.1". The resulting nonlinear deflections are about one beam thickness for both modes. The static solution is then used with a regression scheme to estimate the modal model. The backward regression procedure [9] eliminates important terms in the nonlinear model, specifically the  $A_1(1,1,1)$  term. This is the primary nonlinear term that regulates the response in the first mode. Figure 23 shows the predicted mid-span displacement for the regression model in comparison to the experimental response for the 4-g input case. The nonlinear effects are not adequately represented and the prediction is terrible. Also shown in the figure, is the prediction when the regression scheme is not used and all the terms are retained in the estimated model. The nonlinear effects are correctly estimated and the prediction is good.

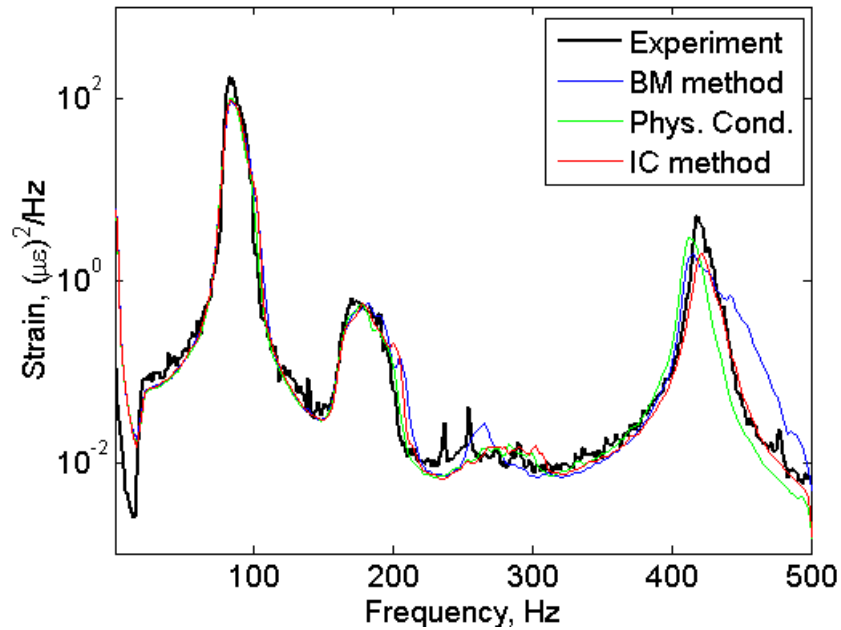


Figure 21. Experimental surface strain and predictions for the 1-g excitation case.

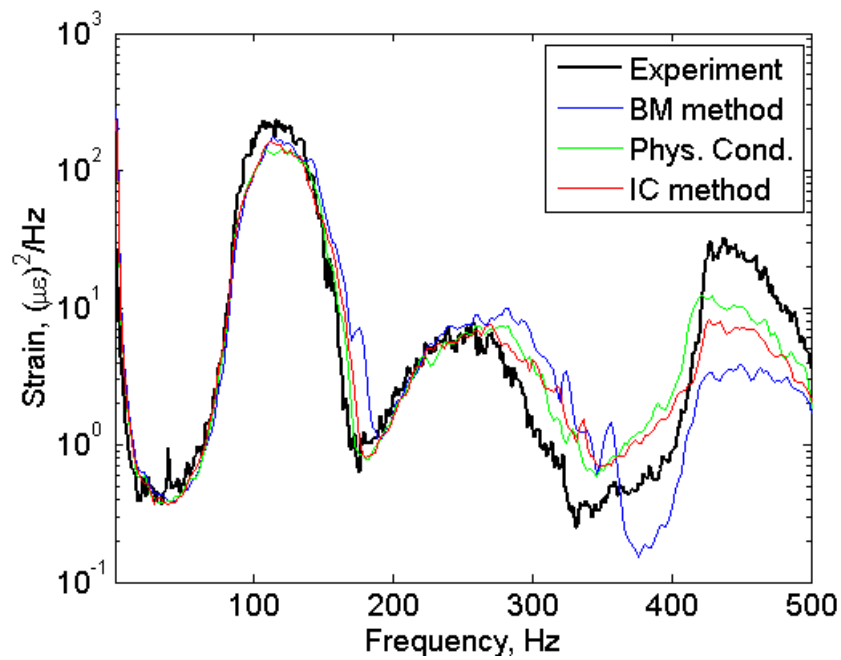


Figure 22. Experimental surface strain and predictions for the 4-g excitation case.

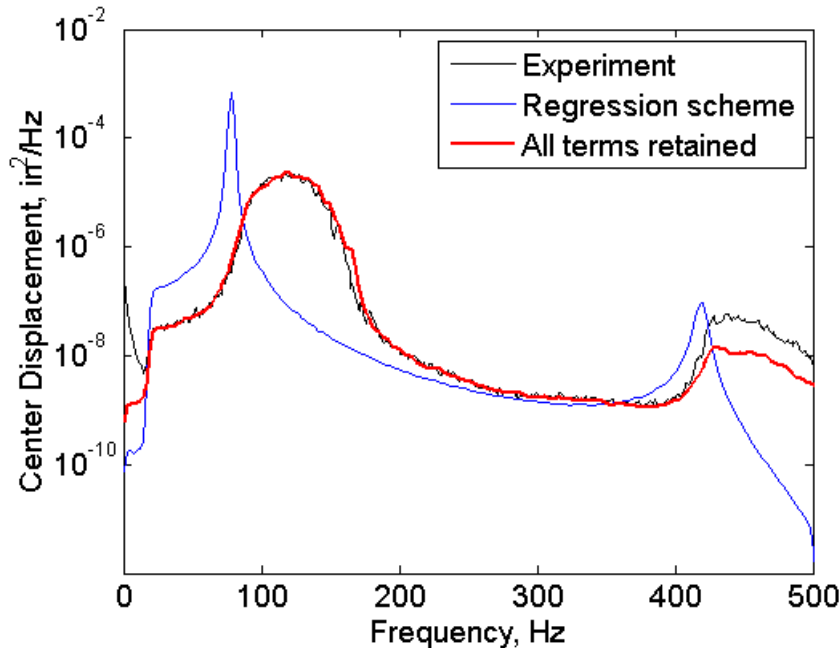


Figure 23. Displacement spectra for 4-g excitation case using variations of the IC method.

The effects of damping on the response of the nonlinear system can be counterintuitive. In both a linear and nonlinear system, increased damping decreases the RMS response. In a linear system, increased damping results in a broader spectrum peak and a reduced peak response. In a system with cubic nonlinear stiffness, increased damping results in a narrower spectrum peak with reduced peak response. This effect of damping on the response of the clamped-clamped beam is shown in Figure 24. The figure was generated using the modal model built with the IC method. In contrast, an increase in the cubic nonlinear stiffness coefficient will broaden the spectrum and reduce the peak amplitude. Thus, the effects of damping can be easily confused with the effects of the nonlinear stiffness.

Loading due to thermal expansion can drastically alter the natural frequencies and the resulting response of the structure. Small temperature excursions can be incorporated into the modal models through modification of the linear stiffness terms. One case in the experimental study had a thermal preload [39]. To model the change in the beam, the modal model from the IC method was modified. The linear stiffness terms were changed to correspond to the preloaded natural frequencies. The other portions of the model were not changed. Figures 25-26 show the predicted displacement and strain in comparison to the experimental results. Note that the bandwidth of the excitation for this case was 20-800 Hz.

Although, the predictions from the two general methods were similar, there are important differences in the implementation of the methods. Direct evaluation of the nonlinear stiffness requires access to internal coding of the finite element method. Physical condensation involves direct manipulation of the finite element nonlinear stiffness matrix. The IC method evaluates the nonlinear stiffness function by curve fitting finite element solution results. Direct access to the internal workings of the finite element code is not required. Any adequate commercial finite

element code can be used to generate nonlinear static solutions. The estimation of the nonlinear stiffness terms is implemented in external code.

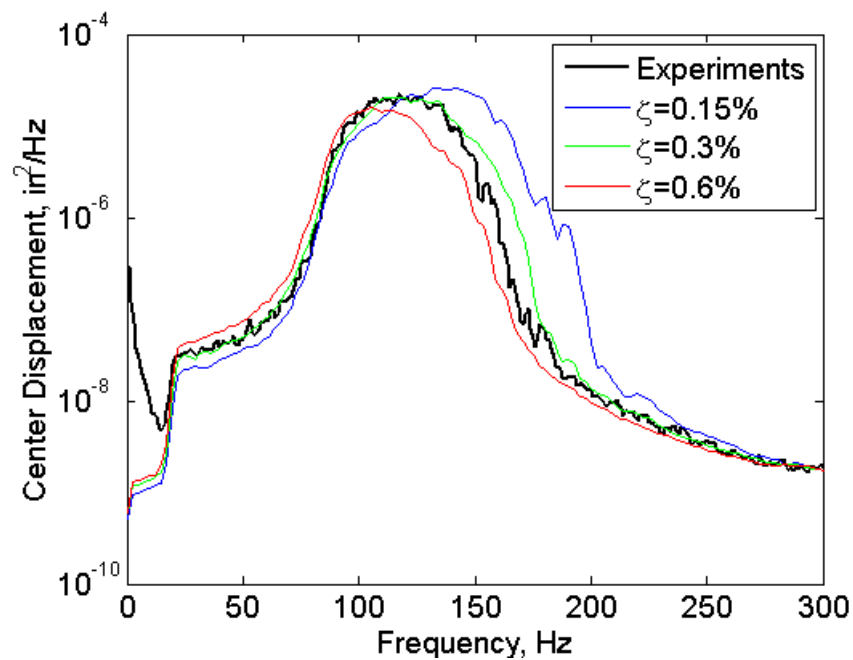


Figure 24. Displacement spectra for the 4-g excitation case showing the effects of damping upon predictions.

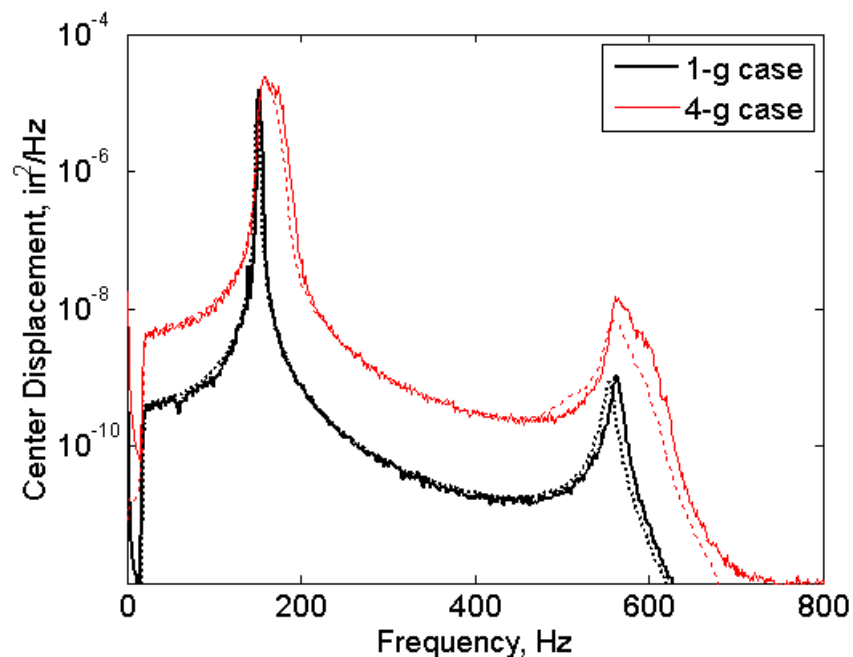


Figure 25. Experimental displacement data (solid) and predictions (dotted) for a thermally preloaded beam.

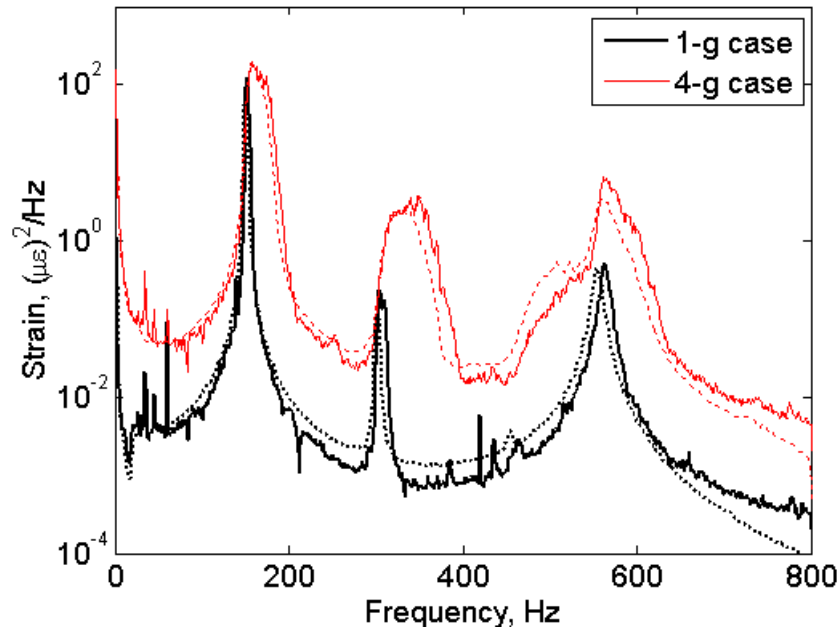


Figure 26. Experimental surface strain (solid) and predictions (dotted) for a thermally preloaded beam.

Another difference between the methods is the procedure for including the effects of membrane softening. Typically, only bending modes are retained in the modal basis set. However, normal bending modes don't contain the membrane displacements necessary to model structures with large displacement nonlinearity. So, either membrane modes must be included in the model or their effects must be condensed into the nonlinear stiffness coefficients for the bending modes. In the IC method, the effects of the membrane modes are implicitly condensed into the bending modes during the process of estimating the nonlinear coefficients. But in the BM method, the membrane modes must either be explicitly included in the solution, or explicitly condensed into the bending modes. Physical condensation can be implemented if the membrane degrees of freedom can be separated from the bending degrees of freedom. However for a general structure, physical condensation may not be feasible. A general method for condensation in the modal domain is shown to be as effective as physical condensation.

The methods presented here compute stresses and strains differently as well. In both the BM and physical condensations methods, stress and strain are computed on the element level by the finite element code in a post-processing scheme. For a condensed modal model, the membrane displacements have to be recovered through an expansion process. In the IC method, the condensation is implicit and there is no explicit means of determining membrane displacements without ICE. Thus the typical post-processing of strain cannot be accomplished. Instead, the IC method estimates a mapping between stress or strain and modal displacements. Computation of a stress/strain time record is much quicker than the general post-processing methods. However, the mapping approach can be sensitive to the static load cases used to compute nonlinear stiffness coefficients.

The major drawback of the IC method is that it requires more user intuition to build a successful model. A static force set must be constructed which reasonably exercises the nonlinear effects

without overemphasizing any mode. Regression schemes can eliminate important terms for some poorly scaled static solution sets. These difficulties can be overcome using proper user judgment. It is suggested that all terms be retained in the nonlinear model to insure that all dynamic effects are included.

The comparison presented here was conducted on a beam with widely separated bending modes. Although there was some nonlinear coupling between the two modes in the models, the first bending mode dominated the responses. This example may not fully test whether the methods are able to capture the effects of closely spaced modes and coupling. Comparisons with experimental data from plates and built-up structures are necessary to fully test the methods.

## **4.2 The 18-Inch Clamped-Clamped Beam**

The second application studied in this effort was another straight beam with clamped ends. The purpose of this application was to evaluate the ICE method on a simple example problem. The ICE method adds a novel process to the IC method which synthesizes membrane modal displacements from computed bending modal displacements. The modal basis for implicit condensation uses only bending modes, so membrane modal displacements are not computed directly. This example problem was chosen from Reference [45] so that ICE results could be compared directly to results from the BM method. This work was originally documented in Reference [14].

### **4.2.1 The Example Problem**

The beam was 18 inches x 1 inch x 0.09 inches and was made of aluminum alloy with both ends clamped. The material properties for the beam were:  $E = 10.6 \times 10^6$  psi,  $G = 4.0 \times 10^6$  psi, and  $\rho = 2.588 \times 10^{-4}$  lb<sub>f</sub>-s<sup>2</sup>/in<sup>4</sup> where  $E$  is the modulus of elasticity,  $G$  is the shear modulus, and  $\rho$  is the material density. The forcing function was a spatially uniform load whose magnitude was random. The force magnitude was a band-limited (0-1500 Hz), Gaussian random variable. Two loading cases were considered; the first was a low level, nominally linear case (0.0072 lb/in RMS), and the second was a high level case (0.9216 lb/in RMS) which resulted in significant nonlinear behavior.

### **4.2.2 The Reduced-Order Models**

A symmetric half-model of the beam was constructed using 36 beam elements of equal length. Two methods were used to obtain reduced-order models—BM and ICE. Predictions from these methods are compared to direct integration results from a full-order FEM. Results were computed for two reference locations. Displacements were computed for a point four inches from the clamped end of the beam and element stresses were computed at the center of an element 3.625" from the clamped end. These two locations were chosen since they are close to those reported by Reference [45]. The membrane stress, which is constant throughout the beam cross-section, was computed along with the total stress, i.e., the sum of the membrane and bending stresses, at the top surface of the beam.

The static nonlinear solutions and normal modal analyses required to construct the ROM's were performed in MSC.Nastran. A full-order FEM was integrated using an internal code written in MATLAB to generate displacement and stress results to compare with the ROM results. The basis sets for all the reduced-order methods include the mode shapes for the first four symmetric bending modes. These modes have linear natural frequencies at 57.8, 312, 770, and 1430 Hz, respectively. Mass proportional damping was used in all the simulations. The damping level was chosen so that damping for the first bending mode corresponded to 2.0% of critical.

Long time records are necessary to properly average the predicted response. The two reduced order predictions were obtained using a Newmark-Beta integration scheme, sampled at 80 kHz. Time records of 100 seconds were obtained. A Newmark-Beta approach was also used to integrate the FEM. The sample rate was 100 kHz for the FEM and 60 seconds of data were obtained. All the time records were processed to obtain the PSD of the displacement or stress at the physical locations of interest.

The BM method for this problem used four bending modes and a set of normal membrane modes. It can be difficult to determine how many membrane modes are necessary for convergence for a particular problem. In Reference [45], a ROM with the first four anti-symmetric normal membrane modes was shown to adequately predict the response at a location along the beam. However, the first ten anti-symmetric membrane modes were used in the BM method described here to ensure an adequate membrane basis. Those modes had linear natural frequencies of 11.2, 22.5, 33.8, 45.2, 56.6, 68.2, 79.9, 91.7, 104, and 116 kHz, respectively.

The nonlinear stiffness coefficients were obtained using a series of enforced displacement solutions. In total, 665 linear and 665 nonlinear static solutions were required. The reduced model has 14 equations (4 bending mode equations and 10 membrane mode equations) with 665 nonlinear coefficients in each equation. The ten membrane equations were condensed into the bending equations using general condensation (see Section 3 for more detail) resulting in a model with four equations with 20 cubic coefficients in each equation. Integration of this model produced modal bending amplitudes. These amplitudes were expanded to obtain the membrane amplitudes and the full physical displacement time record.

The IC method was used to determine a condensed ROM using only bending modes. The nonlinear stiffness coefficients were estimated for this model from a set of 32 nonlinear, static, applied-force solutions. The reduced model had four equations with 16 cubic coefficients in each equation. Integration of this model produced modal bending amplitudes. There are ten quadratic combinations of the four modal bending amplitudes. Therefore, there were ten generalized membrane amplitudes and ten membrane basis vectors estimated for the ICE method. The applied-force solutions were used to estimate the ten membrane basis vectors using Equations 54-55. The modal bending amplitudes are expanded to obtain the membrane amplitudes and the full physical displacement time record.

An additional method, the BEM method, was also used for this problem. The BEM method is similar to the BM method except estimated membrane modes from the ICE procedure are used instead of the normal membrane modes. Unlike the BM model, the linear stiffness matrix in the BEM model is not diagonal since the membrane basis vectors are not normal modes. For this



problem, four bending modes and ten estimated membrane modes were used. The ten membrane equations were condensed into the four bending modes. Integration of the condensed model produced modal bending amplitudes. These amplitudes were expanded, using Equation 55, to obtain the membrane amplitudes and the full physical displacement time record.

### 4.2.3 Discussion of Results

Predictions from the full-order FEM are shown in comparison to the two ROM predictions in Figures 27-30. Predictions for both excitations levels are shown in each figure. Membrane (in-plane) displacement at a point 4" from the clamped end is shown in Figure 27. Transverse displacement at the same location is shown in Figure 28. Membrane stress at the center of an element 3.625" from the clamped end is shown in Figure 29. Total stress at the same location is shown in Figure 30. The membrane and transverse displacement predictions for the low level excitation shown in Figures 27-28 agree very well, virtually lying on top of one another. The stress and displacement predictions for the high level excitation shown in Figures 27-30 also agree very well with only slight variations due to the random nature of the response.

A small discrepancy can be found in the membrane stress predictions at the low excitation level. These predictions are plotted in Figure 29. The two highest frequency peaks of the ICE stress prediction are somewhat lower in amplitude than those from the other predictions. The resulting RMS membrane stress prediction from the ICE method differs by only 3% from the other predictions. The reason for this minor difference is not known. At this low excitation level, the bending stress dominates the total stress prediction. At the high excitation levels, the membrane stress predictions are all similar.

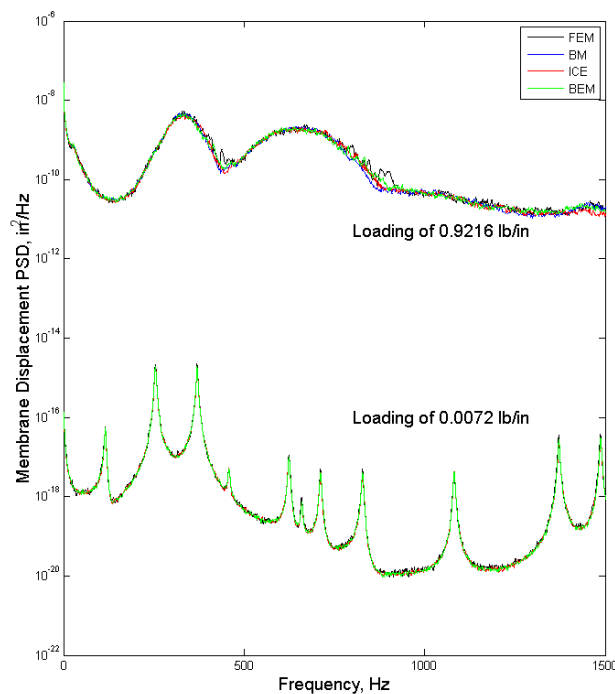


Figure 27. Membrane displacement 4" from the clamped end for a FEM and the ROM's.

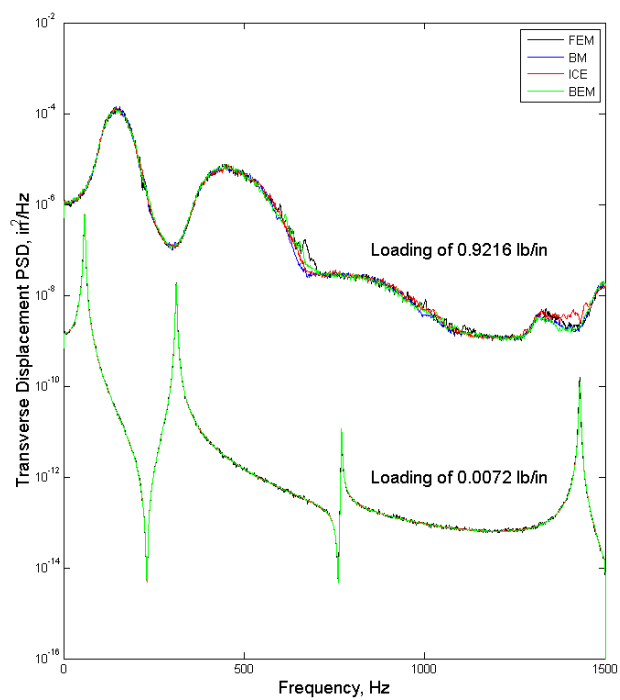


Figure 28. Transverse displacement 4'' from the clamped end for a FEM and the ROM's.

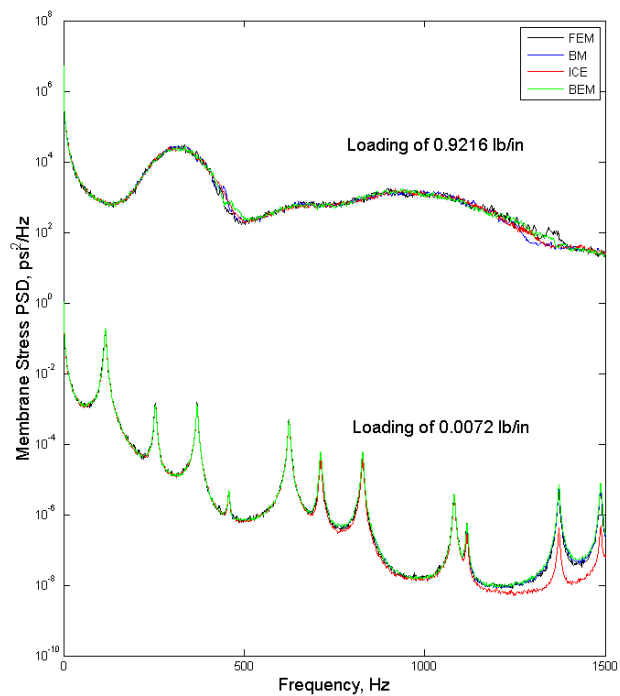


Figure 29. Membrane stress 3.625'' from the clamped end of the beam.

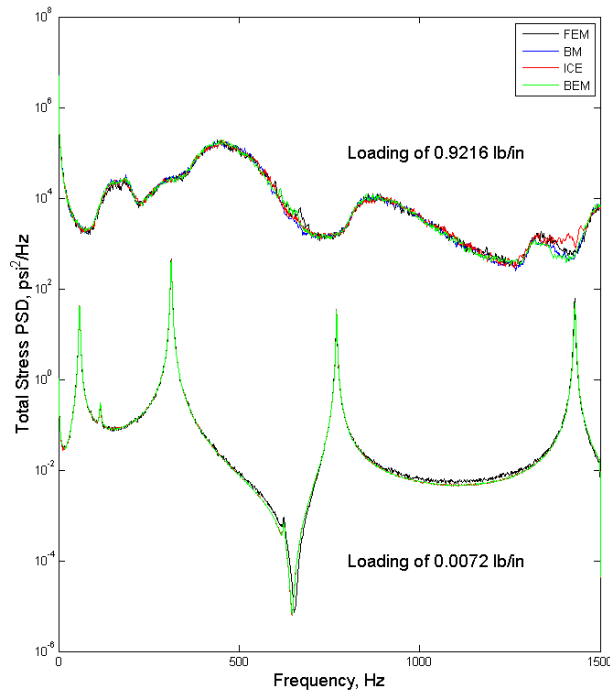


Figure 30. Total stress at the top of the beam, 3.625" from the clamped end.

The ICE method is an extension of the IC method which allows stress recovery using standard finite element procedures. Stress predictions from the ICE method and the IC method are compared in Figures 31-32. Two versions of the IC method were considered. The first version used a nonlinear stress function that was estimated from the static applied-force solutions [9]. The estimated function is a quadratic nonlinear function that maps modal bending amplitudes to stress. Two stress functions were estimated, one for the top surface of the beam and another for the middle surface of the beam. Both locations are 3.625" from the clamped end. The second version used physical transverse displacements predicted from the bending-modes-only IC model. No membrane expansion was performed, thus all physical membrane displacements were assumed to be zero. The transverse displacement predictions for the ICE method and the two versions of the IC method are, by definition, identical. Note that the ICE traces in some cases cannot be seen since the prediction from the IC method with nonlinear stress functions is virtually identical.

Even though the IC method does not compute membrane displacements, there is a membrane stress due to the nonlinear terms in the strain-displacement relationship. The lack of the membrane displacement results in membrane stress predictions that are completely different than the other two predictions. The bending stress is identical among the three predictions. The difference in the total stress, Figure 32, is due solely to the membrane stress differences. For the high excitation level, the IC method without membrane displacements produces a RMS value that is 22% greater than that of the ICE method.

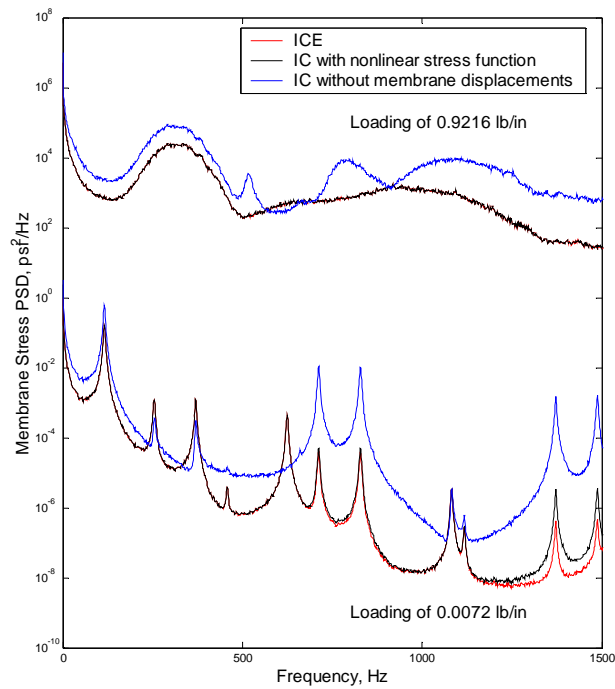


Figure 31. Membrane stress from various implementations of the IC method.

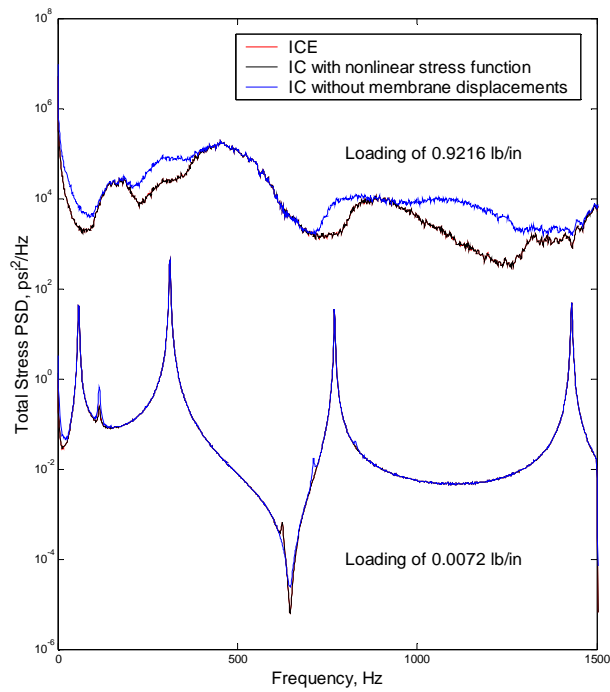


Figure 32. Total stress from various implementations of the IC method.

### 4.3 The Curved Beam

The third application of the nonlinear ROM's was to a curved beam. This example was chosen from Reference [46] to evaluate the ICE method when applied to a structure with shallow curvature. The work reported here was originally published as Reference [47].

#### 4.3.1 The Example Problem

The curved beam configuration investigated in this study is shown in Figure 33. The aluminum alloy beam had dimensions of 18.0 inches long (projected length) x 1.0 inch x 0.09 inches thick with an 81.25-inch radius of curvature. Both ends of the beam were clamped. The beam material elastic modulus was  $10.6 \times 10^6$  psi, the shear modulus was  $4.0 \times 10^6$  psi and the density was  $2.588 \times 10^{-4}$  lbf-sec<sup>2</sup>/in<sup>4</sup>.

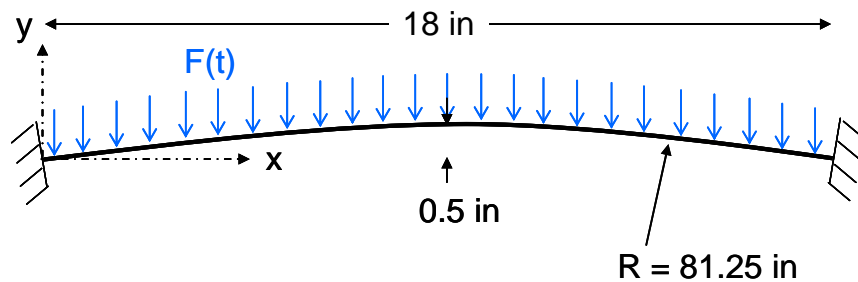


Figure 33. Geometry of the curved beam.

#### 4.3.2 Reduced-Order Models

A FEM of the beam was constructed in Abaqus [35] using 80 B31 beam elements. This model was used to compute mode shapes and frequencies and perform the nonlinear applied loads solutions. Mode shapes and frequencies for the first eight modes of the beam are shown in Figure 34.

Direct time integration of a second FEM was performed using an in-house code written in MATLAB. This model also used 80 two-node beam elements and had 237 DOF. A mass-proportional damping matrix was used to provide 2.0% critical damping at 258 Hz—the frequency of the first symmetric mode of the beam. A band-limited random excitation was applied as a uniform load on the model with a 0-1500 Hz frequency range. Two load levels were applied—0.2304 lb/in and 0.6517 lb/in—giving minimal and significant nonlinear response, respectively. These were the same load levels used in [46]. Simulations were performed for 50 seconds at each load level with a time step of  $1 \times 10^{-5}$  second. It was important to generate relatively long time records so that statistical averaging of PSD's was adequate.

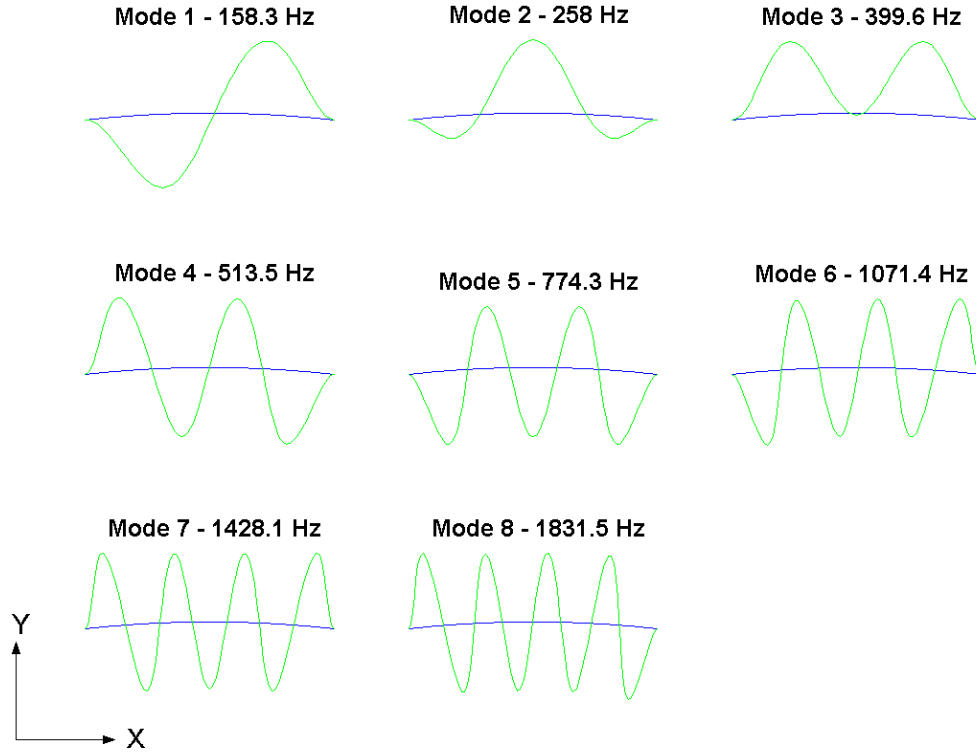


Figure 34. Mode shapes of the curved beam from the FEM.

A nonlinear ROM of the beam was computed using the IC method from a set of nonlinear static solutions. The lowest 8 normal modes of the beam were retained in the model. All of these modes had predominantly transverse displacements. The first seven of these were within the excitation bandwidth. Although the eighth mode was above the excitation bandwidth, it was included to be consistent with [46]. No membrane-dominated modes were retained in the model since the IC approach does not require an explicit membrane basis. The ROM was subjected to the distributed random loading used with the full model simulation. Fifty-second time records were computed using Newmark time integration with a time step of  $2 \times 10^{-5}$  second. The resulting modal displacements were then transformed to physical coordinates using the modal vectors. These physical displacements are the IC model results.

The integration results from the IC method were also used to obtain the ICE results. A set of 36 estimated membrane basis vectors was computed from the static nonlinear solutions using Equations 54-55. The bending modal displacements obtained by the IC method were then expanded to produce the generalized membrane displacements using Equation 55. The bending modal displacements and the generalized membrane displacements were transformed to physical coordinates using the augmented modal basis.

#### 4.3.3 Discussion of Results

PSD's of displacement from the IC and ICE methods are compared to full-order FEM simulation results in this section. Results are presented for four beam DOF: x- and y-direction

displacements at the quarter point and x- and y-direction displacements at the center of the beam. Note that at the quarter point these displacements are approximate, but not identical, to the in-plane and transverse components, respectively.

Displacement PSD's for the 0.2304 lb/in input level are shown in Figures 35-38. The y-direction PSD's are virtually identical to the full model simulation at the center and quarter point for IC and ICE models, as shown in Figures 35-36. The x-direction PSD's, which are dominated by in-plane displacements, are shown in Figures 37-38. The ICE model again shows nearly identical agreement with the FEM. The IC model also shows very good agreement near the dominant peaks, but shows some small error near 150, 600, and 1100 Hz. This is probably due to the lack of membrane-dominated modes in the model basis. The bending-dominated modes in the model were an adequate basis for reproducing the major response peaks of the beam.

The predicted PSD's of the models at 0.6517 lb/in are compared in Figures 39-42. Significantly nonlinear response occurred at this level. Again, the IC and ICE models show excellent agreement with the full model for the y-direction results at the center and quarter point of the beam (see Figures 39-40). The ICE results also display excellent agreement with the full model simulation at both x-direction DOF as shown in Figures 41-42. However, the IC model results show some error. The predicted x-displacement at the beam center, shown in Figure 41, agrees very well at frequencies up to the dominant response peak at 250 Hz but begins to show significant deviation above this frequency. The lack of membrane-dominated vectors in the model basis is likely responsible. The predicted x-direction displacement at the beam quarter point, shown in Figure 42, also shows error above 400 Hz, but the error is much less than it was at the beam center.

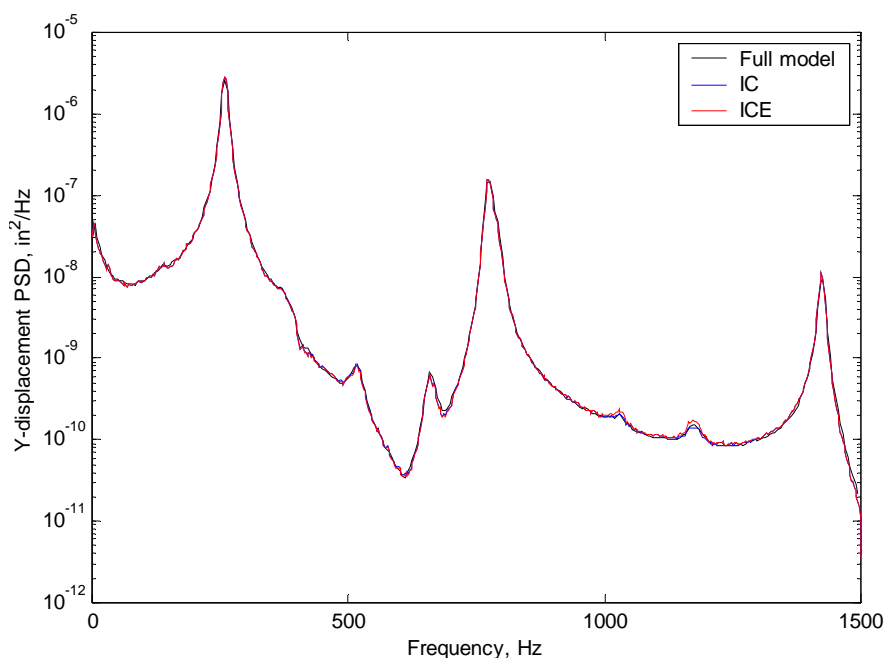


Figure 35. Y-displacement PSD at the beam center, 0.2304 lb/in.

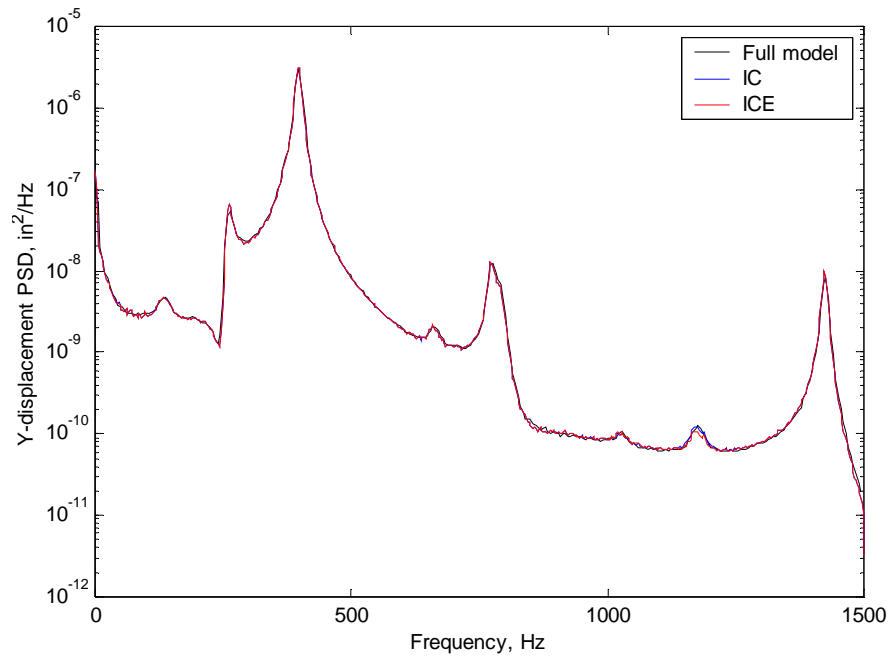


Figure 36. Y-displacement PSD at the beam quarter point, 0.2304 lb/in.

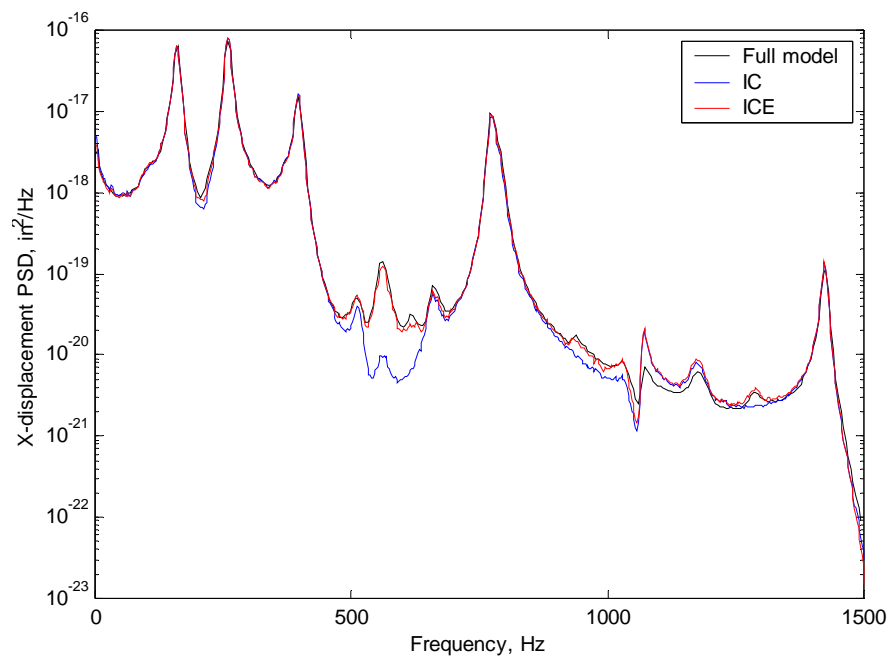


Figure 37. X-displacement PSD at the beam center, 0.2304 lb/in.



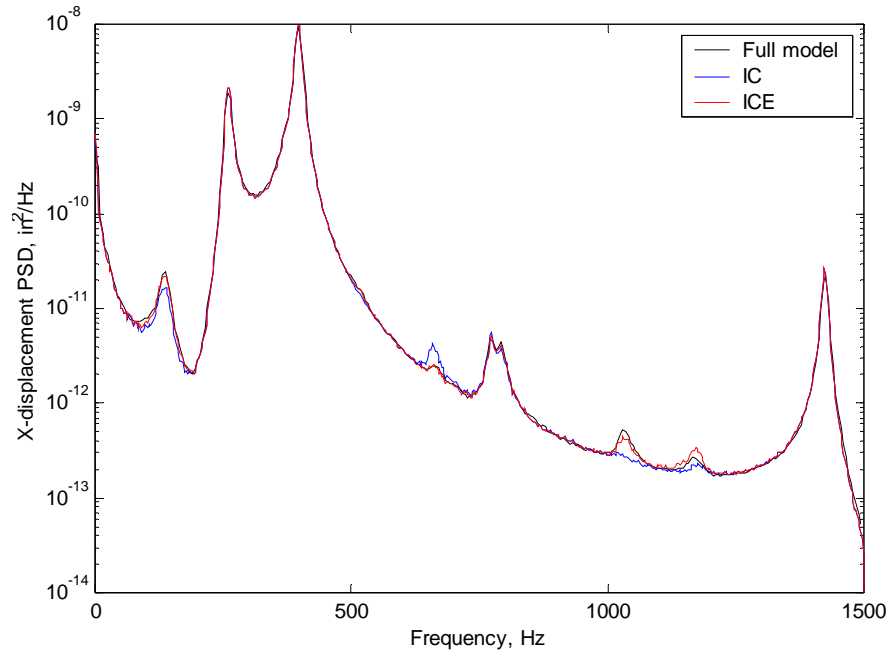


Figure 38. X-displacement PSD at the beam quarter point, 0.2304 lb/in.

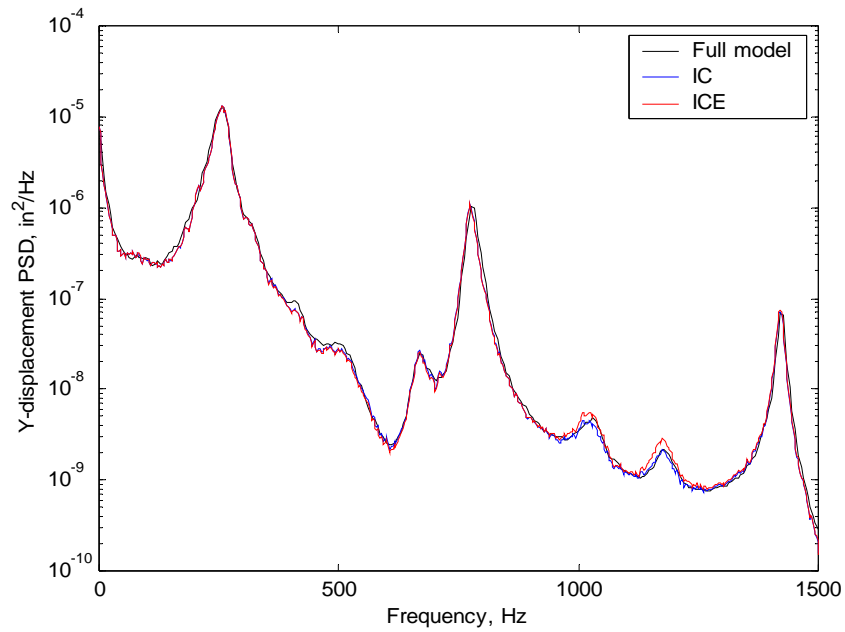


Figure 39. Y-displacement PSD at the beam center, 0.6517 lb/in

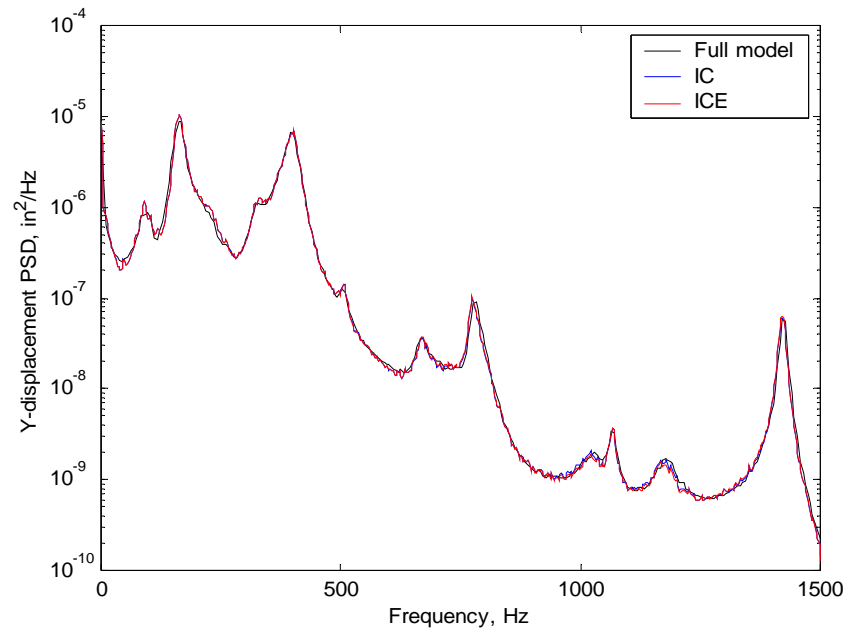


Figure 40. Y-displacement PSD at the beam quarter point, 0.6517 lb/in

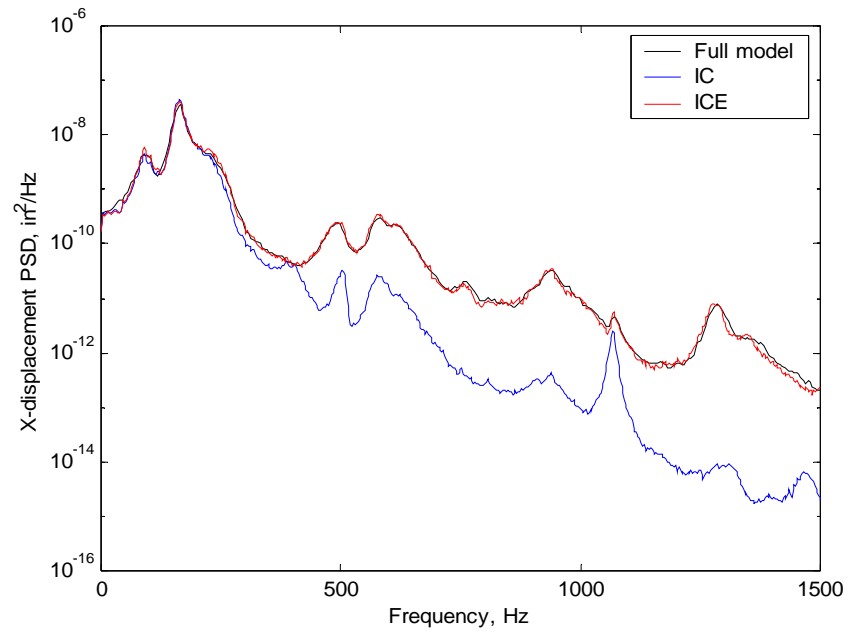


Figure 41. X-displacement PSD at the beam center, 0.6517 lb/in

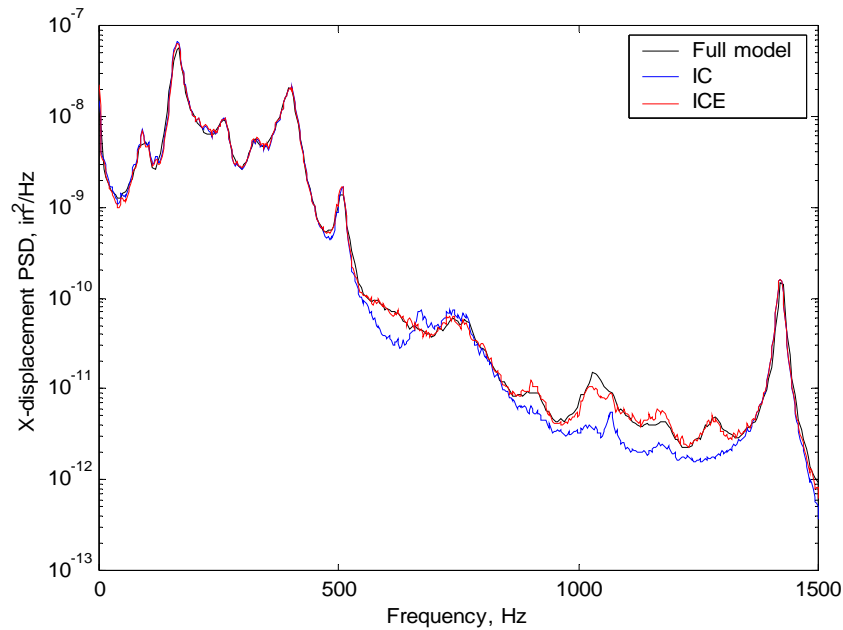


Figure 42. X-displacement PSD at the beam quarter point, 0.6517 lb/in

The IC method was able to reasonably predict x-displacements of the test beam because it was curved. The bending mode shapes of a curved beam contain both x-direction and y-direction DOF. If the beam was flat, the x-direction DOF in the bending mode shapes would be zero and the IC method would be unable to predict any x-displacements. For the curved beam, the IC prediction of the x-displacements was in error as the loading increased. The bending mode shapes were not a complete basis for these DOF. The ICE method, with its estimated membrane basis, did provide an adequate basis for the x-direction DOF. Furthermore, the ICE method worked directly on the IC results in a post-processing operation with little additional computational cost.

#### 4.4 The Clamped Plate

The fourth application of nonlinear ROM's was on a thin rectangular plate with nominally clamped edges. The clamped plate was the first application to a three-dimensional structure, significantly increasing the modal density. Reduced-order models were employed to predict the response of the clamped plate in three test configurations—base excitation on a shaker in air, base excitation on a shaker in near-vacuum, and acoustic excitation in a progressive wave facility. This section will describe the test article configuration followed by details on the three test configurations including ROM development, testing, and comparison of model and test results.

##### 4.4.1 Test Article Description

The goal of the experiments on the clamped plate was to generate random response data for a rectangular plate test article which exhibited significant large-amplitude nonlinearity. The experimental data would be used to verify the effectiveness of the reduced-order modeling methods under development. Several design requirements were defined for the experiment.

First, the test article should be a rectangular metallic plate with nearly rigid boundaries, especially in-plane, so that the large amplitude nonlinearity would be present. The means of clamping the plate boundaries must behave as linearly as possible. The test article should be free of in-plane stresses from thermal or mechanical preloads. Excitation and response sensing must be as non-intrusive as possible. The test article should have at least three symmetric bending modes below 500Hz. Multiple modes are important to investigate the nonlinear coupling induced by the large amplitude response. The method of clamping the test article at its boundaries must minimize damping due to friction and air pumping. Finally, the test article must be relatively inexpensive to fabricate and assemble.

It was important to have an accurate FEM of the test article as a starting point. The ideal test article would be a plate with perfectly clamped edges. This would allow the use of fixed boundaries in the FEM. Unfortunately, any practical means of clamping the edges of a plate test article is not perfectly stiff. There were two approaches to designing a test article for which an accurate FEM could be generated. The first approach was to design a massive, nominally rigid support frame to which the plate would be mechanically fastened or adhesively bonded. Translational and rotational springs would be added at the FEM boundaries to account for the actual stiffness. The stiffness coefficients of the springs must be identified using analysis, test, or a combination of both. This was the approach taken with the beam test article in Section 4.1 and Reference [39]. This approach would result in a simple FEM—a plate with boundary springs. The second approach was to design a reasonably rigid frame for the edges of the plate that could be explicitly included in the FEM. This approach eliminates the need to identify the boundary stiffness since the boundary effects are explicitly modeled. The drawback is a more complex FEM of the boundary frame. The latter approach was selected.

The test article was a 7-inch by 9-inch aluminum alloy plate 0.0195 inches thick adhesively bonded between two aluminum alloy frames. The plate and frames were fabricated from 2024-T3 aluminum alloy with Young's modulus of  $10.4 \times 10^6$  psi, a density of  $2.59 \times 10^{-4}$  lb-sec<sup>2</sup>/inch<sup>4</sup> and a Poisson's ratio of 0.33. The frames had a 1-inch by 1.5-inch "L" cross-section with a 0.25-inch-thick web and flange. The plate was bonded between the frames with Hysol<sup>®</sup> EA9320NA epoxy paste adhesive. The nominal bond line thickness was 0.005 inches. The plate/frame assembly was attached to a 1200 lbf electrodynamic shaker with four steel flexures bolted to the frame flange at the center of each side. The blade-like flexures, each 1 inch by 3 inches by 0.1 inches thick, were very stiff in the long direction to transmit force from the shaker to the frame but were flexible in bending. This allowed the test article to expand due to changes in temperature without building up significant in-plane stress. The test article with flexures and mounting plate is shown in Figure 43.

In-plane stress stiffening due to thermal or mechanical loads can be a significant problem with constrained beams or plates. Relatively small temperature differences can cause large changes in natural frequencies and even buckle the structure. In addition, small amounts of curvature present in the aluminum alloy plates could result in pre-stress as the plates are forced flat during fabrication. Three test articles were fabricated to investigate whether the adhesive bonding process could consistently produce a nominally stress-free article. The measured first-mode frequencies of the articles were 90, 130, and 121 Hz, indicating a large variation in induced pre-

stress. The third article was selected for testing in the study since its first mode frequency was closest to the predicted value of 110 Hz.



Figure 43. The test article shown mounted on flexures with a solid mounting plate.

Initial characterization of the test article indicated that modal damping ratios of the three target modes were quite low—0.0025, 0.003, and 0.005, respectively. Stiffened aircraft skin panels typically have modal damping ratios in the range of 0.005-0.02. Therefore, it was decided to test the plate in two configurations: 1) the lightly-damped original design and 2) with an added constrained layer damper to increase the modal damping ratios in the target modes to approximately 0.01. The damper consisted of a 0.005-inch thick layer of 3M ISD112 viscoelastic damping material and a 0.005-inch thick aluminum foil constraining layer. The damper measured 1.75 inches by 1.75 inches and was located in the center of the plate.

#### 4.4.2 Initial Shaker Test

The first test configuration for the clamped plate was base excitation on a shaker. This work was originally published in Reference [16]. The test article was excited inertially by a large electrodynamic shaker attached to the frame with flexures. The ROM methods being developed are intended for structures loaded acoustically, but base excitation on a shaker is a simple means of simulating in-phase acoustic pressures. Displacement, velocity, and strain were measured at the center of the plate for each test. Displacement and velocity relative to the shaker head were measured with a Polytec Model OVF-512 Differential Fiber Optic Vibrometer. The object beam was aimed at a small retro-reflective target at the center of the plate while the reference beam was aimed at a target on the shaker head. The vibrometer controller processes the object and reference beams to produce differential velocity and displacement. Dynamic strains were measured with a pair of small resistive strain gages bonded to the plate surface, in the center of the plate. The strain gages were oriented parallel to the edges of the plate. Strains were not measured at the edges of the plate, where they would have the highest magnitude, because the strain gradient is high near the edge and the measurement is sensitive to location of the gages. Strains at the center of the plate were much less sensitive to gage placement. The temperature of the plate and frame were measured with thermocouples and were continuously monitored during

testing. Testing was performed only when the temperature difference between the plate and frame was less than 0.3°F. This insured that thermally-induced in-plane stresses were minimized.

Experimental evaluation of the test article was comprised of modal parameter identification, nonlinear stiffness characterization and random response testing. The procedures used to perform these tests are described in the following paragraphs. Resonant frequencies, mode shapes and modal damping ratios were identified by exciting the test article with a 0-800 Hz low-level random acoustic signal and sequentially measuring the response at a seven by nine rectangular grid using a Polytec laser vibrometer. The excitation was generated by an acoustic driver with a two-inch diameter tubular horn aimed to one side of the plate center at an angle of approximately 30 degrees. Frequency response functions were generated from the acoustic input signal and the measured velocity from the vibrometer for each measurement point. Modal parameters were identified from the FRF's using in-house software in MATLAB.

Attempts were made to identify the cubic nonlinear stiffness term for the fundamental mode of the test article from measured free decay response. This approach was used successfully on the clamped beam in Section 4.1. Two approaches were used to generate the free decay records. The first approach was to attach a small plastic suction cup near the center of the plate then pull the suction cup away from the plate slowly until it popped loose. The ensuing free decay was measured with the differential vibrometer. The second approach was to excite the test article with a loudspeaker at a level high enough to induce significantly nonlinear response. The input was slowly swept above the fundamental mode natural frequency until the "jump down" point was approached. The drive signal was then cut off. The decaying response at the plate center was measured with the differential vibrometer. Linear natural frequency, modal damping ratio and cubic nonlinear stiffness coefficient were identified from the free decay responses using the method described in [39].

Random response testing of the test article was performed on the shaker using a base excitation approach. The induced inertial loading simulated normal-incidence acoustic loading on the plate surface. The original requirement for the experiment was to have three modes excited by a 0-500 Hz force spectrum. However, the input force spectrum was modified to 75-625 Hz to improve the experiment. The lower frequency limit was increased to 75 Hz to avoid low frequency rigid body displacements of the test article which tended to de-stabilize the laser vibrometer. The frequency of the third target mode, which was just below 500 Hz at low amplitude, increased to well above 600 Hz at the highest input level. As a result, the upper limit of the input spectrum was increased to 625 Hz to insure that the third mode would be directly excited at all input levels. Response data were measured at input force levels of 0.45, 0.9, 1.8, 3.6, and 7.2 g's RMS. A closed-loop shaker controller was used with an accelerometer on the shaker head to maintain the desired RMS input level and spectrum shape during testing. The shaker was oriented horizontally so that the plate was positioned in a vertical plane to minimize lateral loading due to gravity. The test article is shown in Figure 44 mounted on the shaker. Data records of displacement, velocity, and strain in two directions were digitally sampled and stored for 100 seconds at each force level. The data were analyzed in MATLAB to compute PSD's and RMS values.

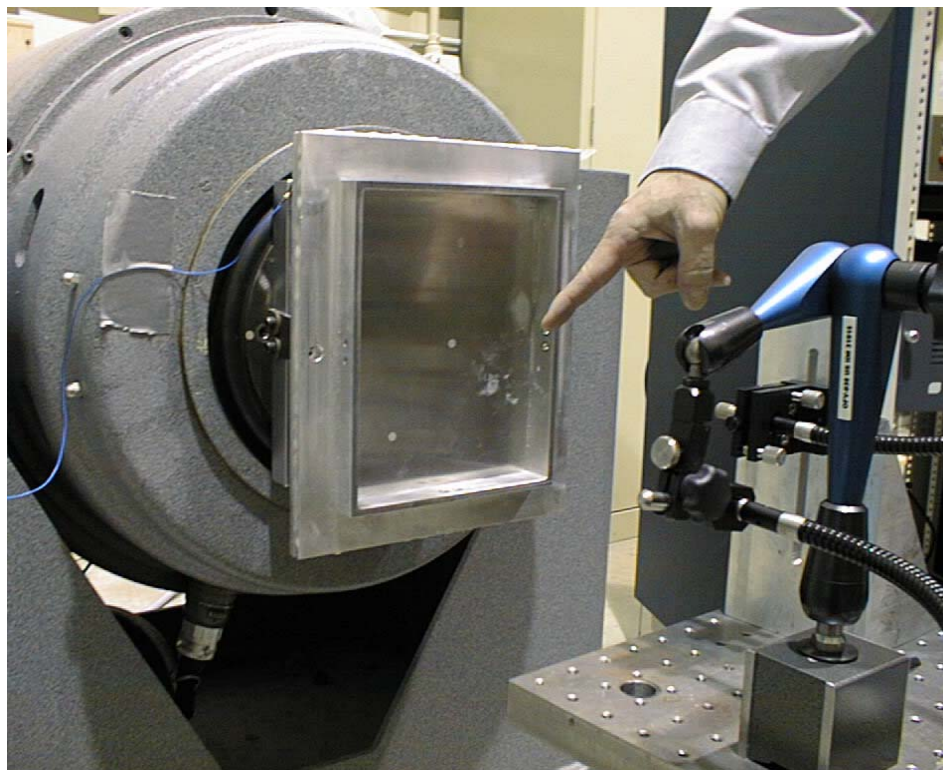


Figure 44. The plate test article mounted on a shaker

A detailed FEM of the test article was developed in MSC.Nastran which explicitly included the plate, frames, adhesive, and flexures. The detailed model used four-node shell elements for the plate and flexures and eight-node solid elements for the frame and adhesive. A 1/4-inch by 1/4-inch mesh size was used for the plate. The only boundary conditions imposed on the detailed model were to fix all DOF at the ends of the flexures that attached to the shaker. The constrained layer damper was not included in the FEM. The added mass and stiffness of the damper were small enough that their effect on the frequencies and mode shapes of the test article were considered negligible.

Nonlinear ROM's of the undamped test article and the test article with the damper were generated from the FEM using the ICE method implemented in MATLAB. The general approach to building a low order model is to include all modes that respond significantly to the acoustic loading. For the present study this was all symmetric bending modes in the 0-500 Hz frequency range. Only symmetric bending modes could be excited by the in-phase shaker input force. The test article had three such modes below 500 Hz. These were the 1<sup>st</sup>, 4<sup>th</sup>, and 7<sup>th</sup> overall modes of the test article. The three mode shapes from the FEM are shown in Figure 45. The three-mode low order models required 18 nonlinear static solutions in MSC.Nastran to compute the nonlinear stiffness coefficients.

Measured modal damping ratios were used in both models. A nonlinear damping term proportional to the square of modal velocity was added to the first-mode equation of the ROM in addition to the linear viscous damping term. The value of the nonlinear damping coefficient was determined empirically based on achieving the same RMS center displacement as the test at 7.2 g's. Both models used the same nonlinear damping coefficient.



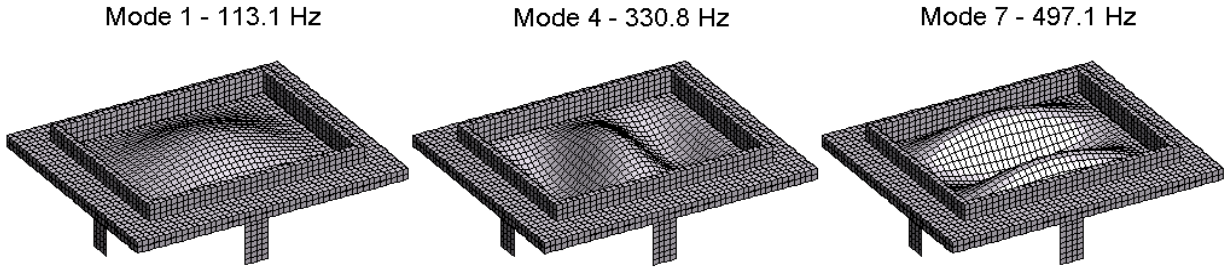


Figure 45. The first 3 symmetric bending modes of the plate test article

Time integration was performed using the Newmark beta method to generate 100-second time histories of displacement for each of five input force levels. Each 100-second integration required less than 5 minutes of CPU time on a personal computer with a 2.8 GHz processor. A time step size of 0.000025 seconds was used in the integration. Physical displacements were recovered using the expansion procedure described above. Strains were computed for a single plate element at the center of the plate, given the displacements at the four nodes of that element. The strain recovery was implemented in MATLAB.

Measured natural frequencies and modal damping ratios for the 3 target modes of the undamped test article are listed in Table 9. Natural frequencies from the FEM are listed for comparison. The FEM under-predicted the natural frequencies compared to the measured values. The suspected cause of the frequency errors is the presence of in-plane tensile pre-stress in the plate. The frequency errors are further illustrated by comparing the PSD's of displacement at the plate center from the test and ROM at the lowest input level—0.45g—as shown in Figure 46. At this input level the response of the plate is essentially linear. The displacement PSD computed from the model with measured frequencies substituted for the computed values is also shown in Figure 46. The agreement with test data is now quite good, indicating the overall accuracy of the linear portion of the model. It is very difficult to build a model of a constrained structure with accurate natural frequencies because of the sensitivity to the pre-stress from fabrication. Frequency errors in a design model are unavoidable. But an analysis model of a specific structure can be made more accurate by using measured frequencies instead of predicted ones. The decision was made to use models with measured frequencies for comparison with test results in the rest of the effort since the primary goal was to demonstrate the accuracy of the ICE method.

Table 9. Natural frequencies and modal damping ratios for the target modes

Mode	Undamped Test Article		FEM	Damped Test Article	
	Freq. (Hz)	Damping Ratio	Freq. (Hz)	Freq. (Hz)	Damping Ratio
(1,1)	121	0.0025	110	115	0.011
(3,1)	343	0.003	322	338	0.016
(1,3)	504	0.005	480	506	0.018



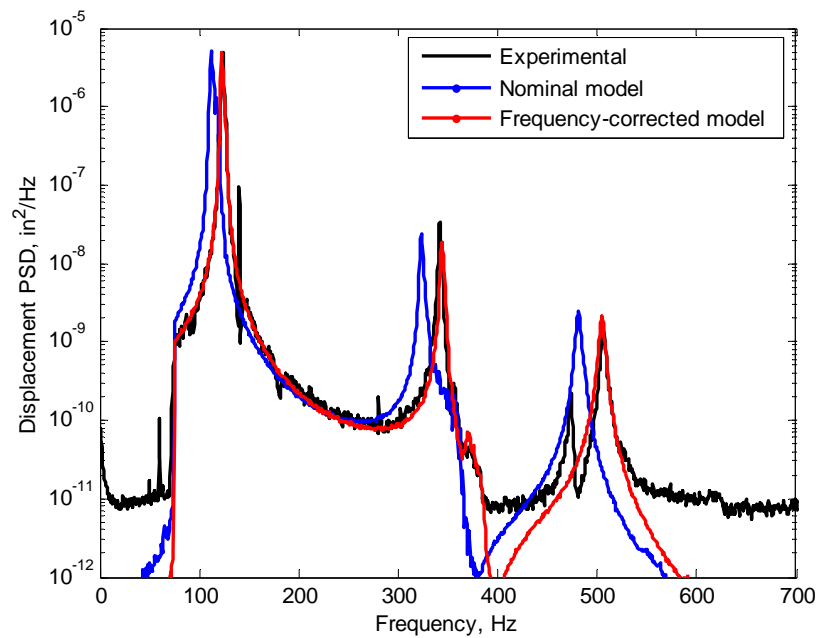


Figure 46. PSD of plate center displacement for the undamped article at 0.45g.

The measured PSD in Figure 46 also shows an additional mode responding near 480 Hz. This peak was determined to be the (3,2) anti-symmetric mode. Ideal anti-symmetric modes can't be excited by a uniform forcing function. However, modal identification results showed the mode shape for this mode to be somewhat distorted, possibly due to un-modeled pre-stress. The distortion allowed the mode to be excited. The effect of this un-modeled mode is negligible.

The modal damping ratios shown in Table 9 for the undamped test article are quite low—0.0025-0.005—compared to typical stiffened aircraft skins. These low values motivated the decision to conduct a second set of tests with an added damper on the test article to increase the damping ratios to values in the range of 0.01-0.02, which would be more representative of real structures.

Attempts were made to experimentally identify the cubic nonlinear stiffness coefficient for the first mode of the test article. This approach was used successfully on a clamped beam in [39]. A value of  $3.5 \times 10^8 \text{ in}^{-2}\text{sec}^{-2}$  was measured for both the damped and undamped test articles. This value is in good agreement with the value of  $4.4 \times 10^8 \text{ in}^{-2}\text{sec}^{-2}$  computed for the ROM's. Therefore, the FEM accurately represented the in-plane stiffness of the test article frame.

Measured and predicted RMS values of the undamped test article center displacement are listed in Table 10 for the five input acceleration levels. The RMS displacements are also plotted vs input level in Figure 47. The model over-predicts the displacements by approximately 20% at three highest excitation levels. While damping controls the response at low input levels, nonlinear effects become important at high levels. Nonlinear damping can also become important at high input levels. Therefore it is important to separate errors due to nonlinear stiffness from those due to nonlinear damping.

Table 10. RMS values of plate center displacement (in) for the undamped test article

Input Level (g's)	Experiment	3-Mode Models	
		Linear Damping	Linear + Nonlinear Damping
0.45	0.004	0.004	0.004
0.9	0.008	0.007	0.007
1.8	0.012	0.014	0.011
3.6	0.018	0.021	0.017
7.2	0.023	0.028	0.023

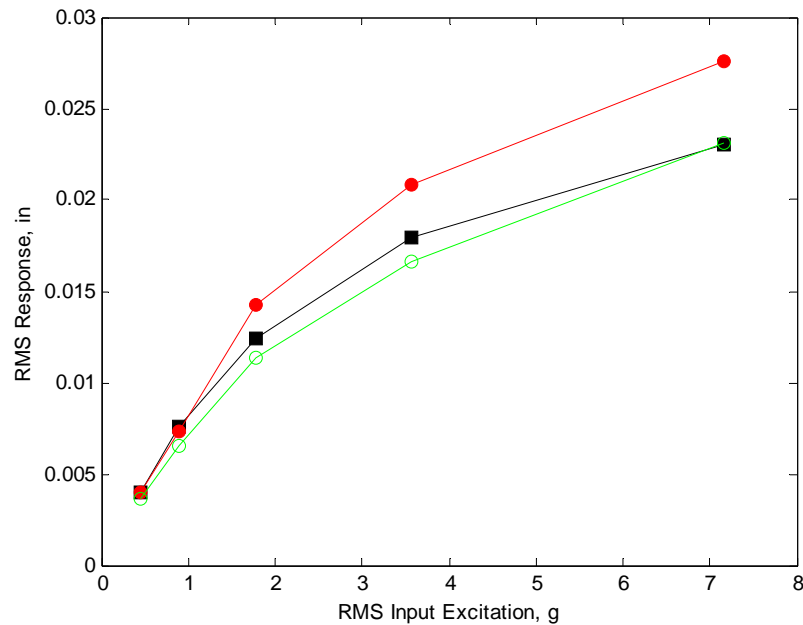


Figure 47. RMS values of center displacement for the undamped article: experimental values (-■-), the frequency-corrected model with viscous damping (-●-), and the frequency-corrected model with viscous and nonlinear velocity squared damping (-○-).

PSD's of center displacement are plotted in Figure 48 for the 1.8 and 7.2 g cases. Predicted PSD's are plotted in the same figure. The figure shows good qualitative agreement between the model and the test data. The low order nonlinear model captures the classical features of the nonlinear response at the high input level, i.e., broadening of the resonant peaks which are shifted higher in frequency. However, the resonant peaks in the predicted PSD's are generally broader and shifted to the right compared to the test data. This is consistent with the over-predicted RMS values.

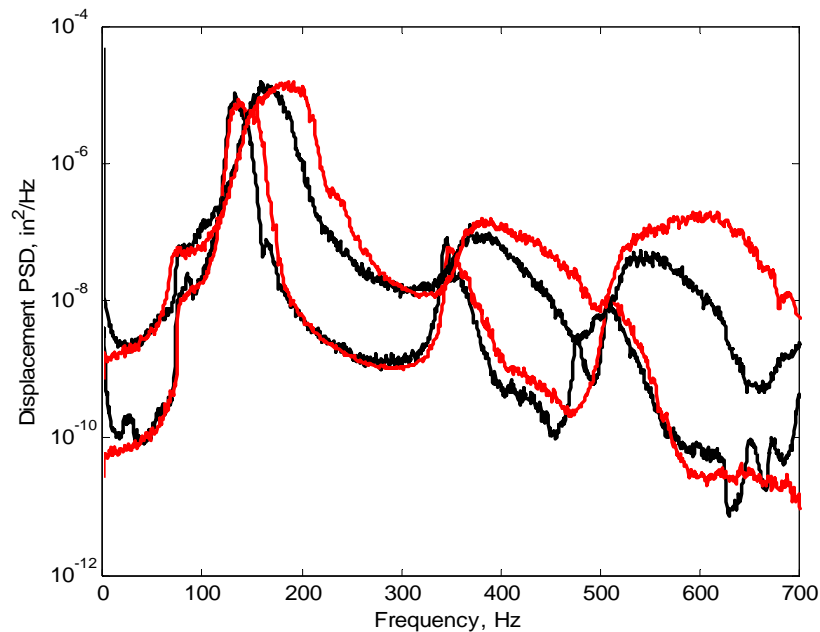


Figure 48. Center displacement PSD for the undamped test article at 1.8g and 7.2g: experimental (—), and the frequency-corrected model with viscous damping (—).

At the time of the initial investigation, it was determined that the most likely cause of the discrepancy was un-modeled nonlinear damping in the test article that increased with response amplitude. The RMS values of center displacement for the ICE model with a nonlinear, velocity squared damping term added to the first mode are shown in Table 10 and Figure 47. The errors compared to the test data are now relatively small. The PSD's for the model with nonlinear damping are compared to test data at the 1.8 and 7.2 g input levels in Figure 49. The agreement at the first mode peak is now much improved at both input levels. Increasing the linear damping in the first mode of the model would also cause the model to agree closely with the test data, but only at one input level. Nonlinear damping is required to match the test at all levels. The very light linear damping in the test article allowed the nonlinear damping to significantly affect the response. The nonlinear damping would be much less noticeable in a real structure with linear modal damping levels in the 0.01-0.02 range. Although nonlinear damping significantly reduced the error in the predicted response, the physical mechanism causing the apparent nonlinear damping could not be reliably identified. The most likely causes are nonlinear acoustic radiation or viscous air effects. A velocity squared damping term was used in the model since it is the physical form of damping for a mass vibrating in a fluid. However, a displacement squared damping term produced similar results.

Results for the test article with the constrained layer damper will now be presented. Measured natural frequencies and modal damping ratios for the target modes are listed in Table 9. The natural frequencies are slightly lower than the undamped values. The modal damping ratios are much higher, and are now more representative of real structures.

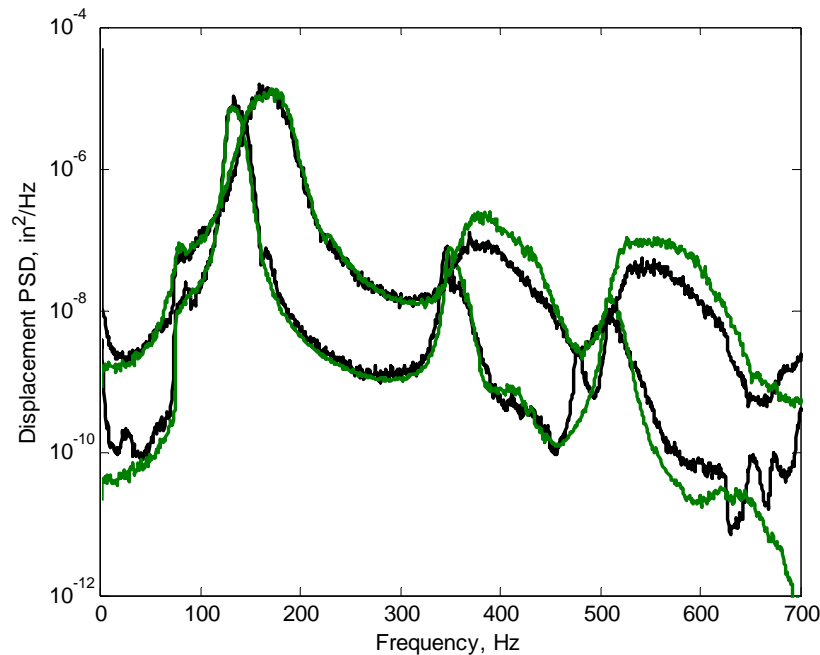


Figure 49. Center displacement PSD for the undamped test article at 1.8g and 7.2g: experimental (—), and the frequency-corrected model with viscous damping and nonlinear velocity squared damping(—).

Measured values of RMS displacement at the plate center are listed in Table 11 and plotted in Figure 50 for the five input acceleration levels. Comparing the values in Table 11 with those in Table 10 for the undamped article, we see that that added damping reduces the displacement by half at the lowest input level. The difference between damped and undamped values gets smaller as the input amplitude increases due to the capping effect of the stiffness and damping nonlinearities. Values from the model with only linear damping, also shown in Table 11, agree more closely with the measurements than in the undamped case. Adding nonlinear damping to the model reduces the RMS displacements slightly as shown in Table 11 and Figure 50. The effect of nonlinear damping on the response of the damped test article is much less significant than it was on the undamped article.

Table 11. RMS values of plate center displacement (in) for the test article with damper

Input Level (g's)	Experiment	3-Mode Models	
		Linear Damping	Linear + Nonlinear Damping
0.45	0.002	0.002	0.002
0.9	0.004	0.004	0.004
1.8	0.008	0.008	0.007
3.6	0.013	0.014	0.013
7.2	0.021	0.021	0.020

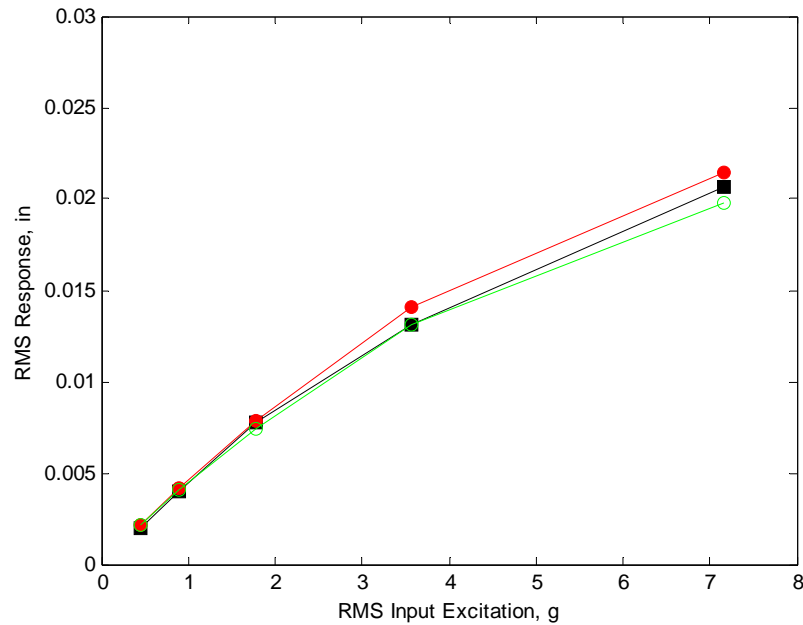


Figure 50. RMS values of center displacement as a function of input level for the damped test article: experimental values (-■-), the frequency-corrected model with viscous damping (-●-), and the frequency-corrected model with viscous and nonlinear velocity squared damping (-○-).

The excellent agreement between model and experiment for the damped test article is clearly visible in the PSD's of center displacements shown in Figure 51. The model prediction now lies very close to the test data for the dominant first-mode peak for both input levels. The agreement is also noticeably better at the other two response peaks. Again, the added damping is masking the nonlinear damping. Adding nonlinear damping to the ICE model, further improves the agreement in the displacement PSD's as shown in Figure 52. The plots are now nearly indistinguishable except near the 3<sup>rd</sup> mode peak.

We will now compare predicted strains at the center of the damped test article with measured values. As discussed above, the primary improvement offered by the ICE method over previous formulations of the IC method is the ability to recover physical membrane displacements from the ROM. This allows the computation of element strains using the finite element strain-displacement equations. RMS strains measured at the center of the damped test article are presented in Tables 12-13 and Figures 53-54 for directions parallel to the short and long sides of the plate. Values from the model are also shown in the tables and figures. The model with linear damping under-predicts the strain in the short direction by 7% (Table 12) and by 13% for strain in the long direction (Table 13) at the highest excitation level. This is considered good agreement. Another observation from the RMS strains is that the absolute strain values are quite low—below levels that would cause sonic fatigue in a real structure. The low values of strain are a direct result of the damping added to the test article. Even though the strains are low, the test article still exhibits nonlinear behavior and is thus good for verification of the low order

modeling methods. Increasing the input level could have produced higher strain levels. But, unfortunately, the shaker used in the experiment was at its limit of output at the 7.2g level.

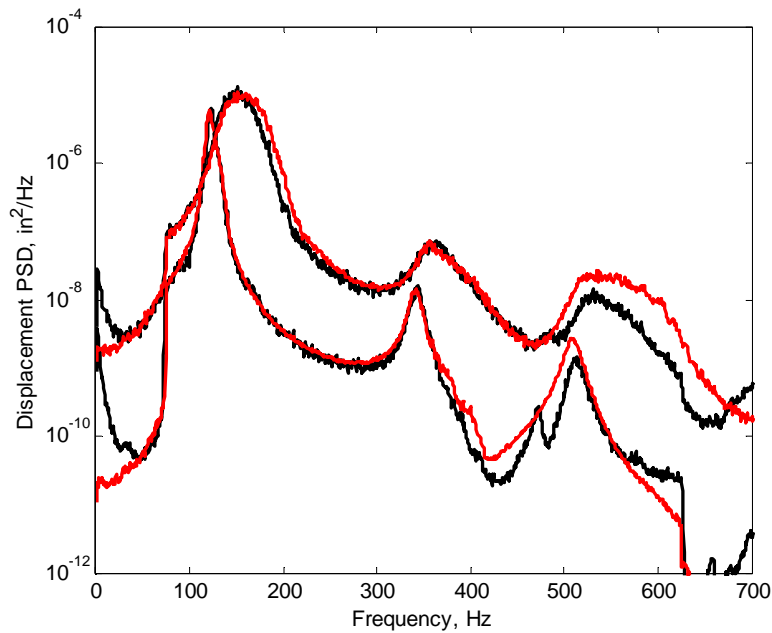


Figure 51. Center displacement PSD for the damped test article at 1.8g and 7.2g: experimental (—), and the frequency-corrected model with viscous damping (—).

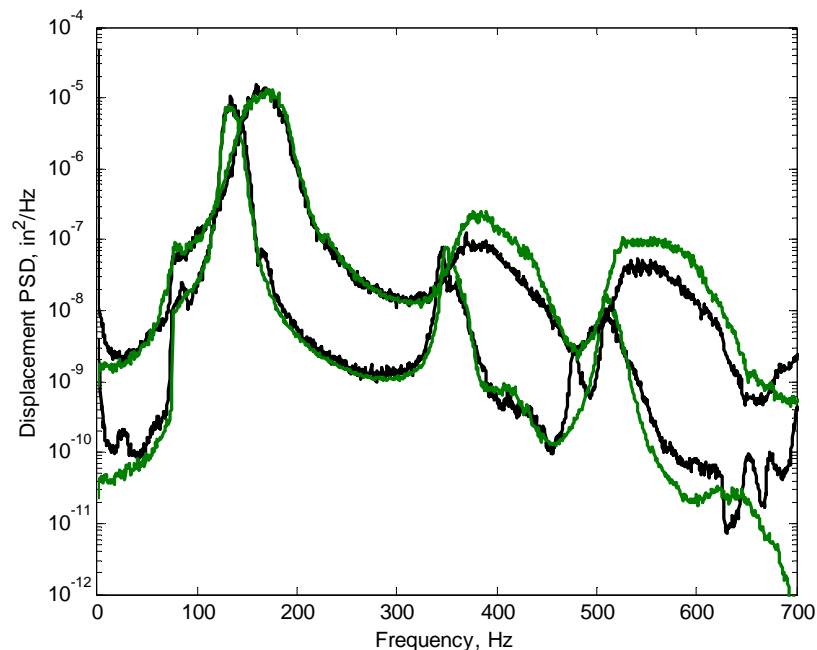


Figure 52. Center displacement PSD for the damped test article at 1.8g and 7.2g: experimental (—), and the frequency-corrected model with viscous damping and nonlinear velocity squared damping (—).

Table 12. RMS values of strain ( $\mu\text{in/in}$ ) at the plate center in the short direction for the test article with damper

Input Level (g's)	Experiment	3-Mode Models	
		Linear Damping	Linear + Nonlinear Damping
0.45	7	7	7
0.9	14	13	13
1.8	27	25	24
3.6	45	43	41
7.2	74	69	63

Table 13. RMS values of strain ( $\mu\text{in/in}$ ) at the plate center in the long direction for the test article with damper

Input Level (g's)	Experiment	3-Mode Models	
		Linear Damping	Linear + Nonlinear Damping
0.45	5	4	4
0.9	10	8	8
1.8	18	15	15
3.6	30	27	26
7.2	47	41	40

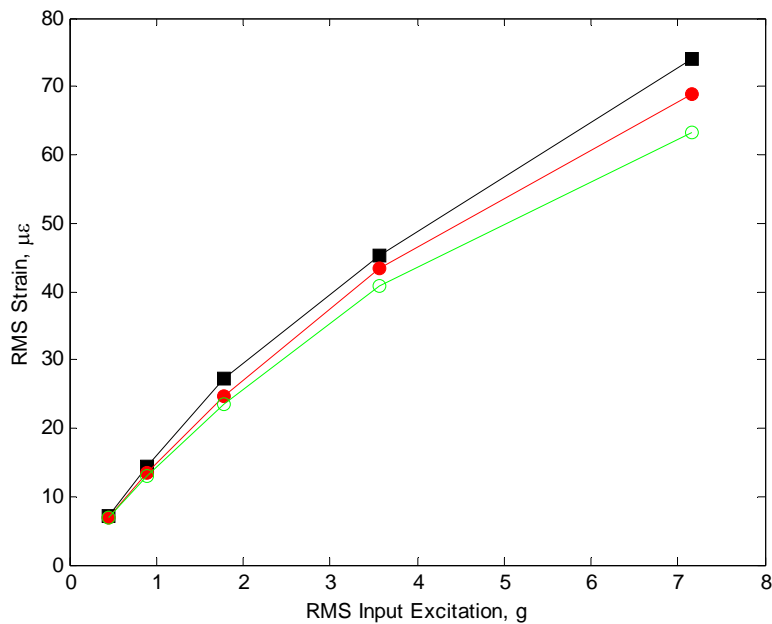


Figure 53. RMS values of strain in the short direction for the damped article: experimental values (-■-), the frequency-corrected model with viscous damping (-●-), and the frequency-corrected model with viscous and nonlinear velocity squared damping (-○-).

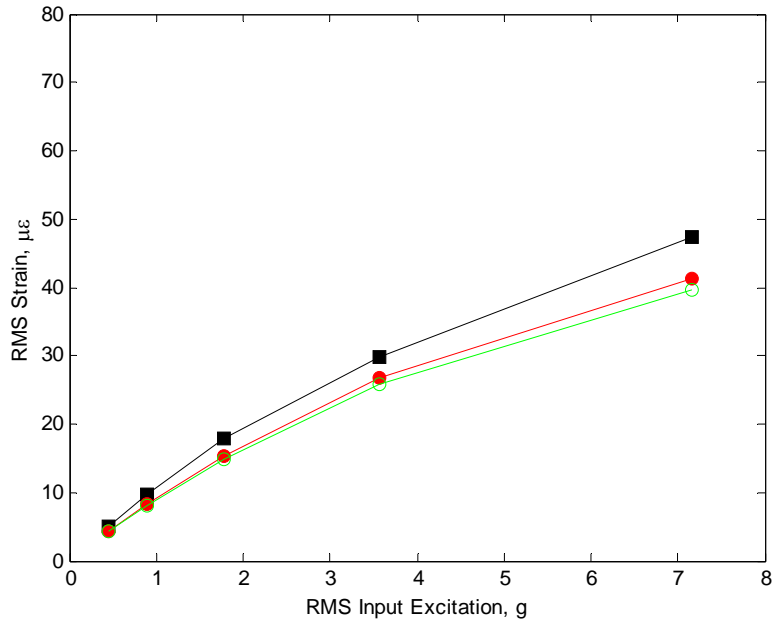


Figure 54. RMS values of strain in the long direction for the damped test article: experimental values (-■-), the frequency-corrected model with viscous damping (-●-), and the frequency-corrected model with viscous and nonlinear velocity squared damping (-○-).

PSD's of strain at the center of the damped test article are plotted in Figures 55-56 for directions parallel to the short and long sides of the plate, respectively at 1.8 and 7.2 g's rms input acceleration. As with the displacement, the predicted strain PSD's show very good qualitative agreement with the experiment. There is some error in the short-direction strain at the 7.2g input level, shown in Figure 55, near 500 Hz and in the long-direction strain, shown in Figure 56, at the first mode peak near 150 Hz and in the vicinity of 500 Hz.

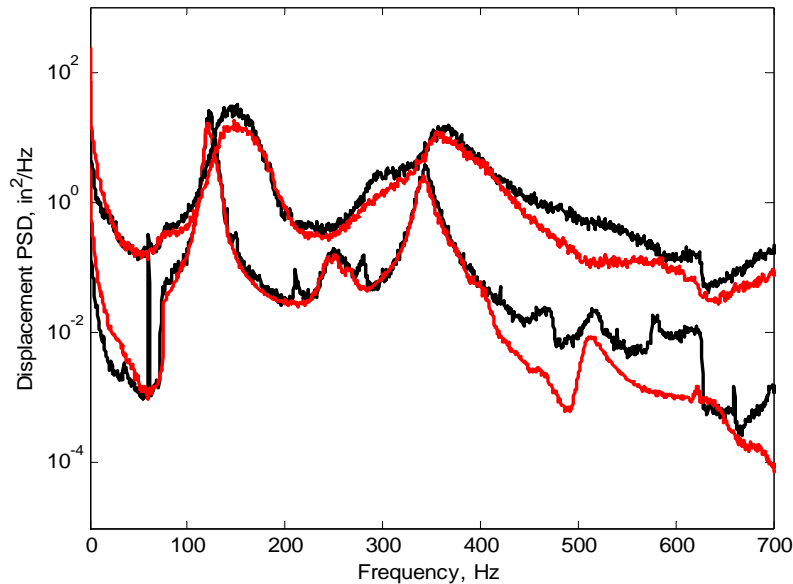


Figure 55. Strain in the short-direction for the damped test article at 1.8g and 7.2g: experimental (—), and the frequency-corrected model with viscous damping (—).



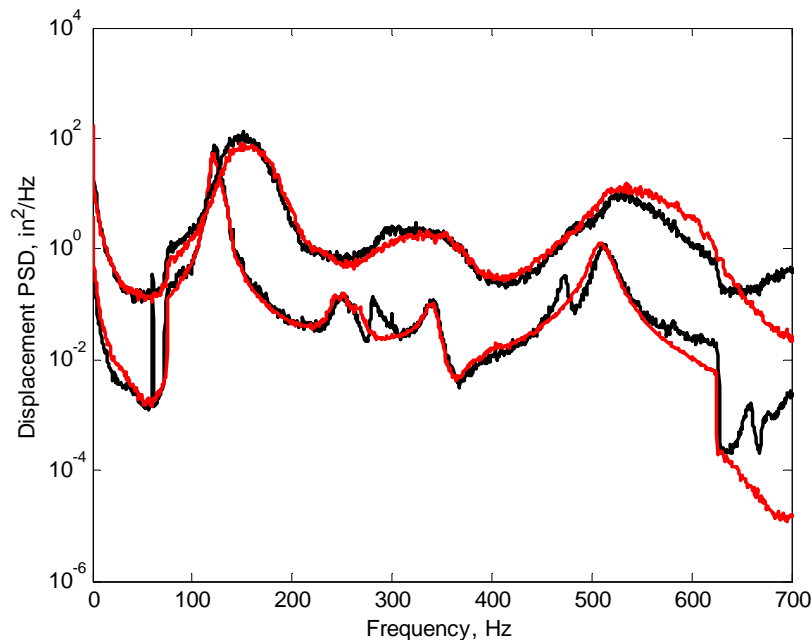


Figure 56. Strain in the long-direction for the damped test article at 1.8g and 7.2g: experimental (—), and the frequency-corrected model with viscous damping (---).

Adding nonlinear damping to the model reduces the RMS strains somewhat as shown in Tables 12-13 and Figures 53-54. The strain PSD's for the model without nonlinear damping are compared to test results in Figures 55-56. Strain PSD's with the addition of nonlinear damping show very little difference compared to the data in Figures 55-56.

The ICE method—an extension of the IC approach—was shown to accurately predict the test article response. It was relatively easy to implement since it does not require special-purpose finite element code or the identification of membrane basis vectors. Generalized membrane displacements were recovered using the procedure and strains were computed from the displacements using strain-displacement equations, instead of the mapping process used in the original IC approach.

The ICE model predicted displacements and strains that agreed reasonably well with experimental data from the original (undamped) test article. There were two general differences, however, between the measured data and the model results. First, the predicted natural frequencies of the test article were lower than the measured values. The most likely cause was un-modeled in-plane tensile pre-stress induced in the test article during fabrication. The frequency errors could be eliminated easily by using measured frequencies in the low order model. The second discrepancy in the model results was the over-prediction of RMS values of displacement and strain. This effect was seen in the PSD's as broadening and shifting of the resonant peaks. Nonlinear damping was added to the model and the agreement of predicted response with the test results improved significantly. However, the physical mechanism producing the apparent nonlinear damping was not identified. Nor was it definitively proven that nonlinear damping was the source of the errors in the predictions and not some other un-modeled phenomenon. This is an area that needs further study.

The addition of the constrained layer damper to the test article resulted in very good agreement between the model and the test data. The improved agreement of the model is likely due to the fact that the added linear damping reduced the overall response at each input level. This tended to lessen the un-modeled nonlinear effects that were causing the errors in the undamped case.

Previous experimental works on random response of clamped plates assumed to have perfectly rigid boundaries have suffered because of un-modeled in-plane boundary stiffness. The approach used in this effort of designing a test article with an integral frame that could be explicitly modeled was successful. The good agreement between the detailed model and the test data confirms this.

#### **4.4.3 Vacuum Shaker Test**

The application of nonlinear ROM's to the clamped plate with base excitation described above showed that the addition of a velocity-squared damping term to the ROM improved the predicted response over a range of excitation levels. In contrast, adjusting the linear modal damping improved the predicted response at only a single excitation level, indicating the nonlinear nature of the damping. The source of the un-modeled damping was believed to be nonlinear acoustic radiation, but this was not proven.

To determine whether acoustic radiation was indeed the source of the nonlinear damping, an experimental study was performed on the clamped plate at several levels of air pressure from ambient to near-vacuum. The details of the experiment along with a comparison of the test and ROM results are presented below. This work was originally published as Reference [48].

To achieve the near vacuum test environment, a chamber was constructed of  $\frac{3}{4}$ -inch-thick aluminum alloy. For ease of fabrication and integration into existing test equipment the chamber is a near cube with internal volume of approximately 3 ft<sup>3</sup>. A 1-inch diameter hole was machined in the front-facing chamber wall and a two-inch diameter by  $\frac{1}{4}$ -inch thick piece of quartz glass was attached with epoxy for laser vibrometer velocity measurement. Chamber gasket material was simply  $\frac{1}{8}$ -inch-thick neoprene rubber. A vacuum pump was used to evacuate most of the air in the chamber. A right angled fixture constructed of  $1\frac{1}{2}$ -inch-thick aluminum alloy was used to secure and position the plate test article so its center was forward facing in view of the quartz window. A 20,000 lbf electrodynamic shaker with a large magnesium slip table attached to the armature was used to excite the entire test assembly. The test setup can be seen in Figures 57-58. The atmospheric test setup is pictured in Figure 57 and the vacuum assembly can be seen in Figure 58. The slip table is hydraulically suspended greatly reducing friction and isolated from the floor to avoid unwanted external excitation. The slip table has a pattern of machined and tapped holes which were used to secure the vacuum chamber and test fixture. A thin film of vacuum grease was applied to both sides of the gasket material to increase its effectiveness.

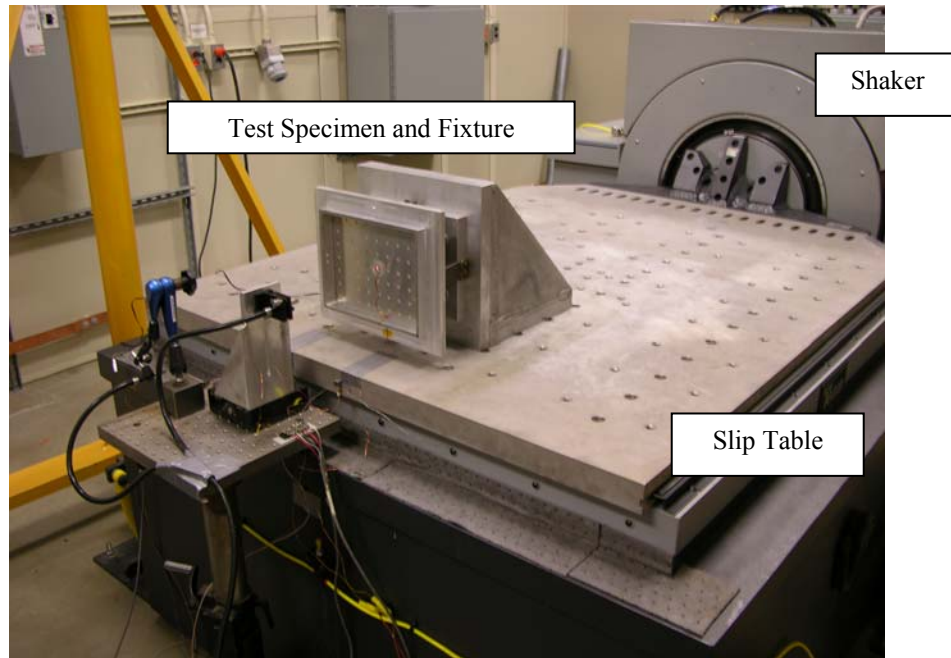


Figure 57. Atmospheric test setup

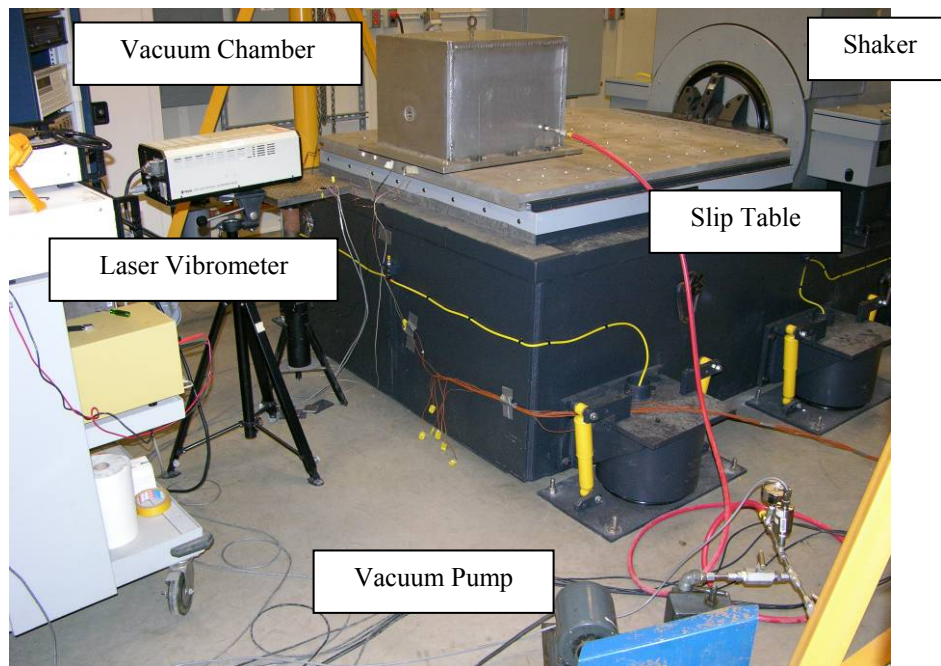


Figure 58. Vacuum chamber test setup

The test procedures followed the same basic profile established in Section 4.4.2 with a random force input, spectrally flat across a 75-625 Hz band, at RMS levels of 0.45, 0.90, 1.8, 3.6, 7.2 g's. Initial tests without the chamber were conducted to confirm baseline values from previous work which included a modal test to establish modal damping ratios for use in the reduced-order modal model. The same test profile was then repeated inside the chamber at decreasing

pressures of 11, 8, 5, 2, 1, 0.5 psia. It was discovered during pretest check-out that 0.5 psia was the limit of the test assembly. Previous work done by Silverman, et al. [49], indicated that changes in clamped plate response below about 1 psia were negligible. This claim was confirmed between the 1 psia and 0.5 psia results of the current study. Time histories of the table acceleration and the panel velocity were recorded for all runs. The record length was 60 seconds, sampled at 4096 Hz.

The panel velocity was measured with a Polytec Model OVF-302 Scanning Laser Vibrometer. The vibrometer beam was aimed through the quartz window on the front of the vacuum chamber at a piece of retro-reflective material placed at the plate center. It was found that the quartz window and any associated vibrations of the chamber wall itself that may have caused possible signal noise generation did not significantly interfere with the plate response signal. The vibrometer used in this experiment was a single beam vibrometer capable only of absolute velocity measurement. The vibrometer used in the previous study was a dual beam vibrometer which provided a differential displacement measurement. That vibrometer was configured to measure the difference between the displacement of the plate center and displacement of the shaker head. In the experiments reported here, the vibrometer measured the absolute velocity of plate center. The absolute velocity approaches the differential velocity as the frequency increases because the table velocity becomes negligible.

The temperature of the plate and frame were measured with thermocouples and were continuously monitored during testing. It was hoped testing would be conducted only when the temperature differential between the plate and frame was less than 0.3°F to conform to earlier work performed by the authors. A relatively low temperature delta would insure that thermally-induced in-plane stresses were minimized. Unfortunately, during atmospheric testing, temperature fluctuations were unavoidable due to the shaker's cooling system. The temperature of the panel was typically 0.5 °F warmer than the frame temperature during these tests. Despite larger than desired temperature deltas, the results still confirmed earlier test baselines after some temperature induced frequency shifting was taken into account. Tests conducted while in the vacuum chamber were within the specified 0.3°F delta as the plate assembly was effectively isolated from the shaker's cooling system. The panel for these tests was 0.1 °F warmer or cooler than the frame depending on the actual test run. In an effort to avoid temperature induced stresses, atmospheric tests were also attempted inside the vacuum chamber. However, acoustic resonances inside the chamber made these results less than desirable for comparison to the near-vacuum results. One acoustic mode of the chamber occurred at about 200 Hz, well within the frequency range of interest, making the atmospheric tests within the chamber useless for the current study. This acoustic mode quickly disappeared as the air pressure dropped in the vacuum tests.

Tests were conducted at the reduced pressures as a means to measure modal damping ratios for use in the ROM as well as later comparison to atmospheric values. To achieve a free decay response of the plate while in the vacuum chamber, the magnesium slip table of the shaker assembly was impacted with a rubber tipped sledge hammer and the resulting plate decaying response was measured with the laser vibrometer through the quartz window.

Finally, the plate was fitted with a 1¼ inch-square piece of constrained layer damping material consisting of a 0.005-inch thick layer of 3M ISD112 viscoelastic damping material and a 0.005-inch thick aluminum foil constraining layer for one series of tests. The damper was designed to provide approximately 1% damping in the first mode. A modal damping ratio near 1% is typical of many stiffened panel structures used in aerospace vehicles. The values of 0.20-0.28% measured for the plate test article were considerably lower than 1%, so the damper was added to see what effect a higher linear damping value would have on the apparent nonlinear damping. The above tests procedures were then repeated with the damped plate.

Experimental results from random response tests, shown in Figure 59, indicated that the plate response was dependant on air pressure, particularly at high excitation levels. Pictured are the PSD's of velocity of the plate center at atmospheric pressure and in a near-vacuum environment for three input acceleration levels. At the lowest excitation level, where response is nearly linear, the atmospheric and near-vacuum results closely track each other. As the excitation level is increased the responses become nonlinear and the atmospheric and near-vacuum results begin to diverge. At the highest excitation level, the measured PSD's are significantly different. At excitation levels where a thin plate exhibits highly nonlinear response, a reduction in damping is associated with peak broadening rather than the narrowing seen in linear response. The data measured at 7.2g in the near-vacuum environment show a greater broadening of the peaks in the PSD when compared to data at atmosphere. This indicates the air is attenuating the response and the attenuation is increasing with amplitude. It should be noted that all results at atmospheric pressure have been frequency-shifted when being compared to vacuum and ROM results due to the previously stated issues with the shaker cooling system.

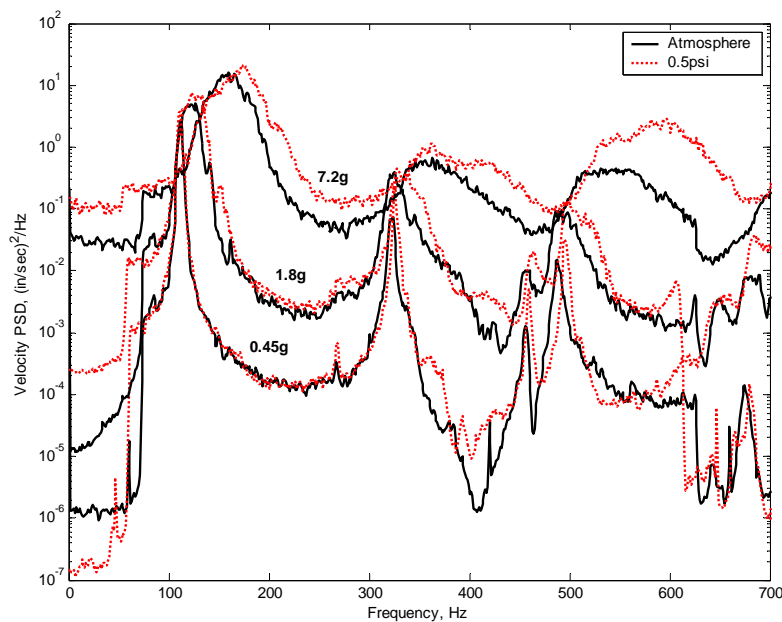


Figure 59. Measured plate center velocity PSD at atmosphere and near-vacuum.

Modal damping ratios were experimentally determined for the plate before the vacuum chamber was added and then again at reduced pressure. Results can be seen in Table 14. The values measured in the near-vacuum environment are, in general, slightly lower than those measured at

atmosphere. This difference would indicate acoustic radiation damping is present. It should be pointed out that the measured damping ratio for the third symmetric mode was suspiciously low compared to the other two symmetric modes of interest. The damping in the third mode would appear to have been reduced considerably more than the other modes when the acoustic medium was removed. It is felt that the impact to the shaker slip table didn't effectively excite the third mode. Therefore, the measured value of modal damping ratio for the third mode was not used in the ROM. Instead, the average percentage of reduction in the modal damping ratio of the first two modes was applied to the third, resulting in a value of 0.005 used for the model predictions for the near-vacuum case. Measured natural frequencies are also shown in Table 14 for the test article at atmospheric and near-vacuum. The frequencies at atmospheric pressure are noticeably lower than those at near vacuum. One cause for this difference could be the mass-loading effect of the air. However, there may also be some thermal stress effect present, since test article frequencies are very sensitive to temperature differences between the plate and the frame.

Table 14. Natural frequencies and modal damping ratios for the target modes

Mode	Undamped Test Article Atmosphere		Undamped Test Article Near-Vacuum	
	Freq. (Hz)	Damping Ratio	Freq. (Hz)	Damping Ratio
(1,1)	112	0.0028	120	0.0020
(3,1)	323	0.0030	335	0.0025
(1,3)	493	0.0070	504	0.0023

The ROM's used here are from Section 4.4.2. The models were based on a detailed FEM developed in MSC.Nastran and reduced to three modes via the ICE method. The natural frequencies and modal damping ratios in the model were adjusted to coincide with measured values. Time integration was performed using the Newmark beta method to generate 60 seconds of velocity data to compare with experiments. The shaker excitation was modeled as a body force so that the output from the integration is actually the differential velocity of the plate center, relative to the shaker. Recall that the experimental results are absolute velocity. Thus, we expect the magnitude of absolute velocity of the experiments to be slightly greater than the differential velocity of the model. This effect is very small and is only noticeable off-resonance and at the lower frequencies.

The experimental results for three input levels at atmospheric pressure are compared to the ROM predictions in Figure 60. The measured damping ratios at atmospheric pressure were used in the model. At the low excitation level the results compare very well. It can be seen that as the excitation level is increased and the response becomes increasingly nonlinear, the agreement between the experimental results and the model predictions decreases. The ROM is over-predicting the response.

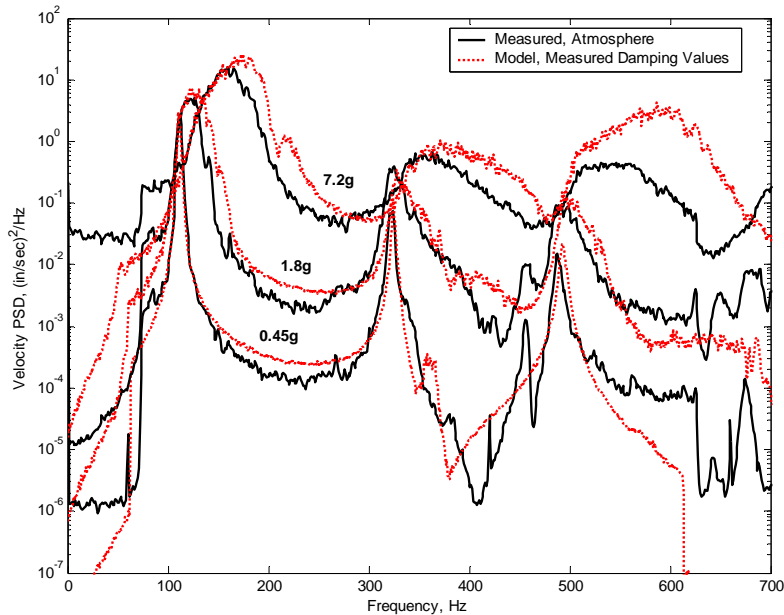


Figure 60. Measured plate center velocity PSD at atmosphere and predicted PSD using measured damping values.

The experimental results for the near-vacuum cases are compared to ROM predictions in Figure 61. Modal damping ratios from the impact test at 0.5 psia were used for model predictions with the exception of the third mode value which was modified as previously stated. With most of the air evacuated, the experimental and model results are in much better agreement than the in-air results. The near-vacuum environment more closely recreates the fundamental assumption present not only in the ROM but in nearly all sonic fatigue response prediction methods, i.e., the structure and acoustic field interaction is negligible. The results in Figure 61 would indicate this decoupled assumption is not valid, particularly for the lightly damped plate in this study.

A very important point to be drawn from Figure 61 is that without the effect of the air, the accuracy of the ROM is quite good! Another important quality of the above comparison is that the ROM uses the same modal damping ratios for all load levels. This point is of particular interest due to the fact that the response is transitioning from a purely linear regime, to one that is highly nonlinear. The peak broadening that occurs with increasing amplitude is not due to any structural nonlinear damping, but is due solely to nonlinear stiffness.

Results from the shaker test described in the previous section showed that a single damping factor for each mode could not accurately model the response for all amplitudes of vibration. The approach there was to add a nonlinear, velocity-dependent damping term to the first modal equation to improve model agreement with experiment. In this study, a trial and error process was used to assign modal damping ratios to the model for each of the five input levels. The obvious starting point is the fact that at the 0.45g level the measured modal damping ratios actually produce an accurate prediction of the plate response. The first-mode damping ratios resulting from this process can be seen in Table 15. It should be noted that in order to simplify the process only the damping ratio of the first mode was manipulated. It was observed that only the level of damping in the first mode has a significant effect on the energy level of the other two modes. Furthermore, being by far the highest energy mode makes fitting the first mode



prediction to the test results the highest priority. Figure 62 shows how well the selected modal damping ratios match the experimental results. As can be seen in Table 15 and Figure 62, the level of damping required in the model increases with the increasing load. At the 7.2g level 1% damping in the first mode is required as opposed to only 0.25% at the 0.45g level. When comparing Figures 60 and 62 one can confirm that manipulating the first mode damping alone has a positive effect on the two higher modes as well.

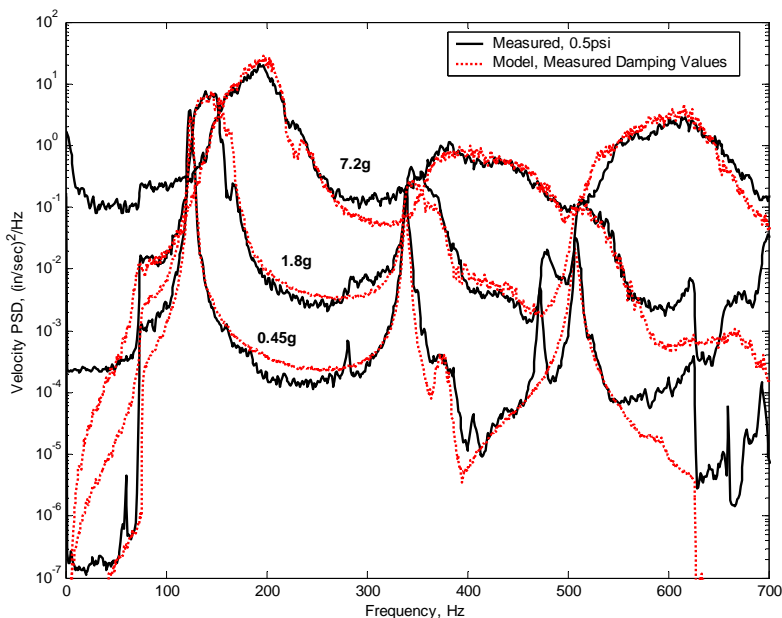


Figure 61. Measured plate center velocity PSD at near-vacuum and predicted PSD using measured damping values.

Table 15. First mode linear damping value needed at pressure/excitation to match experimental results

Input Level (g's)	Model First Mode Linear Damping	
	Atmosphere	Near-Vacuum
0.45	0.0025	0.002
0.9	0.0030	0.002
1.8	0.0050	0.002
3.6	0.0070	0.002
7.2	0.0100	0.002



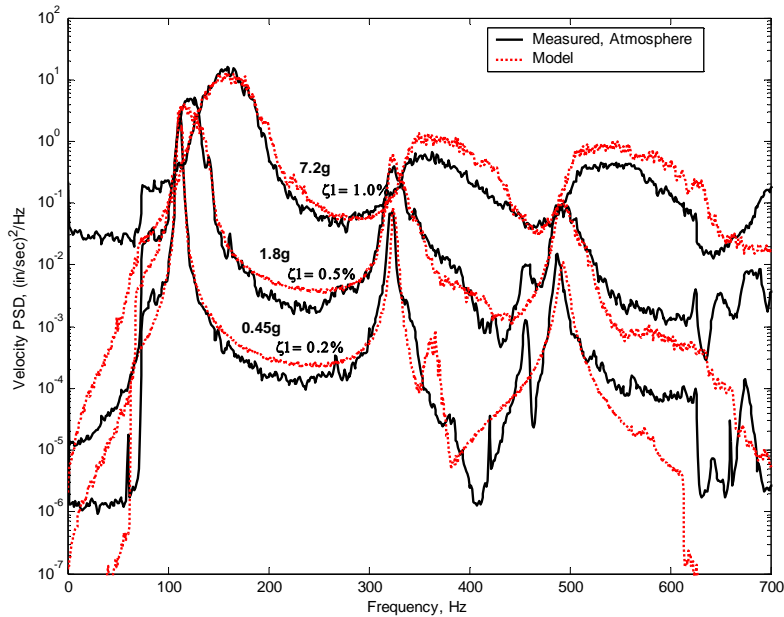


Figure 62. Measured plate center velocity PSD at atmosphere and predicted PSD using increasing linear damping for first mode.

Finally, the plate with added damping was investigated. The same test protocol was repeated with a constrained layer damper attached to the back of the plate. The modal test results for the damped plate are shown in Table 16. The modal damping ratio for the first mode of the damped plate is now 1.2% which is nearly the same damping ratio required to successfully model the response of the experiment at atmosphere and 7.2g. The effects of the added damping on plate random response can be seen in Figures 63-64. In these figures, experimental center velocity PSD's for the damped plate are compared to ROM's for the in-air and in-vacuum cases, respectively. The models used for both figures use measured modal damping ratios from the modal test at atmosphere. This was done out of necessity since the shaker slip table impact tests conducted on the damped plate at reduced pressures didn't produce sufficient levels of response in the plate for near-vacuum damping ratios to be properly estimated. In Figure 63, with the damped plate at atmosphere, measured velocity and the model agree very well at all excitation levels. Figure 64 shows a very similar result in vacuum. Figures 63 and 64 indicate that the more heavily damped structure does not seem to exhibit the nonlinear damping seen with a more lightly damped structure! The response changes little between the atmospheric and near-vacuum environment results.

Table 16. Natural frequencies and modal damping ratios for the target modes of the damped article at atmosphere

Mode	Freq. (Hz)	Damping Ratio
(1,1)	112	0.0120
(3,1)	350	0.0170
(1,3)	512	0.0075

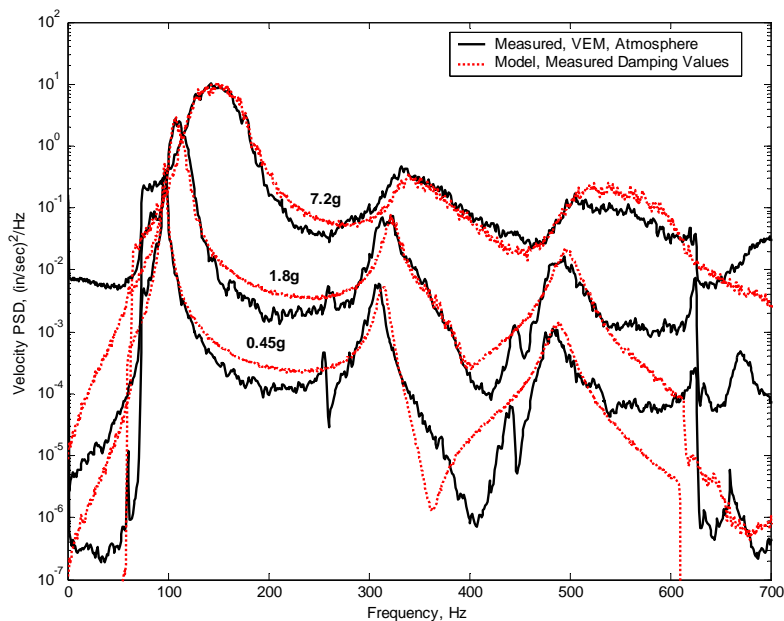


Figure 63. Measured plate center velocity PSD of the damped test article at atmosphere and predicted PSD using measured damping values.

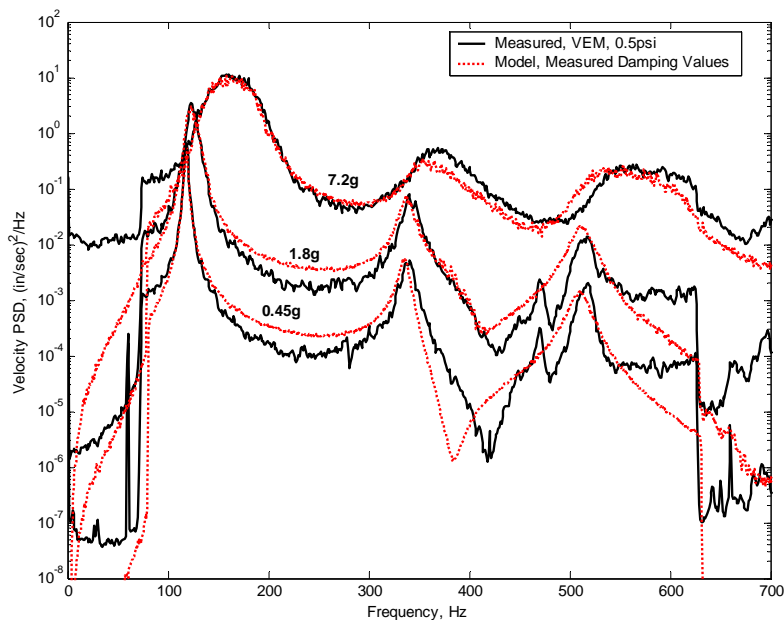


Figure 64. Measured plate center velocity PSD of the damped test article at near-vacuum and predicted PSD using measured damping values.

The effect of the added damping treatment on plate response is further illustrated in Figure 65. Here, the measured response of the damped plate in air at 7.2g's is compared to the response of the undamped plate at the same conditions. The width of the first mode resonant peak of the damped plate is virtually the same as that of the undamped plate, but the peak response of the

damped plate is noticeably lower. This is what would be seen if only the modal damping ratio was different!

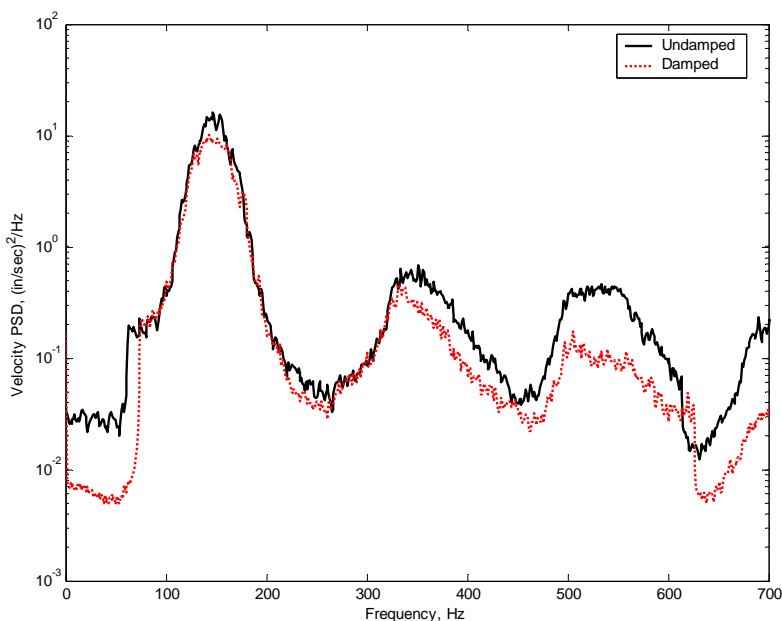


Figure 65. Measured plate center velocity PSD of damped and undamped test article at atmosphere and 7.2g RMS excitation.

Results of the vacuum tests would indicate that there is a physical explanation for the previously un-modeled damping effects. When experimental results at atmosphere and in a near-vacuum environment were compared, it was clear that the response of the plate was a function of air pressure. It was also readily apparent that a ROM with only linear damping terms produced responses that agreed very closely with in-vacuum results. This observation, combined with the fact that a nonlinear damping term was required in the model to match response at atmosphere, proves that coupling with the air is the physical source of the nonlinearity. However, it was not determined conclusively that nonlinear acoustic radiation was the mechanism at play.

The in-vacuum test results provided an excellent validation of the accuracy of the reduced-order modeling approach. Comparison of a model to experimental results in-air has shown some lack of agreement because the model didn't account for coupling with the air. However, when the air was removed, the model agreed very well.

The plate test article investigated in this study was very lightly damped. It was also relatively thin compared to typical skin panels in aerospace structures. The combination of these factors resulted in a test article which was very sensitive to acoustic radiation damping. Furthermore, when the modal damping of the plate was increased to a more representative value with a constrained layer damper, the apparent nonlinear damping disappeared—even at the highest excitation level.

Based on these results, the acoustic medium may have to be included as relevant physics in the solution of highly nonlinear dynamic response. Further study into current coupling capabilities

in commercial software and an addition of acoustical physics into the ROM are needed to further increase the confidence in nonlinear dynamic response predictions.

#### **4.4.4 Finite Element Prediction of Acoustic Radiation Damping**

This section describes the application of finite element analysis to predict the acoustic radiation damping of a thin plate. The work was motivated by the results of the shaker tests of the clamped plate test article in near vacuum reported above in Section 4.4.3. The objective of this study was to determine whether finite element analysis of coupled structural-acoustic models can be used to accurately predict acoustic radiation damping of plate-like structures. This work was originally reported in Reference [50].

Many analytical studies of the acoustic radiation damping of beams and plates have been published since the 1970's. The works of Wallace [51, 52] are good examples. The study by Mangiarotty [53] showed very good agreement of an analytical prediction of the radiation damping of a baffled plate with experiment. Oppenheimer and Dubowsky [54] have shown the potentially large effect baffling has on radiation damping, especially at low frequencies. The analytical methods are accurate for simple structural configuration, like beams or plates, but are not practical for complex air vehicle structures.

Coupled analysis of structural-acoustic models is available in many commercial finite element analysis codes. At least one code, Abaqus, has the capability to use infinite acoustic elements to model unbounded acoustic domains in a complex eigensolution [55]. This combination of capabilities should allow the determination of acoustic radiation damping, although no confirmation of this is found in the literature.

The results of two previous studies were used to judge the accuracy of the finite element-based modal damping predictions. The first was the analytical study by Wallace [51], in which expressions for the acoustic radiation damping of the modes of a simply supported plate in an infinite baffle were developed. The second was the experimental work described in Section 4.4.3 of the damping of a clamped rectangular plate in air and near-vacuum.

In the study by Wallace, the acoustic damping ratios for individual modes of a rectangular plate, simply supported in an infinite baffle, were theoretically determined from the ratio of acoustic energy radiated per cycle to the vibratory energy of the plate. Graphs of radiation damping for a resonant mode as a function of plate thickness-to-length ratio were presented for several plate aspect ratios. The damping ratio for the first mode of the plate model used in this study was determined from one of these graphs.

The near vacuum shaker tests described in Section 4.4.3 produced an experimental example of the effects of acoustic radiation damping. Results from the experimental study of the high-amplitude, random response of a clamped plate in air pressure conditions ranging from atmospheric to near-vacuum can be seen in Figure 59. Shown is the velocity power spectral density (PSD) measured at the plate center under random base excitation. As the magnitude of the load is increased the response at the plate center begins to diverge when comparing atmospheric and near-vacuum conditions. At the highest level response in near-vacuum, the

damping of the system and in the first mode in particular has measurably decreased. For reference, during nonlinear response a reduction in damping is seen as a broadening of the peak. The experimental results indicated the measured linear modal damping ratio of the first plate mode in atmosphere was approximately 0.25%. When the measurement was repeated in a near-vacuum environment the first mode damping ratio was reduced to 0.15%. Acoustic radiation damping becomes a dominant contributor to overall damping levels for a thin plate. Given the 0.020 in. thickness of the plate test article, the difference in damping ratios between the two experiments was considered a reasonable measure of acoustic radiation damping.

The complex eigensolution capability in Abaqus was used to compute the modal damping of a thin plate model coupled to an unbounded acoustic domain. Infinite acoustic elements were used to model the unbounded domain. The basic concept behind the structural-acoustic coupling in Abaqus is fairly straightforward. Transverse displacements of a structure can impart a resulting pressure on a neighboring acoustic element and visa versa. Only transverse displacements are considered as the tangential and rotational effects at the structural-acoustic interface are considered negligible. The acoustic elements only require a pressure degree of freedom. For small deformations of the structure, the acoustic element mesh does not follow the deflection of the structural element. During transient analysis and situations with large structural deflections the acoustic elements are only capable of deforming to the structure by re-meshing the acoustic domain at the end of each time step to re-establish the interface region.

Perhaps the most novel structural-acoustic modeling feature currently available in commercial FEA software packages is the infinite acoustic element. The infinite acoustic element allows the user to minimize or even eliminate the need for large numbers of standard acoustic elements in modeling an exterior domain. Normally the user would need to model a large spherical acoustic domain to sufficiently capture the desired acoustic modes. It is suggested that the radius of the sphere should be at least equal to  $1/3$  the wavelength of the lowest frequency of interest. The current study involved a structure where the first bending mode frequency was near 100 Hz with a resulting wavelength of more than 10 feet. Therefore the sphere of standard acoustic elements could potentially be quite large in terms of degrees of freedom. This large number of degrees of freedom becomes a serious concern during a direct time integration solution of a fully coupled nonlinear model. Therefore, the use of infinite element to reduce model size becomes attractive for the coupled problem in question. For some specific cases the infinite acoustic element can even be directly interfaced with a structural element. Reference 56 describes this procedure.

Another beneficial characteristic of infinite elements specifically available in Abaqus is the ability to perform a complex eigensolution. Beginning with version 6.6, Abaqus has expanded its structural-acoustic coupling capabilities to include a complex eigensolution option when using infinite acoustic elements. The primary benefit with this option is the inclusion of a damping matrix to the system of equations without having to define the damping terms as part of the analysis input. With the more traditional absorbing or nonreflecting acoustic boundary conditions the system acoustic damping needed to be estimated and supplied as input. With the combination of the complex eigensolution and infinite acoustic elements damping is a product of the analysis. The damping value produced can be best described as acoustic radiation damping. When the medium in question is air the damping is quite often small when compared to the structural damping associated with things like friction or air pumping in riveted joints. However,

when you have thin bonded secondary aircraft structure it is possible that acoustic radiation damping becomes a significant and measurable contributor to the overall system damping.

Another means to validate the acoustic radiation damping produced by the complex eigensolution is a transient solution of the coupled problem from an initial deformation of the plate. A static pressure load is applied to initially deform the plate. The initial displacement closely approximates the plate first bending mode shape. The static pressure is then removed and the plate is allowed to vibrate. The damping due to structural-acoustic coupling causes the response to decay over time. Modal damping can be estimated from a resulting time record by fitting a single degree-of-freedom damped sine wave to the time response.

Numerical studies were conducted on three-dimensional models of a thin rectangular plate in an unbounded acoustic domain to compute modal acoustic radiation damping using coupled structural-acoustic FEM's. These studies were conducted using Abaqus. Modal damping was estimated using both complex eigensolutions and free-decay time histories. The Abaqus results were compared to results from similar analyses performed with an in-house finite element code implemented in MATLAB. The plate was analyzed in an infinite baffle and in an unbaffled configuration. Clamped and simply supported boundary conditions were applied. Unbaffled, clamped results are compared to experimental data and baffled, simply-supported results are compared to an analytical prediction.

Baffled and unbaffled models were analyzed in Abaqus. In order to visualize the lower order acoustic modes, a small acoustic domain was explicitly modeled for both cases. The baffled case consisted of a hemisphere of 7597 standard AC3D4 three-dimensional four-node tetrahedral acoustic elements. The plate was interfaced to the flat surface of the acoustic hemisphere utilizing the Abaqus TIE command. The TIE command is quite useful as it eliminates the need for coincident nodes at the interface of varying element types and sizes. The thin plate was modeled with 252 S4R shell elements. The meshed hemisphere model with clamped boundary conditions can be seen in Figure 66. The model's 824 ACIN3D3 three-dimensional triangular infinite elements are not physically seen in the figure since they were constructed outside of the modeling software, but are essentially 2-D triangles tied to the outward facing surface of the outermost standard acoustic tetrahedra. The fact that the flat side of the acoustic hemisphere has no infinite elements and the plate only interacts with air on one side essentially makes it an infinite baffle. To predict the true baffled acoustic radiation damping from both sides of the plate, the value produced by the analysis was simply doubled. For the unbaffled case a mirror image of the original hemisphere was added to the other side of the plate. Therefore the number of acoustic elements was exactly doubled for the unbaffled model. The two flat surfaces of the hemispheres were coupled using the TIE command allowing acoustic pressure fluctuations across the boundary.

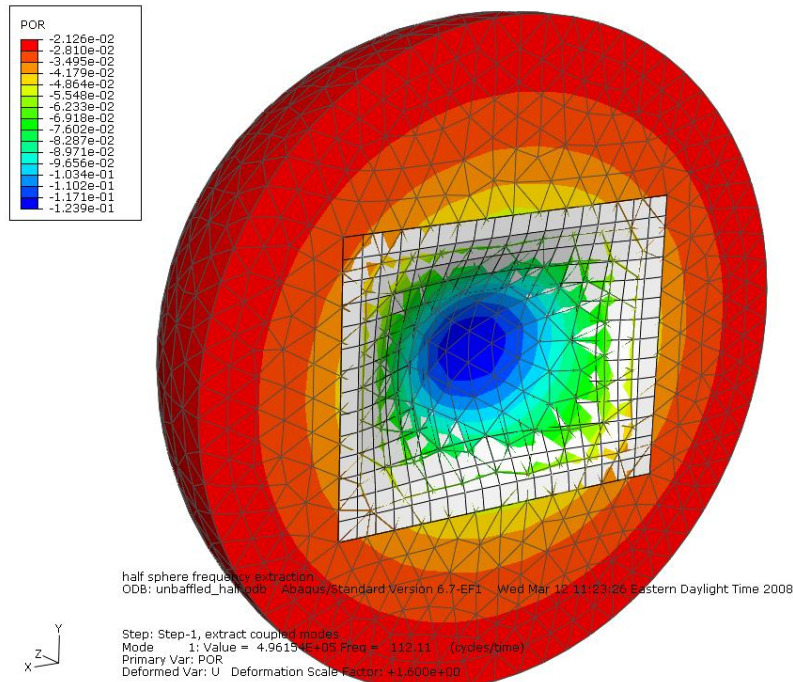


Figure 66. Abaqus acoustic pressure results of the clamped, baffled case.  
First plate mode exciting the air.

Baffled and unbaffled models of the plate were also analyzed with the in-house code. The acoustic and structural meshes of the baffled model with clamped boundaries are shown in Figure 67. The baffled model was a symmetric model of half of the plate. The acoustic domain was included on only one side of the plate. This accurately captured the effect of an infinite baffle, but only modeled radiation from one side of the plate. As with the Abaqus model, modal damping values from analyses were doubled to include radiation from both sides of the plate. The symmetric nature of the plate model did not necessitate an additional doubling of the damping ratio. The model used 126 four-node shell elements and 6800 eight-node linear acoustic elements. Unlike Abaqus, the in-house code required coincident nodes at the structure-acoustic interface for coupling. The in-house model used 600 infinite elements on the surface of the acoustic mesh. These elements used the wave-envelope formulation of Astley [57]. The unbaffled model used the same symmetric plate configuration as the baffled model and was coupled to a contiguous acoustic domain on both side of the plate. For this case, 13600 acoustic elements and 1200 infinite elements were used.

Results for the clamped, baffled case will be discussed first. The first structural mode of the coupled Abaqus model can be seen in Figure 66. The vibrating structure is clearly coupled to the acoustic domain and imparting a pressure disturbance on that domain. The magnitude of the pressure is meaningless as the plate displacement is of arbitrary magnitude. There was a decrease of 5 Hz in frequency of the coupled model compared to an uncoupled plate model. A similar frequency drop was seen in the experiment of Section 4.4.3 when the plate was tested in air versus vacuum. However, this difference was not conclusive given the potential for slight temperature variation between tests that can shift frequencies. The frequency drop in both cases was likely due to a mass-loading effect of the air.

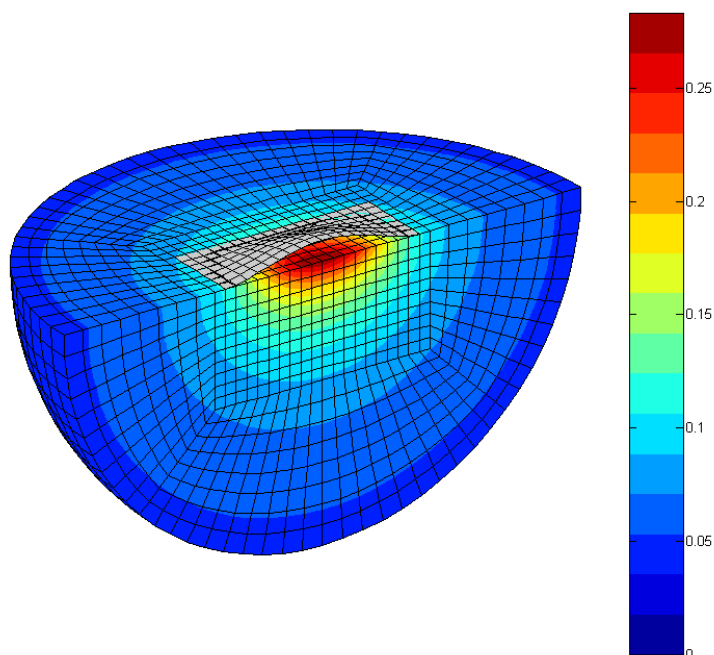


Figure 67. Real part of complex first mode of baffled rectangular plate in infinite acoustic domain with in-house code

The results of the Abaqus complex eigensolution for the first 10 modes of the baffled plate can be seen in Table 17. Note that damping ratios output by Abaqus are really loss factors, and must be divided by 2 to yield the true modal damping ratio. The first mode damping ratios from the Abaqus and in-house code complex eigensolutions are compared in Table 18. The values from the two codes agree very closely. These damping ratios are physically significant. Damping ratios of aircraft panels are usually in the 0.5-2.0% range. However, damping ratios for a baffled plate can be significantly higher than for an unbaffled plate.

Table 17. Abaqus complex eigensolution results for the clamped, baffled case.

COMPLEX EIGENVALUE OUTPUT				
MODE NO	REAL PART OF EIGENVALUE	FREQUENCY (RAD/TIME)	(Hz)	DAMPING RATIO
1	-1.9823	705.09	112.22	0.00562
2	-7.75611E-02	1240.2	197.38	0.00013
3	-0.10459	1706.1	271.53	0.00012
4	-1701.1	2085.8	331.97	1.63108
5	-3.0749	2143.9	341.21	0.00287
6	-1.06289E-02	2181.1	347.14	0.00001
7	-8.59324E-02	3019.3	480.54	0.00006
8	-4.9129	3331.9	530.28	0.00295
9	-0.68927	3449.5	549.00	0.00040
10	-0.54273	3769.8	599.99	0.00029



Table 18. Modal damping ratios of the clamped, baffled case.

Abaqus		In-house Code	
Complex Eigen	Free Decay	Complex Eigen	Free Decay
0.0056	0.0052	0.0054	0.0055

The results of the free decay analysis of the clamped, baffled Abaqus model are pictured in Figure 68. The figure shows the output of a MATLAB function which uses the Hilbert transform to estimate modal damping from a single-mode free decay response. The damping ratios from the Abaqus and in-house codes are shown in Table 18. The estimated modal damping ratio was multiplied by a factor of 2 to capture radiation from both sides of the plate. The damping ratios produced by the two codes are nearly equal at 0.54% and 0.55%, and are very close to the values from the complex eigensolution. The effect of the structural-acoustic coupling within Abaqus can thus at least be considered consistent. However, comparison to experimentally measured values must be made with a full-sphere unbaffled model.

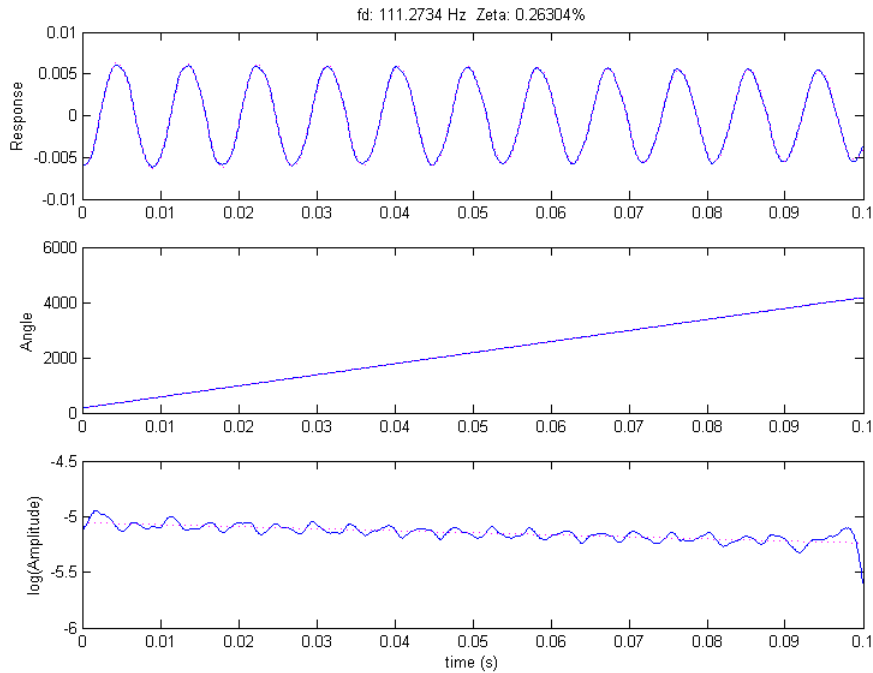


Figure 68. Baffled plate center displacement response to initial pressure in Abaqus. Hilbert transform fit to estimate first mode damping.

To achieve the unbaffled simulation an additional mirror image of the original hemisphere was simply added to the other side of the plate. The model should now be able to produce an accurate prediction of the acoustic radiation portion of the measured first mode damping of the plate from the experiment. The coupled first mode of the plate for the unbaffled case can be seen in Figure 69. Pictured is the acoustic pressure with half of each hemisphere removed for visualization

purposes. Again, the acoustic pressure is of arbitrary magnitude since it is from a modal solution. Clearly the acoustic medium and structure are coupled and unbaffled as there is interaction across the boundary of the two hemispheres. Interestingly, the frequency of the plate's first mode is nearly unchanged compared with the baffled case.

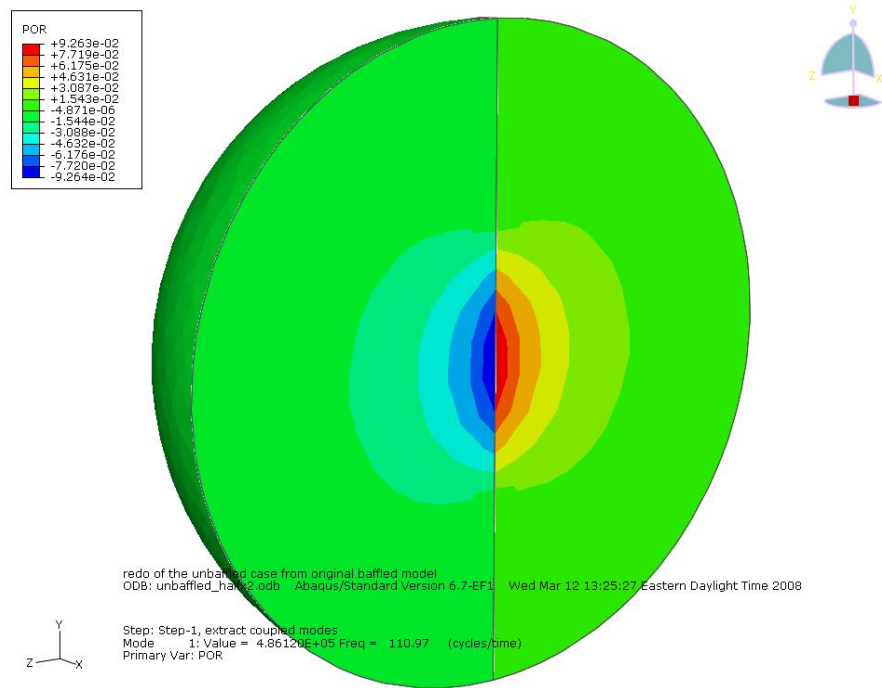


Figure 69. Abaqus acoustic pressure of the unbaffled case cross section view.  
 First plate mode exciting the air.

The results of the Abaqus complex eigensolution for the first 10 modes of the unbaffled, clamped case are listed in Table 19. The Abaqus and in-house code results are compared in Table 20. As suspected, the damping ratios have greatly decreased compared to the baffled case as also noted in the work of Oppenheimer and Dubowsky [54]. However, comparing the two unbaffled finite-element models there is no longer very close agreement. It is not yet known why this discrepancy exists for the unbaffled models despite the consistency for the baffled case.

The time history of plate center displacement for the Abaqus free decay analysis of the clamped unbaffled plate can be seen in Figure 70. It can easily be concluded that the damping has been reduced with the elimination of the acoustic baffle as the response hardly seems to decay at all. Table 20 lists the free decay damping ratio from the Abaqus run. As with the baffled case, the results of the free decay simulation essentially confirm the results of the complex eigensolution with a value of 0.014%.

Table 19. Abaqus Complex eigensolution results for the clamped, unbaffled case.

COMPLEX EIGENVALUE OUTPUT				
MODE NO	REAL PART OF EIGENVALUE	FREQUENCY (RAD/TIME)		DAMPING RATIO (Hz)
1	-0.13353	697.22	110.97	0.00038
2	-9.07521E-03	1226.3	195.17	0.00001
3	-8.23057E-039	1689.8	268.93	0.00001
4	-1689.1	2050.5	326.35	1.64746
5	-0.19652	2125.9	338.35	0.00018
6	-1.51691E-03	2162.6	344.18	0.00000
7	-3.80064E-03	2998.1	477.16	0.00000
8	-1.6255	3305.7	526.12	0.00098
9	-2.94732E-02	3429.1	545.76	0.00002
10	-1.96989E-02	3746.9	596.34	0.00001

Table 20. Modal damping ratios of clamped, unbaffled case.

Test	Abaqus			In-house Code	
Measured	Complex Eigen	Free Decay	Complex Eigen with Frame	Complex Eigen	Free Decay
0.001	0.00019	0.00014	0.0007	5e-5	--

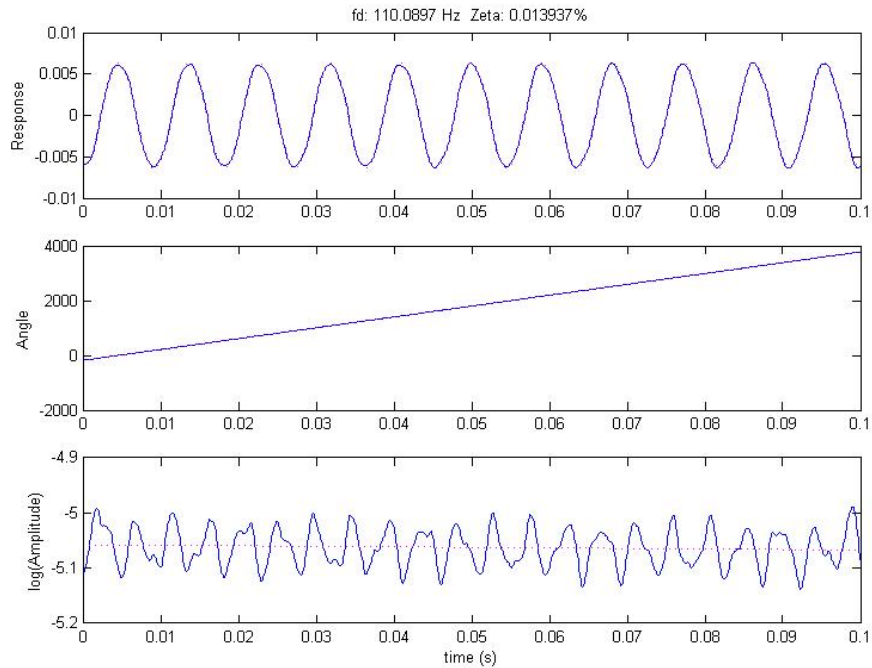


Figure 70. Unbaffled plate center displacement response to initial distributed pressure in Abaqus. Hilbert transform fit to estimate first mode damping.

Comparing the predicted damping ratios of 0.019 and 0.014%, shown in Table 20, to the experimentally measured first mode radiation damping of 0.10%, the disagreement is rather large. One possible explanation for this discrepancy is the frame surrounding the plate specimen. It was theorized that the frame was causing a slight baffling effect to occur in the experiments that were believed to be in a true free-field. The measured difference in damping between modal tests conducted in atmosphere and near-vacuum environment were assumed to be a reasonably accurate measure of acoustic radiation damping. If the frame was in fact causing a baffling effect the atmospheric test damping ratio would be larger than a true unbaffled value and could effectively rule out 0.1% as an accurate measure of pure free-field acoustic radiation damping.

To explore the frame baffling idea an additional complex eigensolution was conducted on an Abaqus model with the addition of the plate frame. A cavity with the dimensions of the frame was removed from the acoustic domain creating a perfect reflecting surface surrounding the plate. As can be seen in Table 20 the results from the new complex eigensolution with the frame were encouraging, producing an increase in acoustic radiation damping to 0.07%. The predicted value could then be considered in relative agreement with the measured value of 0.1%. It is interesting to note that the wavelength of sound at the first-mode frequency is much greater than the dimensions of the frame, yet the frame had a significant effect on the predicted acoustic radiation damping ratio.

The analytically-predicted damping ratios taken from Wallace [51] are a second benchmark for determining the accuracy of the finite element-based methods. Wallace's results are for a simply supported plate in an infinite baffle. Abaqus and in-house analyses were performed on the baffled models previously described with clamped boundary conditions changed to simply supported. Damping ratios for this case are shown in Table 21. The damping ratios from Wallace and the finite element analyses were increased by a factor of two to account for radiation from both sides of the plate. The analytical predicted value of approximately 0.44% agrees reasonably well with the value of 0.38% from both Abaqus and the in-house code. It is interesting to note that changing the boundary conditions from clamped to simply supported causes the damping ratio to drop from 0.55% to 0.38%.

Table 21. Modal damping ratios of simply-supported, baffled case.

Analytical	Abaqus		In-house Code	
	Complex Eigen	Free Decay	Complex Eigen	Free Decay
0.0044	0.0038	--	0.0038	--

#### 4.4.5 Initial Acoustic Test of the Clamped Plate

Initial tests on the clamped plate test article, described in the Section 4.4.2, used base excitation to simulated acoustic loading. The next logical step in verifying the accuracy of nonlinear ROM's was to compare results with test data from acoustic loading tests. This section describes the initial test of the plate with acoustic loading in a progressive wave test facility. ROM prediction of nonlinear plate response are compared to test data for several acoustic load levels

with plate response ranging from nearly linear to highly nonlinear. This study was originally published as Reference [17].

Acoustic testing was performed in the AFRL Sub-element facility (SEF) which is a progressive wave acoustic test facility. The SEF, shown schematically in Figure 71, has a one foot square test section and is capable of subjecting test articles to overall sound pressure levels (OASPL) up to 174 dB with closed loop spectrum shape control. The backing plate of the test article was bolted to a rigid, massive cart for testing in the SEF as shown in Figure 72. An adapter plate surrounded the test article so that when the cart was rolled into place, one side of the framed plate and the adapter plate became part of the PWT side wall. To minimize the amount of noise transmitted through these gaps, a compressible gasket was used to seal the adapter plate into the permanent PWT sidewall. Gaps between the test article and the adapter plate were sealed with duct tape. Figure 72 shows the test article/adapter plate arrangement before the tape was applied.

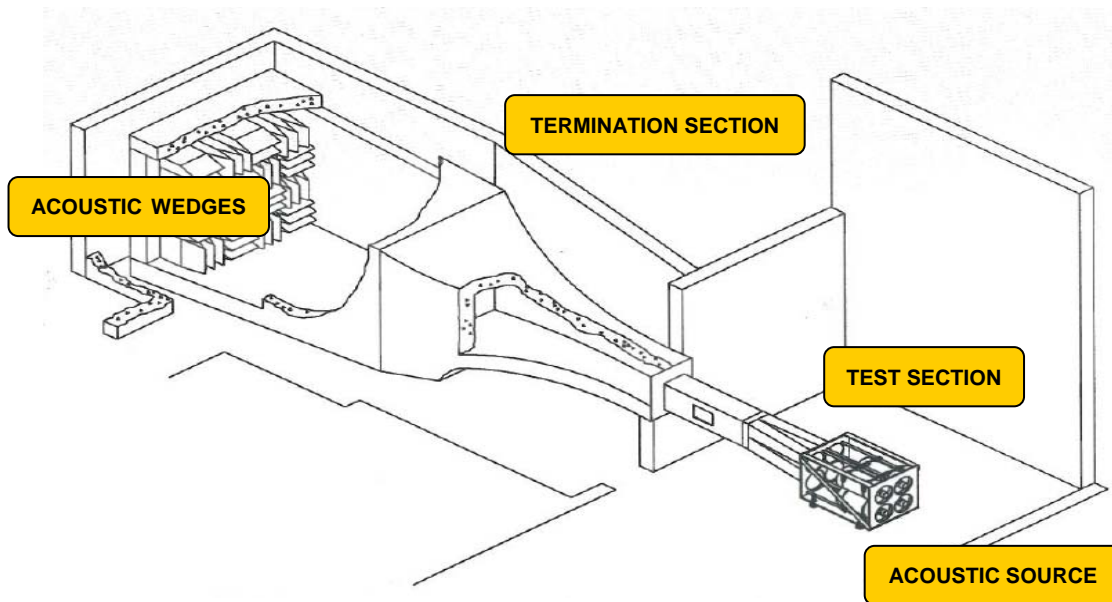


Figure 71. The Sub-Element Acoustic Test Facility

A modal test was performed on the test article before it was positioned in the sidewall of the SEF. The modal test was performed before the duct tape was added. Resonant frequencies, mode shapes and modal damping ratios were identified by exciting the test article with a 0-800 Hz low-level random acoustic signal. The excitation was generated by an acoustic driver with a 1.5-inch diameter tubular horn aimed at the back of the test article. Displacements of the plate were measured at a 7 by 9 rectangular grid (covering a 6-inch by 8-inch area) using a Polytec laser vibrometer. Reflective dots on the plate were used as targets for the laser vibrometer. These dots can be seen in Figure 72. The temperature of the plate and frame were measured with thermocouples and were continuously monitored during the modal test. The temperature difference between the plate and frame ranged from 0.0°F to 0.1°F during the modal test.

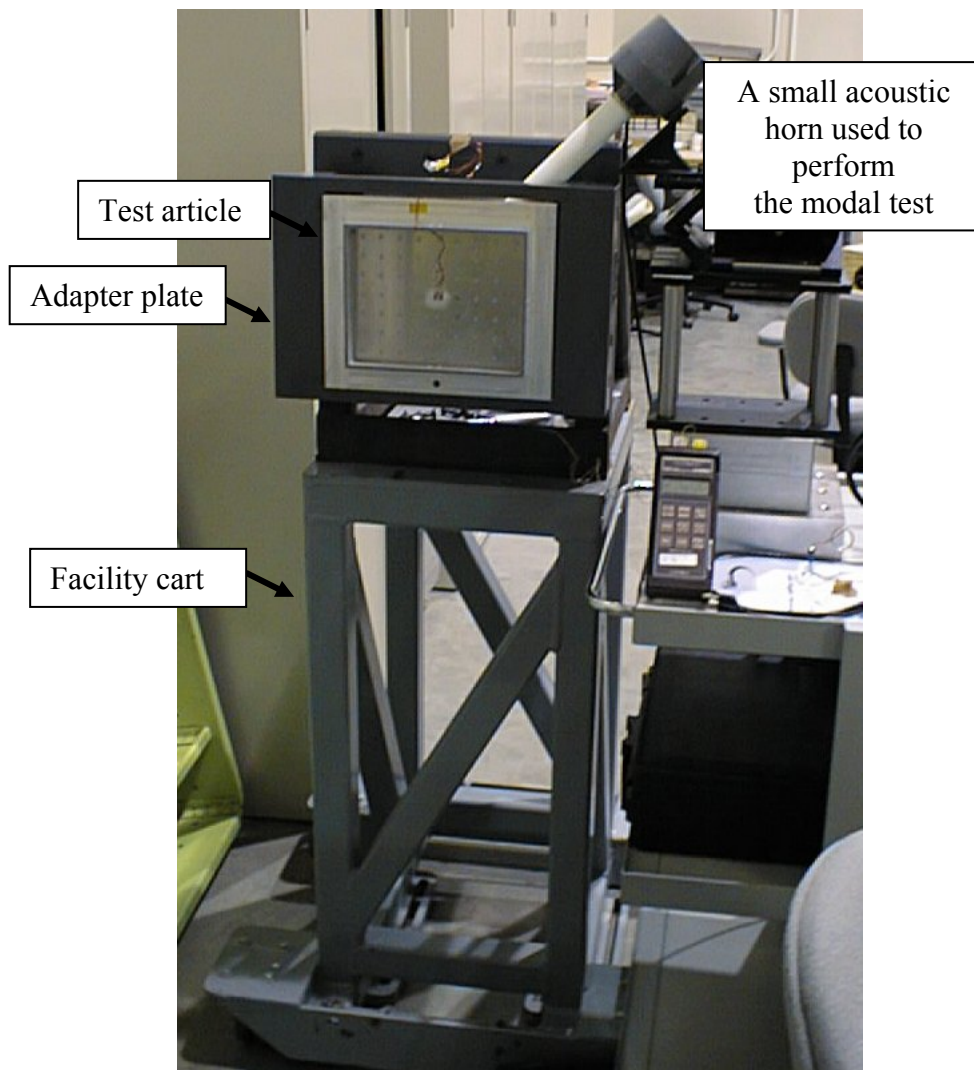


Figure 72. The plate test article mounted on a rigid cart undergoing a modal test.

Frequency response functions were generated from the input signal to the acoustic driver and the measured displacement for each of the 63 measurement points. Modal parameters were identified from the FRF's using in-house software in MATLAB. The identified mode shapes and frequencies are shown in Figure 73. X and Y coordinate directions are also shown in the figure for reference. Frequencies and damping values for the first three symmetric modes of the test article—modes 1, 4, and 7—are given in Table 22. These three modes are the (1,1), (3,1), and (1,3) modes of the plate. (The modal naming convention is (m,n), where m and n denote the number of anti-nodes in the X and Y-directions, respectively.) These three modes were the only symmetric modes in the 75-625 Hz frequency range of interest and thus would be the modes most efficiently excited by the acoustic loading. As shown in the Figure 73, however, these modes were somewhat distorted. The distortion is most likely due to residual stress that occurred during the bonding of the test article. After the modal test was completed, it was decided to add duct tape to seal the gaps. A single input/single output hammer test was performed after the duct tape was added and verified that the tape did not appreciably change the damping or frequencies of the modes.



Table 22. Natural frequencies and modal damping ratios for the target modes

Mode	Modal Test Results		Nominal FEM f (Hz)	Response Peaks at 122dB Loading f (Hz)	FEM with Thermal pre-stress f (Hz)
	f (Hz)	$\zeta$			
(1,1)	115	0.0045	113	105	106
(3,1)	329	0.0040	332	326	320
(1,3)	501	0.0080	499	494	490

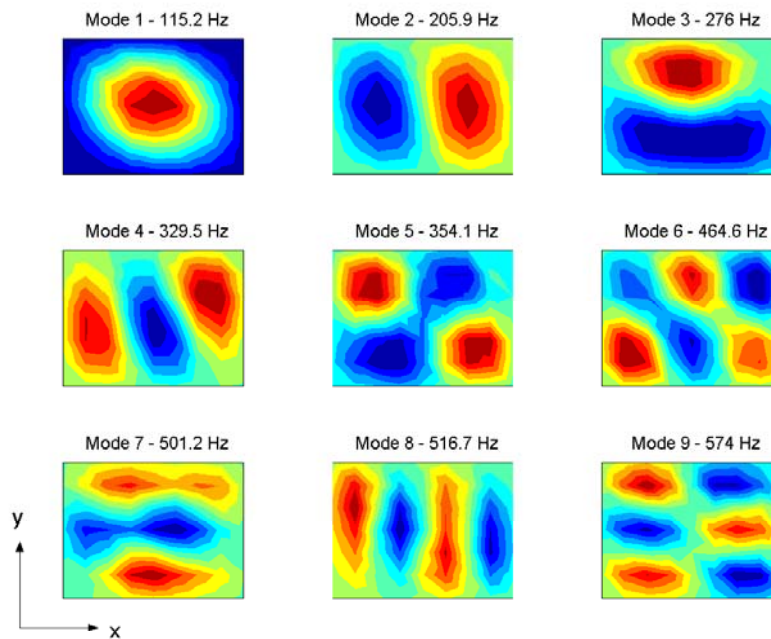


Figure 73. The experimentally measured modes of the test article before mounting in the test facility.

After the modal test, the test article was mounted in the sidewall of the SEF test section as shown in Figure 74. Plane-wave acoustic loading is produced in the SEF test section by compressed air feeding a modified Wyle WAS 3000 air modulator. During testing, one side of the test article was subjected to a controlled, random, acoustic loading traveling in the test article X-direction with grazing incidence. It was desired to have acoustic loading levels that were equivalent to the base excitation levels used in the shaker tests described in Section 4.4.2. Tests were performed with overall sound pressure levels (SPL) of 121.4 dB, 127.6 dB, 133.5 dB, and 139.5 dB. The acoustic load levels were approximately equivalent to root mean square (RMS) base motion levels of 1.8, 3.6, 7.2, and 14.4 g's. Acoustic levels equivalent to 0.45 and 0.9 g's were too low to be generated in the SEF.

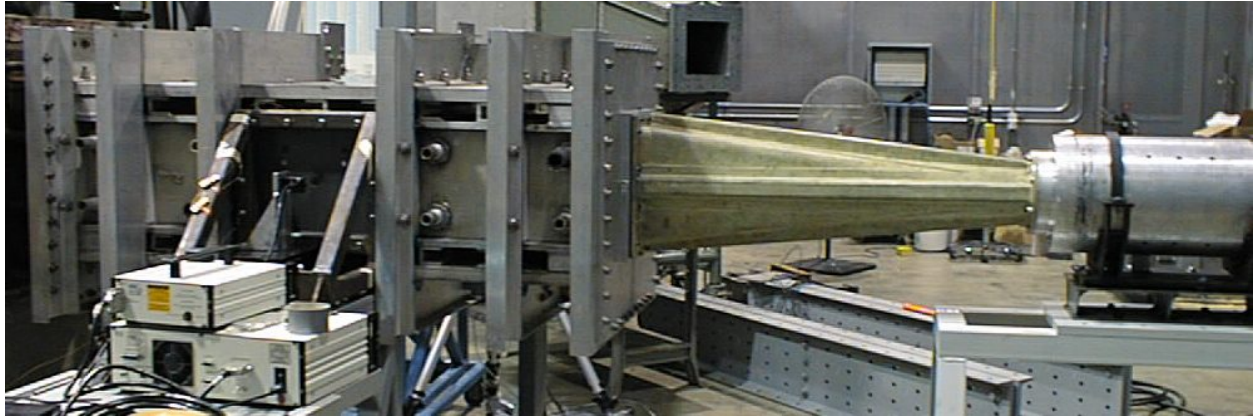


Figure 74. The sub-element facility with the plate test article in place.

The acoustic pressure in the SEF was measured with Kulite flatpack pressure transducers. One pressure transducer was mounted on the center of the floor of the PWT directly in front of the center of the test article. The signal from this pressure transducer was used as the reference signal in a closed-loop control system. The controller modifies the amplitude and frequency content of the random signal sent to the air modulator to achieve a flat 75-625 Hz acoustic spectrum shape at the desired levels. Ideally, the acoustic loading is a plane wave in the SEF test section. So the acoustic pressure should be constant in the cross section. Therefore, the acoustic pressure at the center of the test article was the same as the controlled acoustic pressure. Two additional pressure transducers were mounted on the floor of the test section 18 inches upstream and 18 inches downstream from the reference transducer. These were used to validate that the acoustic pressure was a traveling wave and that a standing wave condition did not exist. A fourth pressure transducer was mounted behind the test article, on the backing plate.

Displacement, velocity, and strain were measured at the center of the plate for each test. Displacement and velocity were measured with a Polytec Model OVF-512 Fiber Optic Vibrometer. A hole in the backing plate was used to access the back of the test article. The laser beam was aimed at a small retro-reflective target at the center of the test article. Dynamic strains were measured with a pair of small resistive strain gages bonded to the plate surface, in the center of the test article. The strain gages were oriented in the X and Y directions. The strain gages and the associated wiring are visible in Figure 72. Strains were not measured at the edges of the plate, where they would have the highest magnitude, because the strain gradient is high near the edge and the measurement is sensitive to location of the gages. Strains at the center of the plate were much less sensitive to gage placement. The temperature of the plate and frame were measured with thermocouples and were continuously monitored during testing. The temperature on the plate was 0.3°F to 0.4°F higher than the frame for all the acoustic tests. This was due to the fact that the air in the SEF test section was somewhat warmer than the ambient air in the SEF room. Data records of the pressures, displacement, velocity, and strains were digitally sampled and stored for 100 seconds at each load level. The data were sampled at 50 kHz and analyzed in MATLAB.

A detailed FEM of the test article was developed in Abaqus. The model explicitly included the plate, frames, adhesive, and flexures. The model used four-node shell elements for the plate and flexures and eight-node solid elements for the frame and adhesive. A 1/4-inch by 1/4-inch mesh



size was used for the plate. The only boundary condition imposed on the model was to fix all degrees-of-freedom (DOF) at the ends of the flexures that attached to the mounting plate. The mass of the strain gages, thermocouples, reflective dots, and wires were not included in the FEM. No thermal loads were applied to the nominal model. The total number of elements in the model was 6536. The 7-inch by 9-inch plate required only 1008 of those elements. Modeling of the plate boundary (the frame, adhesive, etc.) required 84.5% of the total number of elements.

A normal modes analysis was performed on the nominal model. The natural frequencies for (1,1), (3,1), and (1,3) modes are listed in Table 22. The frequencies of these modes differ from the experimental modal frequencies by less than 2%. During the acoustic tests, the frequencies of these modes dropped due to the temperature difference between the plate and frame. The airflow heated the thin plate to a slightly higher temperature than the frame, resulting in a compressive stress in the plate. To account for this effect in the FEM, a temperature load of 0.35 °F was applied to the plate relative to the frame. A normal modes analysis of this FEM produced modal frequencies slightly lower than the nominal model. These frequencies are also listed in Table 22. Since a modal test could not be conducted in the SEF, the response peaks at the lowest level acoustic test are used as approximate modal frequencies. The modal frequencies of the thermally loaded FEM differ from the response peak frequencies by less than 2%. The thermally loaded model was used to compute the nonlinear ROM, and will be referred to as the FEM here.

The first step in constructing the ROM's was to decide on the modes to retain in the model. For the present study, the (1,1), (3,1) and (1,3) modes were retained. These are the symmetric modes in the range of interest. When the acoustic pressure is uniform and in-phase across the plate, these are the only modes that can be directly excited. Since the acoustic excitation was a traveling wave, anti-symmetric modes could also be directly excited. Of primary concern was whether to include the (2,1) mode (mode 2 in Figure 73). This mode appears at approximately 200 Hz. Traveling wave conditions existed in the SEF, but the length of the test article was a small fraction of the wave length of sound at 200 Hz. Therefore, traveling waves were approximately in-phase at this frequency across the test article, and direct excitation of the (2,1) mode should have been small. Indirect excitation through nonlinear coupling was also a possibility. However, for a perfectly flat plate, coupling between symmetric and anti-symmetric modes is small. For these reasons, the (2,1) mode was not included in the ROM.

Reduced-order models were generated from the finite-element model using the ICE method implemented in MATLAB. Abaqus was used to generate the static nonlinear finite element results. The ROM had three nonlinear differential equations, one for each of the three modes of interest. There were nine nonlinear stiffness terms in each equation. The damping terms in the ROM were initially set to the measured viscous damping values listed in Table 22. Time integration was performed using the Newmark beta method. Time histories were generated for each of the acoustic levels. Each time history was a digital record 100 seconds long with a step size of 0.00002 seconds. Generation of each time history required approximately 10 minutes of CPU time on a personal computer with a 2.8 GHz processor. Physical displacements were recovered using the expansion procedure described in Section 3. Strains were computed for a single plate element at the center of the plate, given the displacements at the four nodes of that element. The strain recovery was implemented in MATLAB.

Test results are presented and compared with predictions in the following paragraphs. Some adjustments were made to the ROM's in order to capture the physics of the experimental data. These will be described as the comparisons are made.

The first set of predictions used the three-mode ROM with measured modal damping values. The input to the model was a numerically-generated random signal with the same flat spectrum of 75-625 Hz used in the test. This signal was scaled to correspond to the experimental acoustic levels. The input was applied to the model assuming an in-phase uniform spatial distribution. That is, the traveling wave condition was not applied to the model. The prediction of center displacement is shown in comparison to the experimental results in Figure 75 for the 133.5 dB level. This level is equivalent to the 7.2 g case reported for the shaker test in Section 4.4.2. The (1,1) mode peak in Figure 75 is much broader and is shifted higher in frequency than the experimental data. This type of behavior usually indicates that the nonlinearity in the model is too large. Additionally, the experimental data has a second peak near 200 Hz suggesting that the (2,1) mode may be responding. But the (2,1) mode should be unobservable in the center of the plate. Several modifications were made to the ROM to capture this effect. These included adding the (2,1) mode, skewing the mode shapes by adding static deformation to the FEM, using traveling wave excitation, and adding quadratic stiffness terms to the model. None of these modifications resulted in significant response of the (2,1) mode at the center of the plate.

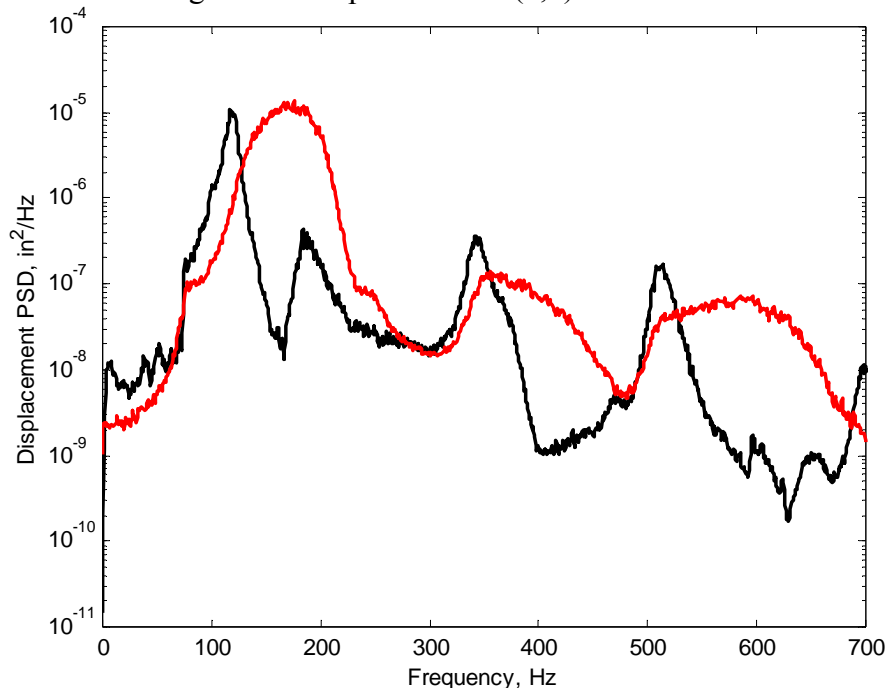


Figure 75. Measured center displacement PSD (—) compared to the model prediction using a flat input spectrum (—), both at 133.5 dB SPL.

Next, the measured acoustic pressure behind the test article was examined. Figure 76 shows the measured pressure in front of and behind the test article for the 133.5 dB case. At some frequencies, the spectrum level behind the test article is actually higher than in front of the article! Apparently, the acoustic pressure transmitted by the vibrating test article is being reinforced. (Note that a hard surface, the backing plate, is three inches behind the test article.) So the test article is actually subjected to an acoustic load on both the front and rear surfaces. As

a result, the differential pressure was calculated for each loading as the difference between the front and rear pressure time histories. The PSD of the differential pressure for the 133.5 dB case is shown in Figure 77. In this figure, two peaks in the input are revealed as well as an apparent zero at 166 Hz.

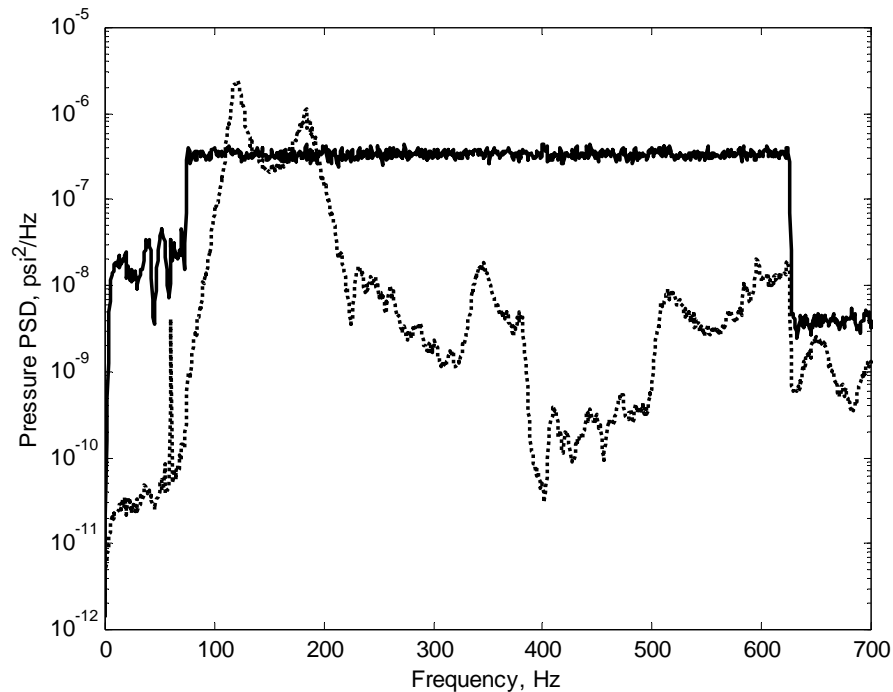


Figure 76. The measured pressure PSDs in front of the test article (—) and behind the test article (---) for the 133.5 dB SPL test.

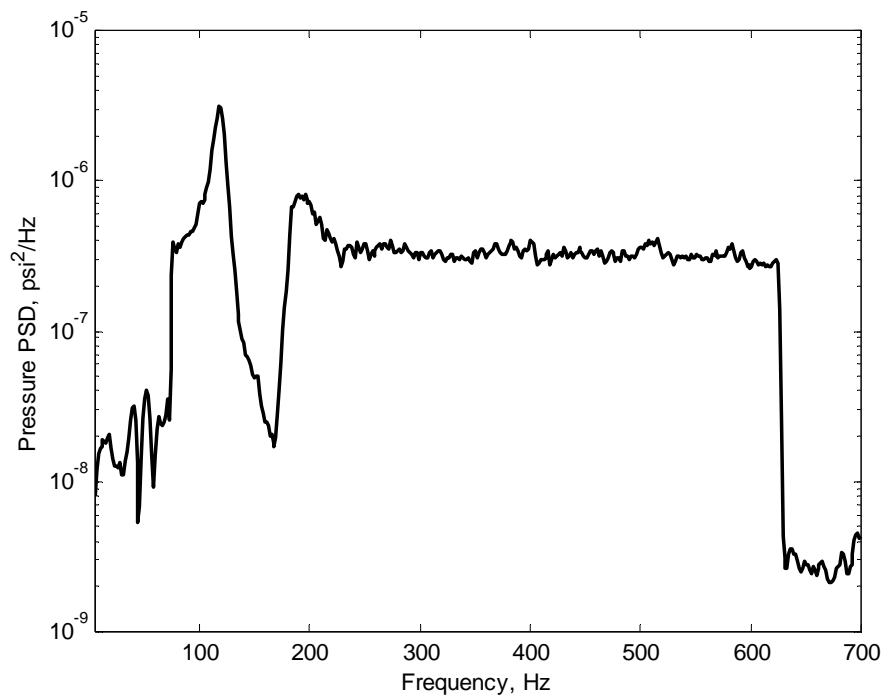


Figure 77. The PSD of the differential pressure for the 133.5 dB SPL test.

In the next set of predictions, the differential acoustic loading was applied to the three-mode ROM with measured modal damping. During the test, the pressure in front of the test article was a traveling wave, while the pressure behind the test article was not. This complicated loading pattern could have been simulated with the models, but a uniform in-phase differential pressure loading was used instead for simplicity. The computed differential pressure time histories were used directly as the loading in the integration of the model. The predictions of the center displacement for the 121.7 dB and 133.5 dB cases are shown in Figure 78 in comparison to test results. The prediction at 121.7 dB is very good indicating that a fourth mode was not needed to capture the peak around 200 Hz. The apparent zero in the input PSD causes the second response peak. It also keeps the first mode response from behaving nonlinearly. At 133.5 dB, the prediction is also much improved. The nonlinearity in the ROM seems to overcome the influence of the zero as the first mode peak is seen to shift and broaden in the classic nonlinear fashion.

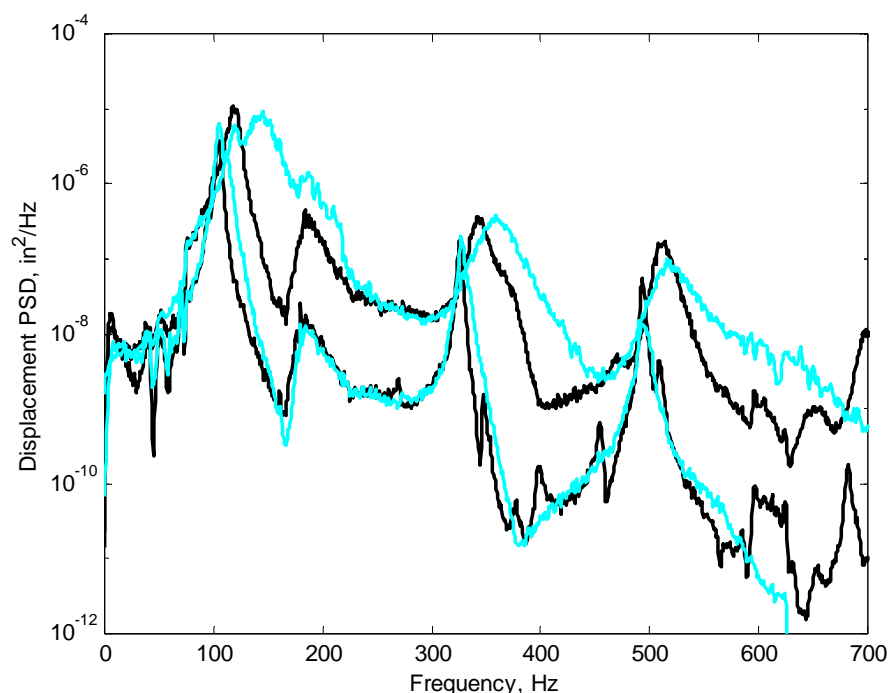


Figure 78. Measured center displacement PSD(—) compared to the model prediction using the measured differential pressure (—) and nominal viscous damping for the 121.7 and 133.5 dB SPL test levels.

In an attempt to further improve the predictions, the damping for the (1,1) mode was increased while still using the differential acoustic pressure. Figure 79 shows the predicted center displacement PSD from the model as the damping in the first mode is increased to 4% and 5%. The predictions are for the 139.5 dB case and are shown in comparison to the test results. The model with 5% damping shows good qualitative agreement with the PSD of the test data at the two resonant peaks. Displacement predictions using 5% damping are shown in Figure 80 for the 121.7 dB and the 133.5 dB cases. The predictions agree very well with the experimental data. Predictions of the strains in the X-direction and Y-direction are shown in Figures 81-82 in comparison to test data. The good agreement with the strains confirmed that the membrane expansion/strain recovery part of the ICE method worked well.

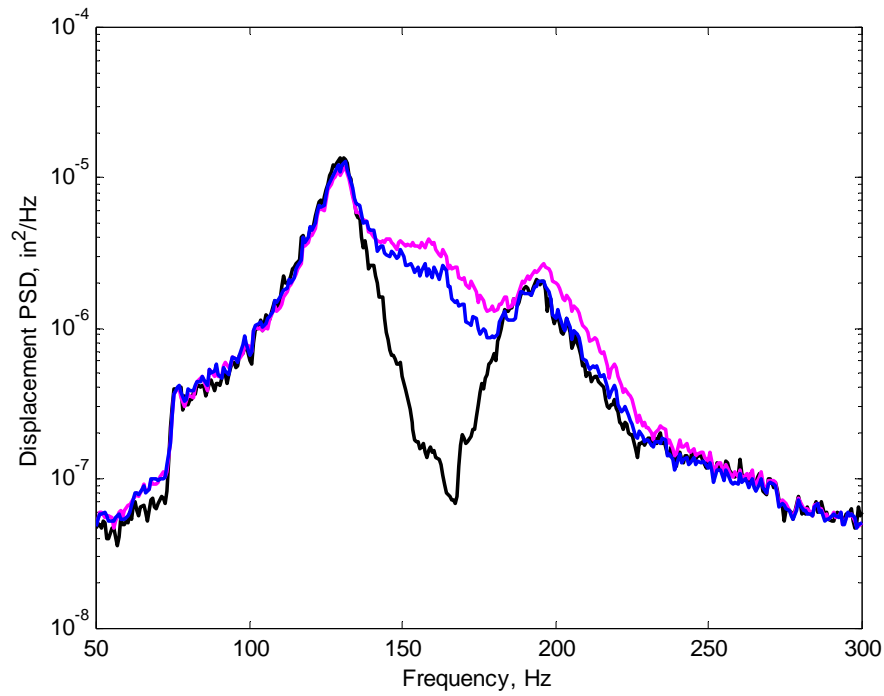


Figure 79. Measured center displacement PSD (—) for the 139.5 dB SPL test level compared to the model prediction using the measured differential pressure and damping values of  $\zeta_1=0.04$  (—), and  $\zeta_1=0.05$  (—).

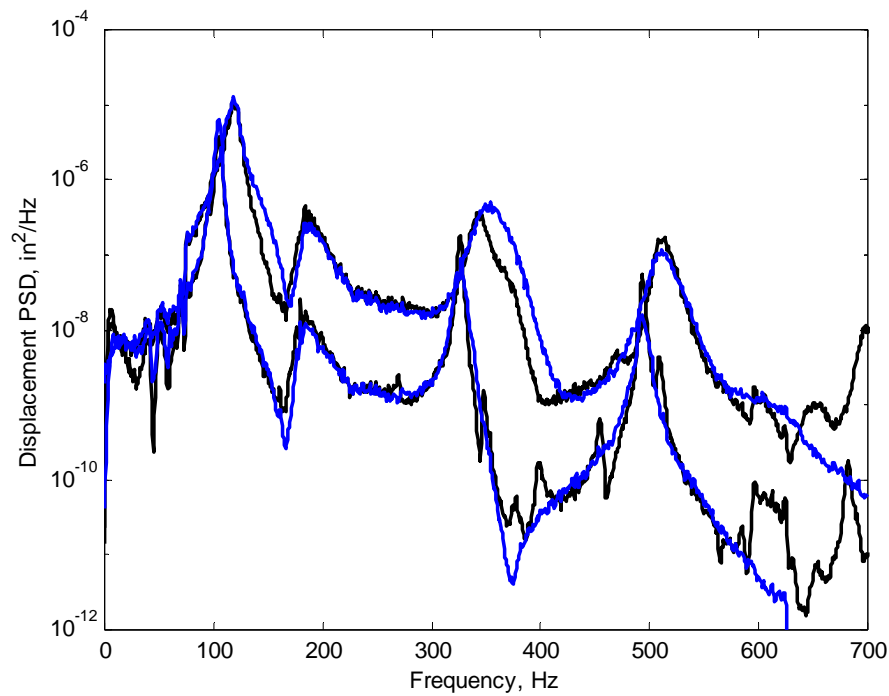


Figure 80. Measured center displacement PSD (—) compared to the model prediction using the measured differential pressure and  $\zeta_1=0.05$  (—), for the 121.7 and 133.5 dB SPL test levels.

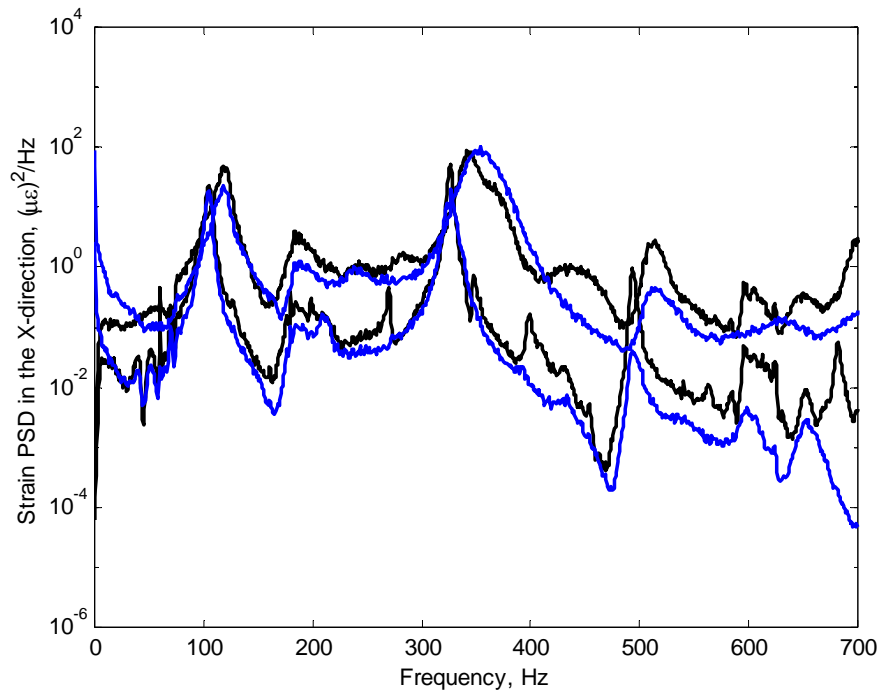


Figure 81. Measured strain PSD in the X-direction at the center (—) compared to the model prediction using the measured differential pressure and  $\zeta_1=0.05$  (—), for the 121.7 and 133.5 dB SPL test levels.

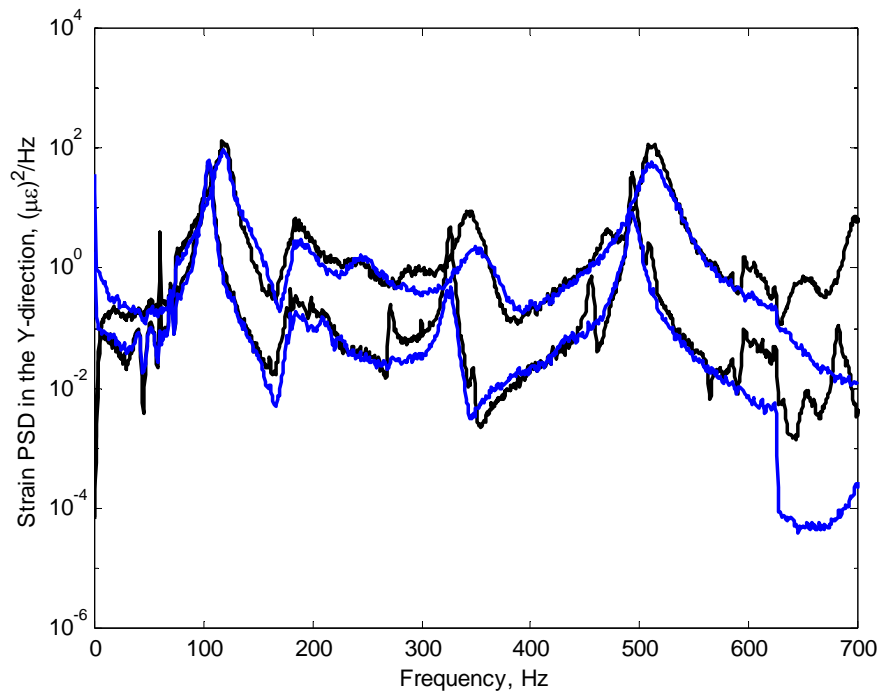


Figure 82. Measured strain PSD in the Y-direction at the center (—) compared to the model prediction using the measured differential pressure and  $\zeta_1=0.05$  (—), for the 121.7 and 133.5 dB SPL test levels.

The next set of predictions evaluated the effect of nonlinear damping on the predicted response. In the shaker test described in Section 4.4.2, nonlinear velocity squared damping terms were added to the ROM to achieve better agreement with the response of the same test article to base excitation. In that study, a single viscous damping value did not give optimal agreement at all the test levels. To evaluate nonlinear damping in the present study, a velocity squared damping term was added to the first mode equation in the model in addition to the nominal measured modal damping. Figure 83 shows the response to the differential input for the 139.5 dB case for values of the nonlinear damping coefficient of 100 and 200. The PSD for the model with a coefficient of 200 is seen to agree very well with the test data, except in the valley between the lowest two peaks. In fact, the PSD for the coefficient of 200 is nearly identical to the PSD for the model with 5% viscous damping.

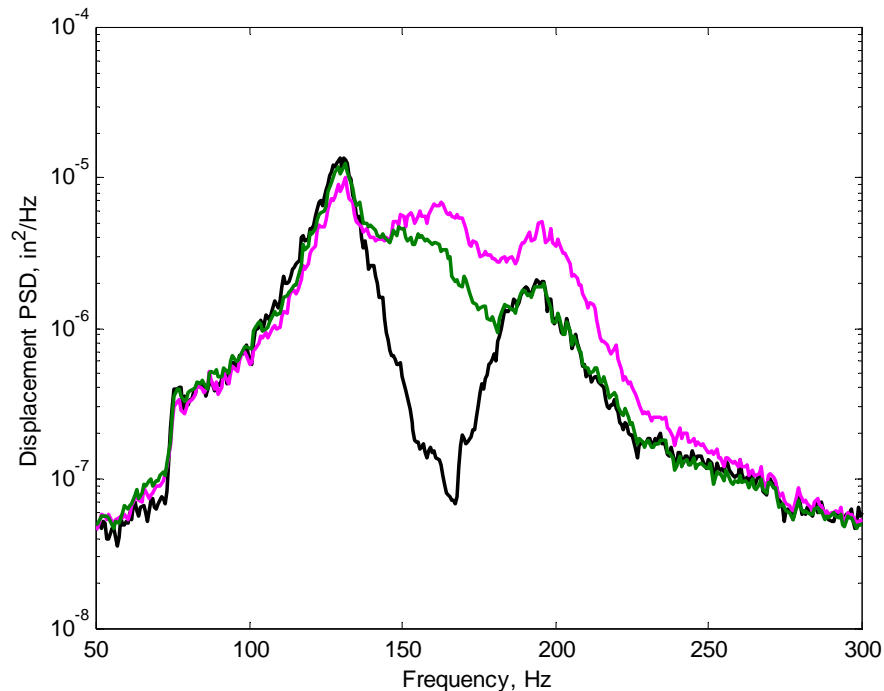


Figure 83 Measured center displacement PSD (—) compared to the prediction using the differential pressure and velocity squared damping values of 100 (—) and 200 (—) for the 1st mode, for the 139.5 dB SPL test level.

The overall effects of the different values of input force and damping are shown in Figures 84-87 for input levels of 121.7, 127.4, 133.5 and 139.5 dB, respectively. If the acoustic pressure behind the test article is neglected and only the front pressure is simulated, the predictions do not compare well with the test data. If differential pressure is used, and the model uses nominal damping values, the predicted PSD agrees well at the lowest input level but becomes progressively worse as the level is increased. Eventually at 139.5 dB, the nominally damped model gives virtually the same prediction whether the pressure behind the test article is included or is neglected. If the damping is significantly increased, either by linear or nonlinear terms, and differential pressure is used, the model predicts the experimental response very well at the lowest three levels and reasonably well at the highest level.

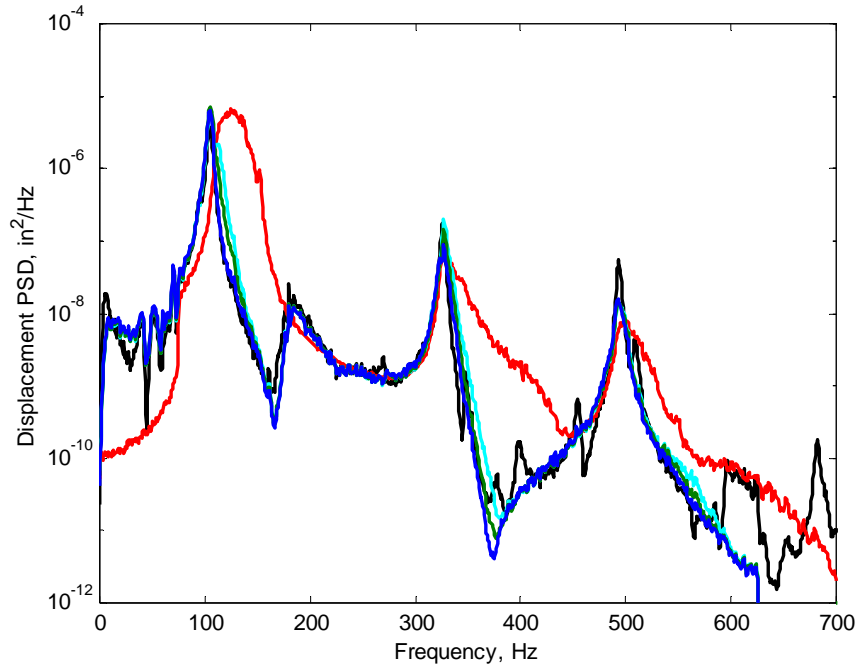


Figure 84. Measured center displacement PSD at 121.7 dB (—) compared to the prediction using: a flat input spectrum and nominal damping (—), differential pressure and nominal damping (—), differential pressure and  $\zeta_1=0.05$  (—), and differential pressure and velocity squared damping in the 1st mode (—).

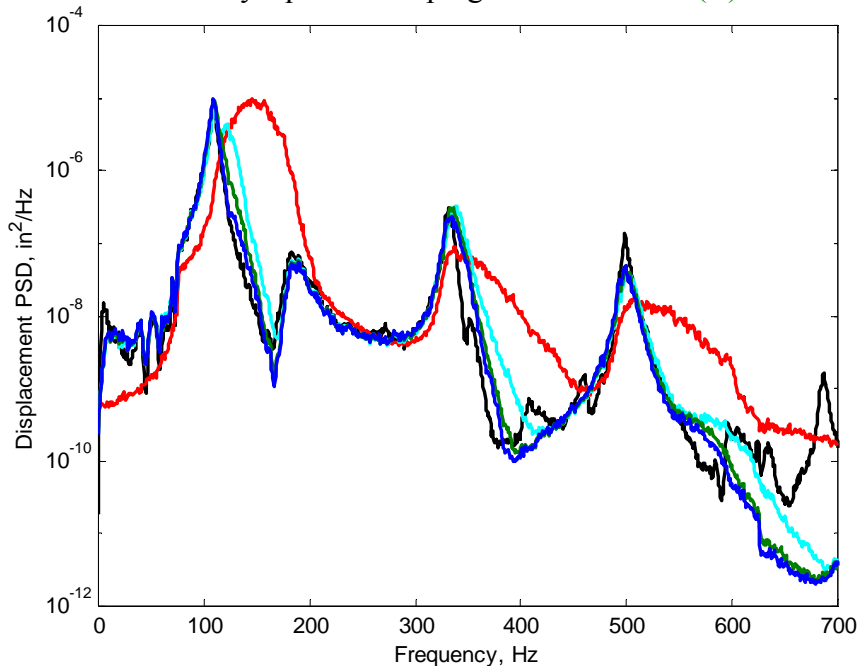


Figure 85. Measured center displacement PSD at 127.4 dB (—) compared to the prediction using: a flat input spectrum and nominal damping (—), differential pressure and nominal damping (—), differential pressure and  $\zeta_1=0.05$  (—), and differential pressure and velocity squared damping in the 1st mode (—).



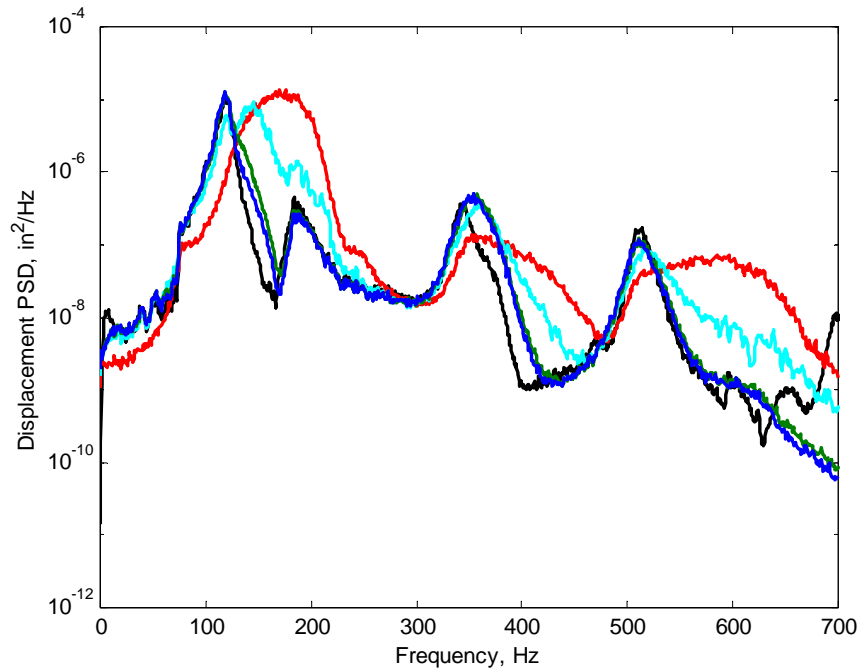


Figure 86. Measured center displacement PSD at 133.5 dB (—) compared to the prediction using: a flat input spectrum and nominal damping (—), differential pressure and nominal damping (—), differential pressure and  $\zeta_1=0.05$  (—), and differential pressure and velocity squared damping in the 1st mode (—).

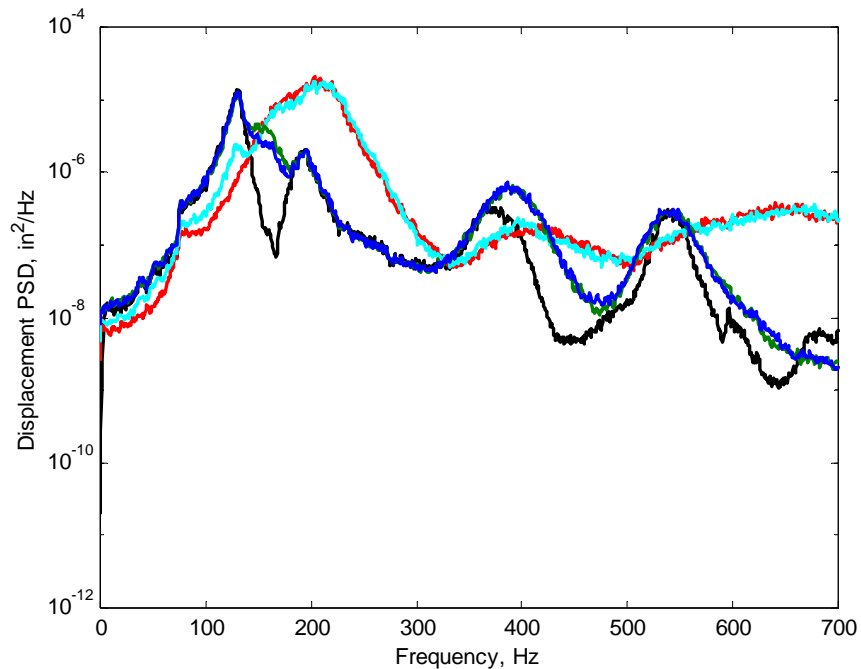


Figure 87. Measured center displacement PSD at 139.5 dB (—) compared to the prediction using: a flat input spectrum and nominal damping (—), differential pressure and nominal damping (—), differential pressure and  $\zeta_1=0.05$  (—), and differential pressure and velocity squared damping in the 1st mode (—).

The ROM accurately predicted the test article response if two adjustments were made. First, the acoustic load applied to the model had to include the pressure behind the test article. A pressure differential was calculated from the measurements and used as the input to the model. The second adjustment was an increase in the damping of the first mode. Predictions using the nominal damping were inadequate at the higher acoustic levels. The viscous damping in the first mode was increased from the nominal value of 0.45% to 5% of critical. Models with the higher damping value predicted the response of the test article very well at all acoustic levels. Models with a nonlinear velocity squared damping term in the first mode were also tried. These also provided good predictions at all acoustic levels.

The two adjustments were necessary to capture the physics of the experiments and did not require modification of the ICE method. The inclusion of the pressure behind the test article was an adjustment to the mechanical force applied to the model. In sonic fatigue testing, typically only the pressure in front of a test article is specified and controlled. The acoustic pressure behind the test article is typically not specified or measured. Clearly, for the tests presented here, the pressure behind the test article is significant. The differential pressure concept is easily incorporated into the model if the pressures are measured. Prediction of the response without knowledge of the rear pressure is more problematic—potentially requiring a coupled structural-fluid model. The presence of the reflecting surface of the backing plate three inches behind the test plate was likely a contributing factor to this anomaly. The second adjustment was a significant increase in the damping of the first mode. Damping is a convenient way to model attenuation by some mechanism. The apparent attenuation could have been due to a transfer of energy to un-modeled modes due to nonlinearity. The presence of the second peak in the pressure behind the test article may be evidence of energy transfer to the (2,1) mode. Energy could have been transferred and not observed in the displacement or strain measurements. Reduced-order models that included the (2,1) mode were investigated, but an attenuation in the response of the (1,1) mode could not be duplicated. Another possibility for the attenuation could be the transfer of energy to acoustic radiation. However, it is not likely that acoustic radiation produced a damping value of 5%. More study on this issue is necessary.

Another possible source of error in the predictions was that the differential acoustic loading was an approximation. The acoustic pressure was not measured directly on the surface on either side of the plate. The measurement in front of the test article may have been in error due to the radiation of sound by the test article as it vibrated. Sound radiated from the test article propagates in a direction normal to the direction of the progressive wave, violating the assumption of a constant pressure in the cross section of the PWT. The measured pressure would not be the same as the pressure directly in front of the test article. The acoustic pressure could have also varied significantly in the cavity behind the article. Even if both measured pressures were valid, one acoustic field is a traveling wave, the other is not. The use of a differential pressure is only an approximation of these loading conditions.

Finally, the relatively light damping in the test article may have contributed to the differences between predicted response and test results. The first mode damping ratio of 0.0045 is at least a factor of 2 lower than damping values seen in typical aircraft structures. The low damping value resulted in higher resonant amplification which probably contributed to the high acoustic levels

measured behind the test article. A viscoelastic constrained layer damping treatment could be used to increase the plate damping values into a more typical range, as was done in Section 4.4.2 for the shaker test.

#### **4.4.6 Acoustic Test of the Clamped Plate with an Improved Fixture**

This section describes a second test of the clamped plate test article in the acoustic progressive wave facility. The initial acoustic test, as described in Section 4.4.5 above, resulted in only fair agreement of a nonlinear ROM's with test results. The second test was performed with additional instrumentation and an improved test fixture which eliminated an enclosed area behind the test article. This work was originally published as Reference [18].

The apparent coupling of the acoustic field with the response of the structure in the previous experiments suggests that the models lacked relevant physics. Specifically, the models did not model the air surrounding the test article. That is, the ROM's were estimated from finite-element models that were purely structural. Inclusion of the acoustic medium in the physical model is a computationally expensive proposition. At the time, the authors were not aware of any studies in which a ROM incorporates both structural nonlinearity and the acoustic medium. In this paper, results from a second set of acoustic experiments are presented in an effort to answer whether the acoustic medium should be modeled.

In retrospect, the acoustic test and ROM reported for the initial acoustic test had significant flaws. First, the test article was mounted in the acoustic progressive wave facility in such a way that a semi-enclosed cavity existed behind it. This cavity resulted in an acoustic resonance that appeared as a resonant peak in the power spectral density (PSD) of the displacement of the test article. In addition, it was assumed that the acoustic pressures in the facility duct would not be affected by the test article. As a result, pressure measurements were taken only at the bottom of the duct and not near the surface of the test article. Finally, modal damping values used in the ROM of the test article were measured before the test article was installed in the duct rather than after it was installed. The study presented here was conducted to correct these flaws and provide a more valid comparison between the model and experimental results.

The test article configuration used in the initial acoustic test is shown in Figures 43 and 72. A thick mounting plate was located directly behind the test article. With the test article and mounting plate installed in the test facility, a semi-enclosed cavity was formed behind the test article. This created a Helmholtz resonator which was acoustically coupled to the test article. In the current experiment, the mounting plate was redesigned as a larger plate with a cut-out directly behind the test article. This configuration is shown in Figure 88. The test article was mounted in the SEF with an adapter plate similar to that used in the initial test (see Figure 72).

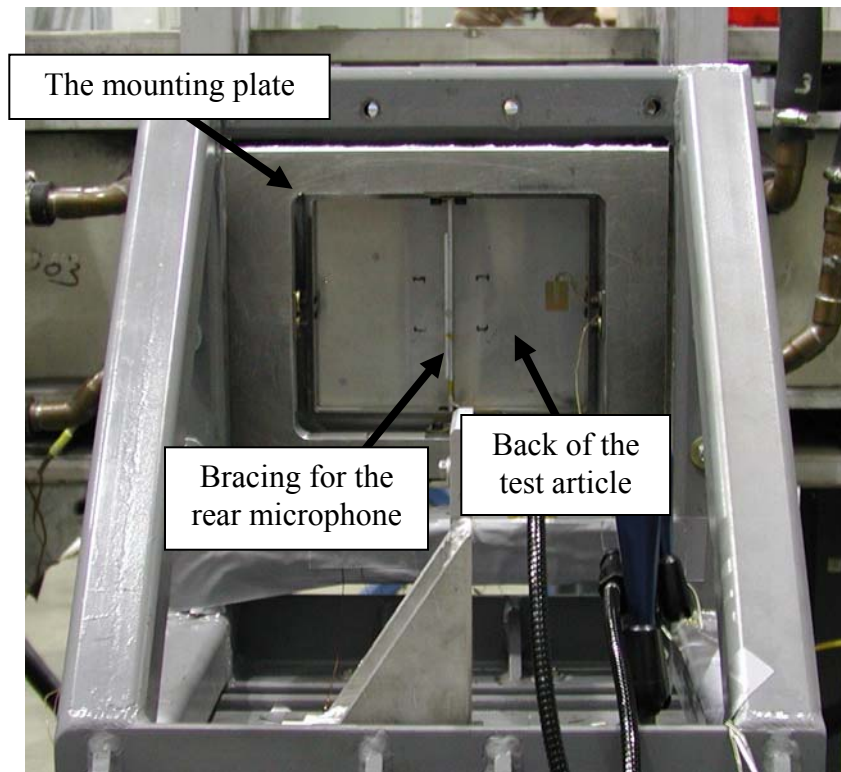


Figure 88. The test article on a facility cart using a mounting plate with a rectangular cutout.

A modal test was performed on the test article before it was installed in the SEF. Resonant frequencies, mode shapes and modal damping ratios were identified by exciting the test article with a 0-800 Hz low-level random acoustic signal. The excitation was generated by an acoustic driver with a 1.5-inch diameter tubular horn aimed at the back of the test article. Displacements of the plate were measured on a 7 by 9 rectangular grid (covering a 6-inch by 8-inch area) using a Polytec laser vibrometer. Retro-reflective dots were used as targets for the laser vibrometer. The temperature of the plate and frame were measured with thermocouples and were continuously monitored during the modal test. The temperature difference between the plate and frame ranged from 0.0°F to 0.1°F during the modal test. Frequency response functions were generated from the input signal to the acoustic driver and the measured displacement for each of the measurement points. Modal parameters were identified from the FRF's. The identified mode shapes are shown in Figure 89. The coordinate directions are also shown in Figure 89 for reference. The naming convention for the mode shapes is (m,n), where m and n denote the number of anti-nodes in the x and y-directions, respectively.

There were three symmetric modes in the 75-625 Hz frequency range of interest. These were the (1,1), (3,1), and (1,3) modes. If the acoustic loading was spatially uniform (i.e. the pressure did not vary across the test article), only these three modes would be directly excited. Ideally, the progressive-wave facility produces planar waves that have a grazing incidence with the test article. Thus, the acoustic loading is a traveling wave in the x-direction. The (2,1), (4,1), and (2,3) modes should be excited by the traveling wave along with the three symmetric modes.

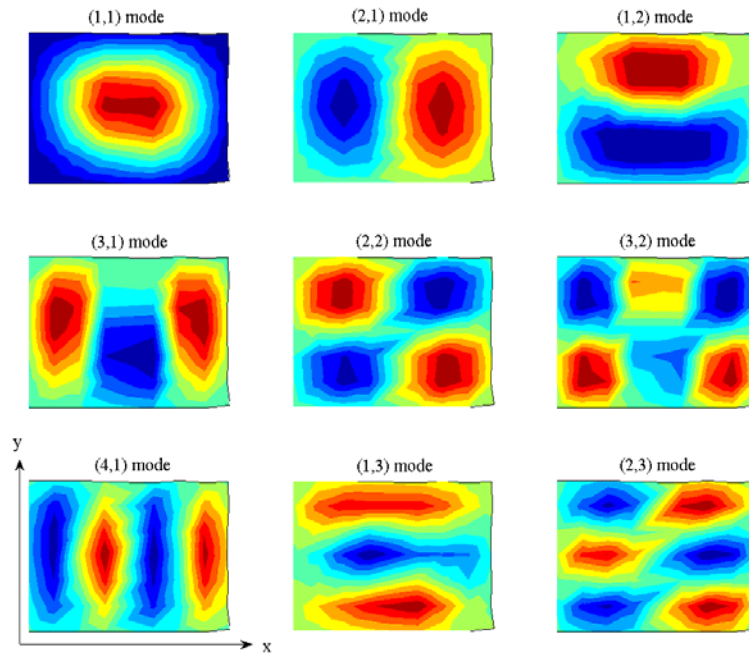


Figure 89. Experimental measured mode shapes of the plate area of the test article.

When installed in the acoustic facility, the surface of the test article was flush with the sidewall of the progressive wave facility. A photograph of the facility with the test article installed is shown in Figure 90. The configuration of the SEF was the same as that used in the initial test. A single-input single-output feedback controller was used with a reference microphone to control the input to the modulator to produce a random, normally distributed, spectrally controlled, sound pressure. The plate was excited with a random acoustic signal in a 75-625 Hz band with overall sound pressure levels (SPL) of 122, 128, 134, and 140 dB at the reference microphone.

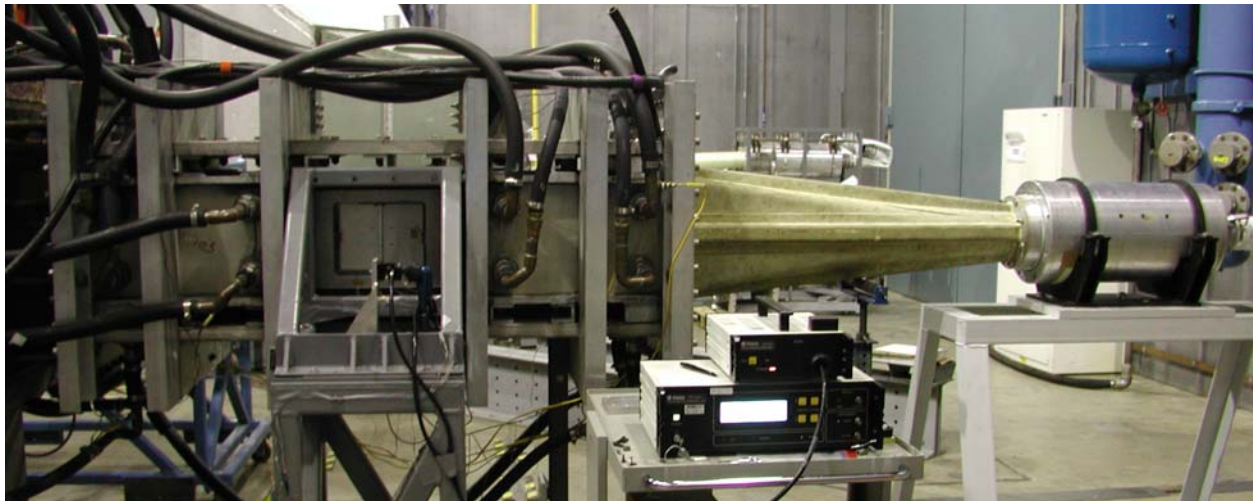


Figure 90. The progressive-wave facility with the test article installed.

The photograph in Figure 90 shows the rear of the test article. The wave propagation direction for the traveling wave is from right to left in the photograph. The propagation direction for the mode shapes shown in Figure 89 is the opposite, from left-to-right (i.e. the positive  $x$ -direction) since these mode shapes were measured on the front of the test article.

Acoustic pressure was measured at five locations in this series of tests. Kulite LQ-125-5SG pressure transducers (microphones) were used. The reference microphone was centered on the floor of the duct located directly in front of the center of the test article. This microphone was six inches below and six inches in front of the center of the test article. A second microphone was installed on the floor of the duct 18 inches upstream from the reference microphone. The third microphone was installed behind the test article, on the cutout of the mounting plate. That microphone was 3.5 inches behind the test article, 2.5 inches downstream from the center of the test article. Two additional microphones were used in this study. One measured the pressure 0.5 inches in front of the center of the test article and another measured the pressure 0.5 inches behind it. Ideally, the two additional microphones could have been located on the test article. However, since the plate vibrates during the experiment and the microphones were sensitive to axial vibration, it was decided to mount the additional microphones on added bracing. The bracing on each side consisted of two aluminum beams bonded together with ISD-112 viscoelastic adhesive. The viscoelastic material provided damping to reduce vibration of the bracing. The bracing was bonded to the frame of the test article with epoxy. The bracing for the rear microphone is shown in Figure 88. The microphones were mounted on bracing so that they faced toward the test article. The bracing for the microphones was installed before any of the modal tests.

Displacements, velocities, and strains at selected locations on the test article were measured for all tests. Displacement and velocity were measured at a point near the center of the plate with a Polytec Model PSV-400 Vibrometer. The point was centered on the plate in the  $y$ -direction and was a quarter of an inch downstream from the center. Displacement and velocity were measured at a second point with a Polytec Model OVF-512 Fiber Optic Vibrometer. This point was 2.25 inches downstream from the upstream edge of the plate area and 1.5 inches above the lower edge of the plate area. Dynamic strains were measured with a pair of small resistive strain gages bonded to the center of the test article. The strain gages were oriented in the  $x$  and  $y$ -directions. The temperature of the plate area and the frame were measured with thermocouples and were continuously monitored during testing. The temperature of the plate area was 0.1°F to 0.3°F higher than the frame for all the acoustic tests. This was due to the fact that the air in the test section was somewhat warmer than the ambient air. Data records of the pressures, displacements, velocities, and strains were digitally sampled and stored for 100 seconds at each test level. The data were sampled at 50 kHz.

Two modal tests were conducted to measure the influence of the acoustic characteristics in the duct on the damping of the test article. A single-input single-output impact hammer modal test was conducted immediately before the test article was installed into the facility sidewall. A second impact hammer modal test was conducted immediately after installation. The estimated frequency and damping factors for the two tests are given in Table 23. There were no physical changes in the mounting of the test article between the un-installed and the installed tests. The cart was simply rolled into place. The only difference was the boundary condition due to the

acoustical field in the duct. Installation significantly affected the damping of several modes. The most significant effect occurred for the (1,1) mode, where the damping increased from roughly a quarter of a percent to almost two percent of critical! This large a change in modal damping would have a very significant effect on the response. The effect of acoustic baffling on radiation damping was one likely cause of the observed damping increase. The influence of the duct acoustics also reduced the frequency of the (1,1) mode by nearly 3 Hz and increased the frequency of the (3,1) mode by 2.5 Hz.

Table 23. Natural frequencies and modal damping ratios.

Mode	Un-installed		Installed		FEM f (Hz)
	f (Hz)	$\zeta$	f (Hz)	$\zeta$	
(1,1)	119.7	0.0024	117.0	0.019	113.4
(2,1)	199.7	0.0024	198.8	0.0027	195.7
(1,2)	286.5	0.0032	285.9	0.0054	264.5
(3,1)	322.6	0.0061	325.1	0.011	331.6
(2,2)	354.7	0.0027	354.2	0.0027	340.0
(3,2)	466.1	0.0033	465.4	0.0030	468.6
(4,1)	498.5	0.0038	497.3	0.010	519.2
(1,3)	512.5	0.0075	512.7	0.0054	498.6
(2,3)	581.1	0.0067	579.5	0.0055	571.0

Two nonlinear ROM's of the plate test article were computed. A three-mode model was built retaining the (1,1), (3,1) and (1,3) modes—the three lowest symmetric modes. The acoustic excitation should be a plane wave with grazing incidence. The pressure appears on the plate as a random amplitude wave traveling in the  $x$ -direction. The traveling wave can directly excite the three symmetric modes. In addition the traveling wave can directly excite modes that are anti-symmetric in the  $x$ -direction and symmetric in the  $y$ -direction. A six-mode model was built retaining the (2,1), (4,1), and (2,3) modes, as well as, the (1,1), (3,1), and (1,3) modes. The ROM's were generated from the finite-element model using the ICE method implemented in MATLAB. The nonlinear static solutions, used to construct the ROM's, were performed in Abaqus. The three-mode model had three nonlinear differential equations. There were nine nonlinear stiffness terms in each equation. The six-mode model had six equations with 36 nonlinear stiffness terms in each equation.

The experimentally measured frequencies were used in the ROM's as opposed to the FEM frequencies that were used in the initial test. The change of frequencies would be difficult to do in a full FEM but was easily accomplished in the ROM. The experimentally measured damping was also used in the ROM's. This model updating was done to remove minor tuning issues from the comparison, so that the major issues of structural-acoustic coupling could be focused on. Two sets of measured frequency and damping were recorded (listed in Table 23) both sets will be explored when comparing predictions to experimental data.

The next consideration is the modeling of the excitation. The acoustic excitation enters the model only as an acoustic pressure that is modeled as an external force. The excitation can be modeled as either uniform or traveling. The uniform pressure is often considered simply because it is easier to model. In the uniform case, the loading is simulated as a spatially uniform pressure. The amplitude of the pressure varies in time. The grazing incident wave in the progressive wave tube is a traveling wave. In the traveling wave case, the pressure amplitude varies in time, is spatially uniform in  $y$ -direction, but varies in  $x$ -direction based upon the speed of the traveling wave. The scheme for simulating the traveling wave was adopted from Reference [11]. The measured time history of the excitation was used as the amplitude of either forcing scheme (more on this, will be discussed later). Time integration was performed using the Newmark beta method. Time histories were generated for each of the acoustic levels. Each time history was a digital record 100 seconds long with a step size of 0.00002 seconds.

The response will be examined using the displacement at the two measurement points. The first measurement point was 0.25 inches from the center of the panel. For convenience, the point will be referred to as the center location. The response at this measurement point will be dominated by the three symmetric modes. The other measurement location will be referred to as the off-center location.

Although data was experimentally acquired for four sound levels, for brevity only the data for the highest and the lowest levels will be presented. The lowest level at 122 dB is the closest to linear response. Predicted response at this level should be dominated by linear parameters such as the natural frequencies and the damping values. The highest excitation level at 140 dB is highly nonlinear. At this level, the nonlinear stiffness effects should dominate the response.

The first response prediction case is the three-mode model with uniform pressure. The measured reference pressure time history is used as the excitation to this model. The un-installed frequency and damping parameters are used in the model. Figures 91-92 show predicted displacement PSD's in comparison to test data for the two measurement locations. The predictions exhibit much more nonlinearity than the experimental data. The predicted peaks show too much nonlinear broadening. This is particularly true for the first mode. It is also evident from the off-center displacement in Figure 92 that more than three modes are excited.

Three changes were made to the model to improve the prediction. First, the six-mode ROM was used instead of the three-mode ROM. The additional three modes can not be excited by the uniform pressure. Therefore, the second change is that the excitation is modeled as a traveling wave. The third change is to increase the damping by using the installed damping parameters. The nonlinear broadening shown in the previous predictions should be reduced by an increase in damping. Installed modal frequencies were also used. Predicted displacement PSD's using the six-mode model are shown in Figures 93-94. The low level model predictions in Figure 93 confirm that the installed damping values are now more reasonable. Additional resonant peaks appear in the low level predictions in Figure 94 indicative of the higher order model. Specifically, the (2,1) mode appears near 200 Hz and the (2,3) mode is evident near 580 Hz. The (4,1) mode should appear near 500 Hz, but is apparently masked by the (1,3) mode near 510 Hz. The high level predictions exhibit less nonlinearity than the previous predictions, but the first mode still exhibits a shift in natural frequency compared to the experimental data.



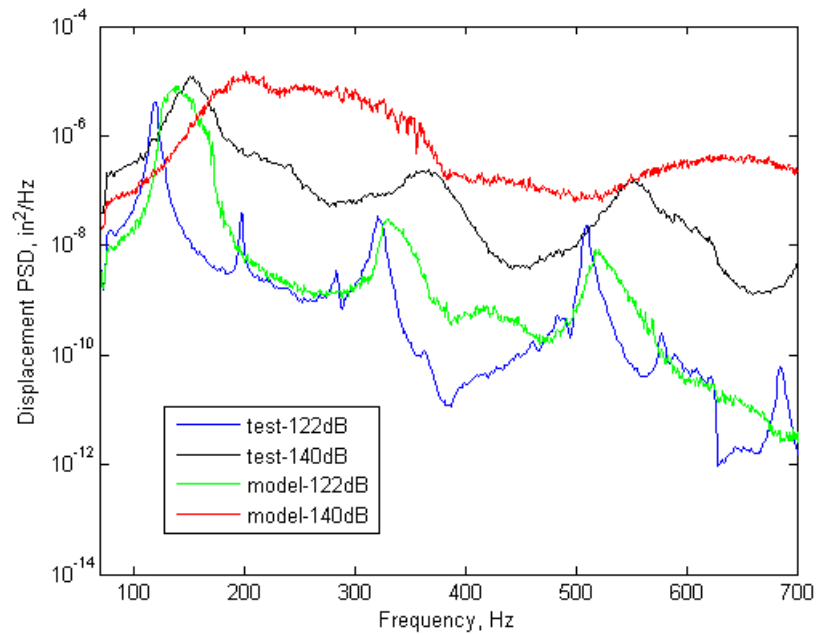


Figure 91. Comparisons for the center location from a three-mode model with the un-installed parameters driven by a random, spatially uniform pressure.

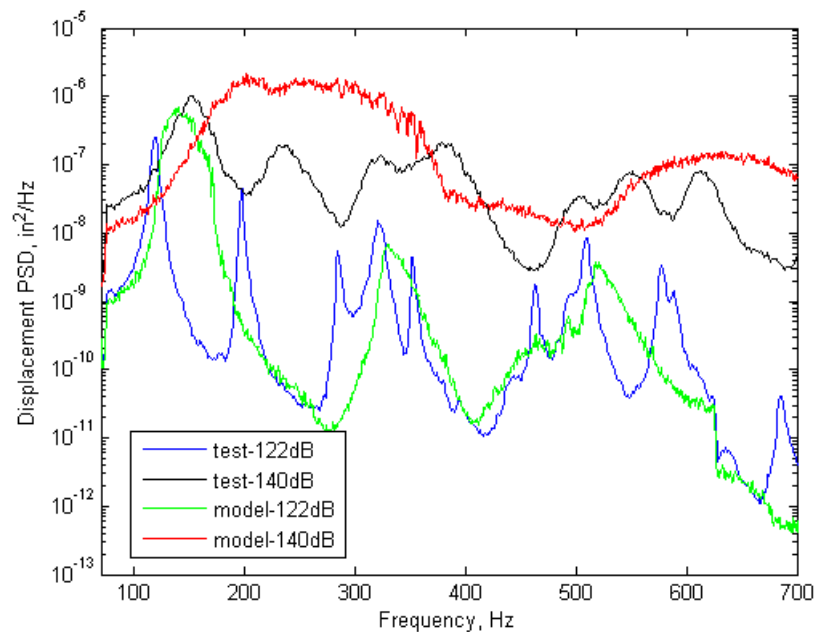


Figure 92. Comparisons for the off-center location from a three-mode model with the un-installed parameters driven by a random, spatially uniform pressure.

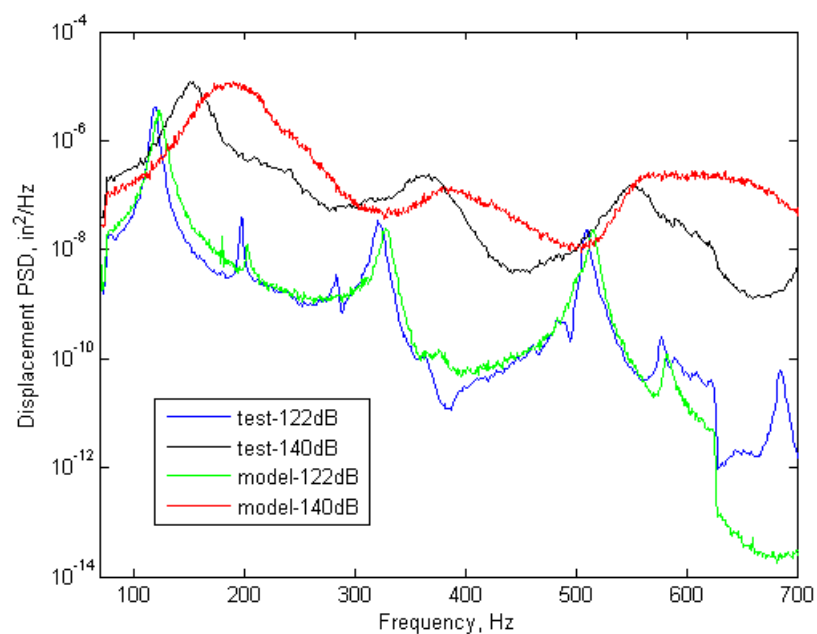


Figure 93. Comparisons for the center location from a 6-mode model with the installed parameters driven by a random, traveling pressure wave.

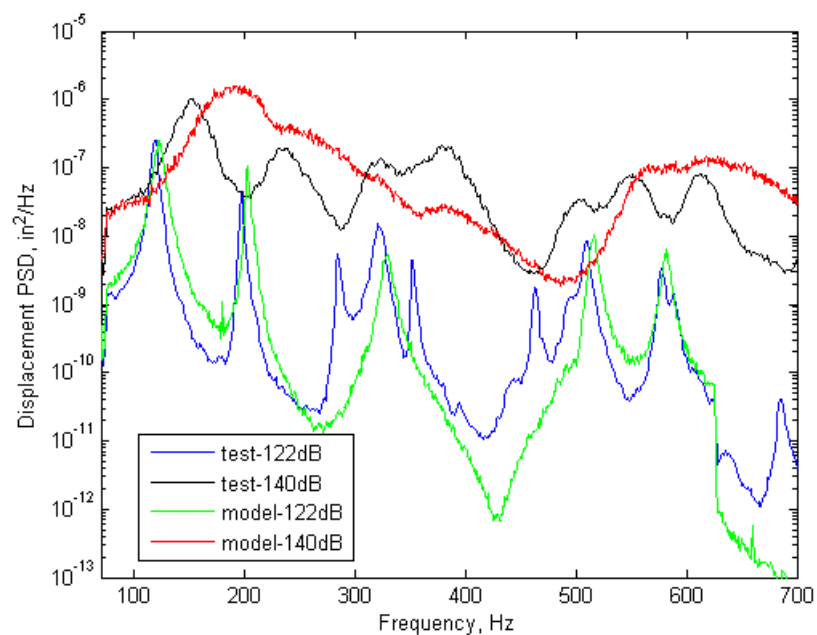


Figure 94. Comparisons for the off-center location from a 6-mode model with the installed parameters driven by a random, traveling pressure wave.

The apparent excessive nonlinearity in the first mode peak could be due to several factors. Since the work described in Section 4.4.3 shows excellent agreement between a three-mode model and the test article in vacuum, the possibility that the model's nonlinear parameters are inaccurate and provide too much hardening is discounted. A second factor that could cause the apparent excessive nonlinearity is a deviation of the acoustic excitation from the flat spectrum measured at the reference microphone. The discrepancies encountered in the initial acoustic test (Section 4.4.5), suggested that acoustic pressure at the plate surface may be different from the reference pressure. Figure 95 shows the measured front, rear and reference pressures for the low level case. The feedback controller forces the reference pressure spectrum to be flat. However, the pressure in front of the plate has a significant peak that occurs at the (1,1) mode frequency. The pressure behind the plate also has this same peak. Also note the acoustic cavity resonance that occurred in the previous experiment is gone. Clearly, there are structural-acoustic coupling effects. The resulting differential pressure (the front pressure minus the back pressure) is plotted in Figure 96. The spectrum level of the differential pressure is more than an order of magnitude higher than the reference at frequencies near the first structural modal frequency. Figures 97-98 show the pressures for the 140 dB case. The difference between the differential and the reference spectrums are lower for this case, but are still significant. Note that for both test levels, the differential pressure exceeds the reference pressure near the first resonance, but the spectrum of the differential is lower than the reference immediately after the resonance.

To further improve the model, the excitation time history was changed from the reference pressure to the differential pressure. The excitation was still modeled as a traveling wave. Note that the component of the pressure field due to the structural response was probably not a traveling wave. However the traveling and stationary components could not be separated and a traveling wave was necessary to excite all the modes. The predicted displacement PSD's for the model with traveling wave differential pressure excitation are shown in Figures 99-100. The predicted response for the center location agrees very well with the experiment for both excitation levels. The prediction for the off-center location is also very good with the exception of the response of the modes not included in the model.

The predictions from the nonlinear ROM's compared well to the data only when the increased damping values were used and the measured differential pressure was used as the excitation force. In effect, the model was adjusted to compensate for the structural-acoustic interactions by modifying the parameters and the input to the model. The results show that structural-acoustic coupling is important. The model could predict the test data, if measured values were used. However, the model could not predict the response without prior knowledge of the effects of the structural-acoustic interaction. Therefore, ROM's built from structural finite-element models may not be adequate to predict the acoustic response of thin panels. Coupling with an acoustic medium may need to be included in the model. A caveat to these observations is that the test article used in this study was extremely thin and may not be representative of typical aircraft structures with thicker skins.

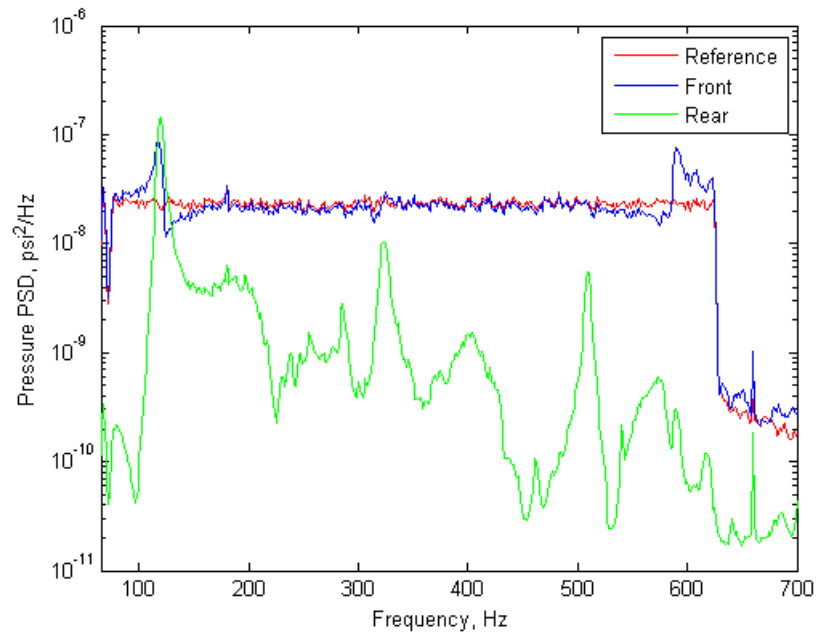


Figure 95. Measured pressure spectra for the 122dB test level.

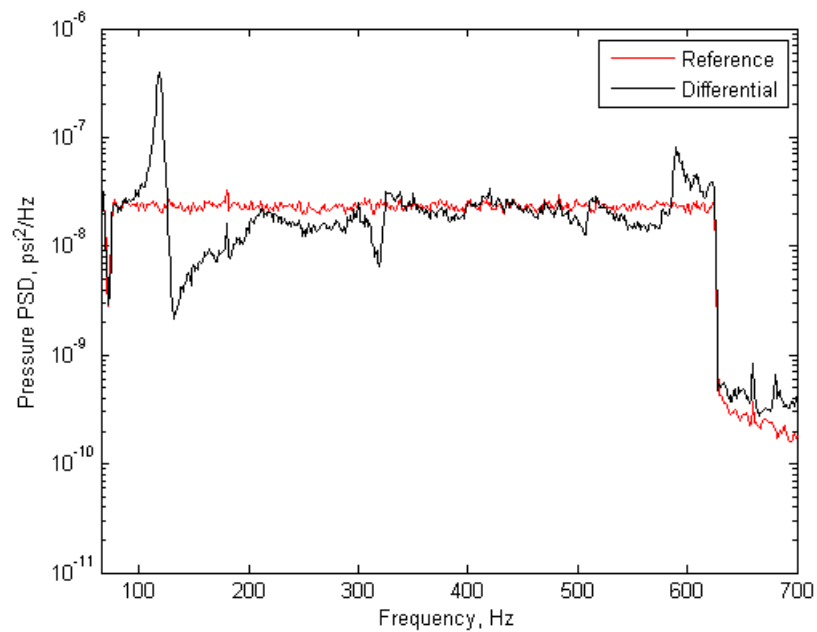


Figure 96. The reference and the differential pressure spectra for the 122dB test level.

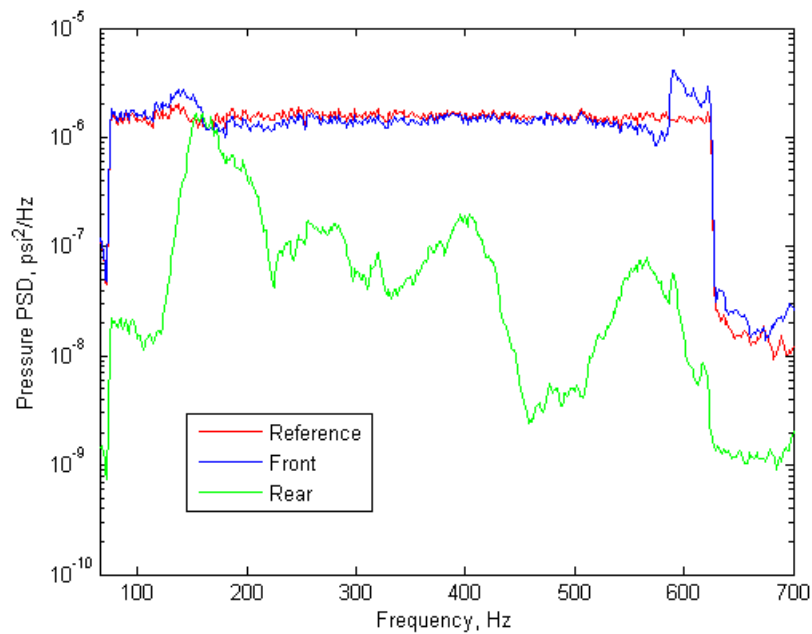


Figure 97. Measured pressure spectra for the 140dB test level.

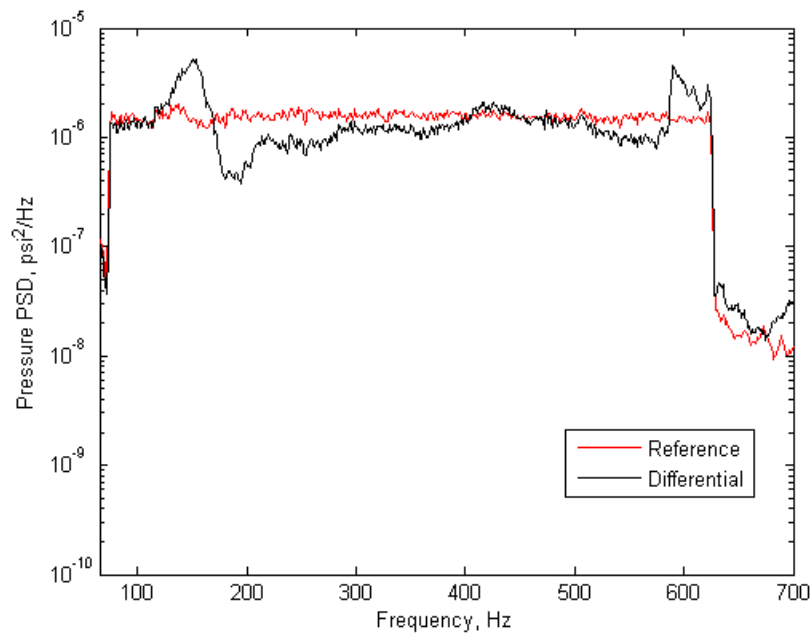


Figure 98. The reference and the differential pressure spectra for the 140dB test level.

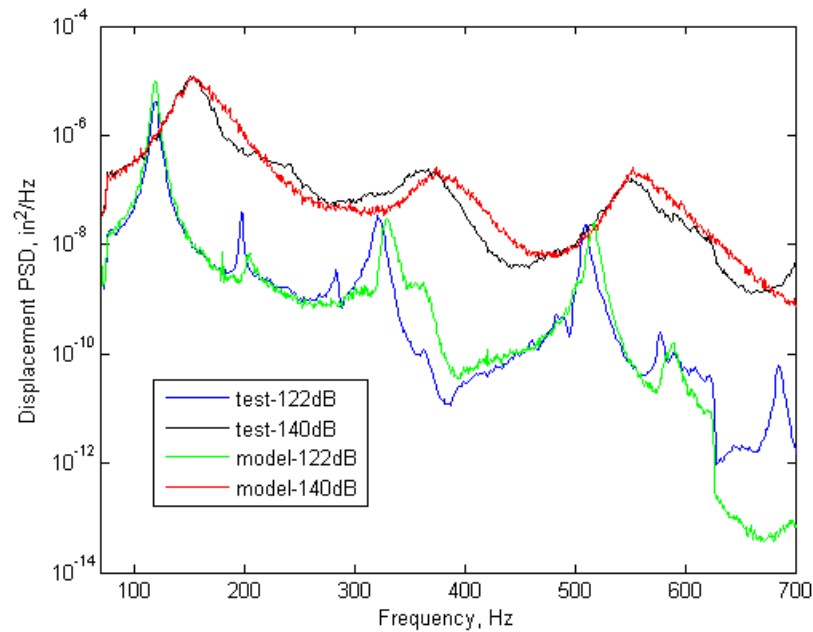


Figure 99. Comparisons for the center location from a 6-mode model with the installed parameters driven by a traveling differential pressure.

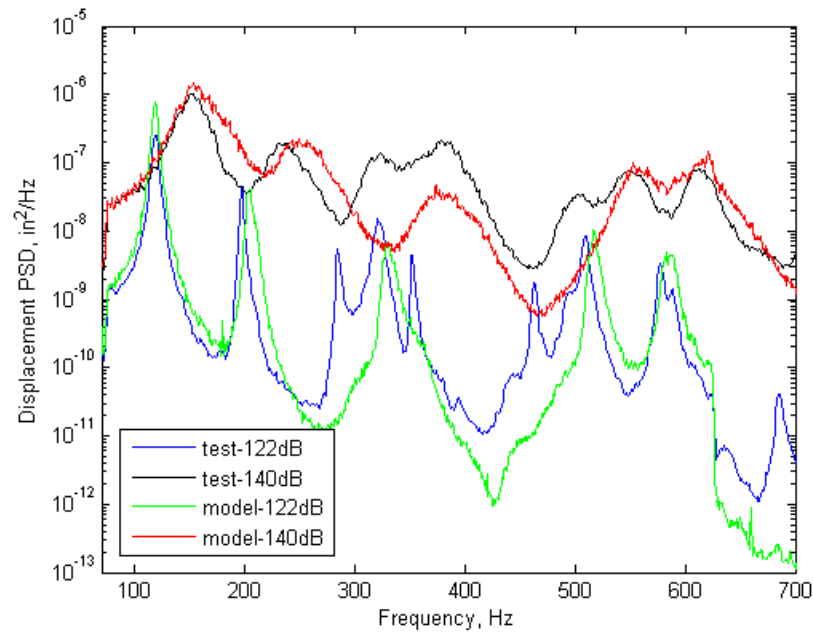


Figure 100. Comparisons for the off-center location from a 6-mode model with the installed parameters driven by a traveling differential pressure.

#### 4.4.7 Coupled Models of the Plate Test Article in SEF

The results of nonlinear ROM predictions of the acoustic test of the clamped plate test article, discussed in Sections 4.4.5 and 4.4.6, motivated a study of the incorporation of acoustic coupling in the ROM's. This development is described in Section 3. It was then undertaken to apply the coupled ROM approach to the results of the second acoustic test of the plate. This section describes that comparison. Nonlinear coupled ROM's were computed from finite-element models of the plate and the acoustic domain inside the acoustic test facility. Results of ROM predictions are then compared to the test data. This work was originally published as Reference [58].

In the coupled ROM approach, an *uncoupled*, nonlinear, structural ROM is supplemented with an *uncoupled* modal model of the acoustic environment. With this approach, the nonlinear structural ROM is built using the methods documented in the literature. The uncoupled acoustic modes are obtained considering a rigid acoustic boundary where the structure occurs. Coupling terms are added to both models. These terms can be determined from a coupled FEM. The nonlinearity is contained in only the structural portion of the model. Other advantages are that the uncoupled modal quantities such as the structural frequencies, the structural damping factors, and the acoustic frequencies appear in the coupled model as uncoupled quantities. These quantities can be independently adjusted to match test values. See Section 3 for details on the coupled approach.

The nonlinear structural ROM built for this study used the structural modes shown in Figure 101. The ROM is identical to the six mode model that was used in Section 4.4.6. Experimental data from the initial shaker test of the clamped plate, describe in Section 4.4.2, was used to verify the accuracy of the nonlinear structural ROM. The predictions from the ROM, shown in Figure 102, confirm that the nonlinear structural model is accurate when modeling primarily an uncoupled structural response. The same model when used to predict the response due to acoustic loading was not as successful. Figure 103 shows the predicted response in comparison to test data from the second acoustic test of the plate (Section 4.4.6). The response is for a point 0.25 inches downstream from the center of the panel. The prediction was obtained using nodal forces equivalent to the random pressures assuming a traveling wave propagation of the acoustic pressure. The frequencies and modal damping factors were adjusted in the model to the *uninstalled* values listed in Table 24. These are frequencies and damping factors measured before the test article was installed in the acoustic test facility.

The nonlinear structural ROM lacks any coupling between the dynamics of the acoustic domain inside the test duct and the structure. Presumably, if those dynamics could be added to the model the prediction would improve. The acoustic test facility, shown schematically in Figure 71, is composed of three major sections—the acoustic source, test section and termination section. The acoustic source is a single modified Wyle WAS 3000 air modulator. The modulator chops the flow of high pressure air to generate sound. The modulator is connected by a transition horn to a constant cross section duct—the test section—that is six feet long and one foot square. The other end of the duct is attached to an expansion horn and termination section. The overall length of the facility is approximately 40 feet. The end wall of the termination section is covered with

fiberglass acoustic wedges to reduce reflection of the acoustic traveling waves propagating down the duct.

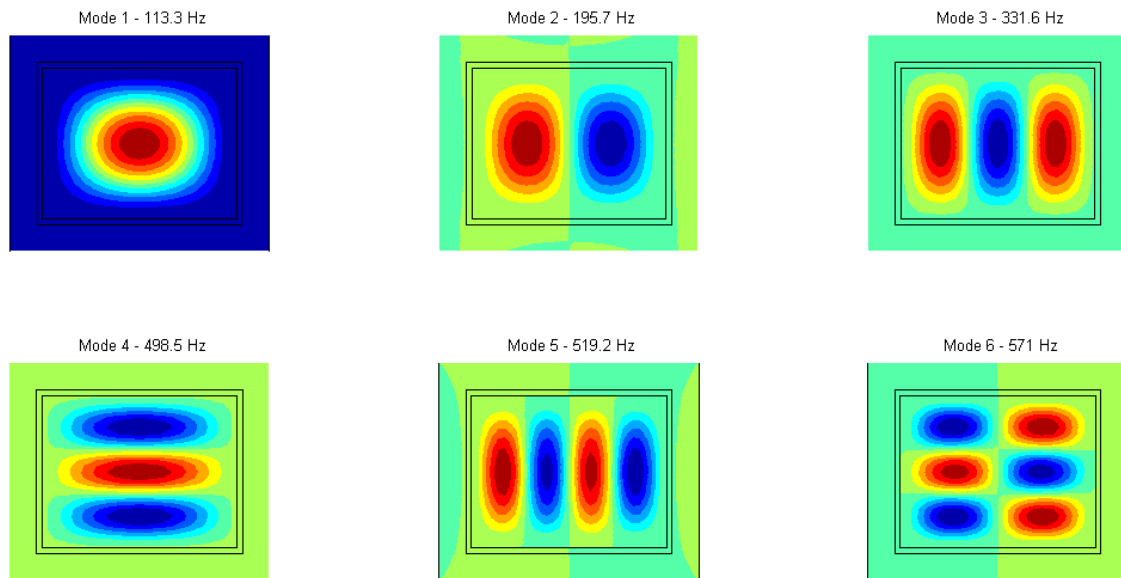


Figure 101. Finite element mode shapes for the clamped plate test article

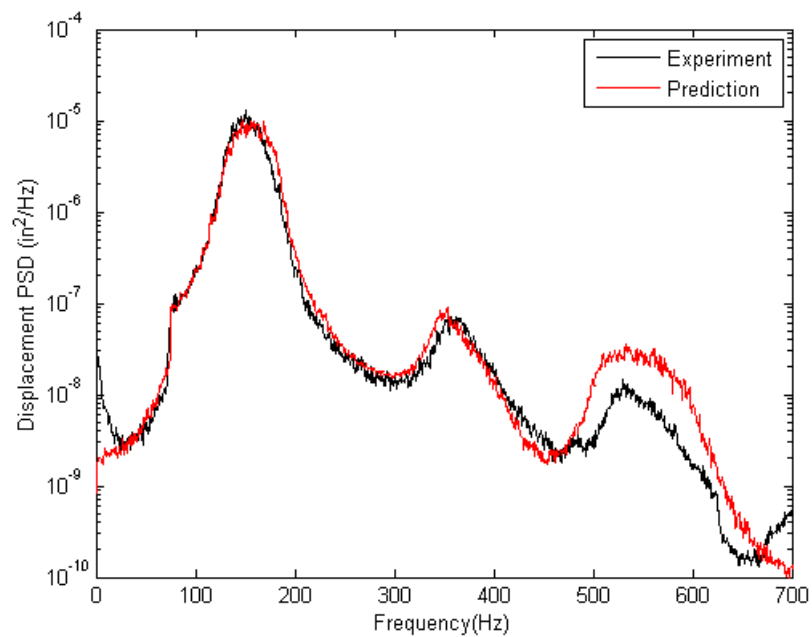


Figure 102. The Power spectral density (PSD) of the center displacement when the test article is driven by a shaker at 7.2 g rms.



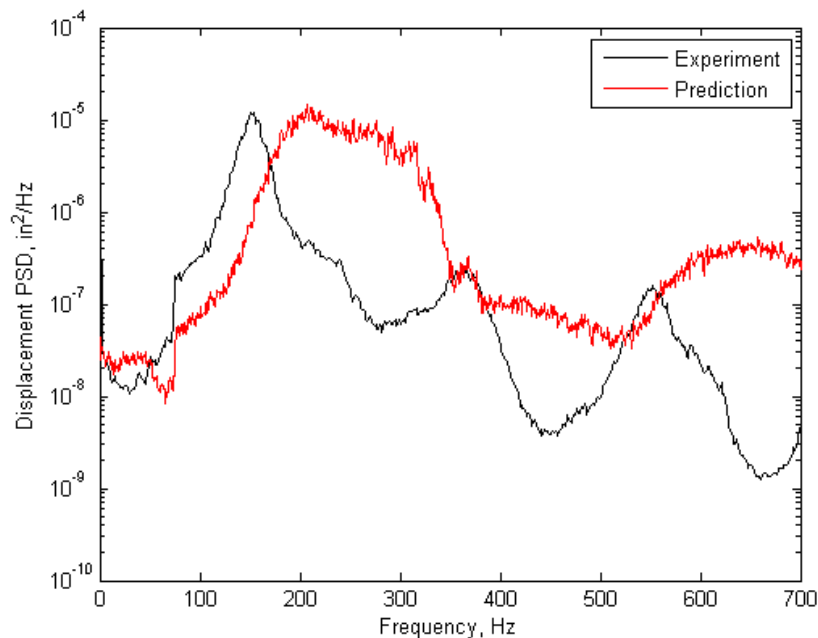


Figure 103. The PSD of the displacement near the center when the test article is driven acoustically at 140dB.

Table 24. Natural frequencies and modal damping ratios for the test article

Mode	Test (Un-installed)		FEM
	f (Hz)	$\zeta$	f (Hz)
(1,1)	119.7	0.0024	113.3
(2,1)	199.7	0.0024	195.7
(3,1)	322.6	0.0061	331.6
(4,1)	498.5	0.0038	519.2
(1,3)	512.5	0.0075	498.5
(2,3)	581.1	0.0067	571.0

A finite-element model of the air inside the SEF was constructed in Abaqus. The element mesh is shown in Figure 104. A cross sectional mesh of twelve elements by twelve elements was used for most of the model except the test section adjacent to the plate mounting area. There, a finer mesh was used to provide coincident nodes with the plate. The total number of acoustic elements used in the model was approximately 46,000. Standard properties for air were used in the model. Acoustic damping wedges in the termination section of the facility were not modeled directly. The acoustic boundary condition on all surfaces was considered rigid.

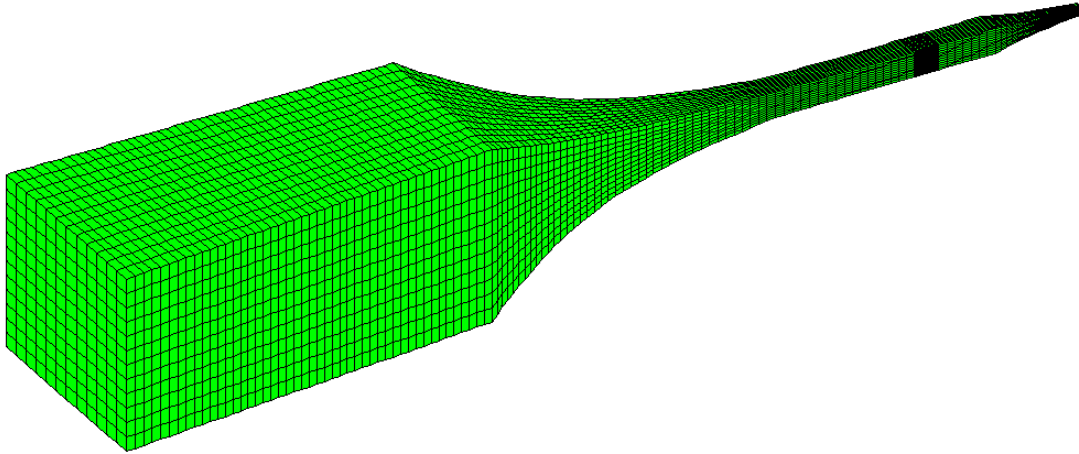


Figure 104. The acoustic finite element mesh.

All modes of the acoustic model in the 0-600 Hz range were computed in Abaqus. Over 4300 modes were computed, most of which were higher frequency modes of the termination section. An acoustic mode shape with a frequency occurring near the first structural resonance is shown in Figure 105. The area where the test article attaches to the test section is shown in Figure 105 for reference.

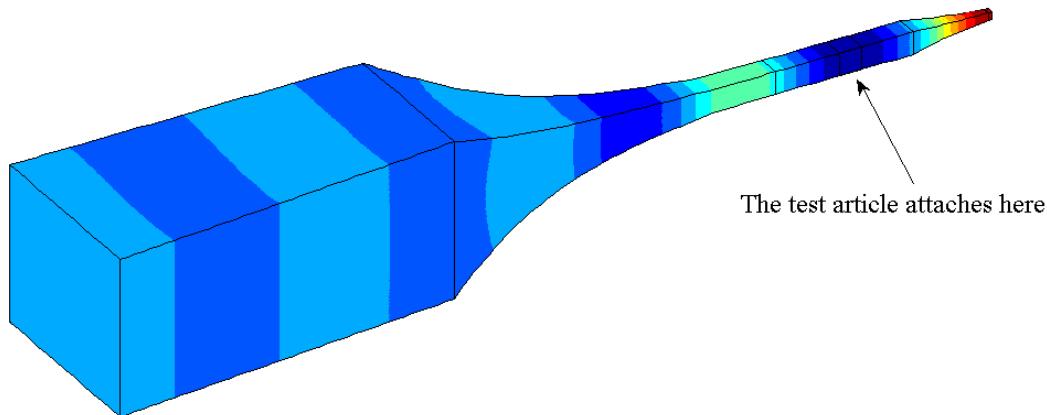


Figure 105. An acoustic mode near the first structural resonance.

There was a second acoustic domain that could couple with the test article. This is the acoustic environment behind the test article which includes the room dynamics and everything in the room that could impact those dynamics. As one can see in Figure 90, the area behind test article is very complicated. Rather than modeling all the details, the area was idealized as a hemispherical domain with infinite acoustic elements on the exterior surface of the hemisphere. The position of the hemispherical model in relation to the interior acoustic model is shown in Figure 106. The hemispherical model is an approximation of an infinite acoustic domain. This idealization assumes that any acoustic energy generated by the test article radiates away from the test article and does not return. This is a reasonable assumption given the fact that room has acoustically treated walls. The hemispherical model was built in an in-house, MATLAB -based, finite element code. The first thirty normal modes of the exterior acoustic domain were

computed in MATLAB. Figure 107 shows the modes of the model that were included in the coupled model. In the figure, an outline of the position of the test article is shown. The modal selection process will be discussed in the next paragraph.

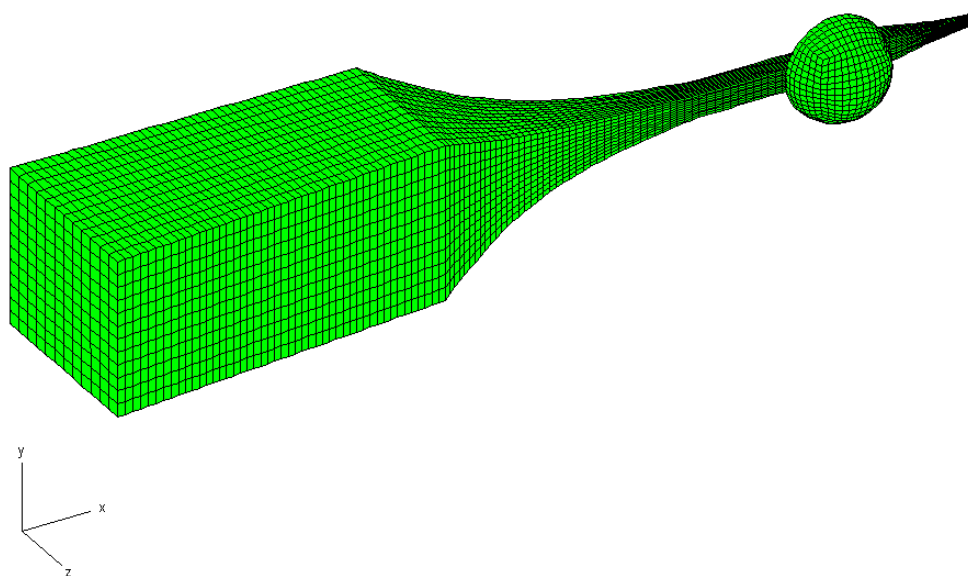


Figure 106. The interior and exterior acoustic meshes

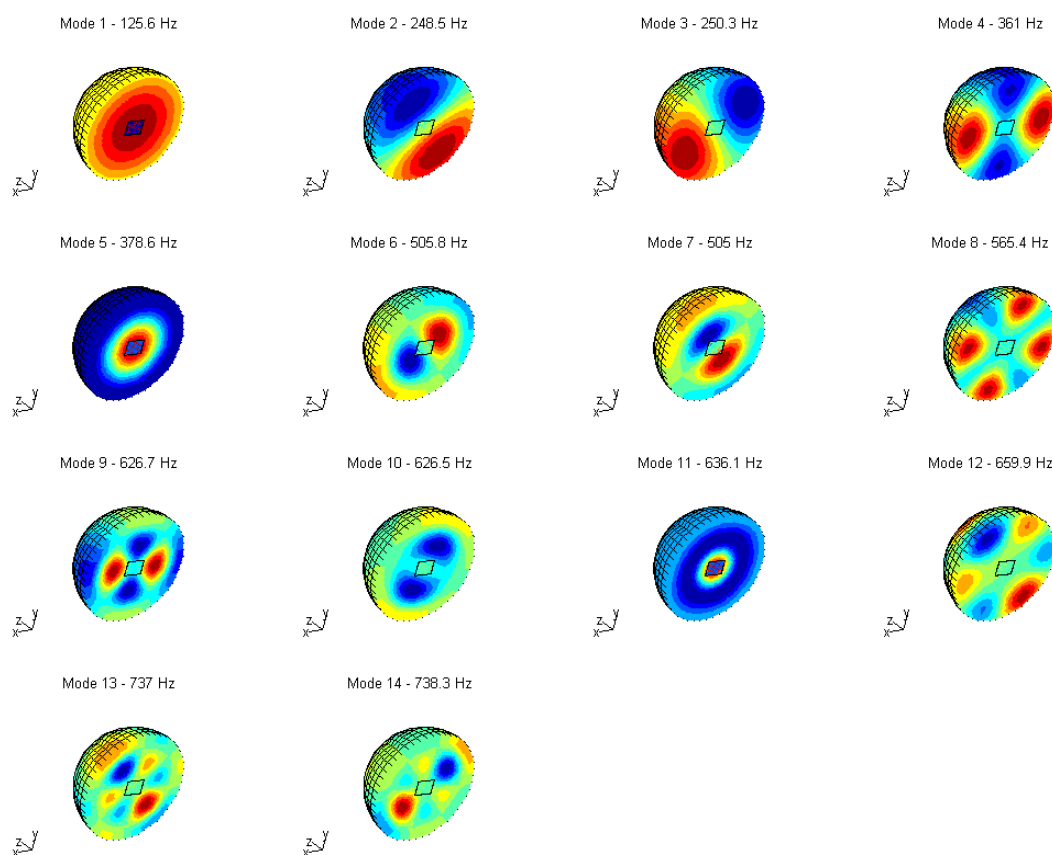


Figure 107. Modes of the infinite acoustic domain behind the test article.

The structural ROM is coupled to the two acoustic regions using Equations 80-81. (The models for the two acoustic domains can be grouped together into a single uncoupled modal model or treated separately which requires an additional set of modal equations.) The modal coupling coefficients are required to implement the equations. The modal coupling between the structure and exterior acoustic domain was calculated by Equation 78 using the normal modes of the infinite domain as the acoustic modes. The physical coupling matrix,  $\mathcal{S}$ , was extracted directly from the stiffness matrix of a coupled FEM of the infinite domain model and a plate with the same dimensions and nodal spacing as the plate area of the test article model. The dimensions of the resulting modal coupling matrix were six by 30. Each element of the matrix is the coupling coefficient for a structural mode and an acoustic mode of the infinite domain. The element of the matrix with the maximum absolute value was determined. Acoustic modes that had coupling coefficients with absolute values greater than one percent of the maximum for any structural mode were retained.

The modal coupling matrix for the modes of the interior acoustic domain was also calculated. This acoustic model was built and analyzed in Abaqus. Extraction of the physical coupling matrix from Abaqus is cumbersome [29]. The matrix is easily built in MATLAB since all the structural elements are equally sized and the acoustic nodes correspond to the structural nodes. The modal coupling matrix is then calculated using Equation 78. A similar procedure as used earlier was used to reduce the number of acoustic modes. In this case, the threshold for modal retention was set at 10 percent of the maximum coupling value. This resulted in 284 acoustic modes retained in the interior model.

The modal damping for the exterior acoustic domain was determined directly from the FEM. The infinite acoustic elements produce a damping matrix. The other acoustic elements provide no damping. The physical damping matrix was assembled and transformed to the modal space using the modal vectors. The damping matrix is not proportional, and is thus not diagonal, as several of the off-diagonal terms in the modal damping matrix are populated. Thus the modal equations for the exterior domain are not only coupled to the structure, but are coupled to each other through the modal damping matrix.

The modal damping for the structural portion of the model was assumed to be diagonal. The uninstalled values of modal damping were used to construct the modal damping matrix. The frequencies of the structural model were also adjusted to the uninstalled values. The structural equations are coupled to the two acoustic domains, but are also coupled to each other through the nonlinear terms.

The modal damping for the interior acoustic model had to be assumed. The acoustic wedges of the facility provide the majority of the acoustic damping but were not modeled. Like the infinite acoustic elements in the infinite domain, the wedges should couple the acoustic modes to each other. However, the damping model of the acoustic facility was assumed to be diagonal for simplicity. Measured modal damping of the interior domain ranged between three and six percent the acoustic modes below 200 Hz. For the model, a value of four percent was assumed for all the interior modes.

The coupled model consisted of six structural modes, 14 modes of an infinite domain behind the structure, and 284 modes of the interior acoustic domain. The modes of the two acoustic domains were selected according to the values of the coupling between the structural modes and the individual acoustic modes. The frequency and damping of the structural model corresponded to values from a modal test of the structure. The damping of the infinite domain was obtained from a FEM. The damping for all the acoustic facility modes was assigned a reasonable single value. Coupling in the model occurs between the structural modes and the modes of each of the two acoustic domains. The only nonlinearity in the model occurs in the structural equations. This nonlinearity couples the structural modes with each other. The damping model of the infinite domain couples the modes of this acoustic domain with each other.

If the structure is coupled to two acoustical domains, another modal equation has to be added to the set of coupled equations given in Equations 80-81. The coupled modal equations are modified as

$$\ddot{\mathbf{q}} + \mathbf{\Gamma}_s \dot{\mathbf{q}} + \mathbf{A}_s \mathbf{q} + \boldsymbol{\theta}(q_1, q_2, \dots, q_n) = \mathbf{D}_a^T \mathbf{a} + \mathbf{D}_v^T \mathbf{v} + \boldsymbol{\Psi}^T \mathbf{f}_s(t), \quad (121)$$

$$\ddot{\mathbf{a}} + \mathbf{\Gamma}_a \dot{\mathbf{a}} + \mathbf{A}_a \mathbf{a} = -\rho \mathbf{D}_a \ddot{\mathbf{q}} + \boldsymbol{\Phi}^T \mathbf{f}_a(t), \quad (122)$$

and 
$$\ddot{\mathbf{v}} + \mathbf{\Gamma}_v \dot{\mathbf{v}} + \mathbf{A}_v \mathbf{v} = -\rho \mathbf{D}_v \ddot{\mathbf{q}} + \mathbf{X}^T \mathbf{f}_v(t), \quad (123)$$

where  $\mathbf{v}$  is the modal amplitude vector and  $\mathbf{X}$  is a truncated set of uncoupled, mass normalized, mode shapes for the exterior acoustic domain. There are two different modal coupling matrices, one for each acoustic domain as denoted by their subscripts.

The input to the coupled model could be any combination of the three external force vectors in Equations 121-123. Here, only the external structural force vector was used. The structural force is calculated from an applied pressure field acting on the plate area of the test article. The applied pressure corresponds to a 140 dB, random, acoustic pressure with a flat spectrum between 75 and 625 Hz. The pressure propagates as a traveling wave across the structure in the negative  $x$ -direction. The pressure is converted to a mechanical force in the model. The pressure field of the interior domain is not used to apply the force, but rather to model the dynamic acoustic response due to the vibration of the structure. The model was integrated using a Newmark-beta scheme. The time increment used in the integration was  $2.0 \times 10^{-5}$  seconds. The time length of each of the integrations was 30 seconds.

The predicted PSD of the displacement near the plate center from the coupled model is shown in comparison with the experimental results in Figure 108. The prediction shows a marked improvement over the structure-only prediction shown in Figure 103. Some discrepancies remain between the coupled prediction and the experiment results. These are likely to be due to structural and acoustic asymmetries not captured in either model.

The damping in the interior acoustic modes was a major assumption in the coupled model. The damping values were varied from the original 4% to 2% and 1%. The predictions for these damping values are shown in Figure 109. The overall character of the structural response does not change as the damping varies. The results show that the structural response is not very

sensitive to the damping in the interior modes. Thus the initial damping value of 4% appears to be reasonable.

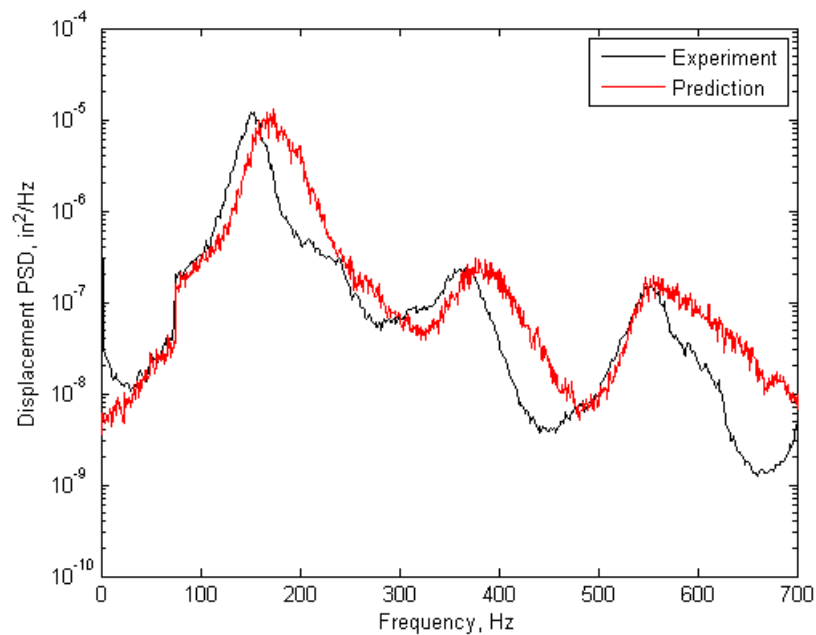


Figure 108. Displacement PSD near the plate center for the 140dB loading case.

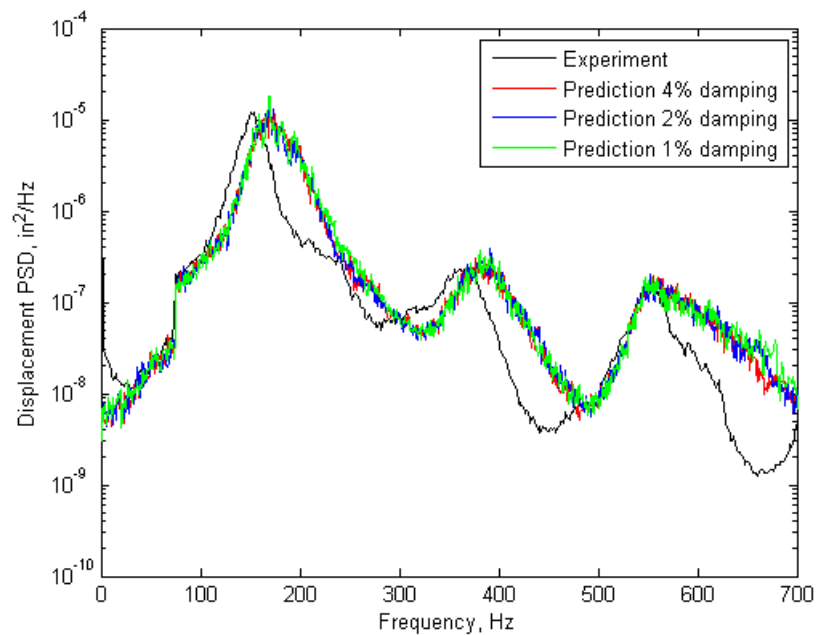


Figure 109. The displacement near the plate center as the damping of the interior acoustic is varied from 1% to 4%.

Next, the model of the interior domain was replaced with a simpler physical model. The termination section was replaced with a constant cross sectional duct. The one foot by one foot cross section of the test area was extended so that the model had the same overall length as the

original facility model. The number of acoustic modes selected for the coupled model was 62 using the same selection process as earlier. A modal damping value of 4% was selected for the acoustic modes of the new duct model. The prediction of plate center displacement using the simplified coupled model is shown in Figure 110. The prediction is nearly identical to the prediction using the original facility modes. This result indicates that the prediction is not sensitive to the dynamics of the termination section of the facility.

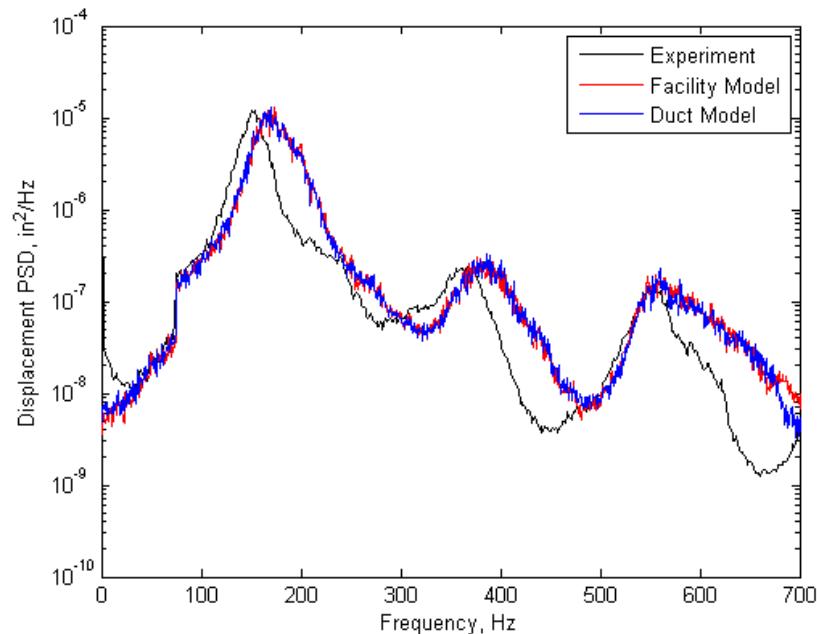


Figure 110. The prediction for a duct with a constant cross section in comparison to the facility model.

The method to produce a coupled, nonlinear structural-acoustic ROM was successfully demonstrated and compared against experimental data. The coupled model was built from a nonlinear structural ROM previously used in the literature and two acoustic modal models. A FEM of the acoustic facility was used to produce one of the acoustic modal models. A FEM of a hemisphere with infinite acoustic elements approximated the open exterior environment behind the test article for the second model. The three models were coupled using an approach documented Section 3.

The coupled model was integrated in time to predict the structural response of the test article. The predictions were able to capture the overall features of the response and showed a marked improvement over a structure-only prediction. Some discrepancies remained between the coupled prediction and the experiment results. These were likely due to structural and acoustic asymmetries not captured in the models.

#### 4.4.8 Structural-Acoustic Coupling Sensitivity Analysis

Following the successful comparison of coupled nonlinear ROM's results to the acoustic test of the clamped plate test article, a question lingered as to the necessity of coupled ROM's for acoustically excited structures in general. When is a coupled model required? What are the salient parameters of the structure and the acoustic environment that determine the need for a

coupled model in a progressive wave facility versus an exterior acoustic domain? To help answer these questions, a parametric study was undertaken to better understand the need for acoustic coupling of plate-like test articles in the SEF. This section describes a study in which structural parameters of a flat plate in a progressive wave test facility, including thickness and modal damping, are varied to explore the need for coupled ROM's. The work was originally published as Reference [59].

An example problem is used here to compare the results from a coupled ROM to that from a structural ROM of a thin plate in a progressive wave acoustic test facility. The SEF progressive wave facility discussed in Sections 4.4.5 to 4.4.7 was idealized in this example. A model of the facility was constructed to be simple yet contain all the relevant features.

The coupled ROM results presented in Section 4.4.7 were not sensitive to the geometry of the termination section of the progressive wave facility. An acoustic model of a duct with a constant cross sectional area and the correct overall length produced coupled results very similar to the more detailed acoustic model of the facility. Thus, the progressive wave facility for this example was modeled as a duct with a constant cross sectional area. The model was chosen to be a 500" x 12" x 12" duct. Figure 111 shows the duct and the plate for the example problem. The plate is shown in red. The test article was chosen to be an 18" x 12" aluminum plate with clamped boundary conditions. The size of the test article is different from that in the previous sections. The new dimensions were chosen to correspond to the size of the actual opening on the side wall of the SEF. The plate center was positioned 420 inches from the termination end of the duct.

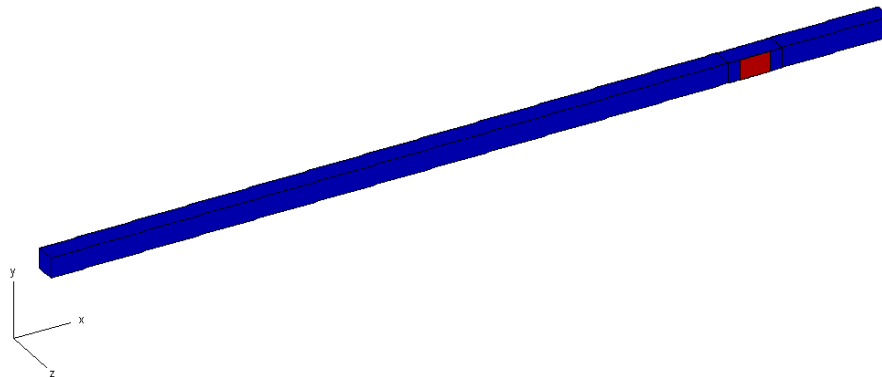


Figure 111. The configuration of the example problem.

The rectangular duct was modeled in Abaqus using eight-node acoustic elements. Over 26,000 elements were used in the model. The majority, over eighteen-thousand, were concentrated in the area 32" x 12" x 12" near the plate. The first few acoustic modes of the duct are shown in Figure 112. The first longitudinal acoustic mode occurs at 13.5 Hz and the higher frequency modes occur at integer multiples of the fundamental frequency. The first transverse mode appears at 556 Hz. The duct model had a total of 121 modes below 700 Hz.

Acoustic damping in the model of the SEF is mainly a result of the wedges in the termination section (see Figure 71). The coupled ROM results in Section 4.4.7 were generally insensitive to the damping of the acoustic modes. The damping in the acoustic modes was assumed to be 4% of critical for each for this study, which is the initial value used in Section 4.4.7 and is approximately equal to experimentally measured damping in the real facility.



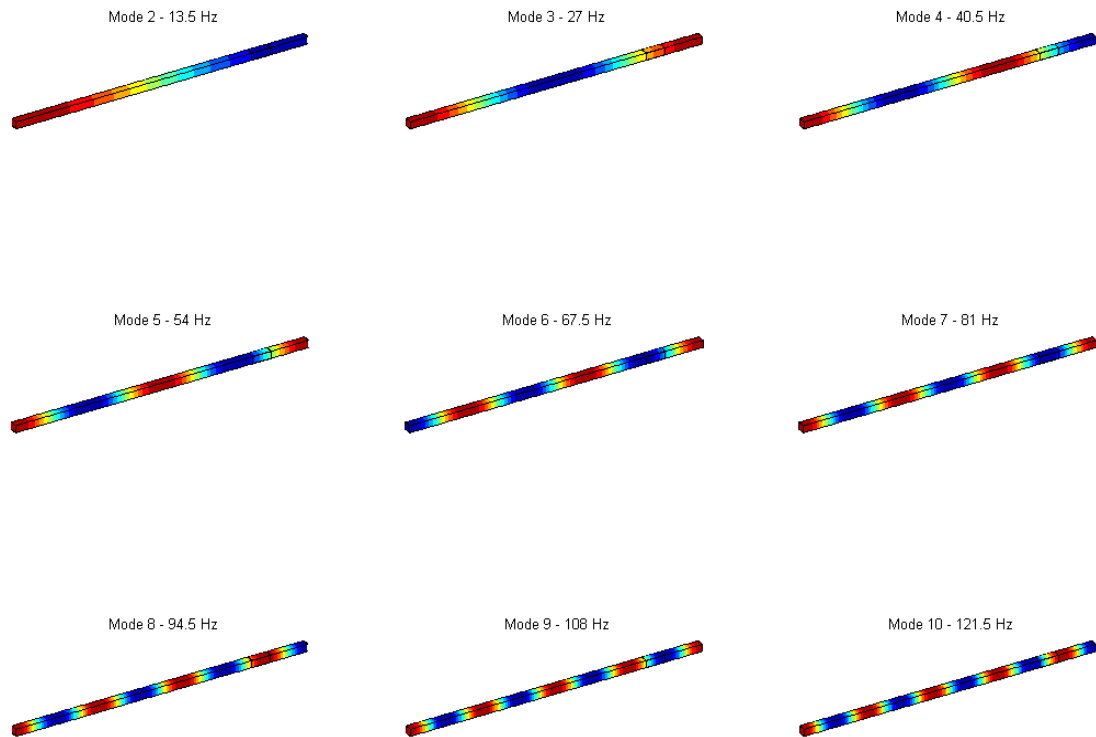


Figure 112. The lowest frequency acoustic modes of the duct model.

The plate used in this example was modeled in Abaqus using four-node plate elements. A regular grid was used with an element size of 0.5" x 0.5". The grid was constructed so that the structural nodes were coincident with a subset of the acoustic nodes. The plate thickness was a variable for the study. Uniform thicknesses of 0.02", 0.03", 0.04", 0.05", 0.06", 0.07", 0.08", 0.09", and 0.1" were used. The first mode shape of the plate is shown in Figure 113, the frequency of which depends linearly on the thickness of the plate. The first mode frequency varied between 35.95 and 179.6 Hz for the range of thicknesses investigated.

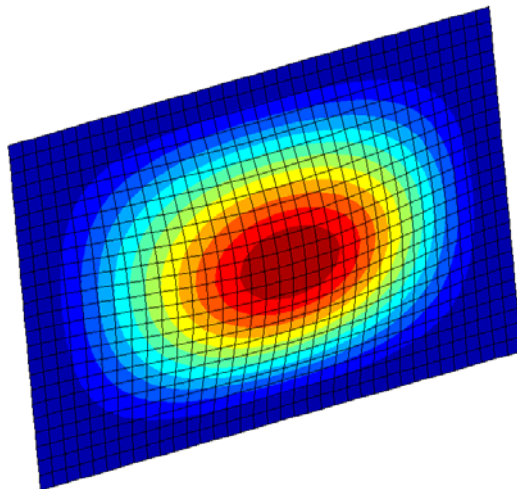


Figure 113. The first mode of the plate.

Only the first mode was used in the structural ROM of the plate. This is the simplest model that demonstrates the nonlinear structural phenomenon. The nonlinear function for a flat plate for a single mode degenerates to a single cubic term. This term was estimated for each thickness.

The coupled model in this example considered only one acoustic domain, the interior of the duct. The work reported in Section 4.4.7 also considered the domain exterior to the duct behind the test article. That domain was neglected here because coupling with it was assumed to be negligible. The coupled model is comprised of the nonlinear structural ROM, the linear modal model of the acoustics, and a coupling term in each equation. The coupling terms depend on the modal coupling matrix,  $\mathbf{D}$ , which can be determined from the coupling matrix,  $\mathbf{S}$ , in Equation 78, and the mode shapes of the structure and the acoustic domain. The coupled model in this example contains one nonlinear structural mode and 121 linear acoustic modes.

The acoustic domain in the duct is comprised of two components of acoustic pressure—pressure resulting from vibration of the plate and an externally generated excitation pressure. The acoustic excitation pressure is not explicitly modeled in this study, i.e.,  $f_a$  in Equation 81 is set to zero. Rather, the applied acoustic pressure is converted to an equivalent, externally applied, structural force. The excitation is assumed to be uniform across the plate with time varying amplitude. The amplitude is generated as a zero mean, band limited (0-500Hz), normal random variable.

A Newmark scheme written in MATLAB is used to integrate the model in the time domain. The scheme uses the average acceleration method with no artificial damping. The two sets of equations for the coupled ROM are integrated simultaneously to provide direct coupling. The sample rate of the integrator is 20 kHz, and the length of the prediction is 200 seconds. The time domain predictions are processed in the frequency domain to obtain PSD plots. The RMS values of the center displacement of the plate are also calculated directly from the time domain predictions.

Predictions from the coupled model and the structural model were compared to determine the need for a coupled model. Parameters in the structural model were varied, including the thickness, modal damping, and in-plane preload of the plate. The plate thickness affected both the linear and nonlinear modal stiffness. The damping of the first structural mode ranged from 0.001 to 0.05, with a value of 0.005 being considered nominal. The effect of the preload was studied by changing the natural frequency of the structure. The excitation level of the applied acoustic pressure was also varied from 128dB to 158dB in steps of 6dB.

First, the effect of plate thickness is demonstrated for the case with nominal damping of 0.005 and an excitation level of 140dB. The PSD of the center displacement of the structure is shown in Figure 114 for both the structural ROM and the coupled ROM. The thickness of the plate is 0.02 inches. For this case, the coupled model prediction is significantly different than the structural prediction. However if the thickness of the plate is increased to 0.10 inches, both models predict nearly identical results as shown in Figure 115.

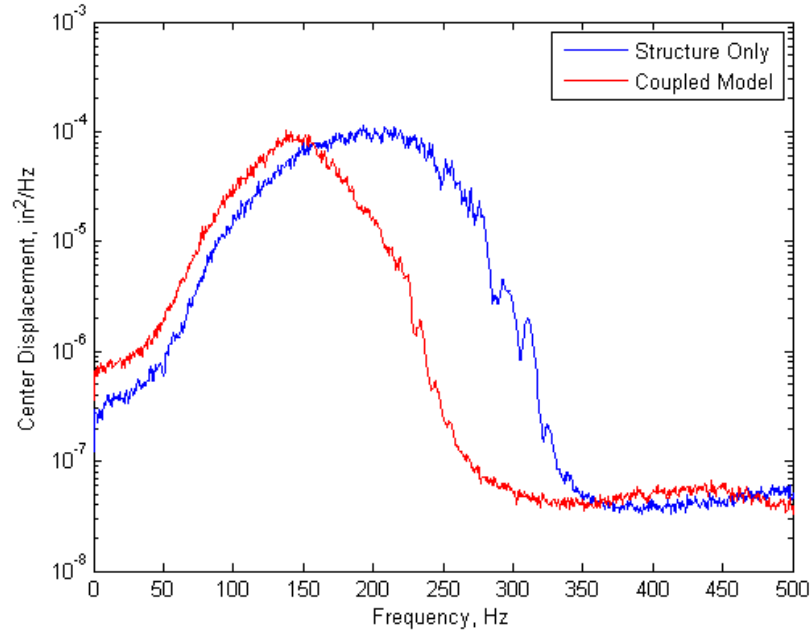


Figure 114. Response for the 0.02" thick plate with  $\zeta_s=0.005$  for 140dB OASPL.

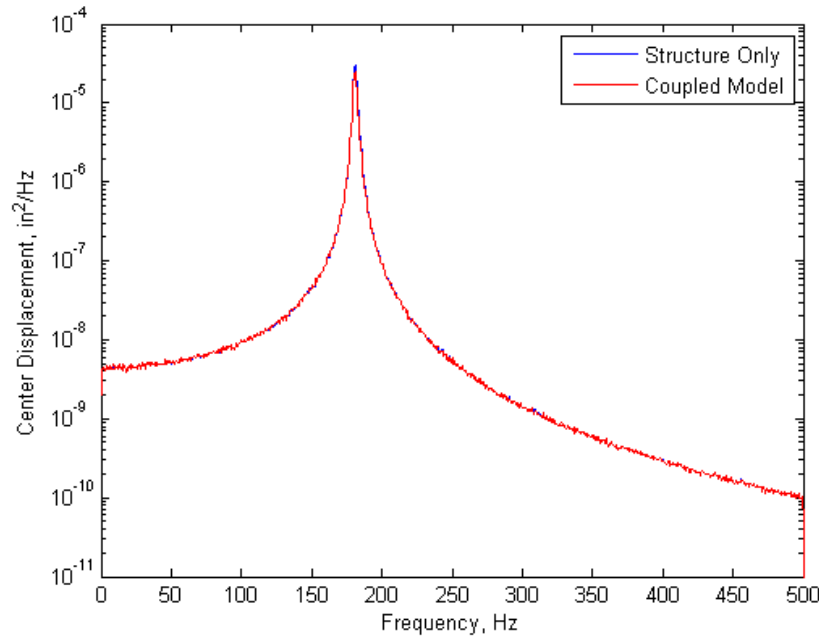


Figure 115. Response for the 0.10" thick plate with  $\zeta_s=0.005$  for 140dB OASPL.

A waterfall plot of the structural model response and the coupled response is shown in Figure 116 as the thickness varies. The plot shows that as the thickness decreases, the response becomes more nonlinear (the peak broadens) and the difference between the two models increases. The effect can be seen more clearly by plotting the RMS response as a function of thickness in Figure 117. For this case, thicknesses less than 0.06" may require the coupled ROM for accurate predictions. The phenomena can be explained as follows: The acoustic modes of the coupled model have to be excited by the structure to affect the response. The acoustic modes are at set frequencies (approximately every 13.5 Hz). When the response is broad in frequency, the

structure can excite the acoustic modes and coupling with the acoustic domain can affect the structural response.

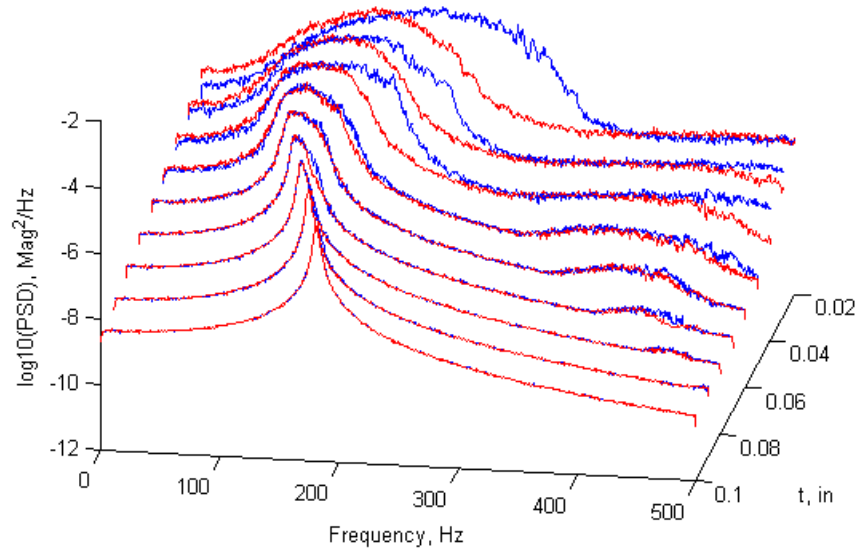


Figure 116. Response for the plate ( $\zeta_s=0.005$ , 140dB) as the thickness varies. The PSD of the structure only model is shown in blue, the coupled response in red.

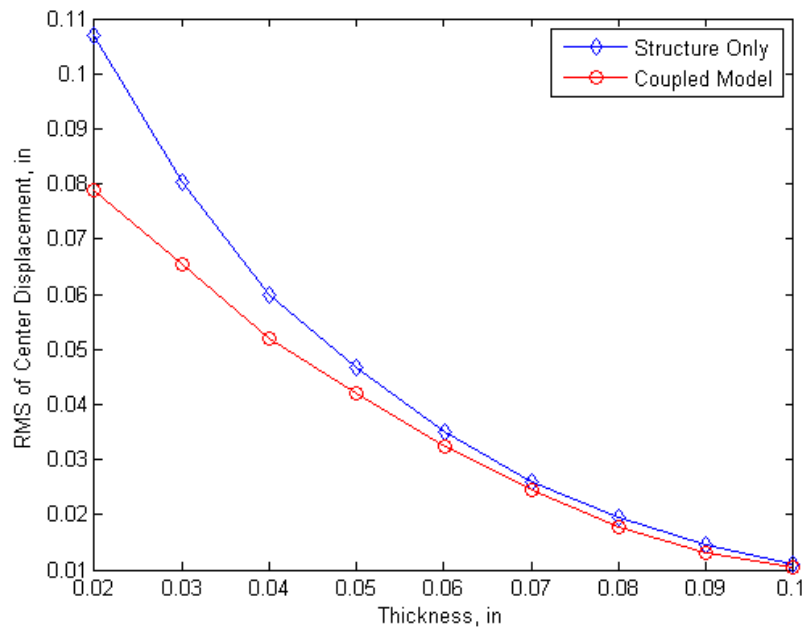


Figure 117. RMS center displacement as the thicknesses varies ( $\zeta_s=0.005$ , 140dB).

Nonlinear structural response does not necessarily mean that acoustic coupling affects the response significantly. Figures 118-119 show the response of a 0.06" thick structure as the excitation is increased from 128dB to 158dB in steps of 6dB. The response exhibits nonlinearity as the excitation is increased, yet the differences between the coupled and structure-only model are insignificant.

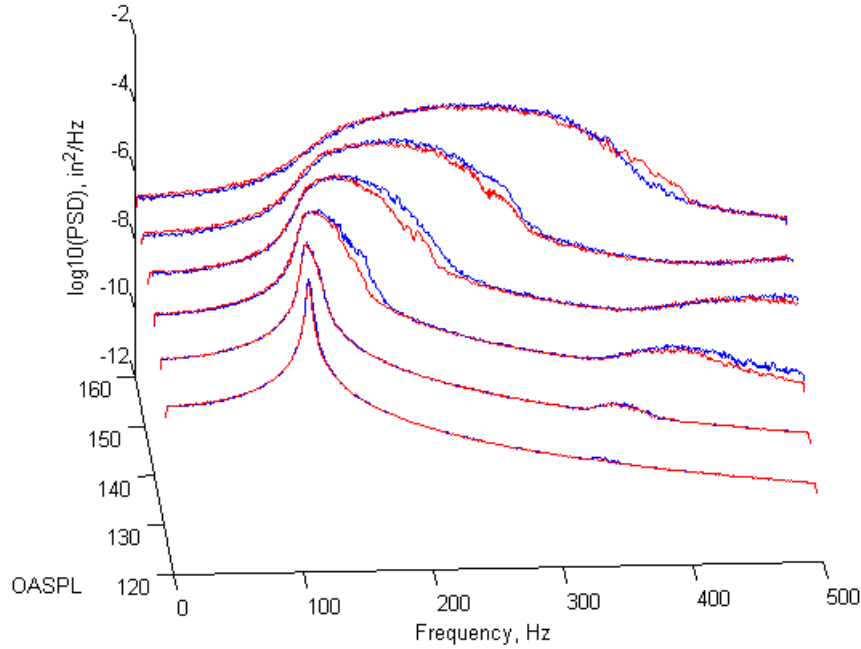


Figure 118. Response for the 0.06" thick plate ( $\zeta_s=0.005$ ) as the excitation varies. The structure only model is shown in blue, the coupled response in red.

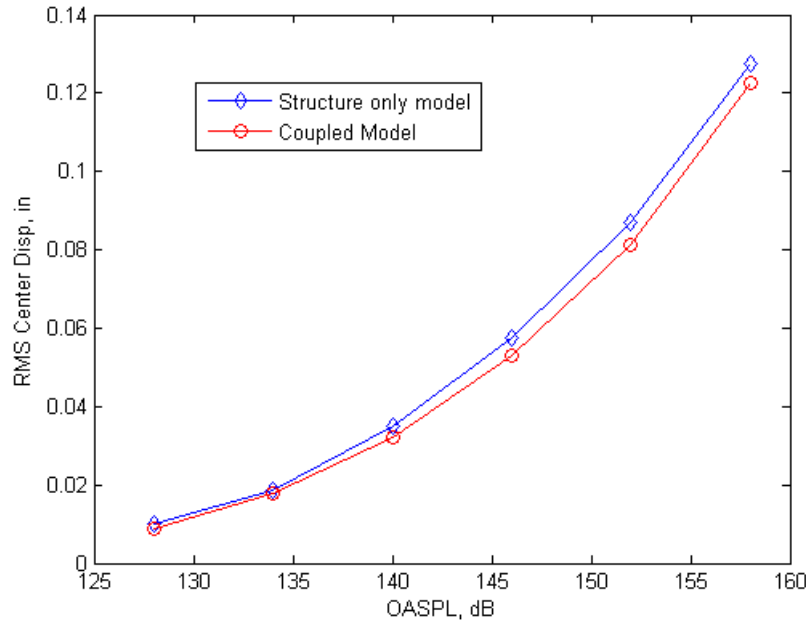


Figure 119. RMS center displacement for 0.06" thick plate ( $\zeta_s=0.005$ ) as the excitation varies.

The nonlinearity has to occur at a low enough excitation level for the acoustic response to affect the structure. This can be seen more readily by rewriting the right hand side of Equation 80 as

$$\mathbf{D}^T \mathbf{a} + \Psi^T \mathbf{f}_s(t) = \Psi^T \mathbf{S}^T (\mathbf{p}_{acoustic} + \mathbf{p}_{applied}) \quad (124)$$

where  $\mathbf{p}_{acoustic}$  is the pressure due to the acoustic response and  $\mathbf{p}_{applied}$  is the applied pressure. Equation 124 is the forcing term on the structural part of the coupled equations. If the acoustic

response pressure is small in comparison to the applied pressure, the coupled response will not be significantly different from the structure only model. That is, if the structural nonlinearity does not excite the acoustic response at a low enough applied pressure, the applied pressure will dominate rendering the coupled model unnecessary.

If damping is used to suppress the nonlinear structural response, the coupled model is unnecessary for all plate thicknesses. This is shown in Figure 120, where plate response is shown with damping is increased to 0.05. We see in Figure 121, that the response goes nonlinear at a relatively low excitation level for a plate thickness of 0.02" but that the structural damping is so high that the acoustic coupling has negligible effect.

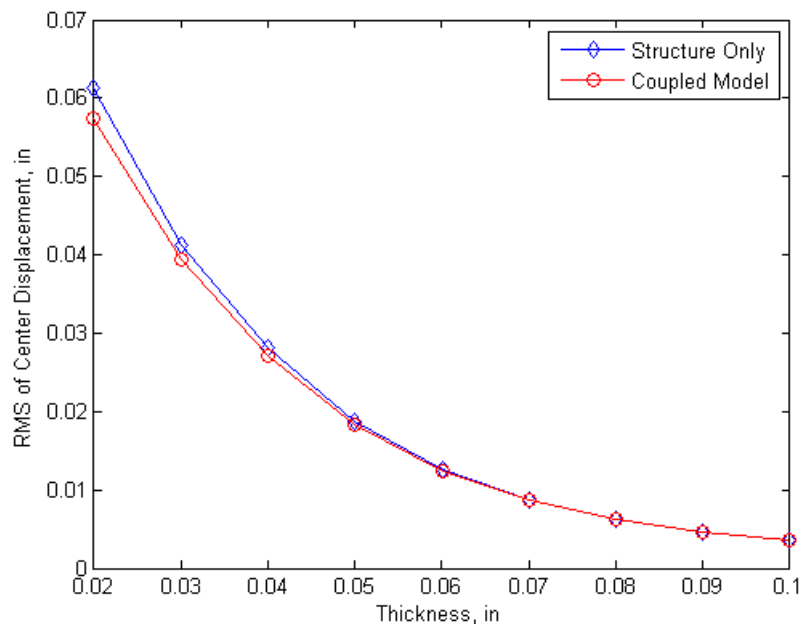


Figure 120. RMS of the center displacement as the thicknesses varies ( $\zeta_s=0.05$ , 140dB).

For the case of light damping, the acoustic coupling affects the response for all plate thicknesses. The case where the damping is reduced to 0.001 is shown in Figure 122. Lower damping equates to more nonlinear vibration at lower excitation levels and more chances for significant coupled response.

A preload that stiffens the plate will reduce the nonlinear effects. A more interesting and more common problem occurs when a preload softens the plate. In this example, the structure-only model is adequate for the 0.06" thick plate with 0.005 damping. However, let's assume a preload due to thermal expansion has softened the plate so that the linear frequency is now a third of the original (equivalent to the natural frequency of a 0.02" plate). The coupled model produces results significantly different from the structural model as shown in Figure 123.

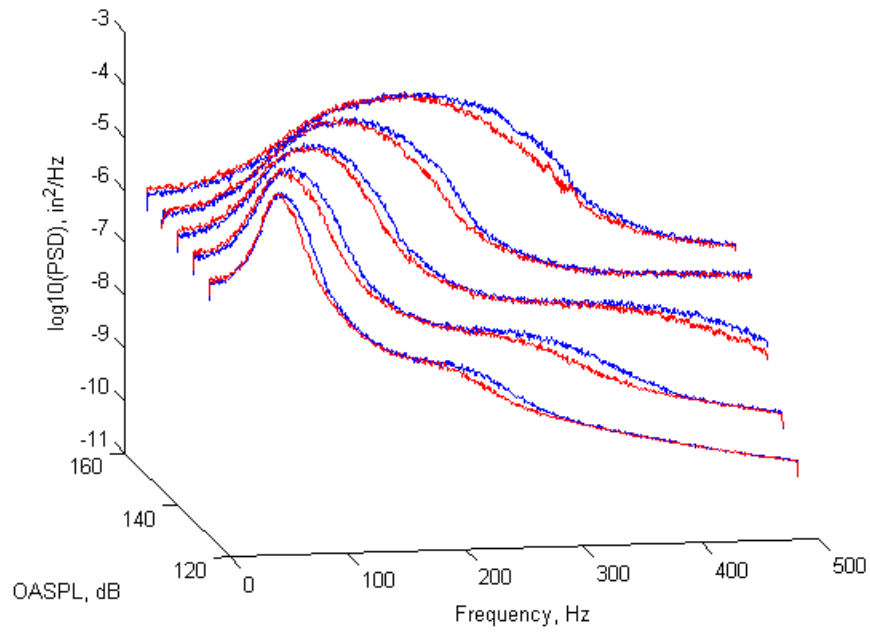


Figure 121. Response for the 0.02" thick plate ( $\zeta_s=0.05$ ) for 128-152dB. The structure only model is shown in blue, the coupled response in red.

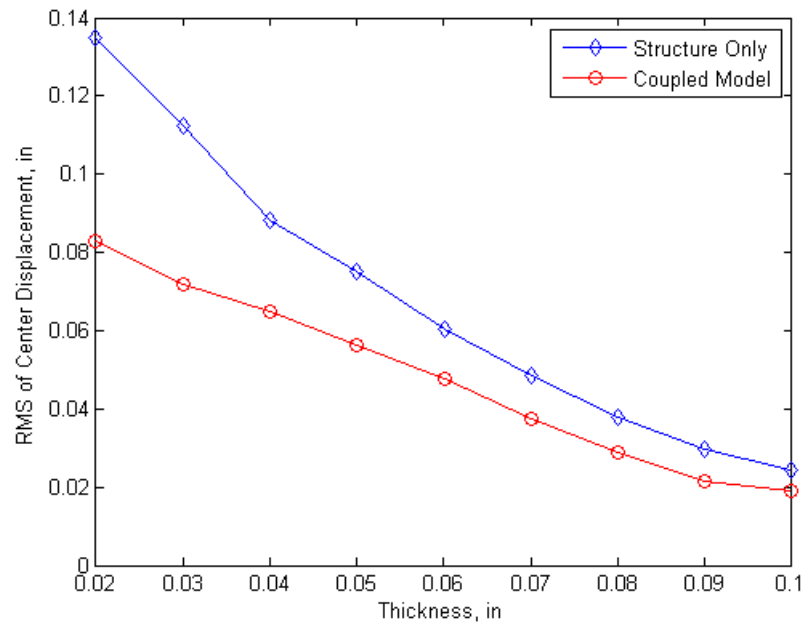


Figure 122. RMS of the center displacement as the thicknesses varies ( $\zeta_s=0.001$ , 140dB).

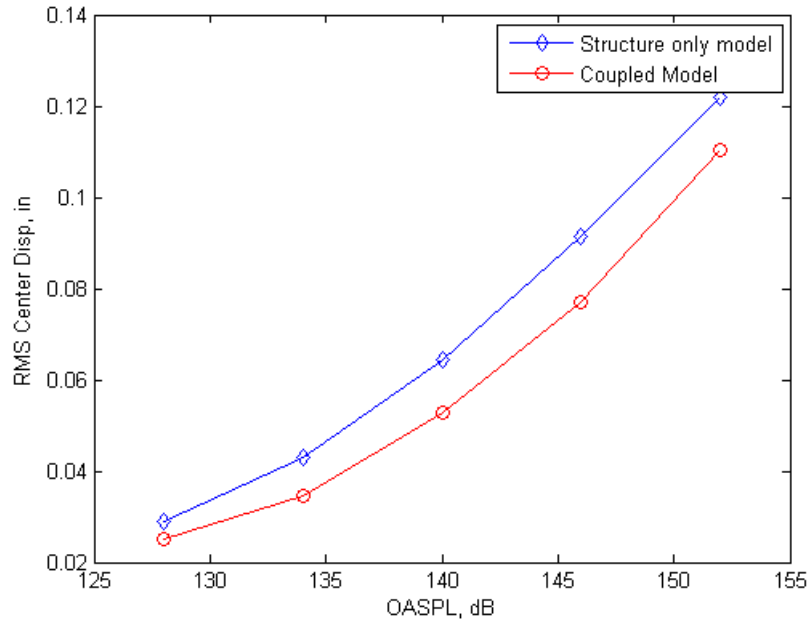


Figure 123. A 0.06" thick plate ( $\zeta_s=0.005$ ) with a softened stiffness.

In this application of nonlinear ROM's, the progressive wave facility was modeled as a long duct with a constant, square, cross section and the test plate was modeled as an 18"x12" aluminum plate with clamped boundary conditions. The thickness and damping of the plate were varied and response was predicted for a range of acoustic load levels. The acoustic coupling effects were found to be significant for thin plates, lightly damped plates, or thicker plates softened by a preload. The trends suggest that as the structural response becomes nonlinear at lower applied pressures, the effect of the acoustic coupling becomes more important. If plate response is significantly nonlinear at 140dB OASPL and has modal damping less than 1%, the acoustic effects may be important.

Conceptually the acoustic domain acts as multiple damped vibration absorbers. As the structural response becomes nonlinear, the frequency response of the structure broadens. As the response broadens, it is able to excite the acoustic modes. The acoustic modes interact with the structural modes. If the structural damping is low, some of the damping in the acoustic modes will be shared. If such is the case, the progressive wave facility has effectively altered the dynamics of the test article.

#### 4.5 The Curved Panel

The final structural application of nonlinear ROM's investigated in this project was a curved, unstiffened panel. Nonlinear ROM's were applied with excellent results to curved beams as discussed in Section 4.3. Curvature adds the effect of linear coupling between normal (bending) and tangential (membrane) displacements which is not present in straight beams or flat plates. A second important manifestation of curvature is the potential for softening nonlinearity. In flat structures, the nonlinearity is only of the hardening type which tends to limit response as excitation levels are increased. Softening nonlinearity can lead to dynamic response that increases more quickly with increasing excitation than linear response. A third effect of



curvature is deformation due to applied temperature. Thermal expansion in a curved structure changes the geometry and therefore the static stiffness. Thus, modal frequencies and mode shapes are also dependent on temperature.

Curved panels (shells) present additional challenges to the application of ROM's compared to straight beams or flat plates due to the two-dimensional displacement and strain fields and the higher modal density compared to curved beams. A few investigations of ROM's applied to acoustically excited curved panels have been conducted (for example Reference [60]). The ROM's employed showed the nonlinear softening that can occur as a result of curvature. Unfortunately, the accuracy of the predicted response could not be determined since the results were not compared to analytical or full-order numerical solutions.

The curved panel application presented here was used in a numerical study with perfectly clamped edges to better understand the performance of nonlinear ROM's applied to three-dimensional structures with curvature and elevated temperatures. In addition, test articles were fabricated and tested with acoustic loading at room and elevated temperatures. The following sections will present a detailed description of the panel configuration, the numerical study and the acoustic tests.

#### 4.5.1 Test Article Description

The example structure was a cylindrical stainless steel panel with bolted edges. The panel had dimensions of 9.75 in by 15.75 in (projected length in the curved direction) by 0.048 in thick and a radius of curvature of 100 in. The panel material had an elastic modulus of  $2.85 \times 10^7$  psi, Poisson's ratio of 0.3, density of  $7.48 \times 10^{-4}$  lb-sec<sup>2</sup>/in<sup>4</sup>, and coefficient of thermal expansion of  $10.5 \times 10^{-6}$  in/in/°F. The panel was bolted at its boundaries to a 1 in thick steel frame with screws on 1 in centers. A 0.25 in thick steel cap strip was used on top of the panel edges at the frame to provide a more rigid clamp. The panel test article and frame are shown in Figure 124.



Figure 124. The curved panel test article.

A FEM of the test article and frame was constructed in an in-house MATLAB code. The plate and frame were modeled with four-node shell elements and eight-node solid elements, respectively. The four support plates used to attach the frame to the support cart were also modeled with solid elements. One of the support plates can be seen at the left side of the picture in Figure 124. Clamped boundary conditions were applied at the nodes where the support plates attached to the cart. The screws and clamping strips which secured the panel to the frame were not explicitly modeled. Instead, the panel was assumed to be perfectly bonded to the frame mating surface. This linear modeling approximation was taken rather than trying to model the very complex bolted joint with nonlinear contact. The finite element mesh is shown in Figure 125.

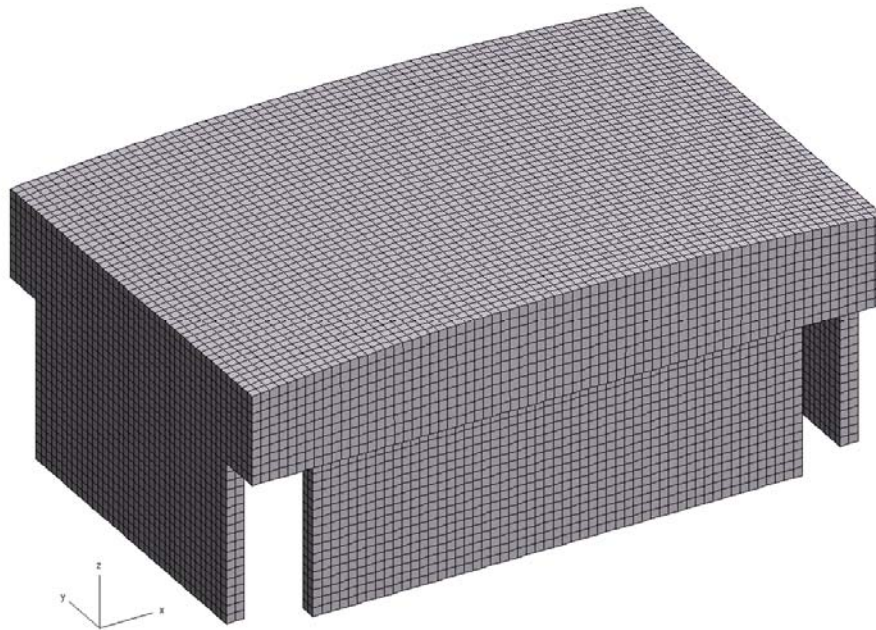


Figure 125. Finite element mesh of the curved panel test article.

#### 4.5.2 Numerical Study of the Clamped Panel

The panel configuration used for the numerical study was a simplified version of the test article model. It had the same dimensions, 9.75 in by 15.75 in, and material properties and thickness. However, the boundary conditions of the support frame were replaced with perfectly clamped edges. This greatly reduced the size of the finite element which enabled full-order nonlinear time integration to be performed. This configuration will be referred to as the clamped panel in the following discussion. This work was originally published as Reference 30.

A FEM of the clamped panel without the frame was constructed with a mesh of 39 by 63 four-node S4 shell elements in Abaqus. The finite element mesh is shown in Figure 126. Mass-proportional damping with  $\alpha=39.93$  was applied to yield a modal damping ratio of 0.01 at the first symmetric mode frequency of 271.5 Hz. Full-order simulations of 5s duration were performed at overall sound pressure levels of 140, 150, 160, and 170dB and uniform applied temperatures of 0, 20, and 50°F above ambient. The acoustic loading was a uniform fluctuating pressure with a flat spectral content in the 0-500Hz band. The numerical simulation was performed in Abaqus with implicit integration and a time step of  $5 \times 10^{-5}$  s. A simulation was also

performed at 160 dB and 20°F with a uniform static pressure of -4 psi applied to the panel. Displacement and strain at a few locations were stored for each Abaqus time simulation. The y-displacement was stored for a node that was 0.125 in from the center in both the x and z-directions. This was the node closest to the center and its displacement will be referred to as the center displacement. Strain was stored for the center element along a long edge of the panel, i.e. a curved edge. The strain is the average element strain in the z-direction at the top surface.

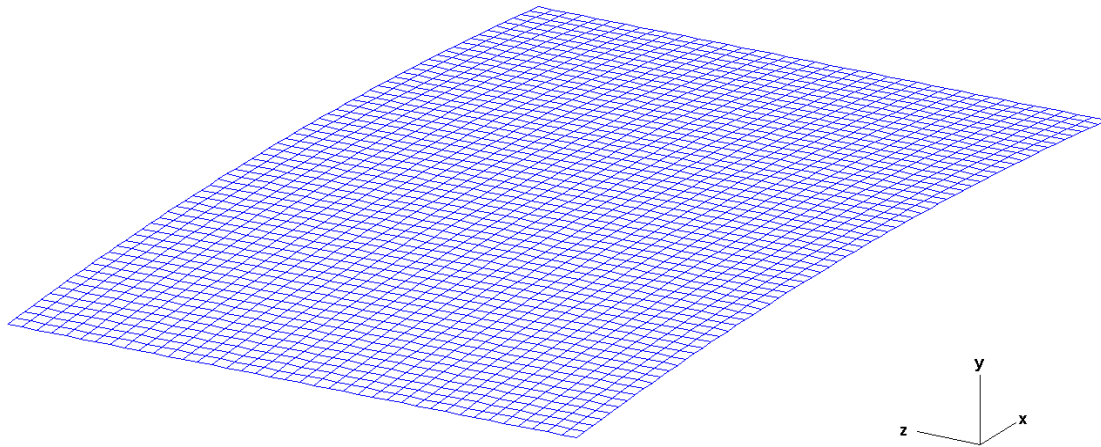


Figure 126. The clamped panel finite element mesh

Nonlinear ROM's were computed from the FEM using the constrained IC method with cold modes and hot modes at the two elevated temperatures. Modal damping ratios equivalent to the mass-proportional damping applied to the full-order model were used in the ROM's. Numerical simulations were performed for 20s using a modified Newmark integration scheme and a  $2 \times 10^{-5}$  s time step at the same loading conditions applied to the full-order FEM. The smaller time step compared to the full-order simulation was necessary to improve convergence.

The modal time history was stored for each ROM simulation. The displacements were recovered from the modal expansion. Membrane contributions to the displacements were added using the ICE process. Although, the displacements for any node and the strains for any element can be recovered from the modal time history, only the "center displacement" and strain along the center of the long edge of the panel were compared to the data from the Abaqus simulations.

Simulations with cold and hot-modes ROM's of the clamped panel were computed and the results compared to results from full-order model simulations. First, natural frequencies and mode shapes of the panel for the three applied temperatures (0, 20, and 50°F above ambient) are described and selection of modes included in the ROM's is addressed. The random response of ROM's at ambient temperature is presented next, followed by quasi-static response to the applied temperature cases. Finally, random response for the elevated temperature cases is discussed, including a special case at 20°F with a -4 psi uniform pressure on the panel. Accuracy of the cold-modes ROM's is emphasized in the work. A single hot-modes ROM is included for comparison at each elevated temperature.

The first 20 mode shapes and natural frequencies of the panel at ambient temperature—the cold modes—are shown in Figure 127. These contour plots, as well as all other contour plots in this

section, are for the y-displacements of the panel. The first 20 modes at 20 and 50°F above ambient temperature—the hot modes—are shown in Figures 128-129, respectively. Notice from the figures that even with a relatively small temperature change, there is a significant change in modal frequencies due to the stiffening effect of increased temperature. For example, when the temperature is increased by 20°F, the frequency of the first mode increased by more than 10% from 254.4 Hz to 282.1 Hz. By contrast, the first mode frequency of a flat rectangular plate will decrease with increasing temperature. Also notice that modes 3 and 4 change order with the application of temperature. The mode shapes for the 50°F case in Figure 129 are significantly different from the ambient temperature modes. This is not unexpected since the geometry of the panel has changed (the panel has bowed) and it has significant thermal stress.

Four sets of modes at ambient temperature were used as bases for cold-modes ROM's. These ROM's were used to compute panel response for each of the three temperature cases. The two-mode ROM included modes 2 and 3—the symmetric modes in the excitation bandwidth. The five-mode ROM added three higher frequency (out-of-band) symmetric modes—8, 10, and 12. The seven-mode ROM added two more symmetric modes, 18 and 20. Notice that the frequency of mode 20 is more than twice the upper limit of the excitation spectrum. The fourth basis set added the lowest two (in-band) anti-symmetric modes in the long direction, 1 and 5, resulting in a nine-mode ROM. Although the acoustic loading was uniform which would only excite symmetric modes in a linear problem, the results of curved beam studies in Reference 46 and Section 4.3 showed that anti-symmetric modes can be important in the nonlinear response if auto-parametric response can occur.

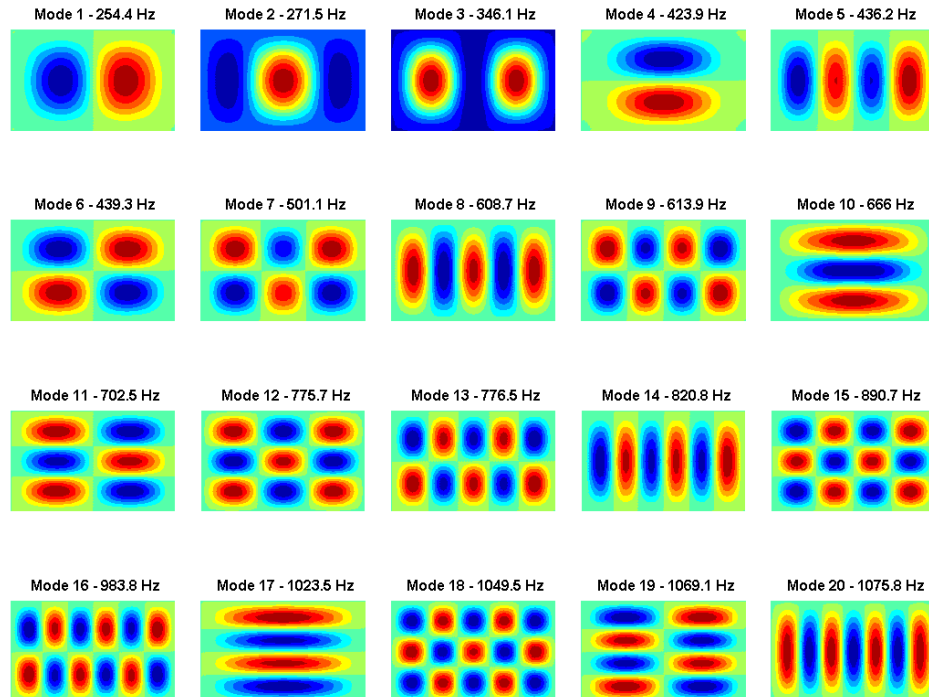


Figure 127. Frequencies and mode shapes at ambient temperature

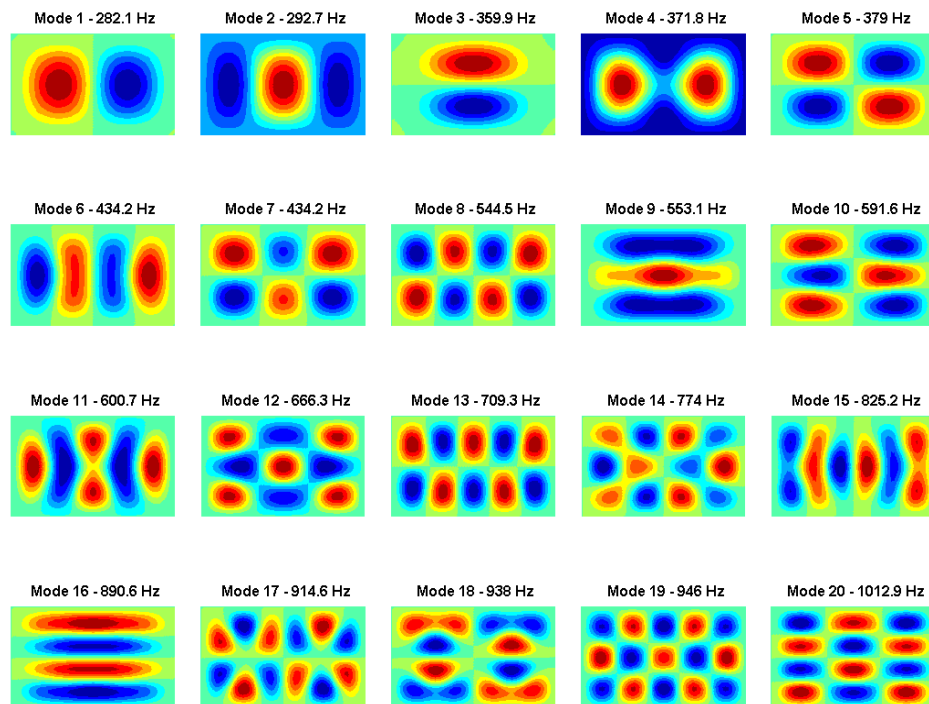


Figure 128. Frequencies and mode shapes at 20°F above ambient temperature

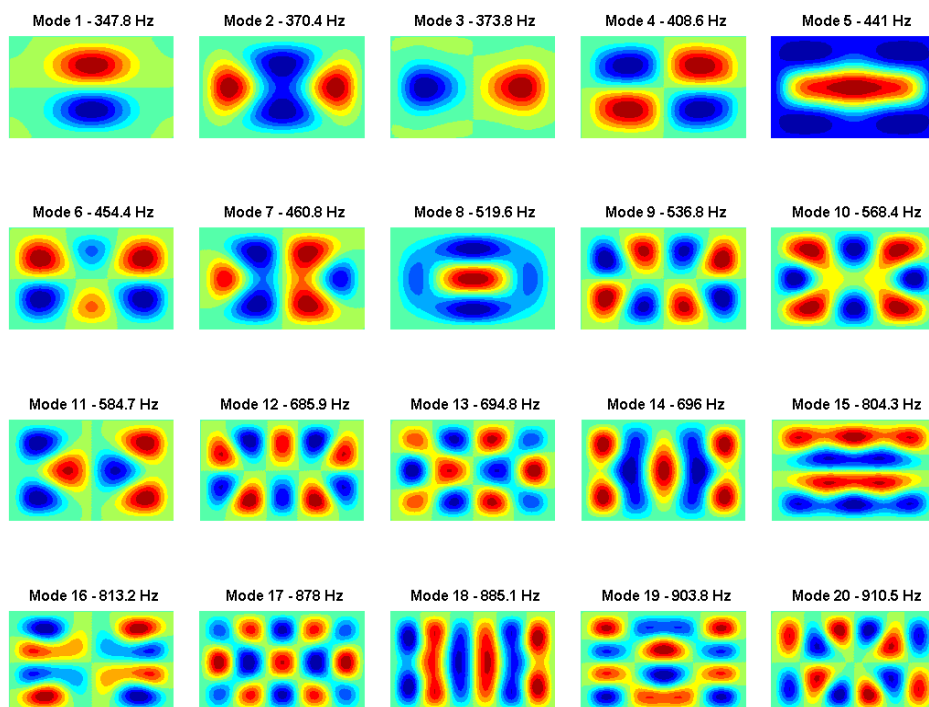


Figure 129. Frequencies and mode shapes at 50°F above ambient temperature



A hot-modes ROM comprised of the seven lowest symmetric modes (modes 2, 4, 9, 11, 12, 19, and 21) was computed for the +20°F elevated temperature case. These modes, except for mode 21, are shown in Figure 128. A hot-modes model with nine modes was also built for the +20°F elevated temperature case. This model contained the seven symmetric modes and two (in-band) anti-symmetric modes in the long direction (modes 1 and 6 in Figure 128). An 8 hot-modes ROM was used for the +50°F case using modes 2, 5, 8, 10, 14, 17, 23, and 26. These modes, except for modes 23 and 26, are shown in Figure 129. All eight modes are symmetric.

Ambient temperature dynamic response of the cold-modes ROM's subjected to the 0-500 Hz acoustic excitation spectrum is shown in Figures 130-132. Figure 130 shows the power spectral density (PSD) of normal displacement at the panel center for the 2, 5, and 7 cold-modes models at 160 dB. Full-order Abaqus simulation results are plotted for comparison. The 5 and 7 mode ROM's agree very closely with the Abaqus results up to 750 Hz. Even the 2 mode ROM shows reasonable agreement at the dominant first peak. Figure 131 shows the PSD of top surface strain for the element nearest the center of the long edge of the panel. As with the displacement results, the 5 and 7 mode ROM's match the Abaqus strain PSD very closely below 750Hz. Although significant peak broadening (a classic indication of nonlinear response) is not noticeable in Figures 130-131, nonlinearity is evident in the displacement and strain spectra. Both figures show relatively high response peaks in the 600-700 Hz range which is well above the excitation bandwidth of 0-500 Hz. Strain PSD's from the seven cold-modes ROM are shown in Figure 132 for the 140, 150, 160, and 170 dB loading cases compared to Abaqus results. The figure shows the excellent agreement of the seven-mode ROM, even at 170 dB where the response is highly nonlinear. Results from the nine-mode ROM, with two anti-symmetric modes added, were no better than the seven-mode ROM and thus are not shown in the figures. Apparently, the anti-symmetric modes did not contribute to the response as they did for the curved beam.

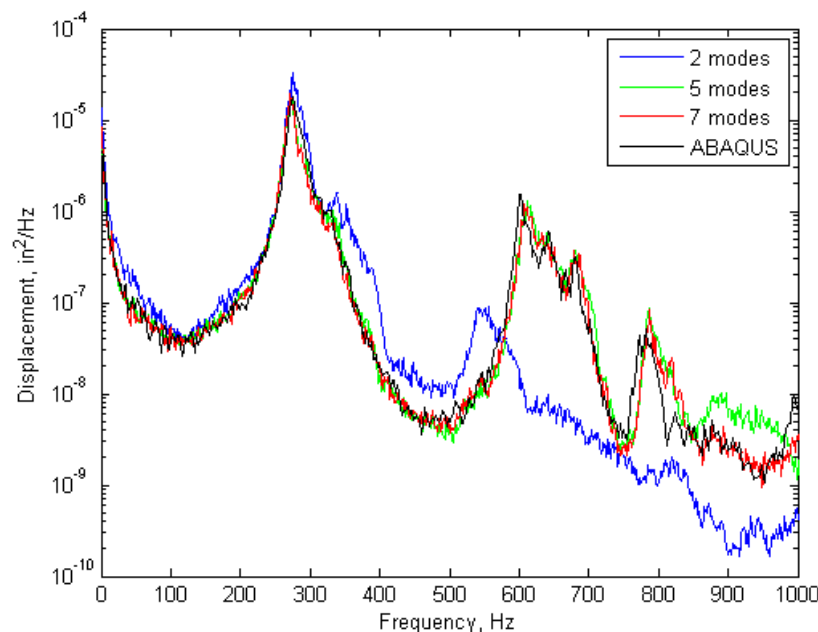


Figure 130. PSD of displacement at the center, 160dB, ambient temperature

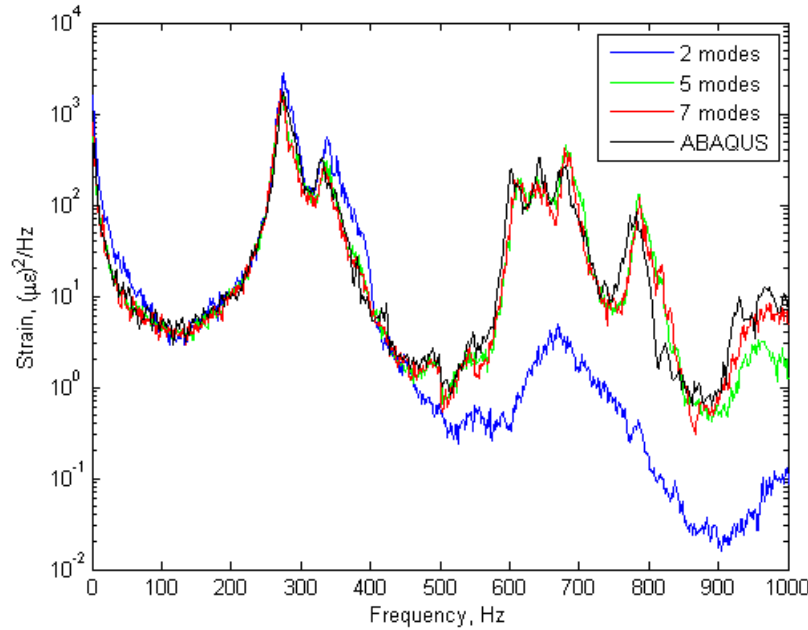


Figure 131. PSD of strain at the center of the long edge, 160dB, ambient temperature

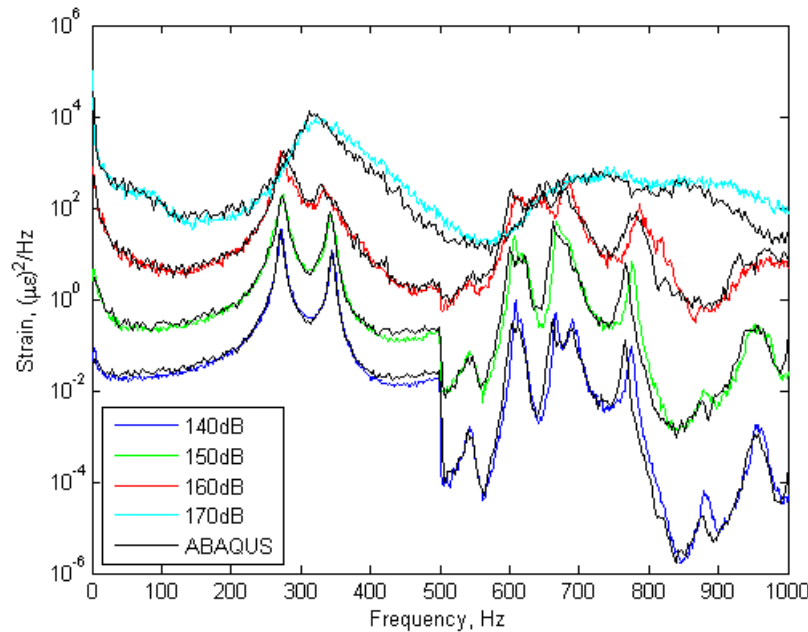


Figure 132. PSD of strain at the center of the long edge, 140-170dB, ambient temperature, for the 7-mode model

The seven cold-modes ROM was used to compute the nonlinear static deformation of the example panel to applied temperature fields of 20 and 50°F above ambient. The nonlinear modal equations were integrated for 2 s with the thermal force vector (and no acoustic loading). Quasi-static time integration was used because static solutions of the thermally-loaded modal models were unstable. Contour plots of the static deformation are shown in Figure 133 along with full-order FEM results from Abaqus. The deformed shapes and maximum displacements from the cold-modes ROM's are shown to agree closely with the Abaqus results. It should be noted here

that a cold-modes ROM must be able to accurately approximate the static thermal deformation in addition to nonlinear dynamic response.

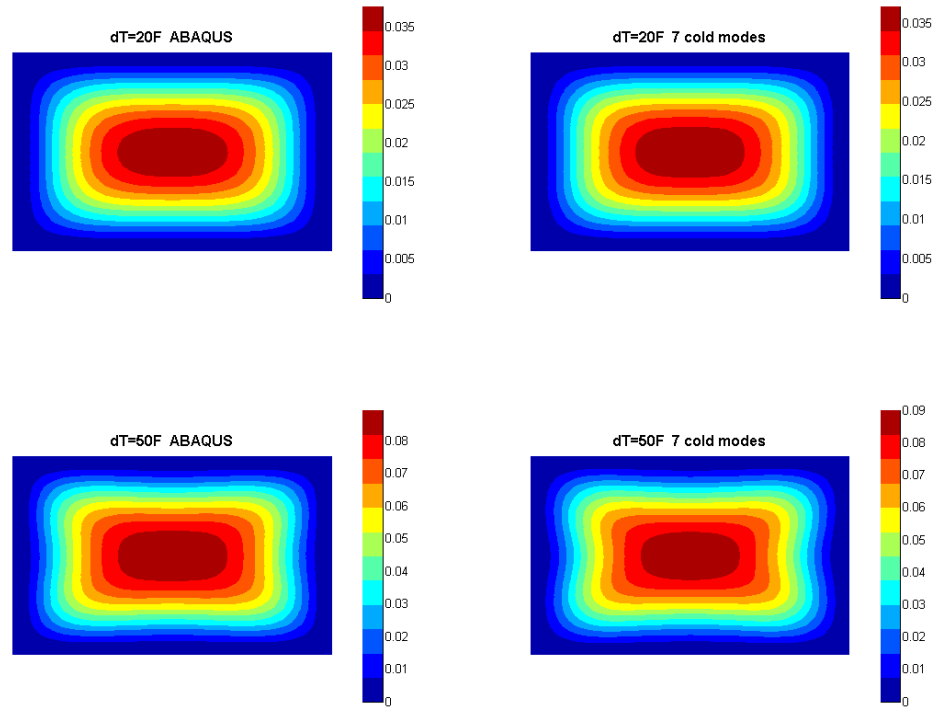


Figure 133. Static deformation due to applied temperature

The accuracy of the cold-modes ROM's in predicting quasi-static buckling of the thermally loaded example panel under pressure loading was investigated. A  $+20^{\circ}F$  temperature field was applied to each of the cold-modes ROM's at the beginning of a 2 s time simulation. During the simulation, a uniform static pressure was ramped linearly from 0 to -4 psi. The resulting displacement at the center of the panel is plotted versus time for each of the cold-modes models in Figure 134. The full-order Abaqus solution is also plotted in the figure. All five models show a nearly linear decrease in center displacement until approximately 1.2s into the simulation. At this point the pressure is -2.4 psi. Then, the displacement begins to increase followed quickly by a buckling event. The three ROM's with only symmetric modes (2, 5, and 7), along with the Abaqus solution, experience a decaying oscillation about the new equilibrium position and then continue to decrease in amplitude. The 9 cold-modes ROM buckles to a much different equilibrium position and also continues to decrease. The contour plots of the two buckled deformed states are shown in Figure 135. The 5 and 7 mode ROM solutions agree closely with the Abaqus result, but the 9 mode ROM solution is very different. Both solutions are assumed to be valid, but it is unclear why the 9 mode model buckles to a different shape.



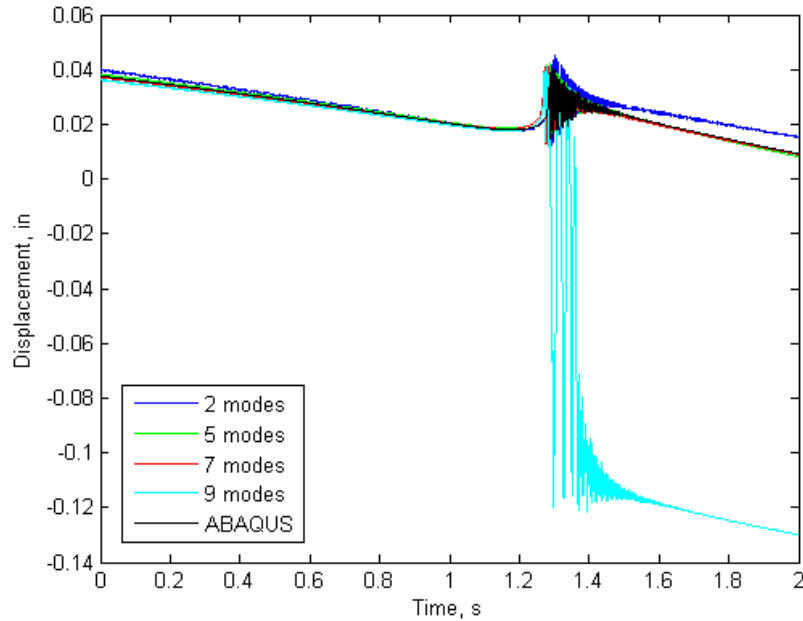


Figure 134. Center displacement vs time for ramped static pressure, +20°F, using the cold-mode models

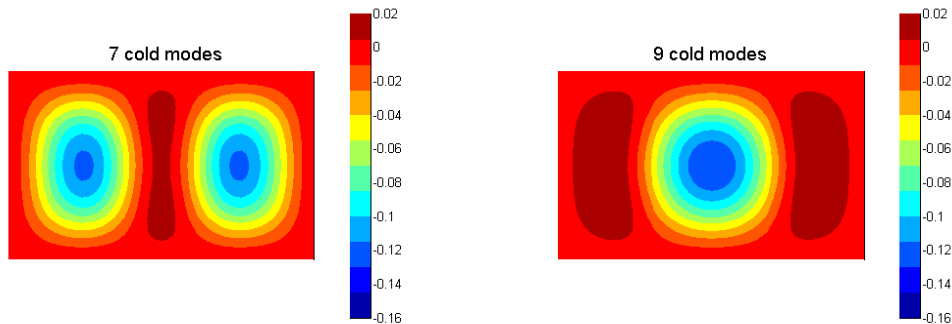


Figure 135. Post-buckled shapes for -4psi static pressure, +20°F

Simulations with random acoustic loading were performed with the cold and hot-modes ROM's at 20°F above ambient temperature. PSD's of top surface strain at the center of the long edge are shown in Figure 136 for the seven cold-modes model and the seven hot-modes model along with the Abaqus result. The cold and hot-modes ROM's agree closely and show good qualitative agreement with Abaqus, but the ROM predictions are somewhat higher than Abaqus at the dominate peak near 670 Hz. Adding modes to the cold and hot bases should improve the prediction, but was not investigated in this effort. Further evidence of the accuracy of the cold-modes ROM's is shown in Figure 137. Strain PSD's from the seven cold-modes ROM are shown for sound pressure levels of 140, 150, 160 and 170dB. The agreement with Abaqus predictions is very good over the range of excitation amplitude from nearly linear at 140dB to highly nonlinear at 170dB.

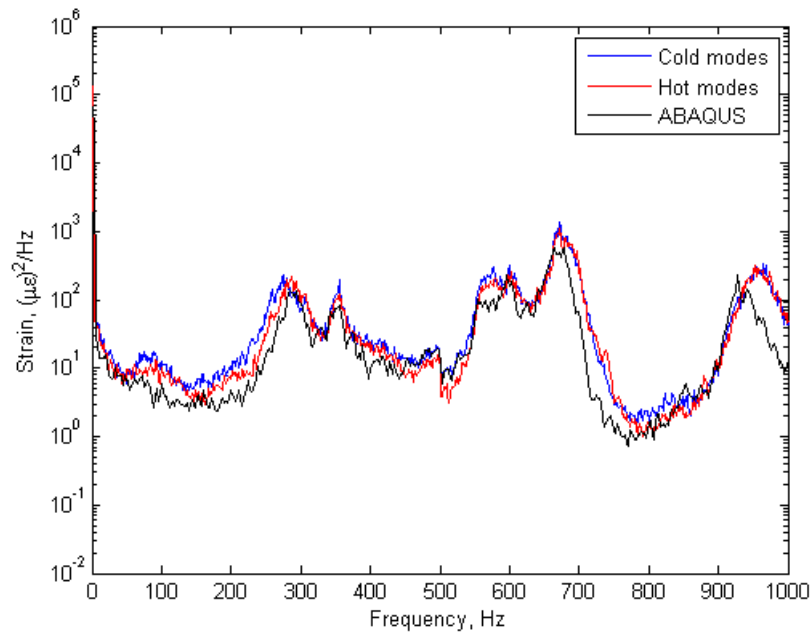


Figure 136. PSD of strain at the center of the long edge, 160dB, +20°F, for 7-mode models

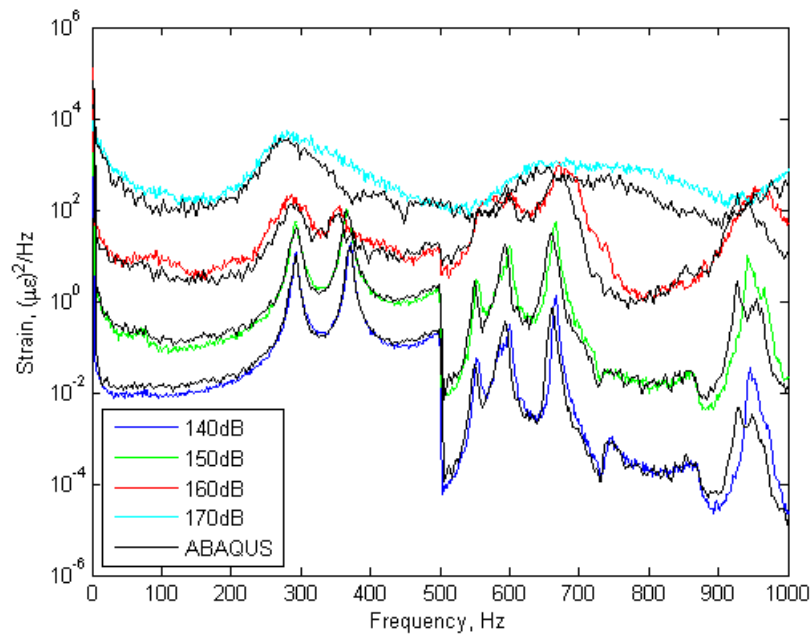


Figure 137. PSD of strain at the center of the long edge, 140-170dB, +20°F, for the 7-mode cold model

The effects of nonlinearity in the response are very noticeable in the strain PSD's of Figures 136-137. The dominant peak in the strain PSD's shown in Figure 136 occurs near 670 Hz, considerably above the excitation bandwidth. The amplitude of this peak is nearly an order of

magnitude higher than the highest value in-band. Curiously, the sum of the frequencies of hot mode 2 (292.7 Hz) and hot mode 4 (371.8 Hz) is 664.5 Hz; which is close to the frequency of hot mode 12 (666.3 Hz). All of these are symmetric modes. Thus, it is conceivable that the peak at 670 Hz may be due to the quadratic nonlinear interactions of two in-band modes driving the resonance of an out-of-band mode. The hot-modes model contains these three modes and is able to predict the response. It is remarkable that the cold-modes model does not contain any of these three modes; yet the model is able to predict this nonlinear behavior using a completely different basis.

Another manifestation of nonlinearity is shown in the frequencies of peaks in the strain PSD versus sound pressure level in Figure 137. The traces for 140 dB loading have response peaks near 290 and 370 Hz corresponding to linear modes 2 and 4 in Figure 128. These response peaks broaden and move to lower frequencies at the 150 and 160 dB levels indicative of nonlinear softening. The two peaks finally coalesce into a single broad response near 280 Hz at 170dB. The amplitude of this single peak at 170dB is also significantly higher than that suggested by the trend of the two peaks at 140, 150, and 160dB. The ROM's are shown to capture this rich nonlinear response very accurately.

Results of ROM simulations at 50°F above ambient temperature are shown in Figures 138-139. Strain PSD's for the 2, 5 and 7 cold-modes ROM's are plotted in Figure 138 for the 160dB loading case. The qualitative comparison with Abaqus is good, just like the +20°F case, but the agreement at the dominant response peak could be better. Strain PSD's from the 7 cold-modes ROM at the 4 acoustic load levels are shown in Figure 139. The qualitative agreement with Abaqus is not as good as the +20°F case, but this is to be expected. As the applied temperature is increased, the normal modes of the panel become less and less similar to the cold modes. So a given set of cold modes becomes a less accurate modal basis as temperature is increased. Including additional modes in the cold ROM basis should improve the accuracy, but was not investigated in this study. Hot-modes ROM results are not presented here for the +50°F case due to convergence problems with numerical integration. An 8 hot-modes model produced good results at 140 and 150dB, but would not reliably converge at 160 or 170dB. The source of the convergence problems could not be determined.

The severely nonlinear character of the response for the +50°F case at high acoustic pressures is evident in the strain PSD's in Figure 139. The traces for the 170 dB loading case in the figure show a nearly flat response from 0-1000 Hz. Compare this trace to the corresponding data from the ambient temperature and +20°F cases shown in Figures 132 and 137, respectively. The modal nature of the response seen in Figure 132 at ambient temperature is almost completely gone at +50°F. The curvature and thermal stress induced by the applied temperature cause significant linear and nonlinear stiffening resulting in a marked change in the response.

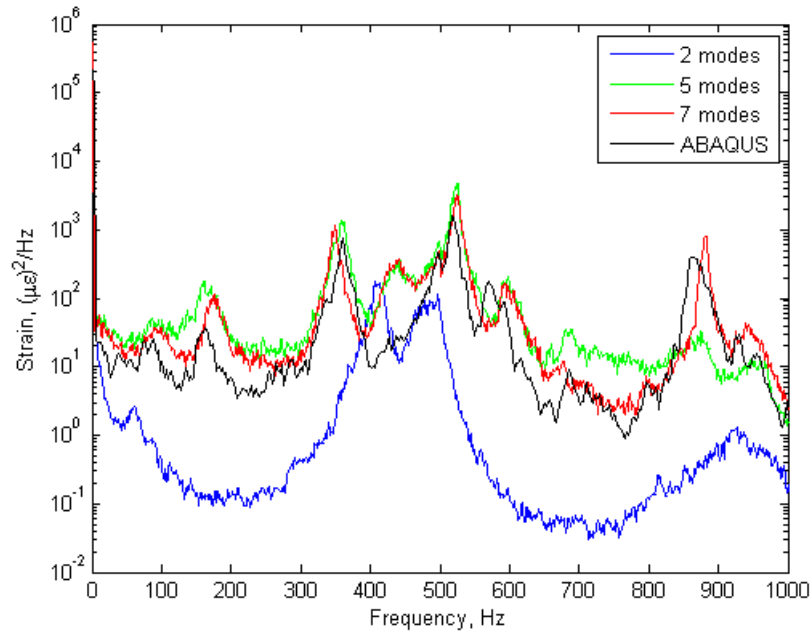


Figure 138. PSD of strain at the center of the long edge, 160dB, +50°F, for cold-mode models

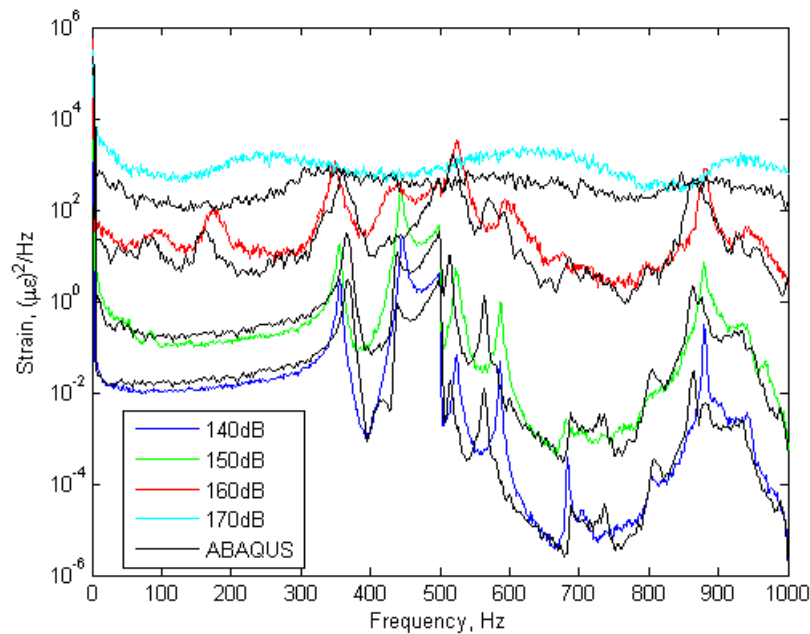


Figure 139. PSD of strain at the center of the long edge, 140-170dB, +50°F, for the 7-mode cold model

The final numerical test of reduced-order models applied to the example problem was a 160dB acoustic load combined with +20°F applied temperature and a uniform static pressure of -4 psi. This combined loading produced quasi-static buckling of the panel followed by dynamic snap-through. Simulations were performed on ROM's with 9 cold modes and 9 hot modes. The +20°F

uniform temperature field was applied initially along with a uniform static pressure decreasing linearly for 0 to -4 psi in 2 sec. These conditions are identical to those for the results shown in Figure 134. The temperature and static pressure were then held steady, and the 160dB fluctuating pressure was applied for an additional 5 s. The resulting displacement at the panel center versus time is shown in Figure 140 along with Abaqus full-order data. All three models are seen to buckle at approximately 1.2 sec into the simulations. This time corresponds to a static pressure of -2.4 psi. The hot-modes ROM and the full-order model buckle to one equilibrium position (shown on the left in Figure 135) while the cold-modes model buckles to a second equilibrium (shown on the right in Figure 135). Although the cold-modes ROM buckled to a markedly different deformed shape than the other two models, the random response of the three models is very similar. The time responses in Figure 140 show predominant oscillation about the first equilibrium with some large negative excursions. Occasionally the response will oscillate about the second equilibrium and then snap back. The PSD's of panel center displacement for the acoustic loading portion of the simulations are shown in Figure 141. Both the cold and hot-modes ROM's accurately capture the dominant portion of the response spectrum. Dynamic snap-through represents large stress events that can be very damaging to air vehicle panels. The scenario just described is analogous to an exterior aircraft panel exposed to aerodynamic heating, static pressure, and broadband acoustic loading.

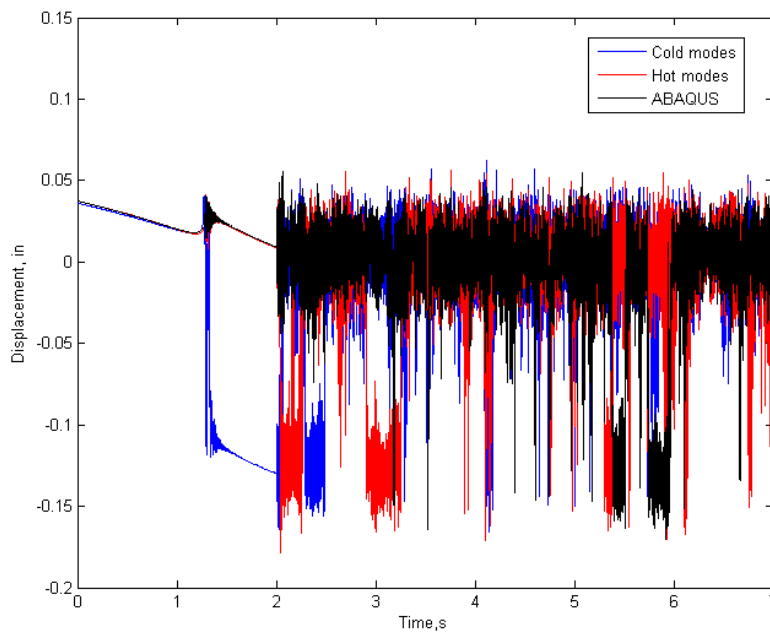


Figure 140. Center displacement vs time for -4 psi pressure, +20°F, 160dB, for 9-mode models

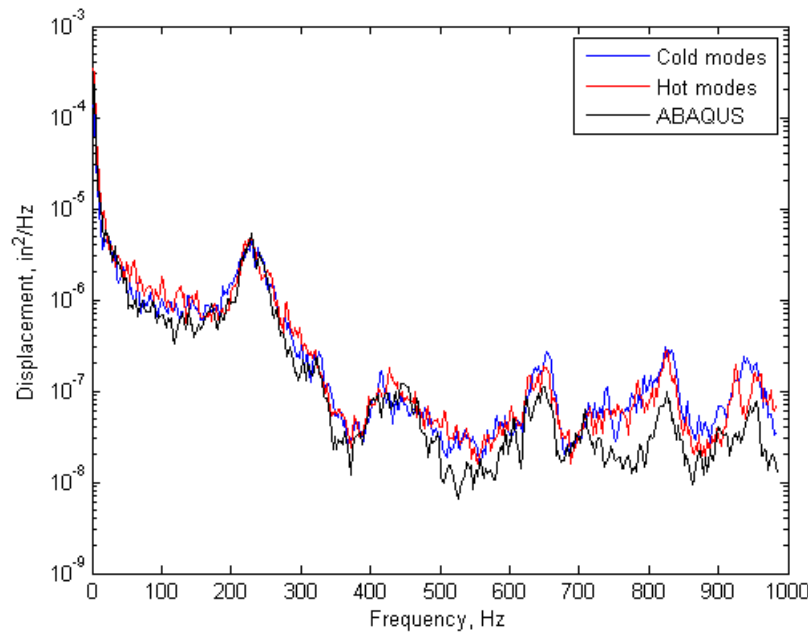


Figure 141. PSD of center displacement, -4psi, +20°F, 160dB, for 9-mode models

This section has demonstrated the successful application of nonlinear ROM's to a curved panel with clamped edges subjected to constant temperature fields and fluctuating acoustic pressures. The curved panel example problem posed significant challenges to the reduced-order models including static deformation and stiffening due to thermal loads, nonlinear softening, nonlinear modal coupling, quasi-static buckling, and dynamic snap-through. The example problem was not ideal. The applied differential temperatures in the example were modest in comparison to real conditions. However the clamped boundary conditions were much less flexible than the boundary conditions in real aerospace structures, producing strong nonlinear behavior.

Several cold-modes ROM's were computed and used to predict response to random acoustic loading at ambient temperature. Predicted displacement PSD's at the panel center and strain PSD's at the center of the long edge agreed closely with results from full-order Abaqus simulations. A cold-modes ROM was shown to accurately predict the static thermal deformation of the panel subjected to applied temperature fields of 20 and 50°F above ambient. The cold ROM's were also shown to accurately predict quasi-static buckling of the panel at +20°F due to a uniform static pressure.

Both cold and hot-modes ROM's were used to predict random acoustic response at the two elevated temperature states. Both types of ROM's produced good qualitative agreement with full-order results for panel edge strain, but showed some error at dominant peaks in the response spectra. The error was more pronounced for the +50°F case. This behavior is to be expected from a cold-modes ROM, since the modal basis becomes less accurate as the temperature is increased. Adding modes to the cold basis should improve the accuracy of the response, but no models incorporating more than 9 cold-modes were investigated. Performance of the hot-modes ROM's was problematic. A hot-modes ROM should be more accurate than a cold mode ROM with the same number of modes. However, this was not the case in this study. Furthermore, the hot-

modes ROM's were more prone to convergence problems in numerical integration than the cold ROM's due to thermal expansion.

The quadratic nonlinearity associated with curvature presented an interesting behavior for the +20°F case. Two in-band modes appeared to combine to excite an out-of-band resonance. This interesting nonlinear behavior was captured by both the hot and cold-modes models. Finally, post-buckled response of the panel at +20°F and -4 psi uniform pressure included snap-through response. This was well predicted by both the cold and hot-modes models.

A potential improvement to the IC method for computing nonlinear ROM stiffness coefficients was developed. The new approach, dubbed constrained IC, incorporates the inherent dependencies among the nonlinear coefficients to achieve a mathematically consistent solution. Anecdotal evidence suggested that constrained IC models were somewhat more stable when integrated at very high sound pressure levels compared to models using the original formulation, but this was not proven. A minor drawback to the constrained IC approach is the increased order of the identification problem to be solved which can potentially increase the error in the identified coefficients.

#### **4.5.3 Initial Acoustic Test of the Curved Panel Test Article**

An initial, exploratory acoustic test was performed on the curved panel test article in the SEF. The test was performed to experimentally evaluate the nonlinear response of the curved panel to provide data for planning a more thorough set of tests in the future. All testing was done at room temperature. No comparison of the test results was made with ROM predictions.

The test article configuration was described in Section 4.5.1. The test article is shown in Figure 124 mounted on the support cart prior to installation in the SEF sidewall. Displacement and velocity were measured at two locations on the panel surface during testing—near the center of the panel and a point in the upper left quadrant when viewed from the back. Measurement was performed with laser vibrometers. The two locations allowed measurement of dynamic response due to both symmetric and anti-symmetric modes. The panel was excited with a 50-500 Hz random spectrum at overall sound pressure levels of 140, 148, 152, 156, 160 and 164 dB. This range of levels was intended to excite panel response ranging from nearly linear to highly nonlinear.

A modal test was performed on the panel test article before it was installed in the facility. Identified mode shapes and frequencies are shown in Figure 142. The measured resonant frequencies shown in the figure are considerably lower than the frequencies from the FEM of the clamped panel shown in Figure 127. This difference was not unexpected since the model had perfectly clamped edges while the test article had the panel bolted to the frame.

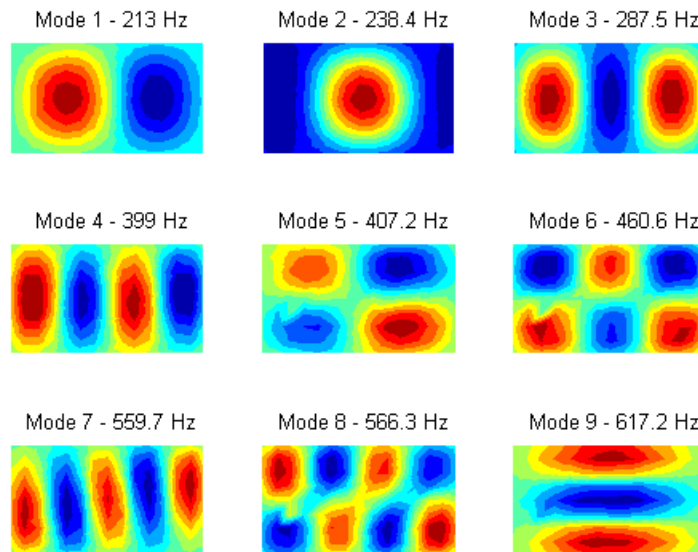


Figure 142. Mode shapes and frequencies of the curved panel test article

The PSD of velocity near the panel center is plotted in Figure 143 for the 6 excitation levels. The 140 dB graph in the figure shows resonant response peaks near three frequencies—240, 280 and 400 Hz. The first two peaks correspond to modes 2 and 3, both of which are symmetric and should have high response near the panel center. The third peak near 400 Hz should also correspond to a symmetric mode, but the two modes with frequencies near 400 Hz, modes 4 and 5, are both anti-symmetric. Anti-symmetric modes can be excited by the traveling wave acoustic loading but should not be observable near the panel center. As the excitation amplitude is increased, the mode 2 response peak near 240 Hz broadens and shifts lower in frequency. This behavior is indicative of nonlinear softening, a behavior seen typically in curved structures. In contrast to the mode 2 behavior, the mode 3 peak near 380 Hz broadens and shifts to higher frequencies—classic nonlinear hardening. The peak near 400 Hz also exhibits nonlinear hardening. Another interesting observation from the data in Figure 143 is the response peak near 450 Hz. This peak is not present in the 140 dB trace, but appears at 152 dB and then shows softening behavior as the input level is increased.

The off-center PSD's of panel velocity are shown in Figure 144. Several more response peaks are present in these data compared to the near-center measurements. The most noticeable difference is the peak near 210 Hz in the 140 dB trace. This peak corresponds to mode 1, an anti-symmetric mode. This peak eventually coalesces with the mode 2 peak at 164 dB. Additional modes can be seen responding in the 400-500 Hz range. These modes are most likely anti-symmetric.



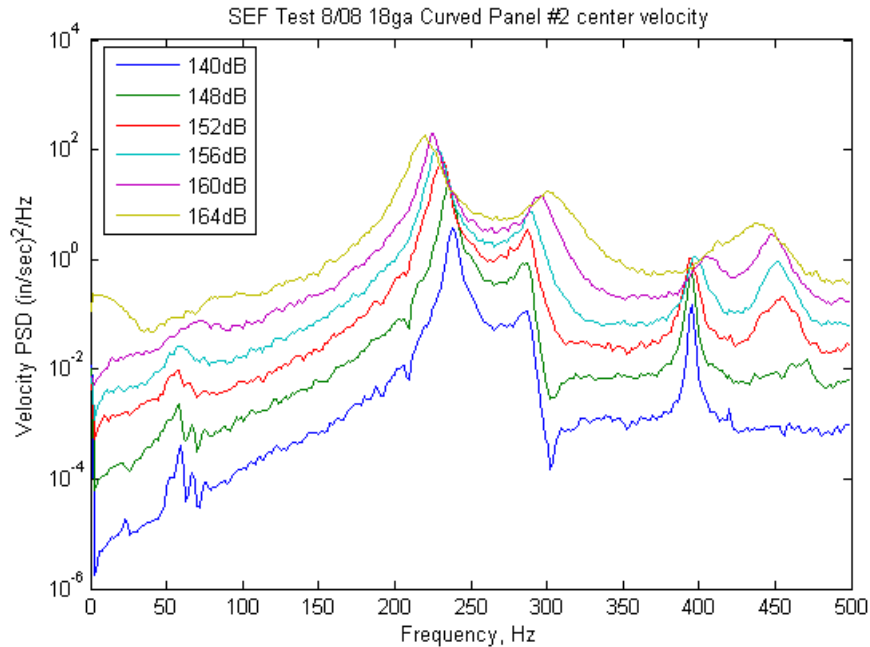


Figure 143. Velocity near the panel center for several sound pressure levels

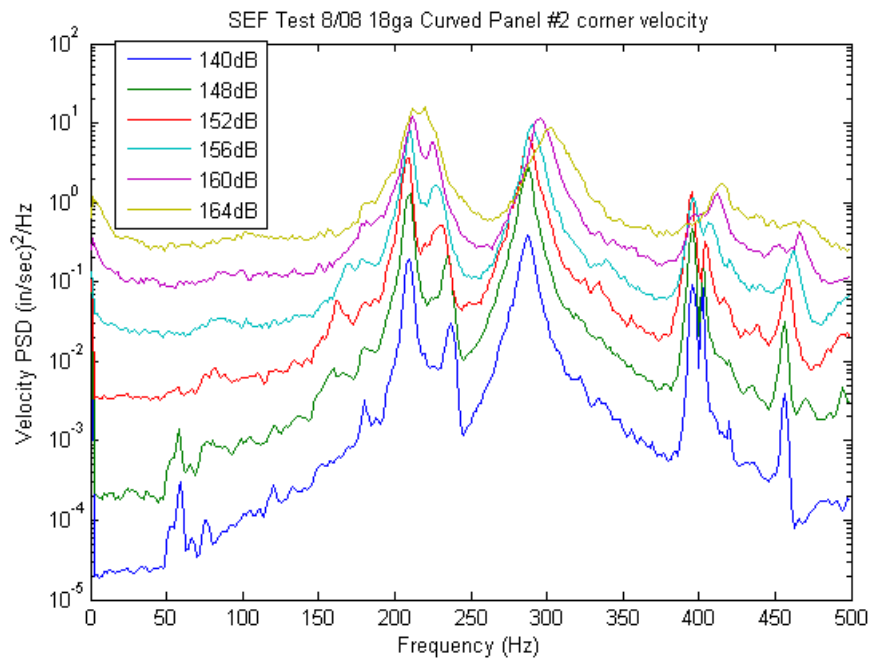


Figure 144. Velocity at a point in the upper left quadrant of the panel for several sound pressure levels

A single point modal impact test was performed after the acoustic testing to verify that panel frequencies had not changed due the high-level response. The tap test results indicated that the first mode frequency had dropped from 213 to 201 Hz and the second mode dropped from 238 to 219 Hz. When the panel was unbolted from the frame following the test, it was found that permanent deformation had occurred in the panel at the edge of the frame. Subsequent

simulations of panel response suggested that dynamic stresses in the panel at 164 dB could have exceeded the yield strength of the material. As a result of this finding, subsequent acoustic tests were limited to a maximum overall sound pressure level of 158 dB.

#### 4.5.4 Elevated Temperature Tests of the Curved Panel Test Article

A second series of tests was performed on the curved panel test article (with a new skin panel) to generate quantitative acoustic response data for comparison with nonlinear ROM predictions. The first step in computing nonlinear ROM's of the panel was to update the FEM of the test article to better match measured frequencies from the initial test described Section 4.5.3. The lowest 12 resonant frequencies and mode shapes of the original FEM are shown in Figure 145. These frequencies are 15-20% higher than the measured values shown in Figure 142. Several models were built to more accurately capture the stiffness of the bolted joint between the panel and frame and improve the frequency agreement. However, none of the detailed models were able to produce consistently better frequency agreement with physically realistic parameters. So, the decision was made to use the original model with a perfectly bonded joint between the panel and frame. Some effort was made to generate a model of the panel skin with discrete springs at the boundary to simulate the stiffness of the frame. This approach yielded a model with better frequency agreement than the model with the frame, but again, the model was not used due to uncertainty regarding physical realism of the boundary conditions.

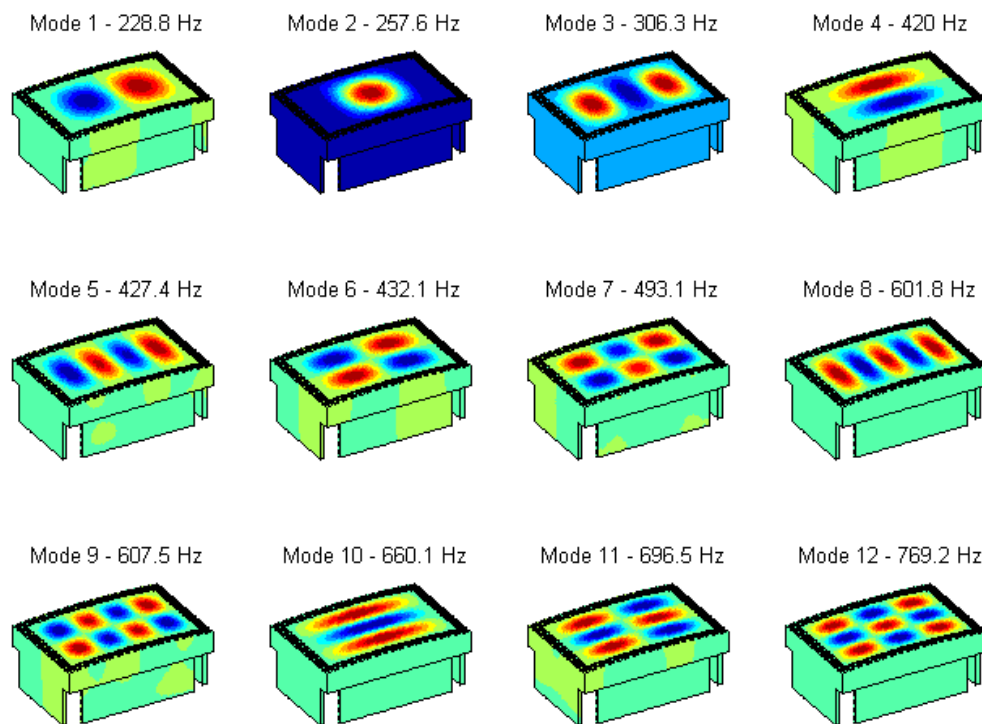


Figure 145. Resonant frequencies and mode shapes of the test article FEM

Two points should be emphasized regarding the "tuning" of the FEM of the test article to match measured data. The first is the effect of in-plane versus rotational stiffness at the boundary of the panel. The rotational stiffness primarily affects the linear response of the panel since it resists

rotation of the skin due to bending. Thus, rotational stiffness directly affects linear resonant frequencies. The in-plane stiffness primarily affects the nonlinear response of the plate since it resists the membrane stretching induced by large displacement nonlinearity. So, in-plane stiffness has a negligible affect on frequencies. Tuning a model to better match measured frequencies will therefore improve prediction of linear response but not necessarily nonlinear response. The second point to be emphasized is that a nonlinear ROM can be no more accurate at predicting the response of a structure than the FEM on which it is based. Therefore, inaccuracies in the nonlinear ROM's of the plate test article are just as likely to come from an inaccurate finite-element model as an inaccurate ROM. It is for this reason that the simplified clamped panel described in Section 4.5.2 was studied. The clamped panel ROM results were compared with full-order model results, not test results.

A nonlinear ROM was computed from the test article finite element model using the lowest four symmetric modes (2, 3, 8, and 10) plus the lowest two anti-symmetric modes (1 and 4). Resonant frequencies identified from a modal test performed before the test article was installed in the test facility were used in the ROM. Modal damping ratios of 1% were used in modes 2 and 3 with ratios of 0.5% in the other modes. The ROM was used to predict static deformation at uniform applied temperatures of 50 and 110 °F above ambient. The ROM was also used to predict acoustic response at ambient temperature with overall sound pressure levels of 140 and 158 dB. ROM predictions were not performed at the elevated temperatures. The simulations were computed with traveling wave loading, a time step of  $2e-5$  s, and a record length of 20 s.

A modal test was performed on the test article with a new skin panel prior to installation in the test facility. The resonant frequencies and mode shapes are plotted in Figure 146. The frequencies of the two test articles are compared in Table 25. Most of the frequencies for the second test article are higher than those for the first article. The exceptions are the (4,1) and (5,1) modes. The (4,1) mode of the second article is nearly identical to that of the first article while the (5,1) mode of the second article is lower. Also notice that modes 5 and 6 in Figure 146 both appear to be the (2,2) mode. It is likely that one of the modes is the (1,2) and the modal identification was not able to cleanly separate the two. The mode shapes of the second test article are noticeably less symmetric than those of the first article. The differences in frequencies and asymmetry in mode shapes is likely due to stresses in the article induced by clamping forces or thermal gradients. These stresses can have significant effects on linear frequencies.

The test article was subjected to radiant heating in the acoustic facility using a bank of quartz lamps mounted on the wall of the test section opposite the test article. The goal of this test was to measure the static deflection and strain of the article at uniform temperatures of 50 and 110 °F above ambient. The air flow used to power the facility noise generator was turned on during the static thermal tests to be consistent with a later test in which the same thermal loading would be applied along with acoustic loading. The temperature distribution on the back of the test article for the +50 °F case is shown in Figure 147. The measurement was performed with a calibrated thermal imaging system. It is obvious from the figure that the actual temperature distribution was far from the uniform temperature of 120 °F (50 °F above ambient) desired. The peak temperature at the panel center exceeded 140 °F while the temperature near the one corner was approximately 110 °F. The primary reason for the non-uniformity was the lack of a high-emissivity coating which is usually applied to the front surface of test articles. In addition, there

was a relatively large amount of silicone sealant applied to the strain gage at the center of the panel front surface which acted as a heat sink.

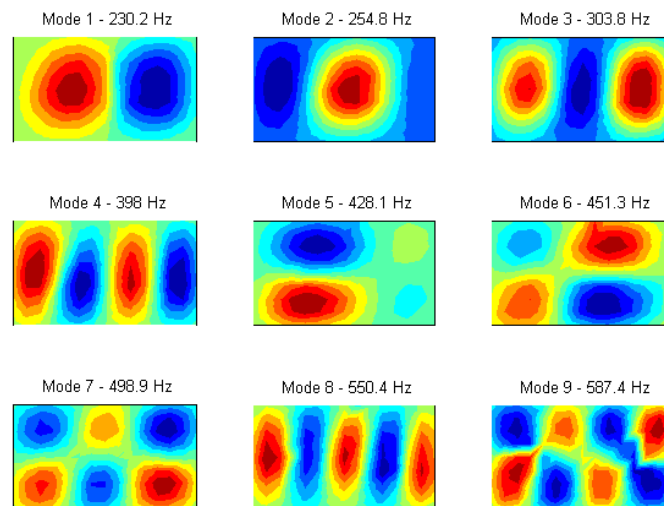


Figure 146. Resonant frequencies and mode shapes of the second curved panel test article

Table 25. Resonant frequencies of the two curved panel test articles

Mode	(2,1)	(1,1)	(3,1)	(4,1)	(2,2)	(3,2)	(5,1)	(4,2)	(1,3)
Test article 1	213	238	288	399	407	461	560	566	617
Test article 2	230	255	304	398	?	498	550	587	--



Figure 147. Temperature distribution on the test article for the +50 °F case

A vector of nodal temperatures was formed to approximate the measured distribution. The temperature vector was applied to the finite element model and nonlinear ROM to compute the resulting static deformation and strain. The applied temperature distribution on the test article is shown in Figure 148. The finite-element model prediction of panel displacements due to the applied temperature is shown in Figure 149. Displacements were measured at five points on the back of the panel while it was being heated. Displacement measurement was done with a digital image correlation (DIC) system. The DIC targets can be seen in Figure 147 as the darker colored dots. The predicted displacements at the five measurement points are compared to the measurements in Table 26. The predicted displacements are much greater than the measured values. The reason for the over-prediction was most likely error in the applied temperature field and not stiffness or boundary conditions of the model. The model was shown to be too stiff based on measured resonant frequencies, so it should have under-predicted, not over-predicted displacements.

Strains were also measured at seven locations on the panel with resistive strain gages. A pair of gages was located the center of the short edge of the panel (left edge when viewed from the front), one gage on each side of the panel surface, oriented normal to the panel edge. This back-to-back arrangement of the gages allowed independent computation of bending and membrane strains. A similar pair of gages was located at the center of the long edge of the panel (lower edge when viewed from the front) also normal to the edge. The remaining three gages were a rosette at the center of the front surface of the panel. The measured static strains for the two pairs of gages are listed in Table 27. Predicted values from the FEM are shown for comparison. The strain values from the rosettes are not listed because the local heating at the center of the panel caused large strain gradients there. The FEM over-predicted the strains as it did the displacements, except for the value on the front of the panel at the center of the left edge. Here the predicted strain was lower than the measurement by roughly one third.

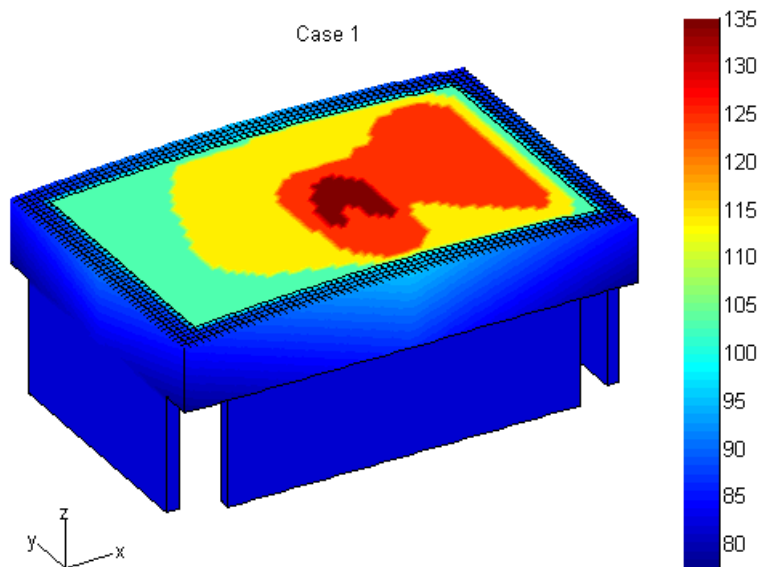


Figure 148. Temperature distribution ( $^{\circ}\text{F}$ ) for the FEM and ROM for the  $+50^{\circ}\text{F}$  case

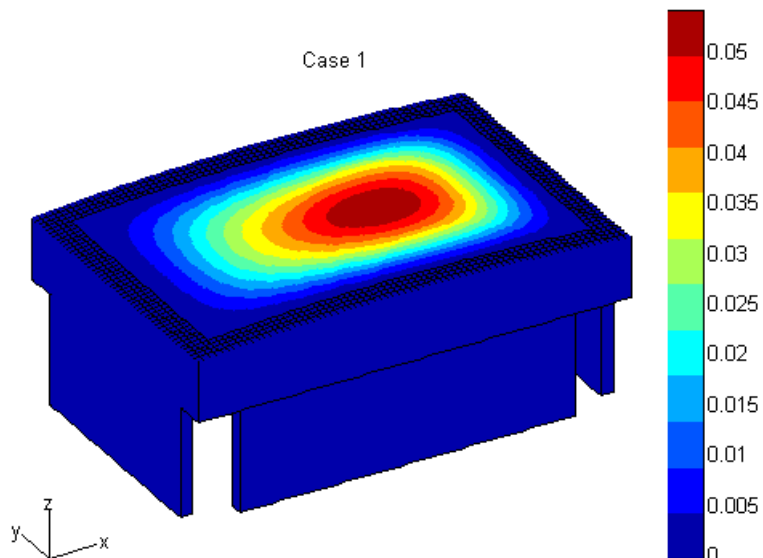


Figure 149. Predicted displacements (in) of the FEM for the +50 °F case

Table 26. Predicted vs measured panel displacements for the +50 °F case

	Measurement location:				
	upper left	upper right	center	lower left	lower right
Measured (DIC)	0.0175	0.0117	0.0327	--	0.0132
Predicted (FEM)	0.0354	0.0200	0.0484	--	0.0257

Table 27. Predicted vs measured panel strain ( $\mu\text{in/in}$ ) for the +50 °F case

	Measurement location:			
	left edge front surface	left edge back surface	lower edge front surface	lower edge back surface
Measured (strain gage)	-210	122	-407	352
Predicted (FEM)	-133	206	-514	550

The static thermal test was repeated for a nominal temperature of 110 °F above ambient. The measured temperature distribution is plotted in Figure 150. The distribution at +110 °F is very similar in shape to the +50 °F case. A vector of applied temperatures was formed for the +110°F case and is shown in Figure 151. The finite-element model prediction of panel displacements due to the applied temperature is shown in Figure 152. Measured and predicted displacements for the five locations are listed in Table 28. Again the panel displacements are over-predicted. Measured strains are listed in Table 29. Again the strains are over-predicted except at the value at the front of the panel at the center of the left edge.

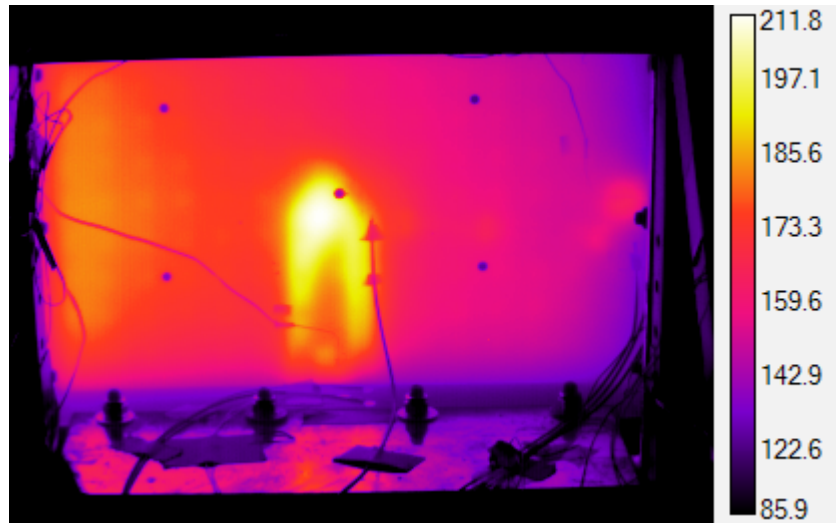


Figure 150. Temperature distribution on the test article for the +110 °F case

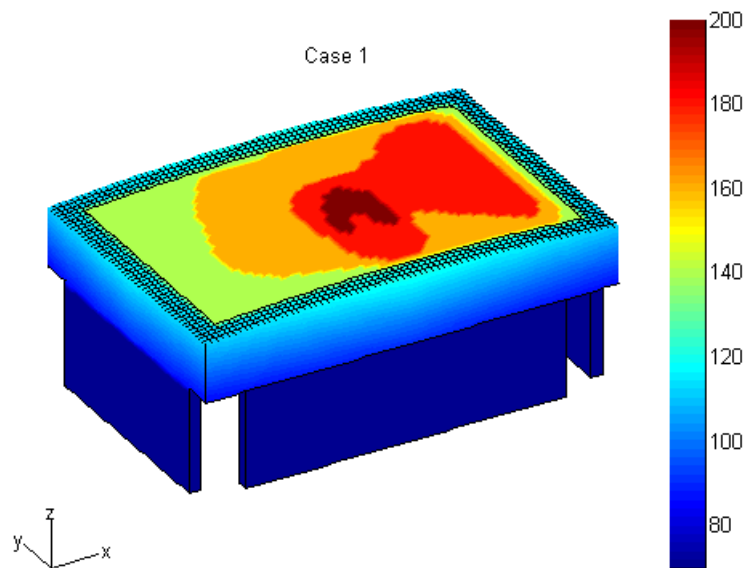


Figure 151. Temperature distribution (°F) for the FEM and ROM for the +110 °F case

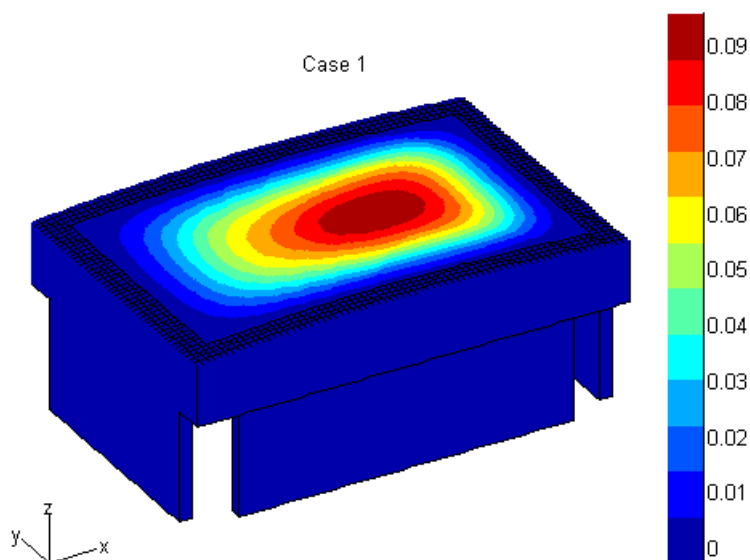


Figure 152. Predicted displacements (in) of the FEM for the +110 °F case

Table 28. Predicted vs measured panel displacements for the +110 °F case

	Measurement location:				
	upper left	upper right	center	lower left	lower right
Measured (DIC)	0.038	0.039	0.064	--	0.0342
Predicted (FEM)	0.0368	0.040	0.087	--	0.050

Table 29. Predicted vs measured panel strain ( $\mu\text{in/in}$ ) for the +110 °F case

	Measurement location:			
	left edge front surface	left edge back surface	lower edge front surface	lower edge back surface
Measured (strain gage)	-470	243	-833	352
Predicted (FEM)	-297	439	-948	1141

Ambient temperature acoustic testing was performed on the curved panel test article. Tests were conducted with a 50-500 Hz random spectrum at overall sound pressure levels of 140, 146, 152, and 158 dB. Sound pressure levels were limited to 158 dB due to the suspected overloading of the first test article at 164 dB. Velocities and displacements were measured near the center of the plate and at a point in the upper left quadrant (as viewed from the back) using laser vibrometers.



The PSD of velocity at the center point is plotted in Figure 153 for the 4 excitation levels. The traces in the figure look very similar to those for the first test shown in Figure 143. The major differences are the higher resonant frequencies and missing peak near 450 Hz in the second test data. The velocity PSD's for the corner point are plotted in Figure 154. There are noticeable differences in this figure compared to the previous test, again due primarily to changes in panel frequencies.

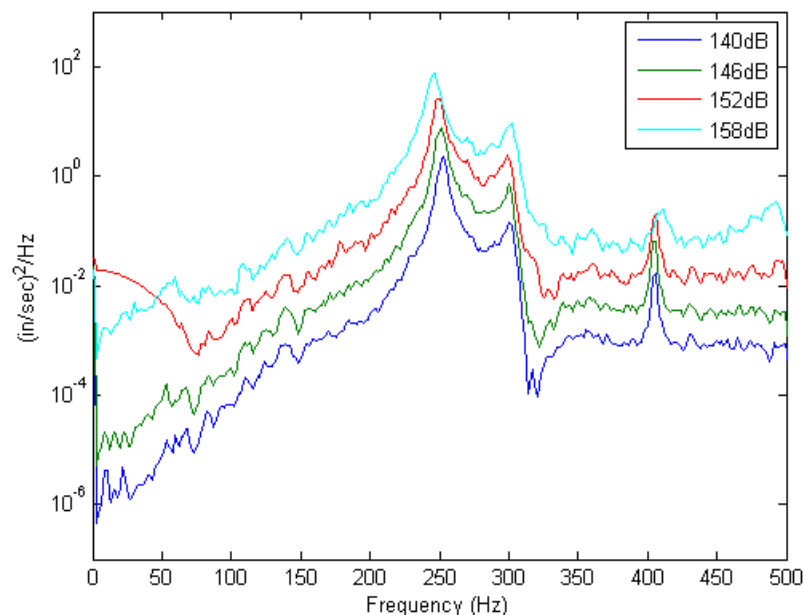


Figure 153. Measured PSD of panel velocity near the center

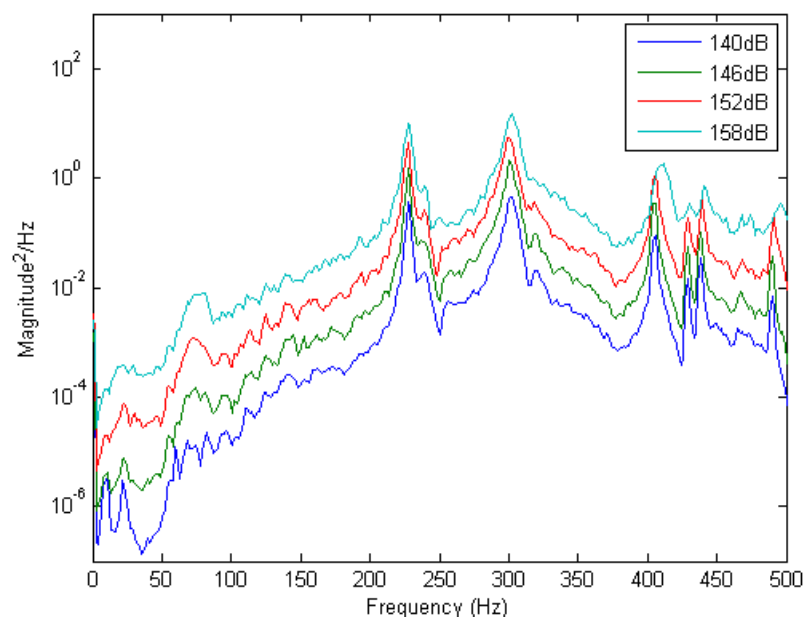


Figure 154. Measured PSD of panel velocity at the corner point

Predicted PSD's of center velocity from the 6-mode nonlinear ROM are plotted in Figure 155 with test data for the 140 and 158 dB cases. The results for the corner point are shown in Figure 156. The agreement at both locations is very good. It should be noted that the nonlinear ROM used measured frequencies from the modal test.

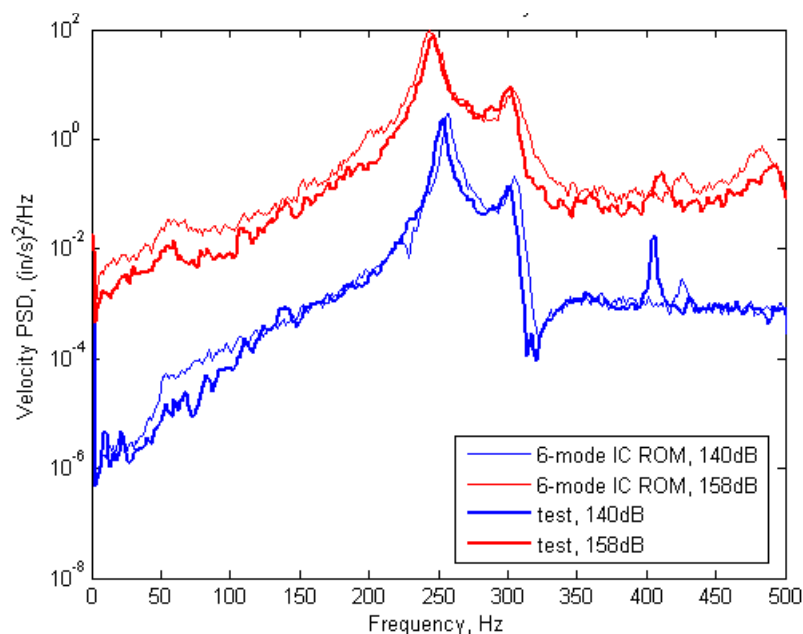


Figure 155. Panel center velocity from test and IC ROM at ambient temperature

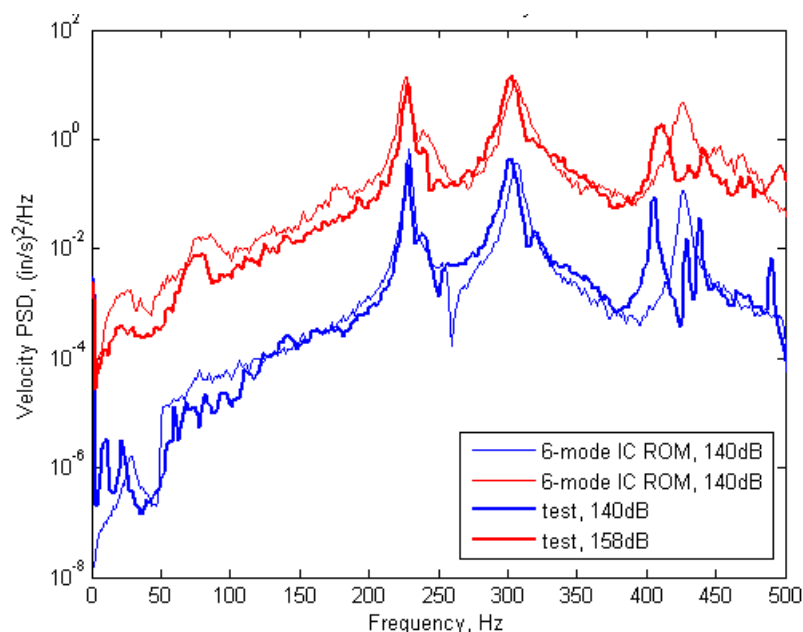


Figure 156. Panel corner velocity from test and IC ROM at ambient temperature

Elevated temperature acoustic testing was performed on the curved panel test article. Tests were conducted with a 50-500 Hz random spectrum at overall sound pressure levels of 140, 146, 152,

and 158 dB for both temperature cases. Velocities and displacements were measured near the center of the plate and at a point in the upper left quadrant (as viewed from the back) using laser vibrometers. The PSD's of velocity at the center point are plotted in Figures 157 for the +50 °F case. The PSD's at +110 °F are plotted in Figure 158.

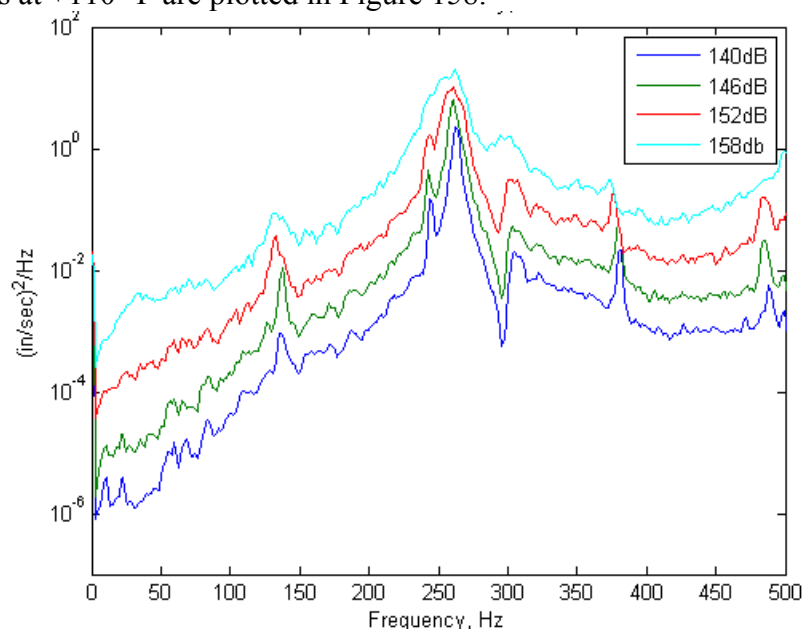


Figure 157. Measured PSD of panel velocity near the center for the +50 °F case.

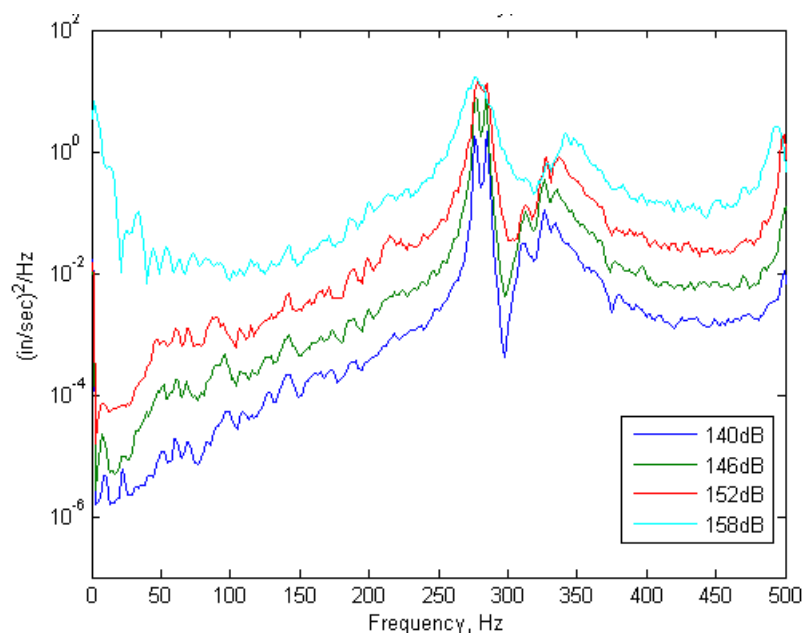


Figure 158. Measured PSD of panel velocity near the center for the +50 °F case.

The normal modes of the FEM with the +50 °F and +110 °F applied temperature distributions shown in Figure 151-152 were computed. The modes are shown in Figures 159-160. The applied temperatures both increased the resonant frequencies and introduced asymmetry into the mode shapes.

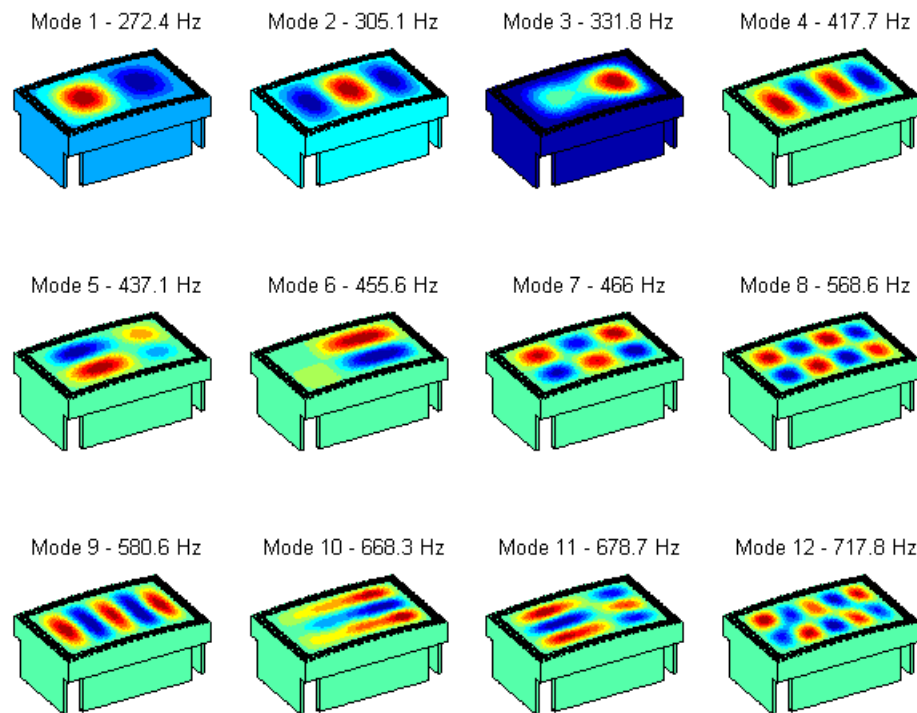


Figure 159. Natural frequencies and mode shapes of the FEM for the +50 °F case.

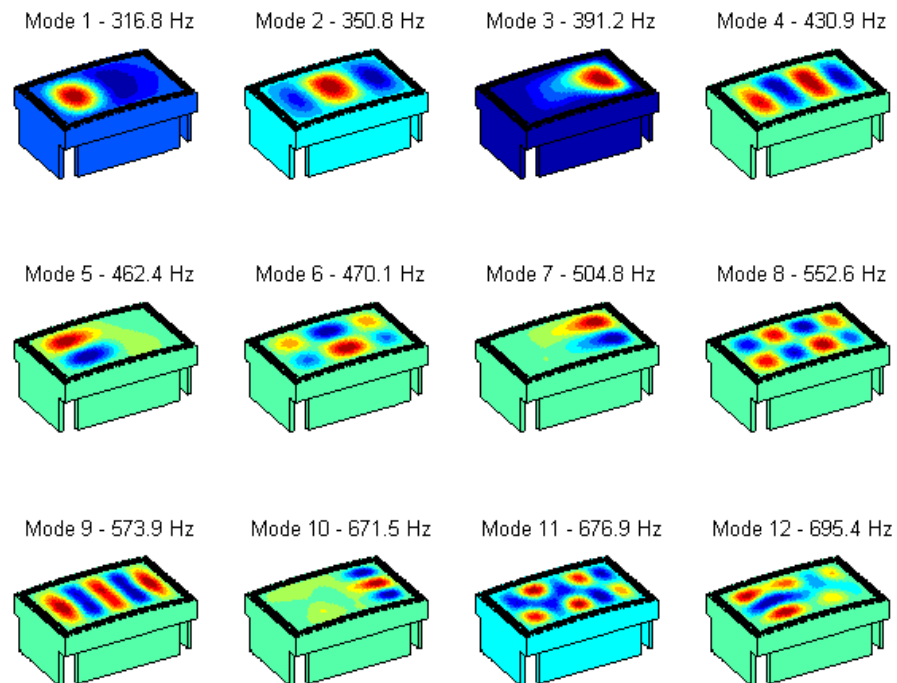


Figure 160. Natural frequencies and mode shapes of the FEM for the +110 °F case.

Nonlinear ROM's were computed based on the hot modes for both elevated temperature cases. However, agreement with measured data was poor. The poor agreement was attributed to inaccuracies in the FEM and the applied temperature fields, not the ICE procedure used to compute the ROM's. At ambient temperature, the ROM, and therefore the FEM, produced very good agreement with measured data using measured frequencies (which corrected the linear portion of the model). So the nonlinear portion of the FEM was assumed to be reasonably accurate too. The major remaining uncertainty was the actual temperature distribution in the test article. Although an applied temperature vector was synthesized to match the measured distribution, it was apparently still a poor approximation of the actual distribution.

#### **4.6 Coupled Structural-Acoustic Examples**

Two simple coupled structural-acoustic example problems were studied to develop and demonstrate approaches to building nonlinear ROM's for this class of problems. The first problem was a clamped-clamped beam in a two-dimensional infinite baffle. This problem was used to develop the complex modes approach to building coupled ROM's. The second example was a clamped-clamped beam coupled to a two-dimensional acoustic duct. This example explored the uncoupled modes approach for generating nonlinear ROM's. The examples are described in the following two sections.

Structural-acoustic problems can occur in both interior and exterior acoustic domains. One exterior problem of interest to the Air Force is the response of a stiffened skin panel to propulsion or aerodynamic noise. In the interior problem, resonant modes of the enclosed cavity of air couple with modes of the structure. A heavily damped acoustic mode can couple with a lightly damped structural mode resulting in two coupled modes with moderate damping. This mechanism is believed to have contributed to the increased damping measured in the test article of Sections 4.4.5 and 4.4.6. This type of behavior does not occur in exterior problems. The unbounded physical acoustic domain does not possess resonant acoustic modes. Modes of the coupled physical system consist of structural modes with associated pressure fields that capture the acoustic radiation from the structure.

##### **4.6.1 2-D Beam in an Exterior Acoustic Domain using Complex Reduced-Order Models**

The complex modes approach to computing nonlinear ROM's was applied to a two-dimensional example problem to evaluate its accuracy. This section describes implementation of the approach and compares predicted results to results from a full-order simulation. This work was originally documented in Reference [28].

The ability to reduce the coupled exterior problem with nonlinear structural response to low order, as has been demonstrated with the uncoupled structural problem, would be a significant advancement which would allow very efficient time simulation. This section describes such an approach using complex modes of the coupled system. A state space formulation was used which uncouples the linear equations of the non-proportionally damped, unsymmetric system. The formulation of the complex ROM (CROM) is discussed in Section 3. An example problem consisting of a beam with clamped ends in a baffled, two-dimensional, unbounded acoustic domain was analyzed.

The problem consisted of a thin beam with clamped ends in an infinite baffle at the center of an infinite circular acoustic domain. The example problem is shown schematically in Figure 161. A monopole source was located on the baffle to the right of the beam in the upper half of the domain. The source was driven by a random acoustic force time history with a shaped frequency spectrum. The source generated a circular acoustic wave which propagated along the beam. This source configuration was used to approximate a plane acoustic wave propagating along the upper surface of the beam. The monopole was used in the example because it was much easier to implement in the FEM than a plane wave. The primary difference between the monopole source and a plane wave is that the circular wave from the monopole attenuates inversely proportional to the square root of the distance from the source while the plane wave does not attenuate.

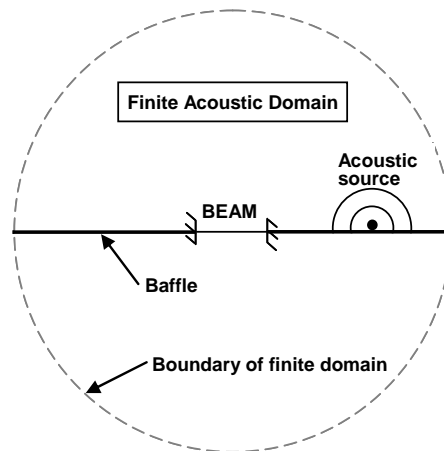


Figure 161. The example problem

The beam in the example problem was identical to that used in Section 4.1 except for its width. The primary design criteria for the beam were that it had multiple bending modes in the 0-500 Hz frequency range and modal damping ratios less than 0.02. These values are typical of stiffened aircraft skins which can experience sonic fatigue. The beam was 9.0 in long, 1.0 in wide and 0.031 in thick. The beam material was steel with an elastic modulus of  $29.7 \times 10^6$  lb/in<sup>2</sup>, shear modulus of  $11.6 \times 10^6$  lb/in<sup>2</sup>, and density of  $7.36 \times 10^{-4}$  lb-s<sup>2</sup>/in<sup>4</sup>. The properties of air were: bulk modulus of 20.5 lb/in<sup>2</sup>, density of  $1.14 \times 10^{-7}$  lb-s<sup>2</sup>/in<sup>4</sup>, and speed of sound of  $1.34 \times 10^4$  in/s. The acoustic source point was located 22.5 in from the end of the beam.

The desired acoustic loading on the beam was a grazing-incidence acoustic wave with a random time history, a flat frequency spectrum from 20-600 Hz, and overall sound pressure levels (OASPL) of 122, 140, and 152dB. This frequency range was specified to excite the first three bending modes of the beam at approximately 79, 218 and 427 Hz. The three input levels resulted in nearly linear, moderately nonlinear, and highly nonlinear response of the beam, respectively. The frequency spectrum of acoustic pressure at the source point had to be “shaped” to achieve the desired flat spectrum at the beam, due to the dynamic characteristics of the acoustic domain. This spectrum “shaping” process was done with a full-order linear model with the beam uncoupled from the air to avoid having sound re-radiated from the beam affect the acoustic

loading. The power spectral densities of acoustic pressure at the source and the surface of the beam center for the 122dB case are shown in Figure 162. The magnitude of the acoustic pressure was not constant along the surface of the beam, as mentioned earlier, due to circular spreading. However, the difference in pressure between the ends of the beam was approximately 15%, which was deemed acceptable.

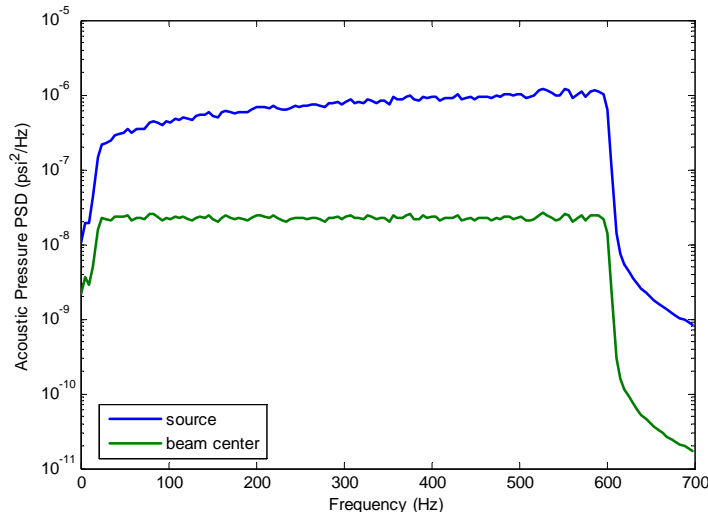


Figure 162. Acoustic pressure PSD at source and beam center at 122 dB

A finite-element model of the example problem was constructed using 36 two-node nonlinear beam elements for the structure and 2148 four-node linear acoustic elements for the air. The finite acoustic domain had a radius of 54 in. The finite element mesh is shown in Figure 163. The largest dimension for any of the air elements was 2.25 in which yielded approximately 14 elements per wavelength at 427 Hz, the frequency of the 3<sup>rd</sup> beam mode. The structural and acoustic meshes were coupled at coincident nodes. The acoustic mesh was refined near the surface of the beam to allow coincident nodes with relatively fine nodal spacing of the beam. The outer boundary of the acoustic mesh was modeled with infinite acoustic elements employing the wave envelope formulation of Astley [57]. The model had 105 structural and 2478 acoustic DOF. A coupled structural/acoustic finite element code written in MATLAB was used for the analyses. Selected analyses were also run in Abaqus to verify accuracy. Results from the two codes agreed closely.

Modal damping is an important factor in the acoustic response problem. Therefore, it was important that the example beam have modal damping ratios typical of real structures, i.e., less than 0.02. There are two primary sources of modal damping in a coupled computational model—structural and acoustic radiation. In the experiments of Section 4.1, the modal damping ratios in the first three modes of the beam were in the range of 0.001-0.003. The coupled FEM of the example problem here produced damping ratios from acoustic radiation alone of 0.015, 0.0003 and 0.0022. The damping ratio for the 1<sup>st</sup> mode of the model was much larger than the experiment due to the 2-D acoustic domain in the example compared to the 3-D radiation in the experiment. Conversely, the damping in the 2<sup>nd</sup> mode—an anti-symmetric mode that should have very low radiation damping—was much lower than the experimental value. The primary source of damping in the experiment was most likely structural. Thus, proportional damping was added to the structural model to increase the 2<sup>nd</sup> mode damping ratio to a more typical value while

adding minimal amounts to the 1<sup>st</sup> and 3<sup>rd</sup> modes. The final damping ratios for the three modes were 0.017, 0.002 and 0.004.

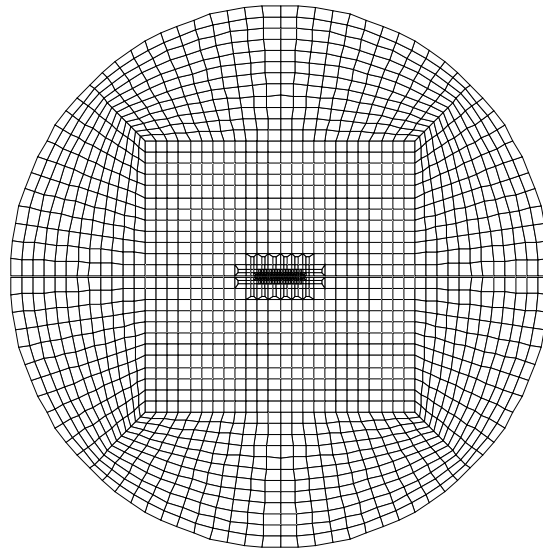


Figure 163. Example problem finite element mesh

The coupled FEM was used to perform three types of analysis; complex eigensolution, nonlinear static analysis and direct time integration. A complex eigensolution was performed to compute eigenvalues and right and left eigenvectors of the model. The eigenvalues and vectors were then used to form ROM's. The complex eigenvalues also yielded the acoustic radiation damping for the structure-dominated modes. Nonlinear static solutions were performed on the structural portion of the model to compute the nonlinear modal stiffness coefficients for the CROM's. Direct time integration of the full coupled model was performed to compute displacements of the beam and pressures at selected points in the acoustic domain. A time step of 1e-5 s was used for the full-order integration. The full-order results were used for comparison with reduced-order model results.

Linear simulation of three CROM's was performed. The first model used only the complex mode pairs of the lowest three structure-dominated modes. This model will be referred to as the three-mode model. The second model used the three structural modes plus 10 acoustic-dominated modes to better capture the acoustic excitation from the source. This is the 13-mode model. The 10 acoustic modes were modes 1-6 and 9-12 which were all critically damped. The third model used all the modes up to 470 Hz which included the three structural modes and will be referred to as the 120-mode model. Nonlinear simulations were performed on the three-mode CROM and a second model consisting of the three structural modes plus eight acoustic modes. Acoustic modes were selected using a trial and error process and the acoustic mode equations did not contain any nonlinear terms. However, nonlinear terms coupling the acoustic modes and the structural modes were included. Quadratic nonlinear terms were neglected for all ROM's since they are negligible for a straight beam. The simulations were performed in MATLAB with a trapezoidal rule integrator for the first-order complex modal equations. Numerical integration was performed with a time step of 5e-5 s. Note that both conjugate equations were integrated for each mode that was not critically damped.



Simulations were performed with two forms of acoustic loading. The first form was the shaped random signal applied at the source point as described above. In addition, forces equivalent to the time history of the acoustic loading at the surface of a rigid beam were applied directly to the beam. This direct loading simplifies the CROM since a set of acoustic modes was not needed to model the acoustic propagation from the source. These two forms of loading will be referred to as acoustic loading and direct loading, respectively.

A nonlinear ROM of the beam without the acoustic domain was constructed for comparison to the coupled models. Modal damping ratios from the full coupled model with added structural damping were used. This ensured that all ROM's used the same damping ratios. The simulations were performed with the direct loading used for the CROM's.

Results of modal analysis and time simulations of the example problem will be presented next. First, the resonant frequencies, modal damping ratios and mode shapes will be discussed. Next, results of nonlinear simulations of a full-order model will be presented followed by comparison with an uncoupled beam model. Finally, linear and nonlinear simulation results for the CROM's will be compared to full-order coupled model simulations. Displacement PSD's at the center of the beam are used to display the results of all models in the following discussion. No predictions of acoustic pressures are presented. It should be noted, however, that the acoustic pressures in the lower half of the acoustic domain were accurately predicted for each case in which the beam displacements were accurately predicted. Acoustic radiation from the beam was the only source of sound in the lower domain. Acoustic pressures in the upper half domain were not accurately predicted, in general. This was due to an insufficient modal basis to capture the sound radiation from the source.

Resonant frequencies and modal damping ratios for the first 20 eigenvalues plus the 2<sup>nd</sup> and 3<sup>rd</sup> structure-dominated modes of the example problem are shown in Table 30. Note that the structural modes are lightly damped and the acoustic modes are heavily damped. It is also interesting that only 6 modes (3 conjugate pairs) out of the first 120 modes are structural modes. All the other modes are acoustic in nature. As discussed above, these modes are computational artifacts of the infinite acoustic domain and are not physical in nature. This presents a problem, in general, in performing an eigensolution of a coupled model. Typically only a few structural modes are sought, but many modes may need to be computed to find the desired structural modes. The first three resonant frequencies of an uncoupled beam model are included in Table 30 for comparison. A small mass-loading effect is evident when comparing the coupled and uncoupled beam frequencies. Mode shapes of the first three structure-dominated modes are shown in Figure 164. The magnitude of the complex-valued pressure field is shown in the figure with a relative scale to the right of each plot. The beam displacements and acoustic pressures are arbitrarily scaled. Notice that the pressure decreases as the distance from the beam increases, indicating acoustic radiation from the beam.

Power spectral densities of beam center displacement estimated from linear and nonlinear simulations of the full-order model with acoustic loading are shown in Figure 165 for an excitation level of 152 dB. The linear curve shows distinct resonant peaks for the 1<sup>st</sup> and 3<sup>rd</sup> structural modes. The second structural mode does not appear since it is an anti-symmetric mode with a node at the beam center. The nonlinear PSD in the figure is very different from the linear

response. The first mode resonant peak is much broader and shifted to the right—a classic indication of cubic nonlinearity. The nonlinear response also has a much lower peak amplitude. The same characteristics are evident for the third structural mode near 420 Hz in the linear response. The root mean square (RMS) displacement of the linear response is 0.066 in compared to 0.031 in for the nonlinear curve.

Table 30. Modal Frequencies and Damping Ratios for the Example Problem

Mode No.	Coupled Model			Uncoupled Beam Freq. (Hz)
	Description	Freq. (Hz)	Damping Ratio	
1	A1*	4.2	1.00	
2	A2	4.2	1.00	
3	A3	24.8	1.00	
4	A4	24.8	1.00	
5	A5	29.2	1.00	
6	A6	29.3	1.00	
7/8	B1**	76.6	0.0173	79.0
9	A7	81.3	1.00	
10	A8	81.3	1.00	
11	A9	100.9	1.00	
12	A10	100.9	1.00	
13	A11	102.9	1.00	
14	A12	104.3	1.00	
15/16	A13	188.5	0.952	
17/18	A14	188.5	0.952	
19/20	A15	190.2	0.789	
35/36	B2	215.7	0.0019	217.7
101/102	B3	424.4	0.0042	426.7

\* Acoustic mode, \*\* Beam mode

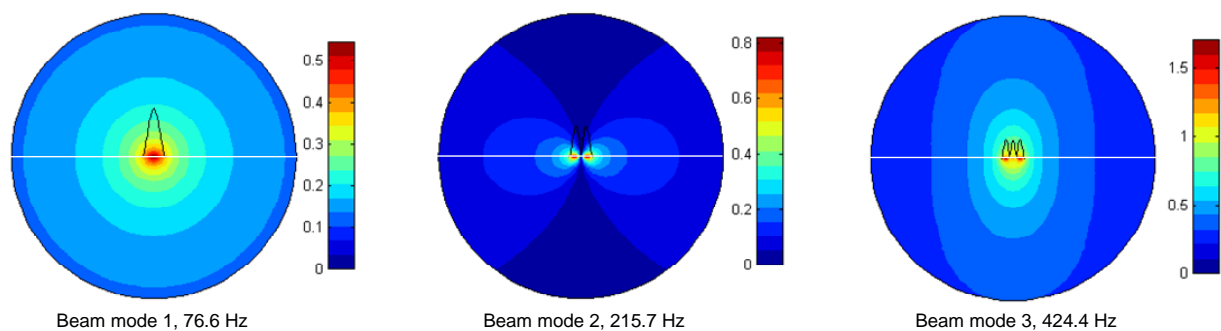


Figure 164. The magnitude of the first three complex structural modes of the coupled model

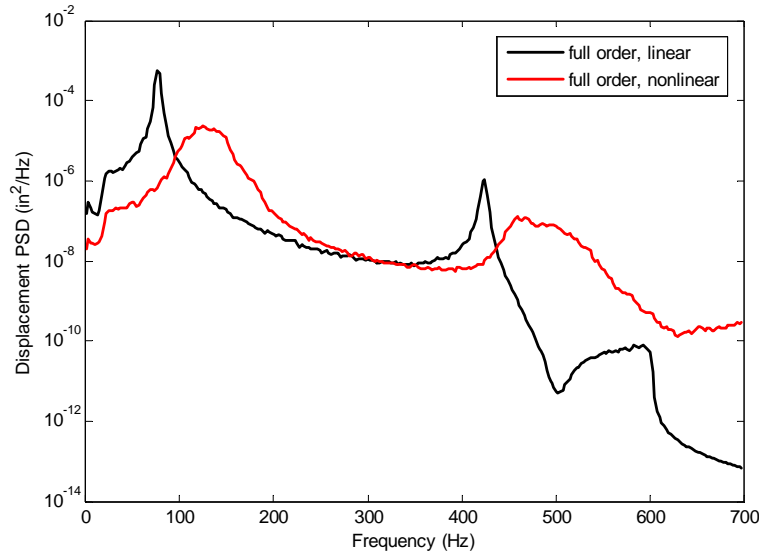


Figure 165. Beam center displacement PSD from linear and nonlinear simulation with acoustic loading of the full-order model at 152dB

The nonlinear response of the full-order model with acoustic loading from the source is compared to that with direct loading in Figure 166 at the 152dB input level. The PSD's of beam center displacement for the two loading cases are virtually identical. This result means that the loading can be uncoupled from the beam response. This is advantageous in that the modal basis for the CROM need only reproduce beam response. It will be shown below that several acoustic-dominated modes are needed in the basis to adequately model the acoustic radiation from the source. Thus, if direct loading can be used, only structure-dominated modes are needed in the CROM.

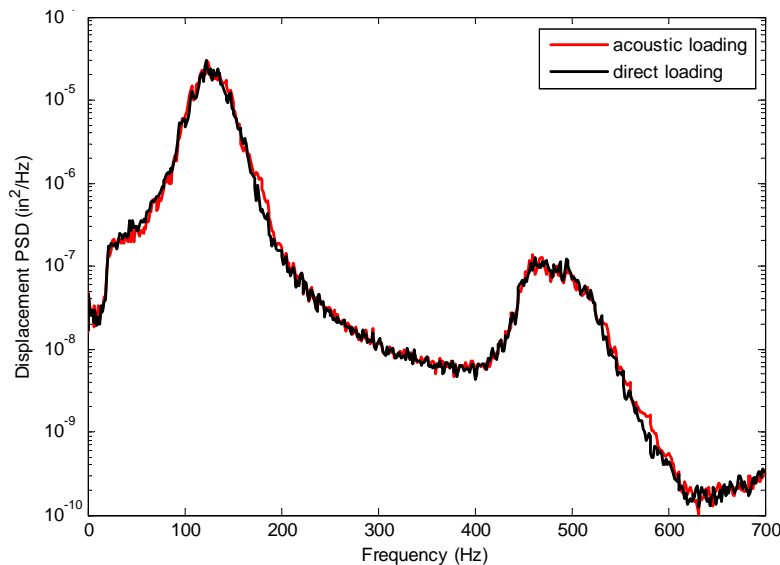


Figure 166. Beam center displacement PSD from nonlinear simulation of the full-order model with acoustic loading and direct loading

The work presented in Section 4.4 showed that neglecting acoustic coupling can result in significant errors in predicted nonlinear response of thin plates. Figure 167 shows the nonlinear

response of the beam in the example problem uncoupled from the air. PSD's of beam center displacement are shown for the 122 and 152dB cases. Results from full-order simulations of the coupled model are shown in the figure for comparison. The beam-only model used modal damping ratios from the full-order model. The first impression from the figure is that the beam-only model agrees very well with the full model at the lower excitation level where the response is nearly linear. However, at the higher excitation level, the beam-only model is too nonlinear. The resonant peaks are broader and shifted to the right. The RMS displacements are 0.037 in and 0.031 in, respectively, for the beam-only and full models at 152dB. The error in the beam-only model is due to lack of coupling with the air. In a coupled model, the beam can re-radiate sound into the air, effectively reducing the excitation level. This effect would be more pronounced if the beam had lower modal damping ratios.

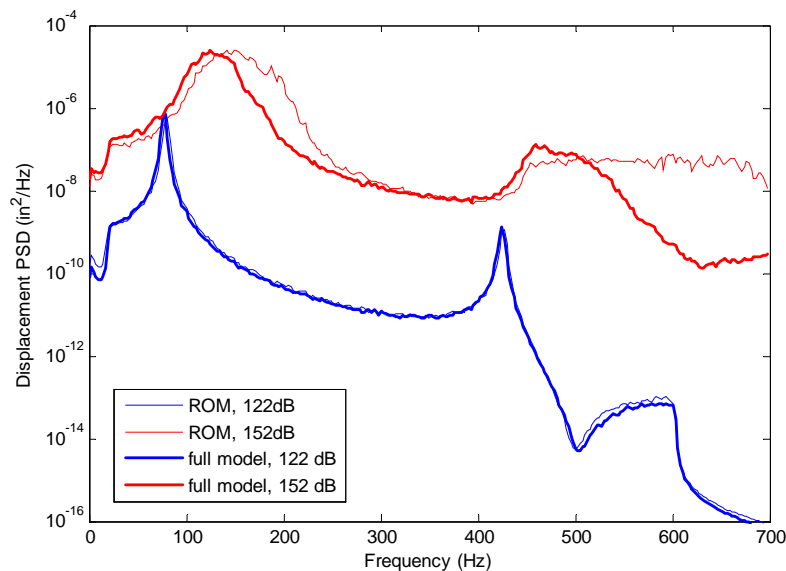


Figure 167. Beam center displacement PSD from nonlinear simulation of the structure-only ROM with direct loading and the full-order model with acoustic loading at 122 and 152dB

Two CROM's were used to predict linear response of the example problem with acoustic excitation at the 120 dB excitation level. PSD's of beam center displacement for the three-mode and 120-mode linear CROM's are plotted in Figure 168 with the full-order model displacement for comparison. Both CROM's predicted the response near the beam resonances reasonably well, although the three-mode model slightly over-predicts the 3<sup>rd</sup> mode peak amplitude. However, the three-mode CROM did not predict the center displacements accurately at frequencies away from the beam resonant peaks. This disagreement is not quantitatively significant, but still indicates a deficiency in the model. The off-resonance agreement is seen to improve greatly with the 120-mode model. This lack of accuracy of the three-mode model is due to the fact that the 3 structure-dominated modes did not accurately capture the spatial distribution of acoustic pressure from the source. The 120-mode model, which had many acoustic dominated modes in its basis, accurately predicted the off-resonant response up to 450 Hz. Using a set of synthesized vectors analogous to Ritz vectors, as are used in conventional structural analysis, might improve the prediction. However, re-orthogonalization of these vectors in the complex state space form is problematic.

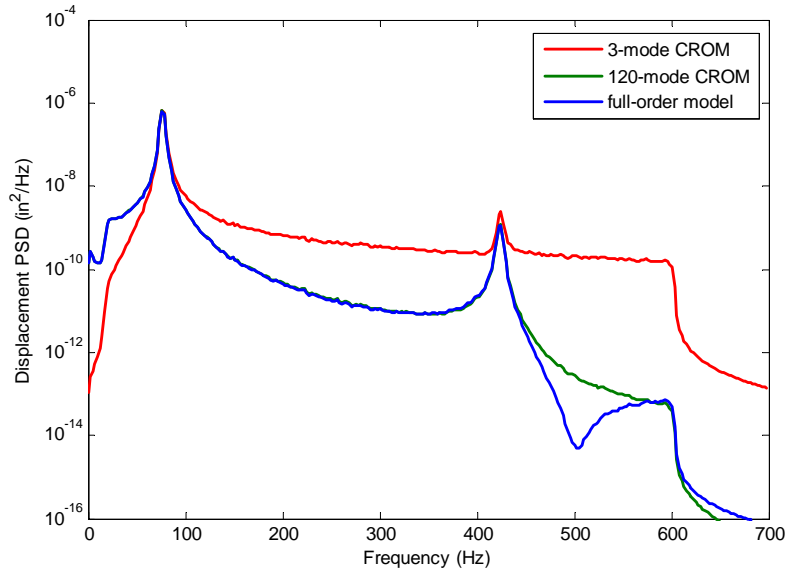


Figure 168. Beam center displacement PSD from linear simulation with acoustic loading of three-mode and 120-mode CROM's and full-order model at 122dB

The predicted response at the beam center improves dramatically when direct excitation is used in a linear simulation. Figure 169 shows the PSD of beam center displacement for the three-mode linear CROM with direct excitation compared to full-order model results. The two curves in the figure are now identical except near the anti-resonance at 500 Hz. It is obvious that the model with only structure-dominated modes is an accurate representation of the full-order model if the acoustic propagation from the source does not need to be modeled.

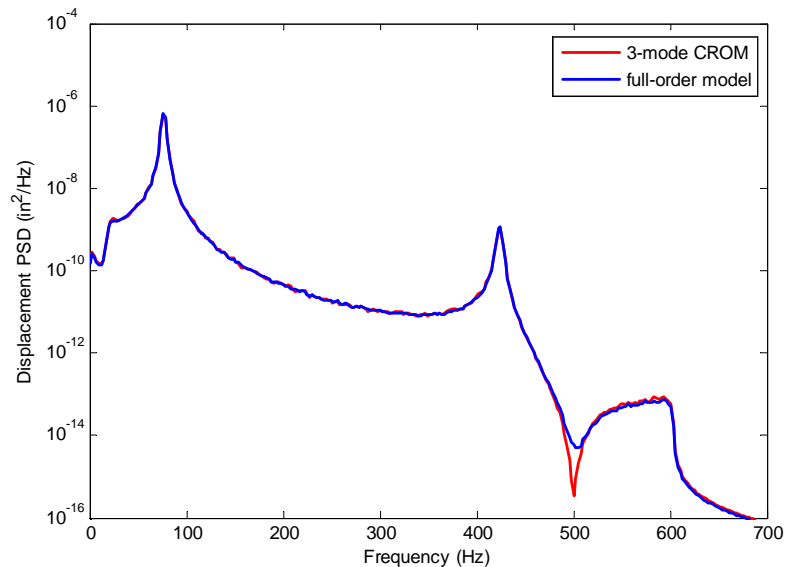


Figure 169. Beam center displacement PSD from linear simulation with direct loading of a three-mode CROM and the full coupled model at 122 dB

Nonlinear response simulations were performed with two CROM's. The first model was the three-mode model from the linear simulations with nonlinear stiffness terms added. The second model used the three structure-dominated modes and eight acoustic-dominated modes. The

acoustic modes were chosen using a trial and error process. It is important to note that no nonlinear stiffness terms were included in the acoustic mode equations, but nonlinear terms which coupled the structural and acoustic equations were added to the structural mode equations. Beam center displacement PSD's from nonlinear simulations with acoustic excitation are shown in Figure 170 for the CROM's and the full-order model. The three-mode model response shows very poor agreement with the full model. The response is much too nonlinear. In contrast, the 11-mode model agrees very well with the full model. As in the linear simulations, the addition of acoustic-dominated modes improves the accuracy of the results. However, in the nonlinear case, the acoustic-dominated modes also add nonlinear coupling among the structure-dominated modes. The PSD of beam center displacement from the nonlinear simulation of the three-mode CROM with direct excitation is shown in Figure 171. As with the linear simulations, the three-mode model agrees very closely with the full-order results. The PSD from a three-mode, uncoupled beam ROM is also included in the figure. The CROM produced a much better prediction of the dynamic response of the beam than the ROM.

Results of linear and nonlinear ROM simulations with shaped random acoustic excitation and equivalent direct excitation were compared to full-order simulations. The simulation results with acoustic excitation agree well with full-order results if the CROM used a set of acoustic-dominated modes in addition to the structure-dominated modes in the excitation frequency range. The results with direct excitation showed very good agreement using only the structure-dominated modes. The method is somewhat more complicated to implement than the reduced-order methods developed for uncoupled structural models in that the modal equations occur in complex conjugate pairs. Further investigation is needed in simplifying the complex modal form and applying the method to more realistic 3-D problems.

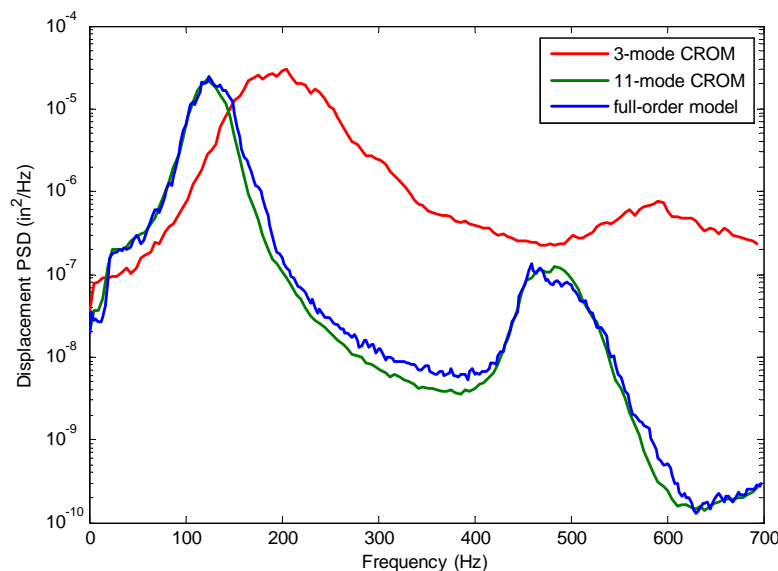


Figure 170. Beam center displacement PSD from nonlinear simulation with acoustic loading of three-mode and 11-mode CROM's and the full-order model at 152dB

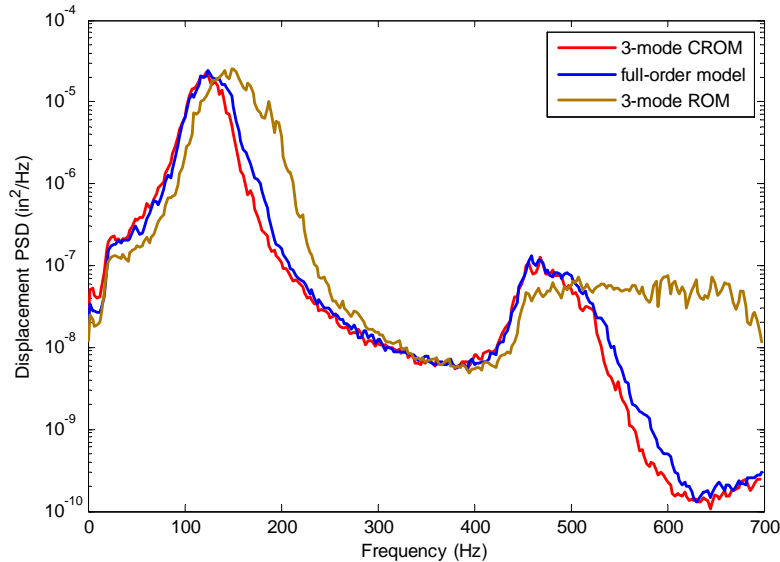


Figure 171. Beam center displacement PSD from nonlinear simulation with direct loading of a three-mode CROM, the full-order model, and a three-mode ROM at 152dB

#### 4.6.2 2D Beam Coupled Structural-Acoustic Examples using the Uncoupled Modes Method

The structural-acoustic response of a clamped-clamped beam coupled to interior and exterior acoustic domains was investigated using nonlinear ROM's computed from modes of the uncoupled structure and acoustic domains. Three examples were studied; a clamped beam at the end of a long cavity, a clamped beam on the side of a long cavity, and a clamped beam in a baffled exterior domain. All three examples were two-dimensional. Coupled nonlinear ROM's were computed from the modes of the uncoupled domains and simulation results are compared to full-order finite element results. This work was originally published as Reference [29].

In the first example, a two-dimensional rectangular cavity is filled with air. Three sides of the cavity are rigid. The fourth side (the top side) is a flexible beam. The dimensions of the cavity were adjusted so that the natural frequency of an acoustic mode was close to the natural frequency of a structural mode. Damping was added to the acoustic cavity. The beam was loaded mechanically, so that results from a structural ROM can be compared to those from a coupled ROM.

A clamped-clamped beam was selected as the flexible structure in this example. The beam was 9.0 inches in length, and was perfectly clamped at its two ends. The beam had a thickness of 0.031 inch and a width of 1 inch. The beam was made from high-carbon steel with a Young's modulus of 29.7 Mpsi, a shear modulus of 11.6 Mpsi, and a mass density of  $7.36 \cdot 10^{-4}$  lb-s<sup>2</sup>/in<sup>4</sup>. The beam is identical to that used in Section 4.1, except here a unit width is used so that a 2D model can be used for the associated acoustics. The beam was modeled with 36 two-node beam elements (B21 elements in Abaqus). The beam was loaded transversely by a dynamic force at the center of the beam. The amplitude of the force was a band-limited normal random variable (1-500 Hz) with an RMS value of 0.2 lb.

The IC method was used to construct a structural ROM. Two structural modes were retained. These are the first two symmetric bending modes. The natural frequencies of these modes were 79.1 and 427.6 Hz. The parameters for the model were identified and compared to those in reported in Section 4.1.

The cavity below the beam was 9 inches by 85 inches and filled with air at standard temperature. The density of the air was  $1.13 \times 10^{-7} \text{ lb}_f \cdot \text{s}^2/\text{in}^4$ . The bulk modulus was 20.6 psi. The cavity was modeled in Abaqus using AC2D4 elements. The mesh on the cavity was  $36 \times 85$  with an element size of 0.25 inches by 1 inch. The nodes of the beam elements coincided with the acoustic nodes at the top of the cavity.

The acoustic modes were obtained from the coupled FEM with the beam DOF constrained. The first nine acoustic modes were retained. The first mode has zero frequency and a constant pressure. The other eight modes are shown in Figure 172, where red indicates a maximum pressure and blue indicates a minimum pressure. All eight modes are axial modes with anti-nodes occurring at the top and bottom of the cavity. The second mode has one nodal line; the third mode has two nodal lines, and so on. The frequencies of the modes occur approximately every 79 Hz. The primary acoustic mode of interest is the second mode, with a natural frequency of 79.4 Hz. This frequency is very close to the first structural frequency of 79.1 Hz. The natural frequencies of the eighth and ninth acoustic modes were 554 and 633 Hz. These modes are outside the frequency range of interest, but were included to provide a more complete modal basis.

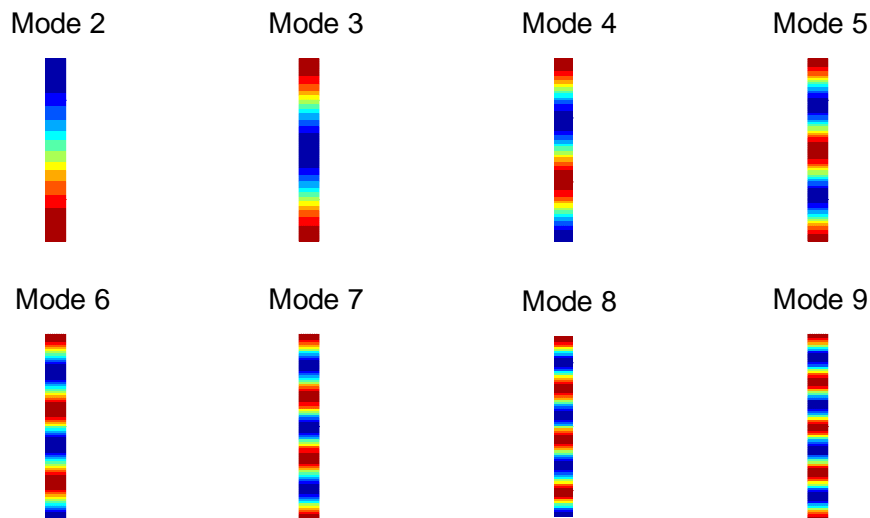


Figure 172. The uncoupled acoustic modes of a rectangular cavity.

Mass proportional damping was added to the structure. The first structural mode had damping equivalent to 1% of critical. Mass proportional damping was also used in the acoustic portion of the model, this value was chosen so that the second acoustic mode had damping equivalent to 5% of critical. (Mass proportional damping is applied to acoustic elements in Abaqus using volumetric drag.) The modal coupling matrix for the coupled ROM was determined using the scheme presented in Section 3.6. The acoustic modal damping was determined from the mass proportional damping constant.



The example problem was first run using linear models. Figure 173 shows the PSD of the transverse displacement at the beam center from a linear structural ROM (i.e. the nonlinear terms of nonlinear ROM set to zero), a linear coupled ROM, and the results using a frequency domain, linear, harmonic solution in Abaqus. The solution for the structural ROM and the coupled ROM used time domain integration. A Newmark-Beta scheme written in MATLAB was used to integrate the models. The scheme used the average acceleration method with no artificial damping. The two equations for the coupled ROM were integrated simultaneously to provide direct coupling. The results show that the effect of adding the acoustics to the model is similar to effects of a damped mechanical vibration absorber. The results also show good agreement between the coupled ROM and the Abaqus results.

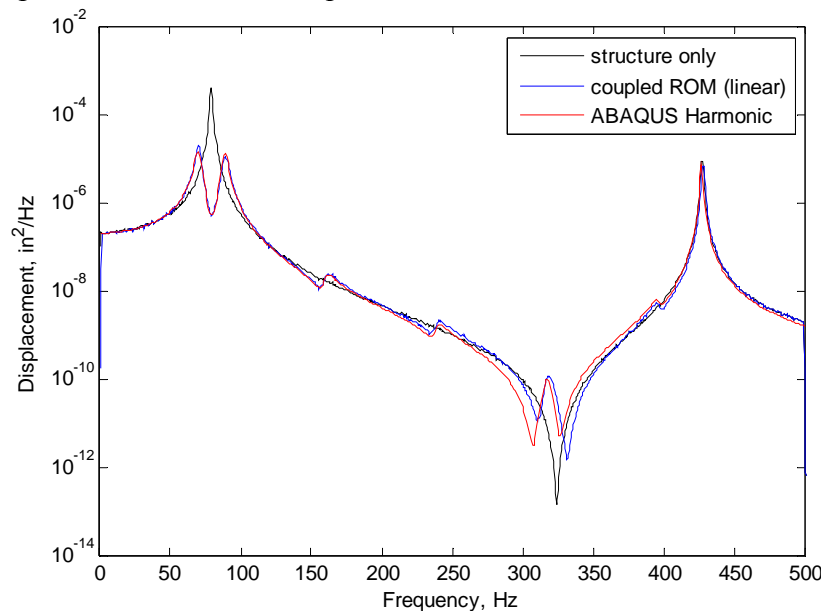


Figure 173. The displacement PSD of the beam center using linear models.

Next, the example problem was run using nonlinear models. Figure 174 shows the PSD of the response using the nonlinear structural ROM, a nonlinear coupled ROM, and the results using an Abaqus implicit integration. Again, the Newmark-Beta scheme was used to integrate the ROMs. The integration scheme used the average acceleration method with a time increment of  $2e-5$  sec. The Abaqus implicit integration used the same time increment. The Abaqus results are for 10 seconds of response compared to 60 seconds for both ROMs. The results also show good agreement between the coupled ROM and the Abaqus results. The results also show a marked reduction in the width of the resonant peak when the acoustic coupling is added to the model.

The second example used the same beam, but the dimensions of the acoustic cavity were increased to 9 inches by 480 inches and the beam was relocated along one of the long sides of the cavity. The ends of the beam are located 160 and 169 inches from one end of the cavity. The boundary along the acoustic cavity is rigid except for the beam. The finite-element model and the corresponding ROM of the beam remains the same as the previous example. The acoustic cavity is meshed with AC2D4 elements. The elements are 0.25 inch by 1 inch in the region near the beam (150 inches to 180 inches along the length of the cavity) and are 1 inch by 1 inch in the

remainder of the model. A total of 5130 elements are used in the acoustic model. Again, the beam nodes coincided with a set of acoustic nodes.

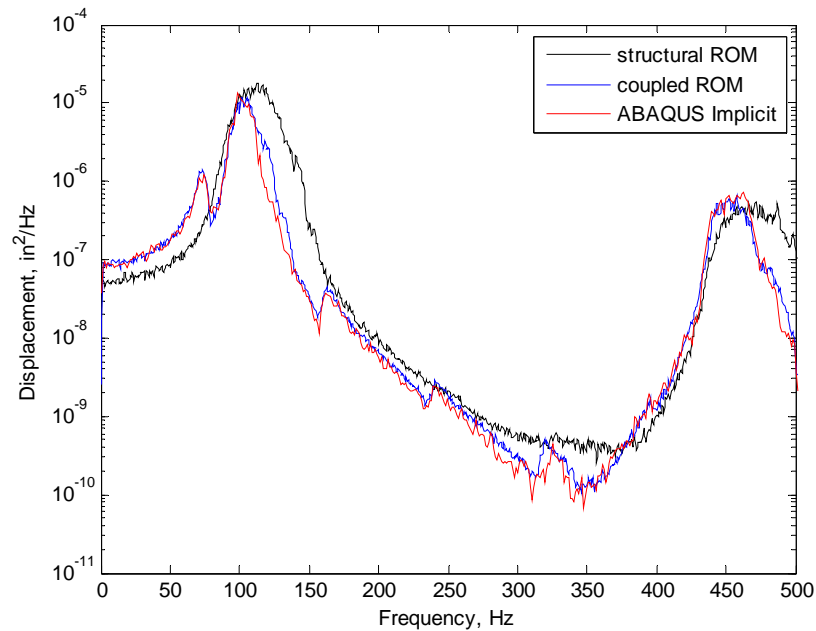


Figure 174. The displacement PSD of the beam center using nonlinear models.

The acoustic modes were obtained using Abaqus. The frequency spacing of the modes was approximately every 14 Hz. In this configuration, the first beam frequency was between the sixth and seventh acoustic modes at 70.3 and 84.4 Hz, respectively. All the acoustic modes with frequencies under 500 Hz were kept (36 modes) in the acoustic modal model. All the modes were axial acoustic modes. The modes were similar to the acoustic modes in the previous example with the second mode containing one nodal line, the third mode containing two nodal lines, etc. Since the beam is located on the long side the cavity, the nodal line locations are important. If the beam straddles a nodal line, the coupling coefficient for that acoustic mode will be small. The nodal line closest to the beam was 120 inches from the end of the cavity for the sixth acoustic mode and 144 inches from the end for the seventh acoustic mode. With the beam center 164.5 inches from the end of the cavity, the two acoustic modes should couple well with the structure.

Again, the beam was loaded mechanically, so that results from a structural ROM could be compared to those from a coupled ROM. The forcing location and statistics remained the same as the previous example. Damping for the structure also remained the same as the previous example. The same mass proportional damping constant for the acoustic elements was used, resulting in 5.6% damping for the sixth acoustic mode and 4.7% damping for the seventh acoustic mode. The acoustic modal damping was determined from the mass proportional damping constant.

This example problem was run using nonlinear models. Figure 175 shows the PSD of the response using the nonlinear structural ROM, a nonlinear coupled ROM, and the results using an Abaqus implicit integration of the coupled FEM. All three time integrations were performed with

time increments of  $2e-5$  seconds. The results also show good agreement between the coupled ROM and the Abaqus results. The results also show a reduction in the response due to the acoustic coupling.

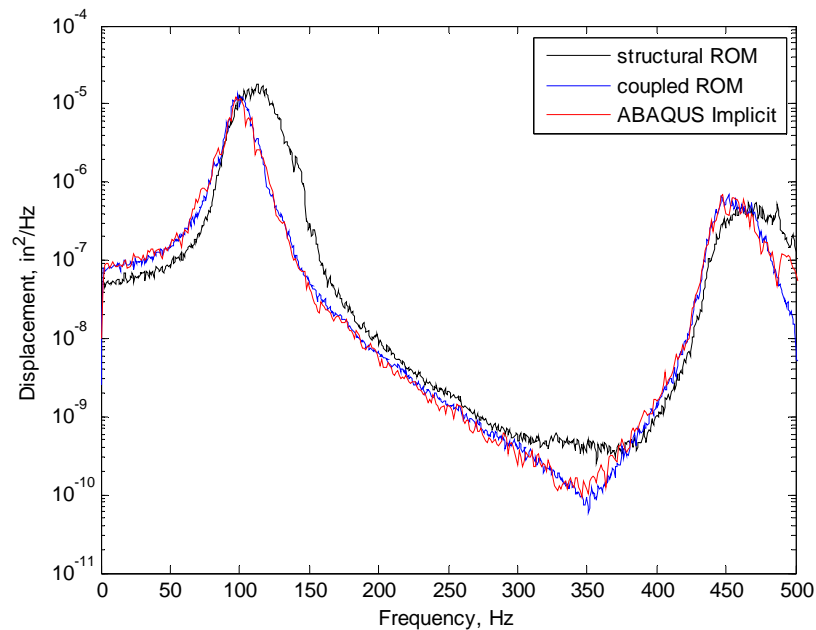


Figure 175. The displacement PSD of the beam center using nonlinear models.

In this example, it is shown that the acoustic modes are capable of reducing structural vibration despite the fact that they are not closely tuned to the resonant structural frequency. The acoustic modes are heavily damped which makes the vibration absorber effect more tolerant of mistuning. The acoustic modes also appear every 14 Hz which in effect establish vibration absorbers at regular frequency intervals.

The final example is a beam in an infinite baffle at the center of an infinite circular acoustic domain. This is the same configuration presented in Section 4.6.1. A monopole source is located on the baffle to the right of the beam in the upper half of the domain. The source is driven by a random acoustic force time history with a shaped frequency spectrum. The source generates a circular acoustic wave which propagates along the beam. This source configuration is used to approximate a plane acoustic wave propagating along the upper surface of the beam. The acoustic source point is located 22.5 in from the end of the beam. The problem is shown schematically in Figure 161.

A finite-element model of the acoustic domain was constructed using 2148 four-node linear acoustic elements for the air. The finite acoustic domain had a radius of 54 in. The finite element mesh is shown in Figure 163. The structural and acoustic meshes were coupled at coincident nodes. The acoustic mesh was refined near the surface of the beam to allow coincident nodes with relatively fine nodal spacing of the beam. The outer boundary of the acoustic mesh was modeled with infinite acoustic elements employing the wave envelope formulation of Astley[57].

The coupled model had 105 structural and 2478 acoustic DOF. A coupled structural/acoustic finite element code written in MATLAB was used for full-order analyses.

The full-order mass, stiffness, and damping matrices were available from the MATLAB finite-element model. It was a simple matter to partition the matrices and extract the acoustic mass, stiffness, and damping matrices. An eigensolution produced the uncoupled, undamped, acoustic modes and frequencies. The acoustic modal damping matrix was obtained by transformation of the physical acoustic damping matrix using the acoustic mode shapes. The acoustic damping is due to the infinite acoustic elements and is not proportional. Therefore the acoustic modal matrix is not diagonal.

The structural ROM was the same as previously used except for the modal damping. In this example, proportional mass damping was added to the structural model to obtain damping ratios of 0.017 and 0.004, respectively for the two retained structural modes. This was done to match the results in Section 4.6.1. The coupling matrix in physical coordinates was obtained from partitioning the full-order stiffness matrix and then transforming to produce the modal coupling matrix. The first 100 modes of the acoustic model were retained in this example. The frequencies of the acoustic modes range from 27 to 781 Hz. In contrast to the complex acoustic modes used in Section 4.6.1, all the acoustic modes used here were real. The acoustic modes do not represent any resonant acoustic behavior. The modes are a set of mathematical basis vectors. Pressure contours for the first twelve acoustic modes are shown in Figure 176. Note that because of the infinite baffle between the two hemispheres, the mode shapes appear in pairs.

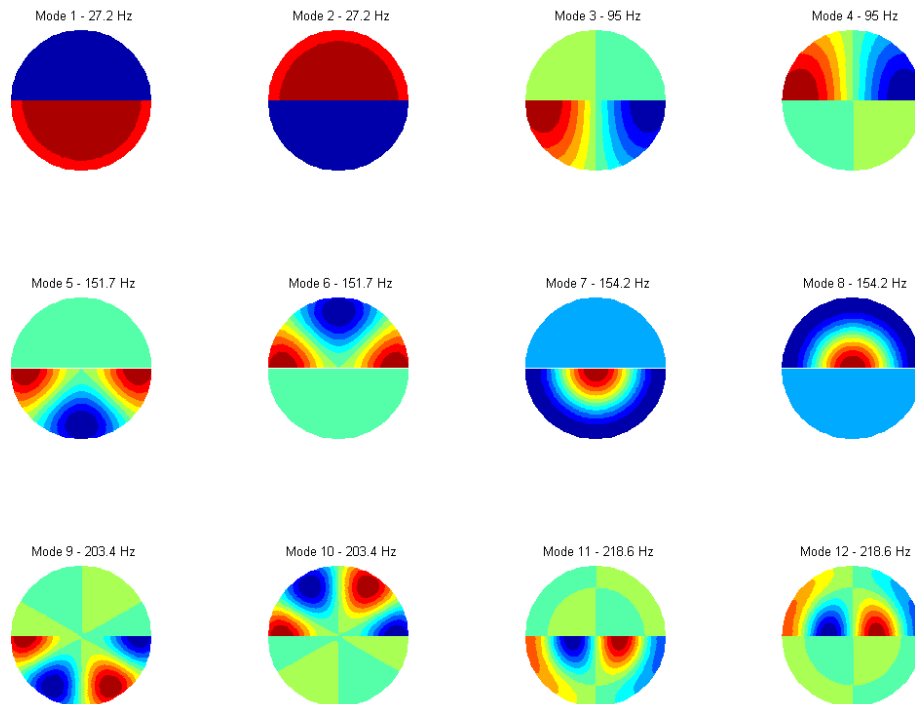


Figure 176. The first twelve acoustic mode shapes for the exterior example.

The desired acoustic loading at the center of the beam was a grazing-incidence acoustic wave with a random time history, a flat frequency spectrum from 20-600 Hz, and overall sound

pressure levels (OASPL) of 152dB. The frequency spectrum of acoustic pressure at the source point had to be “shaped” to achieve the desired flat spectrum at the beam, due to the dynamic characteristics of the acoustic domain. The shaping is achieved through simulation results with an acoustic only model. The input frequency spectrum at the source was adjusted to obtain a flat spectrum at the beam center. This process was done in Section 4.6.1 using the full-order model. It is accomplished here using the acoustic modal model.

The coupled ROM was integrated using the Newmark-Beta scheme with a time increment of  $2.5\text{e-}5$  seconds. A time record of 60 seconds was obtained. Full-order results were obtained from the results in Section 4.6.1. The full-order results are shown in comparison to the coupled ROM results in Figure 177. Again good agreement is achieved. Despite the fact that 100 acoustic modes were retained, the computational time for integration was not markedly increased as compared to the other two examples. This is due to the fact that the acoustic modal equations are all linear.

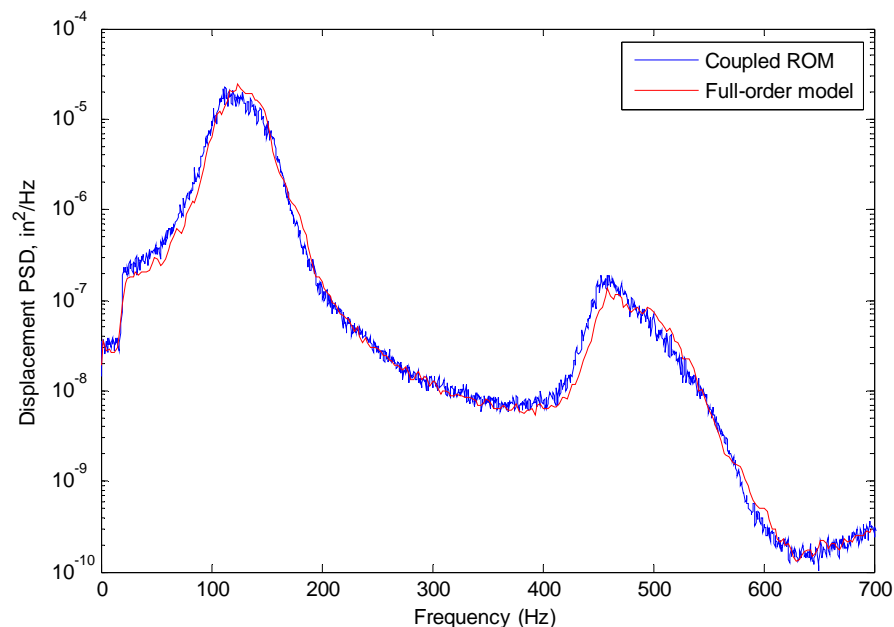


Figure 177. The displacement PSD at the center of the beam for the exterior example problem.

The examples presented above contained both interior and exterior acoustic behavior. The interior acoustic examples showed that acoustic modes can interact with structural modes in much the same way as mechanical absorbers. In the first example, this absorber behavior was demonstrated for a cavity tuned near a structural resonance. Linear results showed the absorber behavior clearly. Nonlinear results showed the acoustic resonance still reduces the structural vibration. Although multiple acoustic modes were included, this example was primarily a single structural resonance interacting with a single acoustic resonance.

The second example was a larger acoustic cavity that had multiple acoustic resonances. If these acoustic resonances are damped, they can interact with the structural resonance even if considerable mistuning between the structural and acoustic resonances is present. These multiple acoustic resonances were regularly spaced in frequency. In this example, the primary structural

resonance frequency fell between two acoustic resonances. The method successfully predicted the results for this multiple acoustic mode interaction problem.

The third example was an exterior acoustic example. In this example, there were no resonant acoustic modes to act like mechanical absorbers. Instead, the acoustic modes provided a mathematical basis to capture the acoustic radiation from the structure. This example shows that the coupled ROMs can successfully predict the structural response when the acoustic environment is non-resonant, highly damped, and is non-proportionally damped.

**THIS PAGE INTENTIONALLY LEFT BLANK**

## 5. CONCLUSIONS

This report has presented a summary of the evaluation, improvement, and application of nonlinear ROM's for predicting the response of aircraft panels subjected to high intensity acoustic loading. In the past decade, reduced-order modeling techniques have been developed to dramatically decrease the huge computational cost of nonlinear, random response prediction using finite element models. The product of these techniques, the nonlinear ROM, captures the geometric nonlinearity in a compact formulation that can be efficiently evaluated with time integration.

Several groups have studied the formulation and use of nonlinear ROM's. All of these works have been analytical or numerical studies. A major goal of this project was to provide a comparison of predictions from nonlinear ROM's with data from experiments. The primary method used was the method of McEwan [8, 9], also called the IC method. The attractive features of the IC method are twofold. First, the method can be implemented using existing commercial finite-element codes. Nonlinear ROMs are built by applying static loads to a FEM, reading the results into a separate computational code, and then estimating nonlinear parameters from the results. Second, the IC method produces a ROM without explicitly including a membrane basis. This has significant advantages. It reduces the number of equations in the ROM and the number of nonlinear terms to be evaluated. And it eliminates the need to identify which and how many membrane modes to include.

The major contribution of this project has been the demonstration of nonlinear ROM's using many example applications, both numerical and experimental. The set of experiments ranged from the simplest structure that exhibited geometric nonlinearity due to membrane stretching—a clamped-clamped beam—to one that demonstrated the complexities of curvature and combined loading. Numerical studies of similar configurations were conducted in parallel with the experimental studies. Experimental studies began with a clamped beam subjected to base motion on a large shaker. The majority of the experiments were conducted with a framed, flat plate. The framed plate was subjected to base motion on a shaker, base motion while in a vacuum, and acoustic loading in a progressive wave tube. The final set of experiments occurred with a curved panel subjected to acoustic loading in a progressive wave tube. The curved panel was tested at room and elevated temperatures.

In the process of understanding the experimental and numerical studies, several refinements and analytical improvements to the nonlinear ROM approaches were developed. The first analytical development was the introduction of the companion mode concept. The companion mode is an estimated mode that is used as a membrane basis in the construction of a nonlinear ROM. A similar concept has been developed as the dual mode concept by Mignolet's group [19, 20]. The companion mode concept was abandoned in this project because the IC method did not require a membrane basis in the estimation of the ROM. However, the companion mode concept eventually led to the ICE method. In the ICE method, an estimated membrane basis is used in a post-simulation step to synthesize membrane displacements and enable accurate calculation of stresses and strains. The ICE method is the major analytical contribution of this project.



The predictions from the ICE method agreed very closely with full-order simulations for all the numerical examples and the experimental in-vacuo plate tests. Comparisons with experimental data from the shaker test of the plate test article in air as well as all the acoustic tests suggested that there was coupling between the structure and the acoustic environment. As a structure vibrates, it radiates sound that provides damping and interacts with the acoustic loading, effectively changing the dynamics of the problem. Another contribution from this project was the development of a modeling approach for the coupled behavior. This modeling approach incorporated the earlier work on nonlinear ROM's to build a coupled structural-acoustic ROM. The coupled ROM was successfully demonstrated with numerical and experimental data.

Experiments with a heated curved panel prompted developments in the cold-modes approach for modeling temperature effects. This contribution extended the ICE method to combined environment problems. The effects of curvature required more modes and triple cubic terms in the ROM which resulted in additional static load cases. The need for additional load cases prompted the development of the constrained identification approach. The constrained approach utilizes mathematical dependencies among nonlinear coefficients in the modal equations to reduce the number of coefficients to be identified. The dependencies allow the identification to be performed with a much smaller set of load cases.

There were difficulties encountered with the nonlinear ROM's and the IC or ICE methods. Basis selection became more difficult as the structures became more complicated. This was demonstrated with the curved panel examples. Stronger coupling exists between symmetric, anti-symmetric, and out-of-band modes for non-planar structures. The size of a nonlinear ROM was not a problem with time integration, but was with model identification. As the number of modes grows, the number of static cases grows geometrically. The IC method is particularly vulnerable because it uses applied loads and parameter estimation. As the number of static cases grows, the possibility of diverging FEM solutions from the applied load problem grows. The selection of load amplitudes becomes more complicated and time consuming for the analyst. The possibility of ill-conditioning also grows in the estimation routine as the number of nonlinear parameters grows.

Stability issues surfaced with the models for curved structures. The time integration could be stable for modest acoustic loading, but might diverge for higher loading. In most cases, the stability problems were solved by re-estimating the ROM with more data. The stability problems increased with cold-modes models for curved structures and combined loading, but given a good set of load cases, the cold-mode models worked. However, stability problems with hot-modes models for curved structures were not resolved.

The prime difficulty in the prediction of experimental data is the construction of an accurate FEM. Modeling of in-plane boundary conditions for bolted or riveted structures is a primary source of error since nonlinear response involves membrane stretching. Another source is the preload that exists from assembly of the panel. It typically is very difficult to quantify this preload, yet it can have great effect on the natural frequencies. Care must be taken to determine whether error in a ROM prediction is due to error in the ROM formulation or error in the FEM on which the ROM is based. After all, the ROM is only an approximation of the FEM and cannot reproduce any physics not included in the FEM.

Another source of error is the modeling of the acoustic environment. For thin or lightly damped structures, the dynamics of the acoustic environment can couple with the structure. The acoustic environment is geometrically complicated and the absorption/reflection properties of the surroundings are generally unknown. Two methods for building coupled ROM's were investigated. The first method, based on a fully coupled FEM, produced good results but was impractical to implement due the need for complex modal vectors. The second method, based on uncoupled models of the structure and acoustic domain, was accurate and relatively simple to implement. Regardless of the method used, it can be difficult to determine whether the acoustic coupling is important enough to warrant a coupled model for a particular problem.

More technical work on the IC method is recommended. The sizing of applied loads is too dependent on user intuition in the current approach. A systematic approach for selecting modes to be included in the ROM is also needed. The current approach is based on linear analysis supplemented with engineering judgment. The approach proposed in [21-22] is promising, but requires integration of the full-model (which the ROM is supposed to eliminate). The method would benefit from more study of constrained identification. Constrained identification has the potential to dramatically lower the number of static load cases. It also produces a mathematically consistent model which anecdotal evidence suggests provide a more stable time integration. More investigation into hot-modes and cold-modes modeling is also warranted. Other technical hurdles include incorporation of temperature dependent material properties.

More work on the implementation of the IC method is also recommended. In this project, the method was implemented in a computing environment external to commercial finite-element codes. The ability to implement the method in a computing environment separate from the finite element code was a central motivation in pursuing the method. However, transfer of data between the finite-element code and the computation environment can be awkward and time consuming. The modular nature of the ROM building process should make it relatively straight forward for the end user to develop an integrated tool, possibly all within a commercial FEM code.

In summary, the primary conclusion of this study is that a nonlinear ROM with fewer than 10 equations can replace a FEM with thousands of DOF with little loss of accuracy. The nonlinear ROM can thus achieve orders-of-magnitude savings in computational cost. The reduction in cost will allow the ROM's to be used in design trade studies, something that is currently prohibitive with a full-order model.

**THIS PAGE INTENTIONALLY LEFT BLANK**

## 6. REFERENCES

1. Rogers, L., et al., "Durability Patch: Repair and Life Extension of High Cycle Fatigue Damage on Secondary Structures of Aging Aircraft," proceedings of the 1st Joint DoD/FAA/NASA Conference on Aging Aircraft, July 1997.
2. Rogers, L., et al., "Add-On Damping Treatment for the F-15 Upper-Outer Wing Skin," WL-TR-92-3069, July, 1992.
3. Mei, C. and Prasad, C., "Effects of Nonlinear Damping on Random Response of a Beam to Acoustic Loading," *J. of Sound and Vibration*, Vol. 117, pp. 173-186, 1987.
4. Reinhall, P. and Miles, R. N., "Effect of Damping and Stiffness on the Random Vibration of Non-Linear Periodic Plates," *J. of Sound and Vibration*, Vol. 132, pp. 33-42, 1989.
5. Rudder F. and Plumblee H., "Sonic Fatigue Design Guide for Military Aircraft," AFFDL-TR-74-112, 1975.
6. Mei, C., "Response of Nonlinear Structural Panels Subjected to High Intensity Noise," AFWAL-TR-80-3018, 1980.
7. Rizzi, S. and Muravyov, A., "Equivalent Linearization Analysis of Geometrically Nonlinear Random Vibrations Using Commercial Finite Element Codes," NASA/TP-2002-211761, 2002.
8. McEwan, M., Wright J.R., Cooper J.E., and Leung Y.T., "A Finite Element / Modal Technique for Nonlinear Plate and Stiffened Panel Response Prediction," AIAA-2001-1595, 2001.
9. McEwan, M., "A Combined Modal / Finite Element Technique For The Non-Linear Dynamic Simulation Of Aerospace Structures", PhD. Dissertation, Univ. of Manchester, England, 2001.
10. Nash, M., "Nonlinear Structural Dynamics by Finite Element Modal Synthesis", PhD. Dissertation, Imperial College, The University of London, 1977.
11. Mei, C. and Moorthy, J., "Numerical Simulation of the Nonlinear Response of Composite Plates under Combined Thermal and Acoustic Loading," NASA-CR-197426, 1995.
12. Shi Y., and Mei C., "A Finite Element Time Domain Modal Formulation for Large Amplitude Free Vibrations of Beams and Plates," *J. Sound and Vibration*, 193(2), 453-464, 1996.
13. Muravyov, A., and Rizzi, S., "Determination of nonlinear stiffness with application to random vibration of geometrically nonlinear structures," *Computers and Structures*, Vol. 81, 2003, pp. 1513-1523.

14. Hollkamp, J. and Gordon, R., "Modeling Membrane Displacements in the Sonic Fatigue Response Prediction Problem," AIAA-2005-2095, 2005.
15. Hollkamp, J., Gordon, R. and Spottswood, S., "Nonlinear Sonic Fatigue Response Prediction from Finite Element Modal Models: A Comparison with Experiments," AIAA-2003-1709, 2003.
16. Gordon, R., and Hollkamp, J., "Nonlinear Random Response of a Clamped Plate: A Well-Characterized Experiment," AIAA-2006-1924, 2006.
17. Hollkamp J., Beberniss, T., and Gordon R., "The Nonlinear Response of a Plate to Acoustic Loading: Predictions and Experiment," AIAA-2006-1928, 2006.
18. Hollkamp J., Gordon, R., and Beberniss, T.J., "Revisiting the Nonlinear Response of a Plate to Acoustic Loading," AIAA-2008-2233, 2008.
19. Mignolet, M. and Radu, A., "Validation of reduced order modeling for the prediction of the response and fatigue life of panels subjected to thermo-acoustic effects," *Structural Dynamics: Recent Advances, Proceedings of the 8<sup>th</sup> International Conference*, University of Southampton, UK, 2003.
20. Kim, K., Wang, X.Q., and Mignolet, M. P., "Nonlinear Reduced Order Modeling of Functionally Graded Plates," AIAA-2008-1873, 2003.
21. Rizzi, S. and Przekop, A., "System Identification-Guided Basis Selection for Reduced-Order Nonlinear Response Analysis," *J. Sound and Vibration*, 315, pp 467-485, 2008.
22. Przekop, A., Guo, X, and Rizzi, S., "Alternative Modal Basis Selection Procedures for Nonlinear Random Response Simulation," *Structural Dynamics: Recent Advances, Proceedings of the 10<sup>th</sup> International Conference*, University of Southampton, UK, 2010.
23. Nash, M., "Nonlinear Structural Dynamics by Finite Element Modal Synthesis", PhD. Dissertation, Imperial College, The University of London, 1977.
24. Hollkamp, J., Gordon, R., and Spottswood, S., "Nonlinear Modal Models for Sonic Fatigue Response Prediction: A Comparison of Methods," *J. of Sound and Vibration*, Vol. 284 (3-5), 2005, pp. 1145-1163.
25. Tiso, P. and Jansen, E., "A Finite Element Based Reduction Method for Nonlinear Dynamics of Structures," AIAA-2005-1867, 2005.
26. Rizzi, S.A., and Przekop, A., "The Effect of Basis Selection on Static and Random Acoustic Response Prediction using a Nonlinear Modal Simulation," NASA/TP-2005-213943, 2005.

27. Dowell, E., Gorman, G., and Smith, D., "Acoustoelasticity: General Theory, Acoustic Natural Modes and Forced Response to Sinusoidal Excitation, Including Comparisons with Experiment," *J. of Sound and Vibration*, Vol. 52 (4), 1977, pp. 519-542.
28. Gordon, R., and Hollkamp, J., "Coupled Structural-Acoustic Response Prediction with Complex Modal Models" AIAA-2009-2307, 2009.
29. Hollkamp J., and Gordon, R., "Coupling Acoustic Modal Models to Nonlinear Structural Reduced-Order Models," AIAA-2010-2542, 2010.
30. Gordon, R.W., and Hollkamp J.J., "Reduced-Order Models for Acoustic Response Prediction of a Curved Panel," AIAA-2011-2081, 2011.
31. Craggs, A., "The Transient Response of a Coupled Plate-Acoustic System using Plate and Acoustic Finite Elements," *J. of Sound and Vibration* Vol. 15(4), 1971. pp. 509-528.
32. Fahy, F. and Gardonio, P., Sound and Structural Vibration, Academic Press, Oxford, UK, 2007.
33. Foss, K.A., "Co-Ordinates Which Uncouple the Equations of Motion of Damped Linear Dynamic Systems," *Journal of Applied Mechanics*, Sept. 1958, pp. 361-364.
34. MSC.Nastran, Ver. 2004, MSC.Software Corporation, Santa Ana, CA, 2003.
35. Abaqus, Ver. 6.9, Dassault Systemes, Simulia Corp., Providence, RI, 2009.
36. MATLAB, Release 12.1, The Mathworks, Inc., Natick, MA, 2001.
37. Hilber, H.M., Hughes, T.J.R., and Taylor, R.L., "Improved Numerical Dissipation for Time Integration Algorithms in Structural Dynamics," *Earthquake Engineering and Structural Dynamics*, Vol. 5, pp. 283-292, 1977.
38. Newland, D.E., *An Introduction to Random Vibrations, Spectral and Wavelet Analysis*, Longman Scientific, New York, 1993.
39. Gordon, R., Hollkamp, J., and Spottswood, S., "Nonlinear Response of a Clamped-Clamped Beam to Random Base Excitation," *Structural Dynamics: Recent Advances, Proceedings of the 8<sup>th</sup> International Conference*, University of Southampton, UK, 2003.
40. Singh, G., Rao, G., and Iyengar, N., "Re-investigation of large-amplitude free vibrations of beams using finite elements," *J. of Sound and Vibration*, Vol. 143, pp. 351-355, 1990.
41. Schudt, J. A., "Identification and response of a nonlinear clamped-clamped beam with an axial tensile load: theory and experiment," Ph.D. Dissertation, The Ohio State University, 1994.

42. Yamaki, N. and Mora, A., "Non-linear vibrations of a clamped beam with initial deflection and initial axial displacement, Part II: Experiment," *J. of Sound and Vibration*, 1980, **71**(3), 333-346.
43. Feldman, M., Non-linear free vibration identification via the Hilbert transform. *J. of Sound and Vibration*, 1997, 208(3), 475-489.
44. Agneni, A. and Balis Crema, L., Analytic signals in the damping coefficient estimation. Proceedings of the International Conference: 'Spacecraft Structures and Mechanical Testing', Noordwijk, The Netherlands, Oct 1988, ESA SP-289, 133-139.
45. Rizzi, S., and Przekop, A., "The Effect of Basis Selection on Thermal-Acoustic Random Response Prediction using Nonlinear Modal Simulation," AIAA-2004-1554, 2004.
46. Przekop, A. and Rizzi, S.A., "Nonlinear Reduced Order Random Response Analysis of Structures with Shallow Curvature," AIAA-2005-2260, 2005.
47. Gordon, R.W., and Hollkamp, J.J., "Reduced-Order Modeling of the Random Response of Curved Beams using Implicit Condensation," AIAA-2006-1926, 2006.
48. Beberniss, T., Gordon R., and Hollkamp J., "The Effect of Air on the Nonlinear Response of a Plate," AIAA-2007-2085, 2007.
49. Silverman, S., Woolam, W.E., Cox, P.A. Jr., and Baker, W.E., "Damping of Vibrations of Clamped Flat Plates," U.S. Army Research Office Interim Technical Report No. AROD5615:4-E, June, 1972.
50. Beberniss, T., and Gordon R., "Finite Element Prediction of Acoustic Radiation Damping," AIAA-2008-2230, 2007.
51. Wallace, C. E., "Radiation Resistance of a Rectangular Panel," *J. of the Acoustical Society of America*, Vol. 51, pp. 946-952, 1972.
52. Wallace, C. E., "The Acoustic Radiation Damping of the Modes of a Rectangular Panel," *J. of the Acoustical Society of America*, Vol. 81, pp. 1787-1794, 1987.
53. Mangiarotty, R. A., "Acoustic Radiation Damping of Vibrating Structures," *J. of the Acoustical Society of America*, Vol. 35, pp. 369-377, 1963.
54. Oppenheimer, C. H. and Dubowsky, S., "A Radiation Efficiency for Unbaffled Plates with Experimental Validation," *J. of Sound and Vibration*, Vol. 199, pp. 473-489, 1997.
55. Cipolla, J., "Extension of Infinite Elements and Absorbing Boundary Conditions to Eigenanalysis of Submerged Structures," presented at the 76<sup>th</sup> Shock and Vibration Symposium, 2005.

56. "Sound Radiation Analysis of Automobile Engine Covers" ABAQUS Technology Brief, ABAQUS Inc. 2006.
57. Astley, R., "Transient Wave Envelope Elements for Wave Problems," *J. of Sound and Vibration* Vol. 192(1), pp. 245-261, 1996.
58. Hollkamp J., Gordon, R., and Beberniss, T., "Coupling Acoustics to Nonlinear Structural Models: Predictions and Experiments," AIAA-2010-2544, 2010.
59. Hollkamp J., and Gordon, R., "The Importance of Structural-Acoustic Coupling in Progressive Wave Testing," AIAA-2011-2080, 2011.
60. Przekop, A., Guo, X., Azzouz, S., and Mei, C., "Reinvestigation of Nonlinear Random Response of Shallow Shells Using Finite Element Modal Formulation," AIAA-2004-1553, 2004.